Macro- and Micro-Structure Comparison of Ancient and Modern Iron-Rich Stromatolites

Presented by:

Adrian Arts

A thesis submitted in partial fulfillment of the requirements
for the degree of Master of Science in Geology

Faculty of Graduate Studies
Lakehead University

Abstract

The Gunflint and Biwabik Formations comprise the middle units of the Paleoproterozoic Animikie Group that crop out near the northwestern shore of Lake Superior. Stromatolitic units were investigated and sampled at 9 outcrop sites, 4 mine sites and in 12 drill-cores. Controversy exists as to whether the stromatolitic units that are now composed of chert were deposited as a silica gel or represent carbonate replaced by chert. There is also debate in the literature as to whether the iron oxides that coat many microfossils are primary or deposited during later diagenesis. Younger examples of siliceous stromatolites are very rare and iron hydroxides coating bacteria are only known from limited modern environments. Thus, understanding the primary composition of the Gunflint microbialites will provide information on ocean chemistry during this interval.

Three stromatolitic members have previously been described within these formations: the Lower Stromatolitic Member containing stromatolites that grow directly on the peneplained Archean basement or on the conglomerate which forms the base of the Animikie Group, a Middle Member 45 to 50 meters above the base, and the Stromatolitic Limestone Member at the top of the formation directly beneath the Sudbury impact layer. Based on this work, a new Upper Stromatolitic Member 50 meters below the Limestone Member in the Gunflint Formation was recognized. This member contains abundant iron-silica-carbonate-manganese oncolites, and is correlative to stromatolitic units described from the Biwabik. The oncolites represent a primary-to-very-early authigenic, precipitated mineral assemblage. The accretion of lacustrine ferromanganese nodules at the sediment-water redox boundary provides a modern analogue for the development of the oncolites described in this work.

The presence of exceptionally well-preserved, hematite coated microfossils, encased in chert in the relatively unmetamorphosed Middle Stromatolitic Member together with positive cerium and europium anomalies indicates that these sediments were deposited at a redox boundary in ocean waters near saturation with respect to silica and iron. Conversely, precipitates containing carbonaceous filaments in the Lower Stromatolitic Member contain a distinct negative cerium anomaly, indicating deposition in an oxidized environment.

Alternating manganese- and iron-rich laminae within the Upper Stromatolitic Member indicate a fluctuating redoxcline and oxygen levels in the shallow subtidal to peritidal environments within the Animikie Basin. The fluctuation reduces the Fe:Mn ratio, allowing for the less readily oxidized manganese to precipitate. The presence of dehydration cracks which cross-cut original ooid and stromatolitic laminae indicate that deposition of the silica and iron most probably occurred as amorphous gels of opal-A and iron hydroxides.

This study strongly indicates the Gunflint and Biwabik stromatolites were originally siliceous and formed by a different precipitation mechanism than that of Proterozoic carbonate stromatolites or modern agglutinated forms.

Acknowledgments

I would like to acknowledge the support, direction and guidance I have received from Dr. Phil Fralick, both in this work and my undergraduate degree. Also, I would like to recognize the support the geology faculty provided over the years.

I would also like to acknowledge the outstanding group of technicians at Lakehead University: A. Hammond, K. Traverner, G. Kepka, M. Sorokopud and G. Wu. A. Hammond and K. Traverner prepared countless thin sections and polished slabs, G. Wu for his guidance and training on the SEM, and G. Kepka for his assistance running geochemical analysis. The technicians make research significantly easier.

The staff at the drill core libraries in Thunder Bay, Ontario (M. Smyk, R. Cundari. D Campbell, and M. Puumala.) and in Hibbing, Minnesota (R. Oberhelman. and T. Pastika) and A. Wilis the geologist at Northshore Mine were all instrumental in acquiring the massive amount of sample material examined within this thesis.

A major thank you to my lab mate and field partner Chris Yip – it's been a good 3 years my friend. Also, I must extend my appreciation to my friends and family for their support, especially Yasantha, Megan, Justine and Dana who supported me through the good and bad.

Table of Contents

List of Tables

List of Figures

1 Introduction

1.1 Introduction

Microbialites are organo-sedimentary deposits made up of diverse microbial communities, which are indicators of the earliest life on Earth, dating back over 3 billion years (Riding, 1991). Despite initial controversy as to their biogenic origins, laminated forms termed stromatolites (Kalkowsky, 1908) are now widely accepted as biogenic in origin. The definition of what constitutes a stromatolite has undergone significant debate since its initial use by Kalkowsky (1908). Recently the term stromatolite was redefined as "a laminated, benthic, microbial deposit" (Riding, 1991), and this definition will be used in this work.

Two distinct formational mechanisms for the accretion of stromatolites are described in the literature; agglutination and precipitation. Agglutination is the process of trapping and binding ambient carbonate sediment suspended in the water to sticky substances produced by microbes termed extra polymeric substances (EPS) (Decho, 1990), secreted by microorganisms within the biofilm (Riding, 1991). The accumulation of organic debris (EPS, dead cells, etc.) and agglutinated sediment results in the large domes and columns presently forming in the Bahamas and Shark Bay, Australia (Logan, 1961; Dill, 1986). Conversely, the very fine-grained nature of many ancient stromatolites has led researchers to believe they represent authigenic mineral precipitates (Riding, 2000).

Various extant bacteria can cause the precipitation of minerals from the surrounding environment either through biologically controlled mineralization, BCM, or biologically induced mineralization, BIM (Lowenstam, 1981; Lowenstam and Weiner, 1983; Frankel and Bazylinski, 2003). Direct BCM of minerals containing carbonate and iron oxides within the cell wall provide

vital function. An example of this is the precipitation of small, uniform, magnetite or greigite crystals within a cell creating chains of magnetosomes (Bazylinski *et al.,* 1995). These allow the cell to orientate itself using the earth's geomagnetic field. However, more common is the passive or active precipitation of various mineral species extracellularly due to BIM. Passive precipitation is often caused by cellular metabolic activity whereby organic by-products catalyze reactions resulting in mineral precipitation on the cell wall or EPS (Frankel and Bazylinski, 2003). Active precipitation of dolomite or siderite nanoglobules occurs within the EPS and at the cell wall. They provide nucleation sites for carbonate and iron hydroxide precipitation which can prevent the cell from being entombed (Bontognali *et al.,* 2007; Sanchez-Roman *et al.,* 2014).

Many of the stromatolites described from the rock record, as well as modern examples, are composed primarily of carbonate. However, stromatolites from the Gunflint and Biwabik Formations are composed of fine-grained, alternating bands of iron and silica, with only trace carbonate. Since their initial discovery, speculation as to whether they represent silicification and/or replacement of carbonate or are the result of direct silica and iron precipitation have been raised.

The objective of this research was to provide a detailed analysis of the stromatolitic horizons in the Gunflint and Biwabik Formations to determine whether these iron-silica-rich stromatolites represent primary mineralogy or if there is evidence for silicification of an earlier carbonate phase. In doing so, the Paleoproterozoic stromatolites will be compared to modern iron-manganese-rich microdigitate stromatolites forming in many modern freshwater lakes to provide a possible mechanism for the growth and development of the ancient stromatolites. Careful examination of the macro- and microstructures, biogenetic affinities, and mineralogy of both the modern and ancient samples will be reported to provide insight into the conditions

present in the nearshore marine environment where these stromatolites are believed to form. This will provide key information for determining redox boundary conditions in the Paleoproterozoic Animikie Basin.

1.2 Regional Geology

The Proterozoic eon (2.5 to 0.5 Ga) records a time of significantly different atmospheric and oceanic conditions. Widespread anoxia in the oceans and a reducing atmosphere favoured the deposition of massive iron-silica rich deposits known as banded iron formation (BIF) or granular iron formation (GIF) (Cloud, 1973; James, 1983; Simonson, 1985; Bunting, 1986; Simonson, 1987; Simonson and Hassler, 1996). Large Superior-Type iron formations host many of the world's largest iron ore deposits in Africa, Australia, the Baltic Shield, United States and Canada (Cloud and Licari, 1968; Walter *et al.,* 1976; Knoll and Barghoorn, 1976; Amard and Bertrand-Sarfati, 1997; Lager, 2001).

During the Paleoproterozoic (2.5 to 1.6 Ga) much of northwestern Ontario and northeastern Minnesota were submerged in what is now known as the Animikie Basin. Deposition in this basin records repeated transgressive-regressive cycles of the Animikie Sea over the continent of Columbia (Morey, 1983). The sediments deposited in this basin, collectively termed the Animikie Group, consist of six formations on two broad ranges; the Gunflint north of the Duluth Complex and the Mesabi south of the Duluth Complex (Figure 1). The corresponding formations are the Kakabeka Conglomerate and Pokegama Quartzite (basal

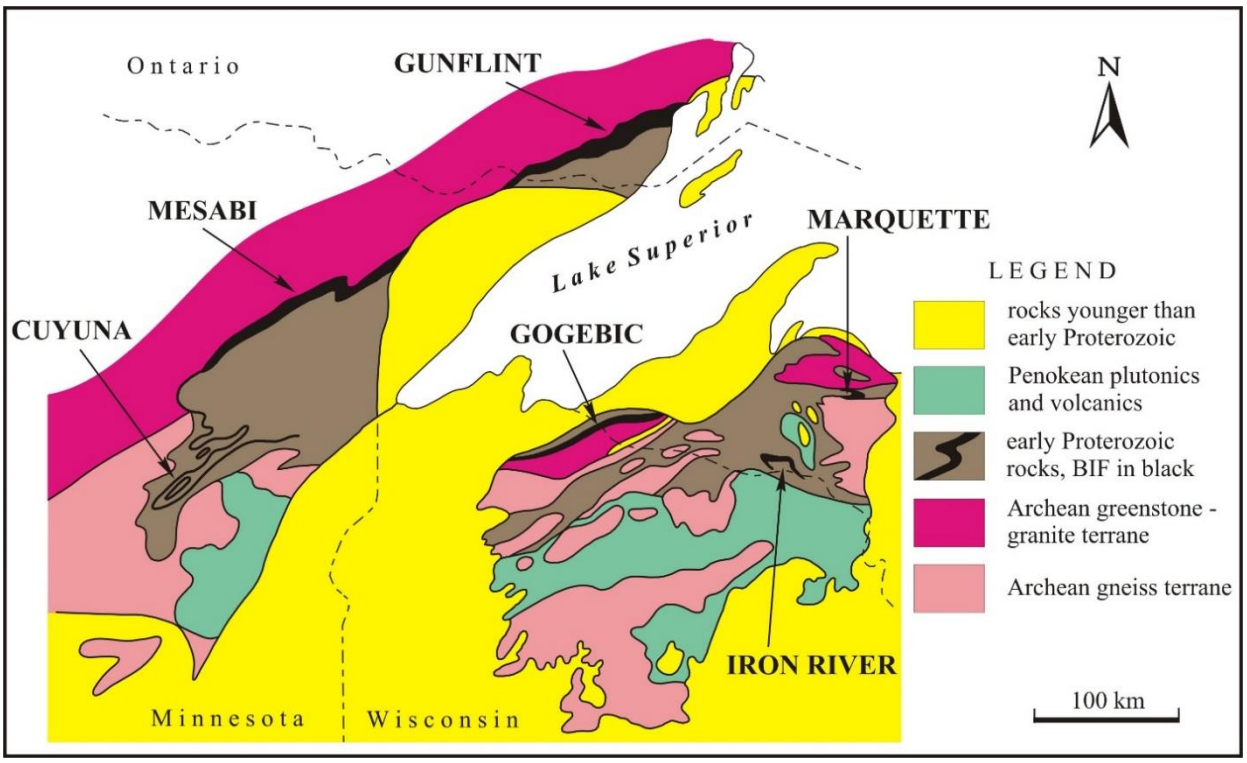

Figure 1. Simplified geologic bedrock map of the Lake Superior iron ranges (modified after Pufahl and Fralick, 2004).

units), the Gunflint and Biwabik Formations (middle units) and the Rove and Virginia Formations (upper units) (Figure 2).

The basal units consist of a clastic sequence, which unconformably overlie peneplained Archean rocks of the Superior Province. The Kakabeka Conglomerate, the basal polymictic member, consists of clasts of Archean volcanic rock rocks, granites and quartz with a variable thickness up to 1.5 m (Southwick ad Morey, 1991). Stromatolites of the Lower Stromatolitic Member of the Gunflint Formation are commonly found covering the Archean basement and cobbles within this member. The Pokegama is divided into three members; a basal shale, middle siltstone and upper

orthoquartzite. It is of variable thickness, ranging from 90 m in the southwest to non-existent in the east (Ojakangas, 1983). A discontinuous layer of conglomerate, lithologically similar to the

Kakabeka Conglomerate is present at the base of the Pokegama locally in the northeast suggesting a correlation (Ojakangas, 1983).

The Gunflint and Biwabik Formations conformably overlie the Kakabeka and Pokegama (Dolence, 1961). The Gunflint extends continuously 170 km from Gunflint Lake, Minnesota, northeast to Loon Lake, Ontario. From there, erosional remnants are intermittently present 100 km northeast in Schreiber, Ontario. Thickness ranges from 120 to 185 m, with an average dip of 5° to the southeast (Goodwin, 1956). In northern Minnesota, the gabbroic intrusions of the 1.1 Ga Duluth Complex truncate the Biwabik Formation (Heaman *et al.,* 2007). The Biwabik consists of a narrow band 0.4 to 4.8 km wide that extends 200 km southwest from the complex, past Grand Rapids, Minnesota. It is up to 250 m thick, with a dip of 2 to 10° towards the southeast. In close proximity to the Duluth complex, dips of 8 to 45° can be locally present (Gruner, 1946). It is likely that prior to the emplacement of the complex, the Gunflint and Biwabik Formations were continuous. A limestone unit is present resting at the top of the Gunflint and Biwabik Formations and reflects a fundamental change in oceanic conditions. In the Gunflint, a top stromatolitic unit containing carbonate stromatolites is present within limestone. In some cases, accretionary lapilli from the overlying Sudbury impact event (Addison *et al.*, 2005; Cannon and Addison, 2007) pile up on top of or erosively truncate the stromatolites.

This discontinuity separates the Biwabik and Gunflint from the overlying Rove and Virginia Formations at the top of the Animikie Group. The Rove and Virginia are composed of thinly bedded to laminated, fine-grained mudstones and turbiditic sandstones. They range in thickness from 380 to 1000 m. Morey (1967), described the stratigraphy and sedimentology of the Virginia, and later it was divided into three distinct units (Geul, 1970). Recently, a detailed

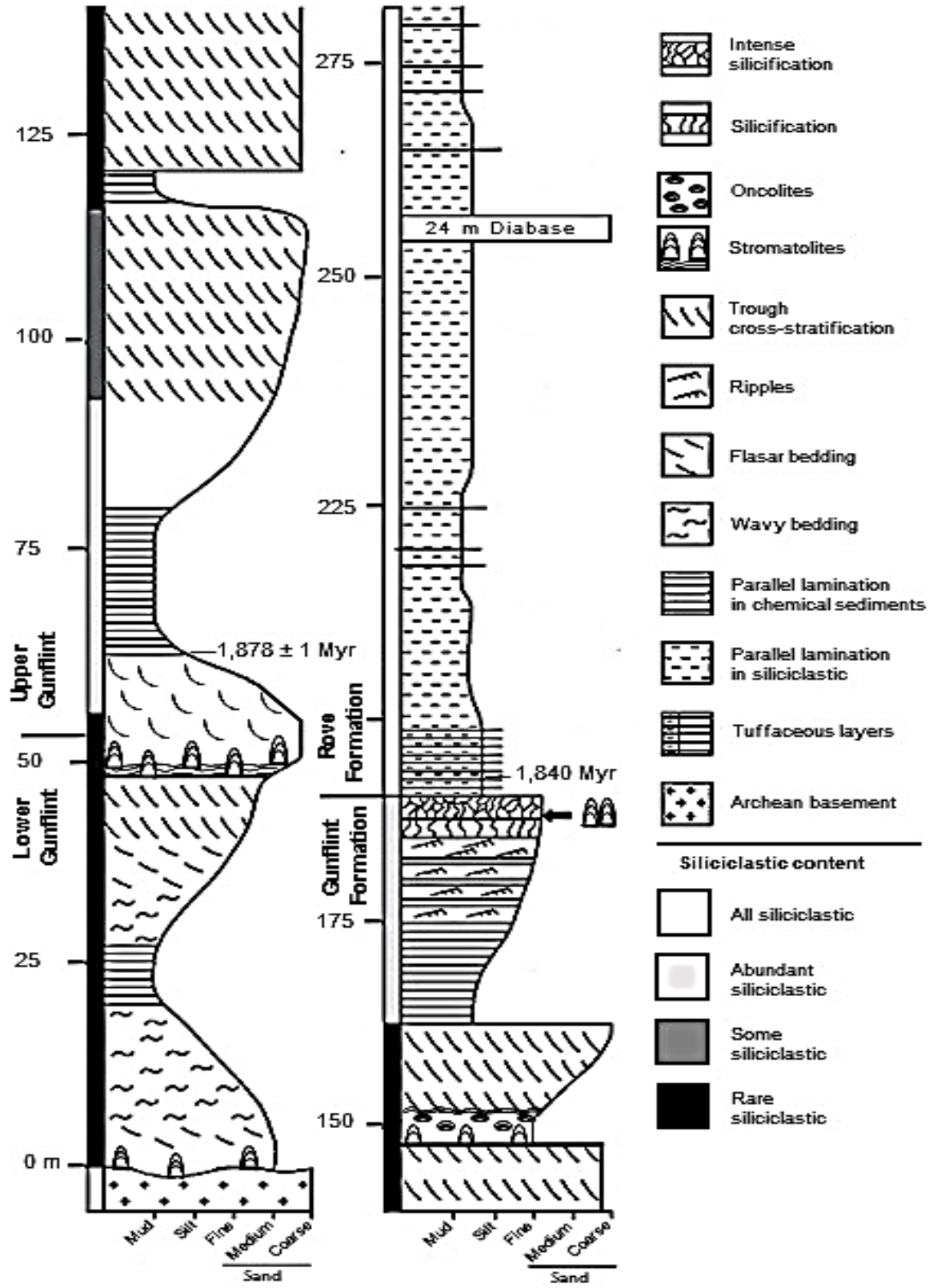

Figure 2. Generalized stratigraphic column of the Gunflint and Formation showing the relative location of the Lower, Middle and Upper Stromatolitic Members (modified after Poulton *et al*., 2004).

analysis of the sedimentology and sequence stratigraphy of the Rove and Virginia formations was conducted by Maric (2006).

Three iron ranges, the Cuyuna, Gogebic, and Marquette Ranges lie to the south and southeast of the Mesabi and Gunflint. It is probable that these ranges are correlative to Gunflint and Biwabik, as they all contain similar formations (Pufahl, 1996). The Gogebic Range consists of the Palms Quartzite, Ironwood Formation, and Tyler Formation. The Mahnomen, Trommald, and Rabbit Lake Formations comprise the Cuyuna Range, and the Ajibik Quartzite-Siamo Slate, Negaunee Iron Formation and Goodrich Quartzite from the Marquette Range (Schulz and Cannon, 2007). Similarly, a number of lithologically similar formations on disparate cratons are well described in the literature. The ca. 1.88 Ga Frere (Rasmussen *et al.,* 2012, Akin *et al*., 2013) and 1.79 Duck Creek (Wilson *et al.,* 2010) Formations in Australia, the 1.8 Ga Xuanlong in China (Dai *et al.,* 2004), the 2.0 Ga Franceville in Gabon (Vachette, 1964), and the 1.88 Ga Sokoman (Cheve and Machado, 1988) in northern Canada all contain similar stromatolitic horizons to the Gunflint and Biwabik iron formations.

The tectonic setting of the Animikie Basin is still debated; mostly due to a lack of supporting evidence. Two prevailing tectonic models are widely accepted. The first suggests a northward migrating foreland basin that developed north of the Penokean Fold-and-Thrust Belt, in response to crustal loading during the Penokean Orogeny roughly 1850 Ma (Hoffmann, 1987; Southwick and Morey, 1991; Ojakangas *et al.*, 2001). However, the more widely accepted model is that of a backarc basin north of the Wisconsin magmatic terrane (Hemming *et al.*, 1995; Fralick *et al.,* 2002) which evolved into a foreland basin during the Penokean Orogeny (Hemming *et al.,* 1995; Ojakangas *et al.,* 2001). On a regional scale, basic intrusions of Late Precambrian (middle Keweenawan) age are intimately associated with the Gunflint and Rove

Formations in Ontario these comprise the Logan intrusive complex which form sills (Moorehouse, 1960).

One significant difference between the Gunflint and Biwabik Formations is the metamorphic grade. Contact metamorphism due to the emplacement of the Duluth Complex affects the northeastern section of the Biwabik Formation and southwestern Gunflint. French (1968) suggested four metamorphic zones based on the proximity to the Duluth Complex. Conditions range from amphibole to sillimanite grade in zone 3 and 4, to lower greenschist facies and diagenesis in zone 1 (French, 1973). See Severson *et al.* (2010) for a detailed review of the metamorphic grades. Conversely, north of the border, the Gunflint rocks are virtually unmetamorphosed and relatively undeformed. Metamorphism was essentially isochemical, apart from the loss of some volatiles (H_2O and CO_2), and the addition of TiO_2 near the contact of the Duluth complex (Klein, 2005).

1.3 Mineralogy

Detailed petrographic descriptions of the mineral assemblages of iron formations have been provided by multiple authors, including those of the Gunflint and Biwabik (Gruner, 1946; French, 1968; Dimroth and Chauvel, 1973; Floran and Papike, 1975; Randazzo and Markun, 1980; Simonson, 1987). Four geochemical facies (oxide, silicate, carbonate, and sulphide) can be distinguished in iron formations based on the dominant iron mineral present (James, 1954). Of these, the major mineral components are chert, magnetite, hematite, siderite, calcite, ankerite, and minor pyrite (Gruner, 1946).

The terminology put forth by Folk (1974) for the description of quartz textures of iron formations will be followed. Thus, megaquartz is used for quartz crystals >35 μm in diameter,

microquartz is used for quartz crystals <35 μm in diameter, chalcedony for quartz with parallel or radial-fibrous extinction and chert for amalgamations of the microquartz and chalcedony (Folk, 1974). Chert (microcrystalline quartz) and iron oxides (magnetite and hematite) are the most abundant minerals in iron formation. Geochemical analysis demonstrate typical concentrations of 50 to 65% Si and 15 to 40% Fe in the iron formations in the Lake Superior regions (Van Hise and Leith, 1911; Gruner, 1946). Very fine-grained hematite in the chert (jasper) is present throughout the Gunflint and Mesabi Ranges, imparting a characteristic reddish colour. Of the carbonate phases found in Superior-Type iron formations, siderite ($FeCO_3$) is the most abundant. LaBerge (1964) provides a good description of the mineral associations with siderite in the Gunflint and Biwabik, and regards it as a primary constituent due to its close relation to primary features (bedding and granules) and very small grainsize (less than 30 μm).

The grains within the Gunflint and Biwabik can be subdivided into ooids, granules, or aggregate grains. Ooids are grains containing a central nucleus surrounded by cortical laminae whose thickness is greater than the diameter of the nucleus. Granules are intraclasts and refer to subangular to rounded grains composed of fine-grained silt. Aggregate grains contain multiple cemented nuclei, surrounded by multiple cortical laminae.

Three iron silicates (stilpnomelane, greenalite and minnesotaite) are almost ubiquitous in varying abundances in the Gunflint and Biwabik (Floran and Papike, 1975). The composition and abundances of these minerals are well-described (Gruner, 1936; 1937; 1944). Stilpnomelane [$Fe_{2\text{-}7}(Si,Al)_4(O,OH)_{12}\bullet xH_2O$] is the most abundant of the three iron silicates found in iron formations and is thought to occur during early diagenesis. However, it also forms during low-grade metamorphism. It commonly occurs with greenalite in cross cutting relationships in radiating clusters (Klein, 2005). Greenalite [$Fe_6Si_4O_{10}(OH)_8$] is generally believed to be

deposited as a primary precipitate; however, arguments suggesting it is a diagenetic or low grade metamorphism mineral have been proposed (Floran and Papike, 1975). It is the only iron silicate thought to be primary in origin, and is present in many primary features such as ooids, granules and as cements (Floran and Papike, 1975). Minnesotaite [$(Fe^{2+}, Mg)\ Si_4O_{10}(OH)$] is thought to be of low-grade metamorphic origin. It is usually not as abundant as stilpnomelane or greenalite, but is still nearly ubiquitous in the Gunflint and Biwabik. It appears as fine-grained, colorless to light green sprays. Klein (2005) suggested that minnesotaite forms via reactions such as the combination of chert and greenalite, the breakdown of greenalite (to form minnesotaite and magnetite), or by the reaction of siderite and chert which produce minnesotaite and carbon dioxide.

For a mineral to be considered primary, it must not replace a pre-existing mineral phase and that the 'primary mineral' constitutes the original precipitate, or one crystalized from it during early diagenesis (Ayres, 1972; French, 1973). Conversely, a secondary mineral is one that replaces a pre-existing one. This can occur during early or late diagenesis or low-grade metamorphism, often leaving ghosts of the primary mineral (Floran and Papike, 1975). Minerals considered primary within Superior-type iron formations include chert, siderite, hematite (after iron hydroxide), greenalite, and possibly some fine-grained magnetite, whereas euhedral magnetite, minnesotaite, stilpnomelane and some carbonates are interpreted as secondary (Gruner, 1946; LaBerge, 1964; French, 1973; Floran and Papike, 1975).

1.4 Previous Work

The first documented report of the Gunflint Formation was by Ingall (1888) in an annual mining report describing the Silver Mountain-Whitefish River area of Ontario. Minor studies of the Gunflint occurred in the early 1900s (Smith, 1905; Silver, 1906). However, it was not until the mid-1920s that comprehensive mapping and stratigraphy work was completed (Tanton 1923). The first detailed stratigraphic description of the Gunflint was provided by Gill (1926), followed by his theory for the depositional origin of the formation (Gill, 1927).

Extensive mapping of the Gunflint resulted in the division of the formation into six sedimentary facies (Goodwin, 1956). These represent two depositional cycles containing four members: a Basal Conglomerate Member, Lower Gunflint, Upper Gunflint, and Upper Limestone. Following this, Moorehouse and Goodwin (1960) published the first geological map of the Gunflint along with detailed descriptions of the mineralogy, chemistry, and economic potential. They proposed a new stratigraphy, consisting of a Lower and Upper Gunflint with 10 members. The Lower is composed of a Basal Conglomerate, Lower Stromatolitic Chert, Lower Shale, Lower Taconite, and Local Lava Flows, whereas the upper is made up of an Upper Stromatolitic Chert, Upper Jasper, Upper Shale, Upper Taconite, and at the top of the sequence the Limestone Member. More recently, a simplified stratigraphy of the Gunflint has been suggested which consists of two members, a lower member made up of lower stromatolitic cherts, and cherty grainstones, and an upper unit with similar stratigraphy (Fralick and Barrett, 1995).

Initially the Biwabik Formation was divided into four divisions: the Lower Cherty, Lower Slaty, Upper Cherty, Upper Slaty (Wolff, 1917; Broderick, 1920). The cherty divisions are granular and are often rich in iron oxides and chert, whereas the slaty divisions are siliclastic

and chemical mudstones consisting of finely laminated, fine-grained phyllosilicate with iron silicate or iron carbonate with local chert beds. These terms are still in use by mining companies; however, the divisions are now regarded as informal members (White, 1954). In reality, these members grade into one another. Further divisions are in use at several mines along the Biwabik. For a review and correlation of these see Severson *et al*. (2009). Correlation between the Gunflint and Biwabik can be made utilizing a tuffaceous layer overlying the Middle Stromatolitic Member at the base of the Upper Gunflint and directly below the reworked tuffs and accretionary lapilli of the Lower Slaty Unit

The ages of the Gunflint and Biwabik are well constrained. A U-Pb zircon age from a tuffaceous unit in the Gunflint provided an absolute age of 1878.3±1.3 Ma (Fralick *et al.,* 2002). A similar age of 1874±9 Ma obtained by U-Pb isotopes methods from a zircon of associated volcanic and volcaniclastic beds in the Gogebic (Schneider *et al.,* 2002) is believed to be correlative to the Biwabik.

The initial discovery by Bell in 1870, of the Gunflint stromatolites west of Thunder Bay, Ontario, was a significant paleontological discovery. In his work, he described small, vertical chalcedony cylinders, noting their morphological similarity to "small coral bodies". Several decades passed before further meaningful study was conducted. In the early 1900's forms similar to those described by Bell were discovered in two horizons in the Biwabik Iron Formation in Minnesota (Grout and Broderick, 1919; Gruner, 1922) and the Belcher Islands, Nunavut. (Moore, 1918).

Further work on the stratigraphy and geographic distribution of the Gunflint stromatolites led researchers to suggest that the structures were of biogenic origin, and most probably

composed of fossilized algae (Cayeux, 1911; Tanton, 1926; 1931). Figures of the microfossils which were absent in Cayeux's initial discovery were provided shortly after by Moore (1911) and Gruner (1922). However, it was not until a brief report by Tyler and Barghoorn (1954), and Barghoorn and Tyler (1965) that the significance of what is now known as the Gunflint microbiota was recognized globally. The importance of the discovery was realized when an age of "roughly two eons" was put forth, pushing back the first life on Earth by hundreds of millions of years.

Considerable progress in classification and identification of the microfossils ensued with the implementation of a linean style of nomenclature. Initially, Tyler and Barghoorn (1954) identified five morphologically distinct microfossil forms. Of these forms, they speculated two were algal, two were fungi and the remaining one appeared to be a unicellular organism (possibly a calcareous flagellate). Later revisions resulted in eight unique genera: *Animikiea* Barghoorn, *Entosphaeroides* Barghoorn, *Gunflintia* Barghoorn, *Archaeorestis* Barghoorn, *Huroniospora* Barghoorn, *Eoastrion* Barghoorn, *Kakabekia* Barghoorn, and *Eosphaera* Barghoorn (Barghoorn and Tyler, 1965). Within the genera, up to 11 species were described based primarily on their general morphologies (Barghoorn and Tyler, 1965; Awramik and Barghoorn, 1977). The exceptional preservation and diversity of microfossils has also been used as an argument in favour of primary silica and iron deposition. It is suggested that the organisms were growing on and being encased in a silica gel (Cloud, 1965). Furthermore, a detailed overview of the structure and morphology of the Gunflint stromatolites was conducted by Hofmann (1969).

Extensive work has been conducted over the last few decades on the general classification and growth morphology of stromatolites. Early work focused on naming and

classifying stromatolites based on their general morphology (Ginsburg, 1967) with subsequent work on the microbial communities found within ancient carbonate forms in Australia, South Africa and northern Canada (Grey, 1982; Grey, 1993)

Recent work has focused on determining: (1) if the present minerals represent the original mineralogy of the stromatolites and grainstone or whether it results from the replacement of a precursor carbonate assemblage; and (2) if the stromatolites were built solely by cyanobacteria or in conjunction with chemolithotrophic and/or photoferrotrophic bacteria. Some authors have interpreted the stromatolites within the Lower Stromatolitic Member of the Gunflint and Biwabik to be primary carbonate precipitates with later diagenetic silicification (Moorehouse, 1960; Lougheed, 1983). This interpretation was carefully re-examined by Sommers *et al.* (2000) at the Whitefish and Schreiber Channel outcrops. In their analysis they noted rare ghosted carbonate and quartz crystals cross-cutting stromatolitic and grainstone boundaries along with euhedral specular hematite in one sample leading to the conclusion that the hematite and chert of the Lower Stromatolitic Member is the product of silicification of a carbonate precursor. Moreover, it has been suggested that the iron within the stromatolites was deposited during the emplacement of the Duluth complex (Shapiro and Konhauser, 2015). They put forth a taphnomic model whereby oxidized, iron-rich fluids precipitated the iron oxides currently observed on the microfossil cell walls (Shapiro and Konhauser, 2015).

However, geochemical analysis conducted on samples from both the Gunflint and Biwabik indicate that the stromatolites were developing in low oxygen conditions, ideal for iron oxidizing bacterial communities to thrive (Planavsky *et al.,* 2009). Furthermore, processes operating in modern iron-silica rich hydrothermal systems (Konhauser and Ferris, 1996; Pierson *et al.,* 1999), and silica-rich lake systems (Sanz-Monteroetal *et al.,* 2008; Kermer *et al.,* 2012)

provide possible analogues to the geochemical conditions that existed during the development of the Paleoproterozoic stromatolites. Also, studies of microstromatolitic ferromanganese nodules in modern lacustrine systems provide further information on the growth of the ancient stromatolites (Sommers, 2002; Asikainen and Werle, 2007; Kerkermeier, 2013).

1.5 Modern Stromatolites (Ferromanganese nodules)

As noted previously, modern stromatolites are most commonly composed of agglutinated carbonate grains (Logan *et al.,* 1964; Reid *et al,* 2000) though several examples of modern iron- and manganese precipitates forming stromatolites can be found in the literature (Harriss and Troup, 1970; Renaut *et al.,* 1998; Bowen *et al.,* 2008). Most notably are the ferromanganese nodules accreting at the sediment-water interface of many lakes in northern latitudes. The nodules form concentrically around a central nucleus and are composed of alternating laminae of iron and manganese. They form via the direct precipitation of iron and manganese at a redox boundary. This can occur abiotically due to a change in redox conditions when anoxic water (groundwater or beep basin water) mixes with oxygenated lake water (Kerkermeier, 2013). However, iron-oxidizing bacteria have been shown to significantly increase the rate at which iron hydroxides precipitate (Ghiorse, 1984; Ehrlich, 2002). Microstromatolitic columns, consisting of millimeter-scale columns, are present within the nodules, on both the top and bottom surfaces, signaling the importance of chemolithotrophic and photosynthetic organisms (Sommers *et al.,* 2002). These stromatolites formed from chemical precipitates may provide a modern analogy for some processes operating in the Precambrian.

1.6 Study Site Locations

Paleoproterozoic study locations were selected from the Lower, Middle and Upper Stromatolitic Members, as well as the Limestone Stromatolitic Member. These sites span a distance of over 500 km from Schreiber, Ontario to Hibbing, Minnesota (Figure 3). Samples were taken from mines, outcrop, and drill core for mineralogical, geochemical, and petrological analysis. Sites were selected to provide a range of metamorphic grades for comparison. Furthermore, samples were selected from sites that contained minimal alteration. Samples of modern microstromatolitic ferromanganese nodules were collected from the bottom of four coves in Lake Charlotte, Nova Scotia. These samples were carefully collected by hand to ensure the proper up direction was known.

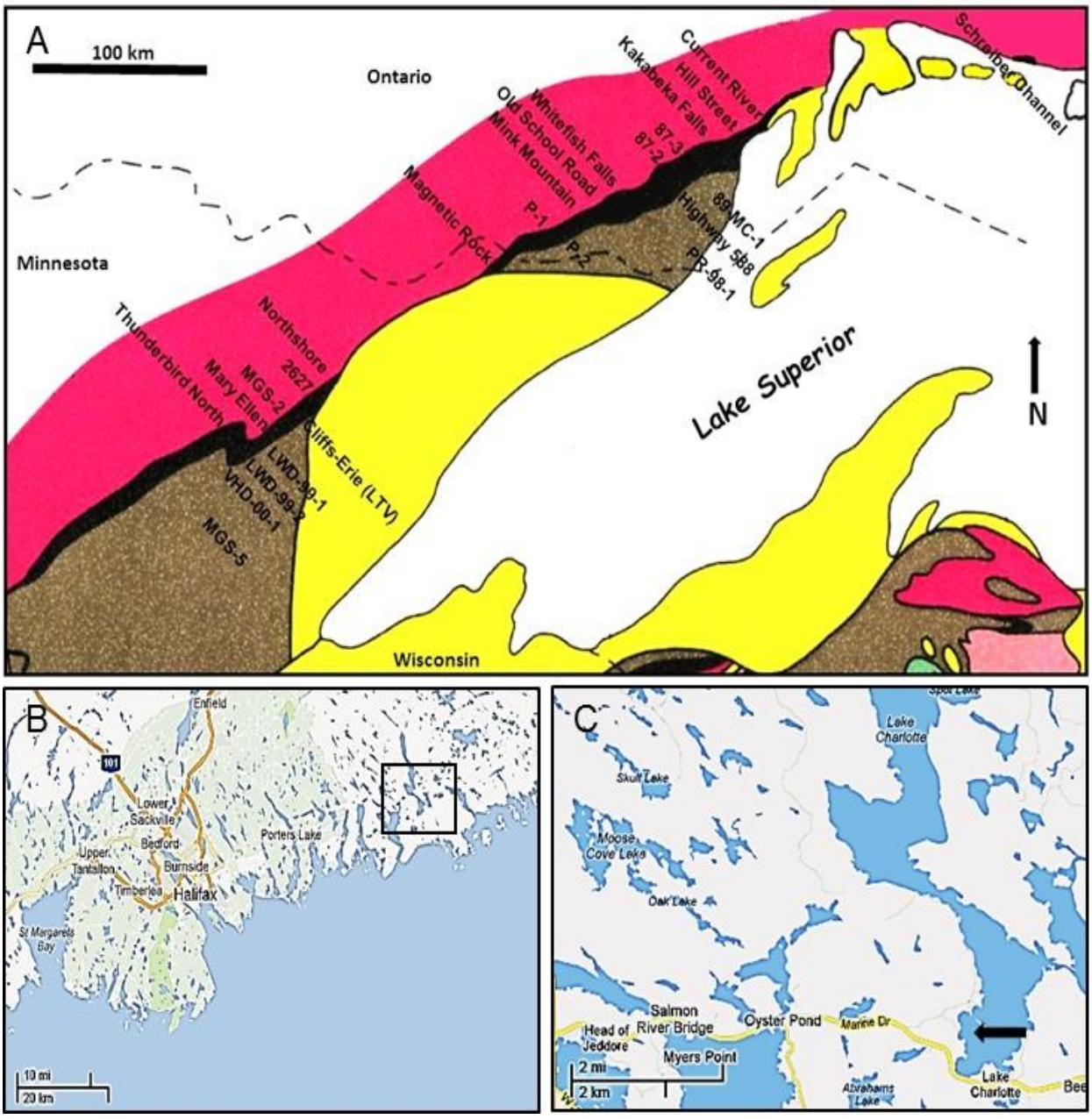

Figure 3. Study site locations. (A) Generalized map of the Gunflint and Mesabi Iron Ranges (Black area) denoting sample locations. For legend, see Figure 1 (Modified after Pufahl and Fralick, 2004). (B) Google map of Halifax area, Nova Scotia. (C) Enlarged view of box in (B) showing location of nodule field in Lake Charlotte (black arrow).

Table 1. Study site locations and stratigraphic location (Lower, Middle, Upper, Limestone) of Gunflint and Biwabik samples.

Study Site	Setting	Stratigraphic Unit	Location
Kakabeka Falls	Outcrop	Lower	Kakabeka Falls, ON
Schreiber Channel	Outcrop	Lower	Schreiber, ON
Whitefish Falls	Outcrop	Lower	Nolalu, ON
Current River	Outcrop	Middle	Thunder Bay, ON
Mink Mountain	Outcrop	Middle	Mackies, ON
Old School Road	Outcrop	Middle	Nolalu, ON
Magnetic Rock	Outcrop	Middle	Grand Marais, MN
87-2 (DH-2)	Drill Core	Middle	O'Connor, ON
87-3 (DH-3)	Drill Core	Middle	O'Connor, ON
89-MC-1	Drill Core	Middle	Neebing, ON
P-1	Drill Core	Middle	Arrow Lake, ON
P-2	Drill Core	Middle	Arrow Lake, ON
PR-98-1	Drill Core	Middle	Neebing, ON
Cliffs-Erie (LTV)	Mine	Upper	Babbitt, MN
Mary Ellen	Mine	Upper	Biwabik, MN
Northshore	Mine	Upper + Limestone	Babbitt, MN
Thunder Bird North	Mine	Upper	Eveleth, MN
2627	Drill Core	Upper	Aurora, MN
LWD-99-1	Drill Core	Upper	Eveleth, MN
LWD-99-2	Drill Core	Upper	Eveleth, MN
MGS-2	Drill Core	Upper + Lower	McKinley, MN
MGS-5	Drill Core	Upper	Buhl, MN
VHD-00-1	Drill Core	Upper	Eveleth, MN
Highway 588	Outcrop	Limestone	Stanley, ON
Hill Street	Outcrop	Limestone	Thunder Bay, ON

1.7 Methods

1.7.1 Sample Collection

A total of 215 hand samples containing stromatolites from the Lower, Middle, Upper and Limestone Members of the Gunflint and Biwabik Formations were collected from nine insitu natural outcrops, twelve diamond drill (DD) cores, as well as exsitu samples collected from waste rock piles at four mines (Table 1). Where possible, multiple samples were collected from the base to the top of the stromatolitic horizon at each outcrop to provide material for determination of stromatolite development over time. Samples were selected which showed little to no weathering and contained a variety of stromatolitic forms for analysis (i.e., stratiform, domal, columnar). Of the 215 hand samples collected, 58 samples and 2.8 m of DD core were polished for macroscopic imaging.

Ferromanganese nodules were collected by hand via snorkeling which ensured the proper up direction was recorded. Once at the surface, the nodules were wrapped in a soft cloth, wetted with tap water, and placed in containers for transport. Upon arrival at the laboratory, the nodules were dried at ambient room conditions for two days, coated in epoxy, and cut to provide both lateral and vertical profiles through the nodules.

1.7.2 Imaging

1.7.2.1 Photography

All outcrop and macroscopic photographs were taken with a Canon EOS Rebel T3i digital single-lens reflex (DSLR) camera with an EFS 18-55 mm, image stabilized MACRO 0.25

m lens. Photomicrographs were taken with the above DSLR camera fitted to a WILD Heerbrugg binocular microscope.

For consistency, only samples containing stromatolitic material were selected for imaging. This included stratiform, domal and columnar forms and the material immediately surrounding the stromatolites (Hofmann, 1969; Hofmann, 1973; Grey, 1982; Grey, 1993; Reid et al., 2003). Imaging was conducted to determine the presence or absence of structures indicative of carbonate replacement (such as ghosting of carbonate rhombs and the presence of cryptocrystalline carbonate inclusions within quartz crystals) and preferential areas where microfossils would be located to determine the original mineral assemblage associated with the stromatolitic horizon. Analysis for microfossils consisted of microscopic analysis to determine possible preferential locations within the stromatolite laminae in relation to both iron and silica, as well as general microfossil form.

1.7.2.2 Petrographic Imaging

In total 118 polished thin section slides (30 μm) were made in the Lakehead University Lapidary Laboratory. The slides were then examined with an Olympus BX51 petrographic microscope. Imaging in plane polarized (PPL), cross polarized (XPL), and reflected (REF) light were conducted using an Olympus DP camera attached to the microscope.

1.7.2.3 Scanning Electron Microscopy and EDS Mapping

Scanning electron microscopy (SEM) imaging was conducted with a Hitachi SU-70 Schotty Field Emission SEM equipped with an Oxford Aztec 80mm/124ev Energy Dispersive Spectrometer. Secondary (SE) and backscatter (BSE) images were taken at 20keV at a working

distance of 15 mm unless otherwise noted. Qualitative elemental mapping and line scans, and qualitative point analysis of the samples was conducted using the Oxford AZtec EDS software on the SEM, at an accelerating voltage of 20 keV and a working distance of 15 mm. False colour elemental maps were generated to provide insight into trends associated with the deposition of iron, manganese and silica which make up the conspicuous alternating laminae of the stromatolites.

1.7.3 Geochemistry

1.7.3.1 Sample Digestion

The composition of each sample was determined using a standard hot acid digestion. Stromatolitic material was cut from the sample with a diamond saw and crushed in an agate mill. Once powdered, 0.250x mg of each sample was accurately weighed on a AND-ER-180 electronic balance into a Teflon crucible. The crucibles were placed on hotplates that were set to 90^0 C. To the crucibles, 10 ml of double distilled water (DDW) and 5.0 ml of concentrated nitric acid were added. This was allowed to digest overnight to eliminate any effervescence from the samples. For three consecutive days 10.0 ml of concentrated nitric acid and 5.0 ml of hydroflouric acid were added to the crucibles and allowed to digest at 90^0 C. On the final night the samples were evaporated to complete dryness. On the fifth day 2.0 ml of nitric acid was added and allowed to simmer for 20 minutes, then 10 ml of DDW was added. The digest was then transferred to a 100.0 ml volumetric flask. The sample was allowed to warm at 90^0 C for 2 hours in the flask. Once cool, the flasks were filled to 100.0 ml with DDW. A 50 ml aliquot of each sample was transferred to a centrifuge tube. Blanks and USGS standards (Hawaiian Basalt, BVO-2; Quartz Latite, QLO-1a) were prepared with the samples.

1.7.3.2 Sample Analysis ICP-AES

Inductively coupled plasma atomic spectrometry (ICP-AES) analysis was conducted on a Varian Vista Pro ICAP Radial utilizing a Cetac Autosampler at the Lakehead University Instrumentation Lab. The ICP-AES analysis was used to determine the major and selected minor elements.

1.7.3.3 Sample Analysis ICP-MS

Inductively coupled plasma- mass spectrometry (ICP-MS) analysis was conducted at the Lakehead University Analytical laboratory on a Perkin-Elmer Elan DRC-e ICP-MS fitted with a Cetac autosampler. The ICP-MS analysis was conducted to determine selected trace and rare earth element (REE) concentrations. All presented data were within acceptable levels of precision and accuracy (±10% of standards) and above three times the blank, which defines the lower detection limit.

2 Results

2.1 Lower Stromatolitic Member

2.1.1 Kakabeka Falls

UTM 305201E, 5364740N 16N

The outcrop is located 1 km northeast of the town of Kakabeka Falls, Ontario, at the junction between Highway 590 and Highway 17 (Trans-Canada Hwy). It consists laterally of a 100 m road cut exposing Archean granodiorites, directly overlain by the Lower Stromatolitic Member. An ankerite grainstone covers the stromatolitic horizon, and in turn is overlain by a siliceous cap. At the base of the outcrop, 50 to 100 cm of Archean granodiorite is exposed, which is unconformably overlain by the Lower Stromatolitic Member of the Lower Gunflint.

The stromatolitic unit consists of a 45 cm thick siliceous stratiform stromatolite at the base, developing into several overlying domes, ranging from well-to-poorly preserved (Figure 4). The lamination within the basal stratiform stromatolite is well preserved and can be traced along the outcrop. The laminae consist of centimeter-scale, milky-white to pale grey chert which irregularly alternate with millimeter-scale, darker grey laminae. It is capped by a sharp, 2 cm dark grey siliceous zone at the upper contact with the overlying carbonate grainstone. A well preserved, subspherical domal stromatolite with a diameter of 50 cm forms from the upper layers of the flat-mat stromatolite (Figure 5A). At its core, closely packed centimeter-scale digitate stromatolites grow out in a radial pattern and are overlain by three distinct growth zones. These zones contain well preserved, roughly parallel, wavy laminae composed of pale grey chert. Each growth zone is roughly 20-30 cm thick. They are separated from one another by a dark siliceous layer a few millimeters thick. There is a notable absence of grainstone within the laminae.

Figure 4. Kakabeka Falls field site. A 45 cm thick siliceous stratiform stromatolite and large siliceous dome make up the Lower Stromatolitic Member at this location.

The stromatolites are overlain by a 1.5 m thick, fine-grained, ankeritic grainstone. In hand sample, the contact between the grainstone and stromatolitic unit ranges from relatively sharp to diffuse. At the base, the contact between the stratiform stromatolite and grainstone is sharp, with only minor silicification of the grainstone. In areas, the ankerite replaces the siliceous stromatolite and can be seen eroding into the upper stratiform laminae (Figure 5C). However, the contact between the well-preserved dome and grainstone is more diffuse. Zones of silicification are prominent within the grainstone, and a thin zone of silicification of the ankeritic grainstone adjacent to the dome can be seen (Figure 5B). A block of broken stromatolite embedded in the ankerite grainstone is present a few centimeters up from the stratiform mat. It has a silica overgrowth replacing the ankerite, particularly on the right where it extends up to 1 cm into the grainstone (Figure 5D).

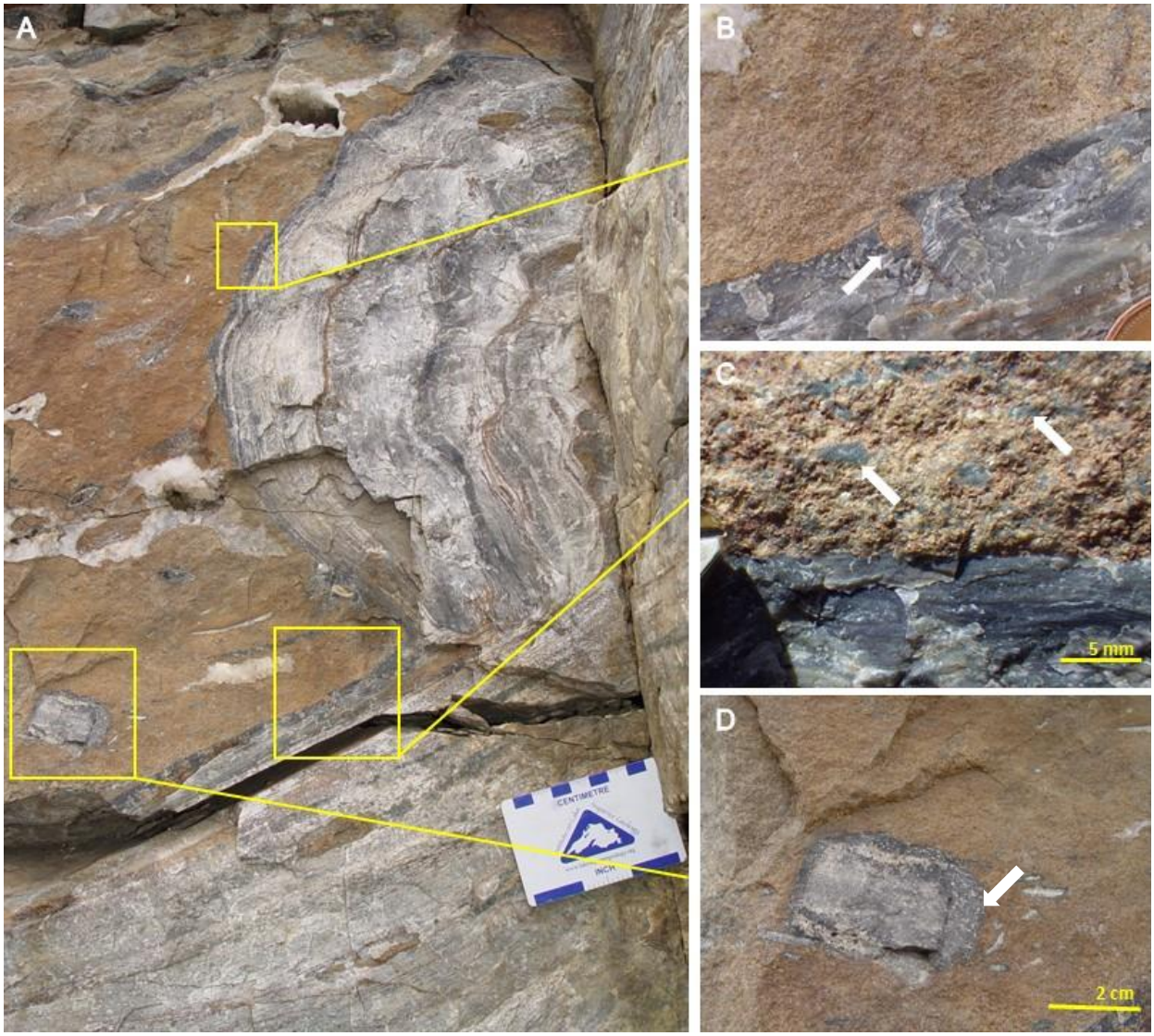

Figure 5. Erosion and reworking of stromatolite fragments. (A) Photograph of the siliceous stromatolite dome. (B-C) The upper left side of the stromatolite head has a thin area of silicification next to it, but the stratiform mat has a sharp contact with the grainstone, with apparently no replacement. (D) The block of broken stromatolite in the grainstone has a silica overgrowth replacing the ankerite grainstone around it, particularly on its right side.

In thin section, the sharp stromatolite-grainstone contact is well defined. A zone of almost complete silicification extends out from the stromatolite-grainstone contact several centimeters into the ankerite (Figures 6A, 6B). Within this zone, replacement of intraclasts and the intergranular cement has occurred, with relict carbonate rhombs replaced by quartz. The replacement of the ooids and granules is evident by the patchy overprinting of microcrystalline

carbonate by megaquartz which crosscuts original ooid laminae and grain boundaries of the granules (Figure 6E).

Within the domal stromatolite large (millimeter-scale) ankerite crystals cross cut the original stromatolitic laminae (Figure 6C). Rarely, laminae containing cryptocrystalline carbonate are found alternating with microquartz laminae (Figure 6D). The carbonate within these laminae are highly diffuse, with traces of the cryptocrystalline carbonate extending into the surrounding quartz. Pyrite is present as small (micrometer-scale) euhedral crystals, often in association with carbonaceous material, imparting the dark, cloudy appearance of the dark laminae. The centimeter-scale digitate stromatolites which make up the core of the dome are composed of clean quartz, with no traces of prior carbonate replacement. The laminae alternate between light microquartz and dark microquartz which is stained by organics, and cryptocrystalline iron oxides with minor pyrite grains.

Evidence of multiple replacement events is present in the silicified grainstone near the stromatolite contact. Granules which have been mostly replaced by quartz, show secondary carbonate replacement, and in some cases have tertiary carbonate rhombs crosscutting the secondary carbonate (Figure 6F). Multiple point analysis of the intergranular replacement carbonate revealed elevated concentrations of manganese oxide up to 4.5 wt%.

One of the samples collected contains a broken fragment of a domal stromatolite, roughly 8 cm in length, which fell upside down on the basal stratiform mat (Figure 7A). A submillimeter rim of quartz cement is present on the three sides exposed to the overlying ankerite grainstone

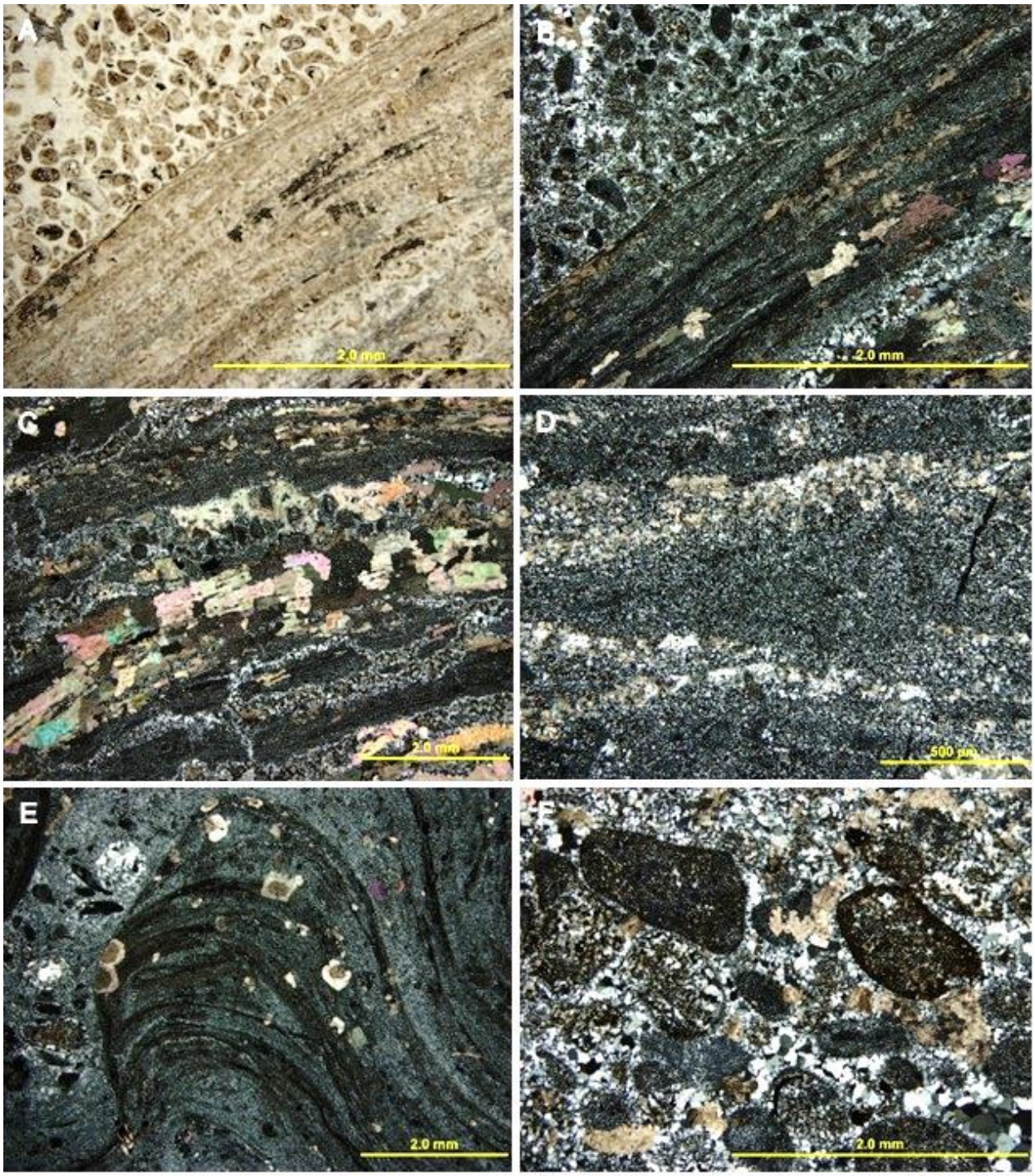

Figure 6. Photomicrographs of the laminations within the domal stromatolite. (A) Stromatolite-grainstone contact (PPL). (B) Same as (A) however the replacement of the microcrystalline quartz by carbonate is more apparent (XPL). (C) The replacement of the siliceous stromatolite laminae by carbonate (XPL). (D) Fine-grained cryptocrystalline carbonate laminae near the outer edges of the domal stromatolite (E) Erosive scour of the mm-scale stromatolites at the core of the dome is highlighted by the absence of the dark fine-grained wall adjacent to the interspace (XPL). (F) Within the silicified grainstone ferroan dolomite can be seen replacing the grains and intergranular cement (XPL).

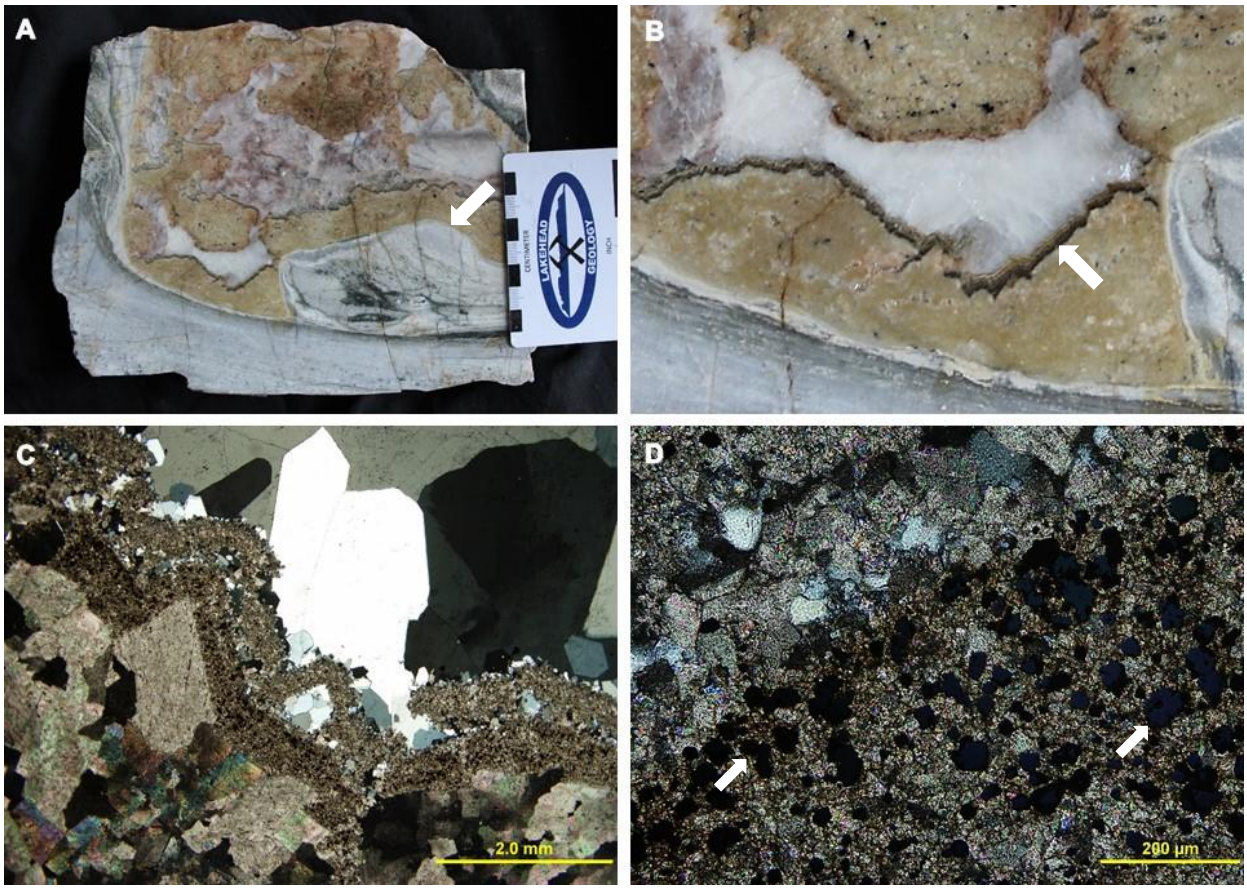

Figure 7. Vadose silt. (A) Polished hand sample showing the basal stratiform stromatolite with a large piece of broken stromatolite (white arrow) resting on it and the surrounding ankerite grainstone. Note the black layer of silt present on the top surfaces of the grainstone. (B) Close up of (a) showing a millimeter-scale vadose silt layer (white arrow) draping the top surfaces of the ankerite grainstone. (C) Photomicrograph of the silt layer draping over the ankerite rhombs (XPL). (D) Within the microcrystalline carbonate silt euhedral, opaque pyrite grains (white arrows) are present (XPL).

suggesting it was precipitated prior to the deposition of the surrounding ankerite. Moreover, partial dissolution of the grainstone has created a thin, millimeter-scale layer of vadose silt which was deposited on the upper surfaces of the remaining ankerite grainstone (Figure 7B). The silt is composed of microcrystalline carbonate with fine-grained euhedral pyrite grains. A second layer of silt is present overlying the first (Figure 7D). This layer lacks the pyrite found below; however, it contains zones of blocky quartz.

The ICP-MS measured rare earth element (REE) values for samples collected from the Kakabeka Falls location were normalized to Taylor and McLennan's (1985) post-Archean Australian shale (PAAS) values and plotted (Figure 8). The samples selected for analysis include light (KF-B) and dark (KF-A) laminae within the large dome, and light (KF-C) and dark (KF-S) laminae within the basal stratiform mat. The plot shows a consistent pattern among the four samples showing a slight depletion in light rare earth elements (LREE) compared to the heavy rare earth elements (HREE), a very slight to more distinct negative cerium (Ce) anomaly and a positive europium (Eu) anomaly.

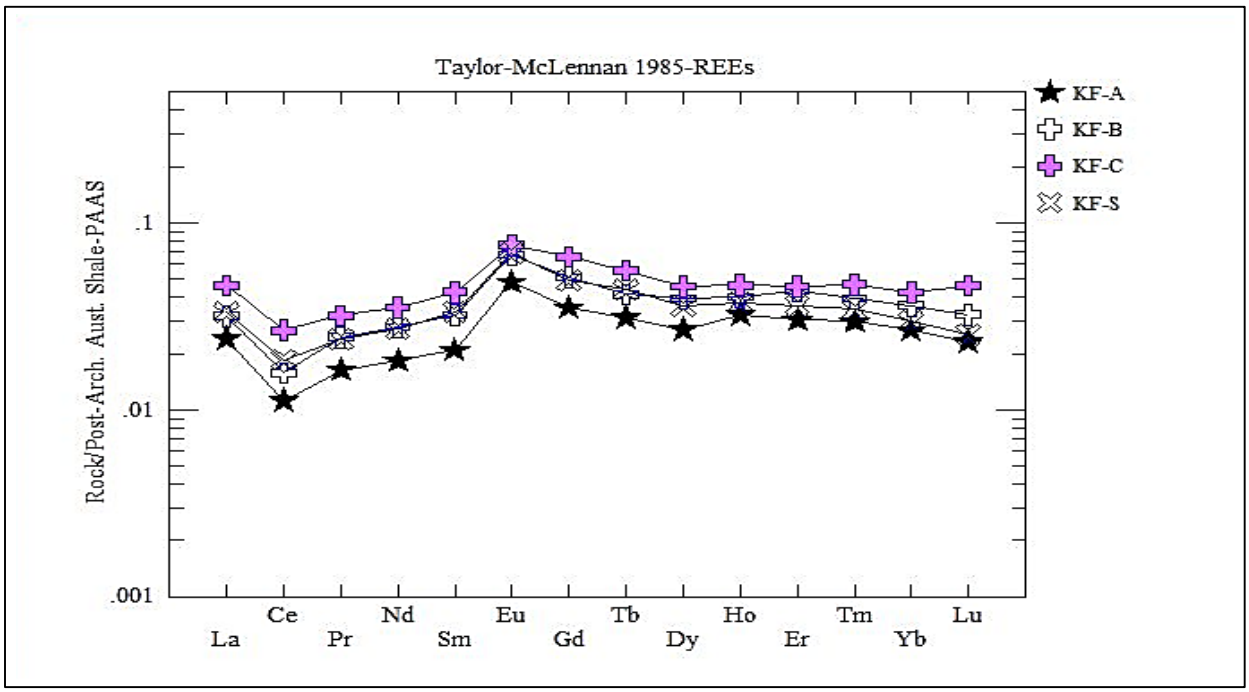

Figure 8. The PAAS normalized REE diagram for Kakabeka Falls showing slight to distinct negative Ce and positive Eu anomalies.

2.1.2 Schreiber Channel

UTM 474637E 5404961N 16N

The field site is located on the northern shore of Lake Superior 6.5 km west-southwest of Schreiber Beach Ontario. The site is accessed via a 6 km hiking trail on the Voyageur Trail network (Casque Isles Trail section). At Schreiber Channel, the Gunflint crops out continuously for 100 m with a variable width of up to 20 m from the shore back into the tree line. It dips moderately 20 to 25 degrees southwest into the lake where it can be traced an additional few meters (Figure 9A). Remnant exposures are also found on Flint Island, 200 m offshore from the mainland site. The site consists of Archean pillow basalt flows, overlain by the Kakabeka conglomerate, which is in turn overlain by the Lower Stromatolitic Member of the Lower Gunflint Formation.

Archean pillow basalts are well exposed at the base of the outcrop in the eastern portion of the beach. They consist of pillows ranging up to 1.5 m with green to black rims. The pillows are overlain by 50 to 75 cm of reddish-brown, poorly sorted conglomerate containing well rounded to angular clasts 5 to 20 cm in diameter contained within a medium grained siliciclastic matrix with minor carbonate (Figure 9B). The Lower Stromatolite Member is 60 cm thick and formed directly on the conglomerate. It consists of numerous bioherms with diameters over 1.5 m and smaller domal stromatolites ranging up to 20 cm diameter. Their height is variable depending on the degree of erosion, however some domes exceed 45 cm in relief (Figure 9D). Areas where the domes have been mostly eroded are marked by centimeter-thick, white rings, lying directly in the conglomeratic unit (Figure 9B). The rings are made up of alternating dark and light wavy laminae identical to that found in less eroded bioherms. Erosion of some of the

Figure 9. Schreiber Channel field site photographs. (A) The Lower Stromatolitic unit crops out 100 meters along the shoreline of Lake Superior, with much of it submerged underwater. (B) Good exposures of the basal Kakabeka Conglomerate are present on site, containing centimeter- to decimeter-scale clasts within a medium grained matrix (C) Large Stromatolitic mounds grow directly on top of the conglomerate unit. Cobbles derived from the conglomerate are often the nucleation site of the large domes (D) The stromatolites range in size from small (10 cm) to large (meter scale), black chert domes, embedded in a medium-grained grainstone. Roughly 25 of these domes are present.

domes reveals cobbles derived from the underlying Archean bedrock at the centre of the bioherms (Figure 9C). The colour of the chert present within the bioherms is gradational outward, from white and grey near the centre to dark grey and black at the outer periphery. The smaller domes are mostly black chert, often heavily stained by iron oxides (Figure 9D).

Polished hand samples show that the bioherms are made up of digitate and pseudocolumnar stromatolites which developed radially outward in a convex pattern from a central cobble nucleus (Figure 10). The colour of the stromatolitic chert is gradational from white to light grey nearest to the cobble, to black and dark green at the outer edges. The digits have a tuberous shape, ranging from 3 to 10 mm in width, and rarely exceed 3 cm in synoptic relief. Branching is common, however, digits show poor horizontal and lateral continuity and are often overlain or integrated into irregular pseudocolumnar forms.

The preservation of the laminae within the stromatolites is poor. However, alternation between light and dark (black) laminae is evident. Where preserved, the dark laminae are commonly highly discontinuous. At the edges of the column the black laminae overlap one another forming a conspicuous wall structure (Figure 11A). The width of the wall varies from 300 to 500 μm, and can be continuous over a couple centimeters. Interestingly, even in the white zones near the base of the dome, the black wall structures are still present. The highly irregular, divergent branching of the columns and transition into pseudocolumnar forms often caps off the interspace between digits with a thin microbial mat. The interspace ranges up to 5 mm in width and is filled with grainstone. The grainstone is composed of a mix of intraformational clasts, ooids and granules. The millimeter-scale intraformational clasts are composed of laminated dark and light chert which are almost indistinguishable from the surrounding stromatolites. The clasts

Figure 10. Polished slab of domal stromatolite. Digitate forms grow out from the rock clast in the bottom left. The colour is transitional from light grey near the base of the dome to black at the outer periphery. The black is imparted by high amount of organic material and pyrite.

vary from highly-angular and fractured to smooth, and rounded (Figures 11B, 11C), suggesting variable transport and erosion times prior to emplacement within the stromatolite. The intra-formational clasts can be seen abutting the stromatolite wall allowing the microbial mat to gently drape onto the clast (Figure 11B). Clasts resting on previously deposited ooids create cavities underneath, devoid of granules (Figure 11C). Other intraformational clasts demonstrate asymmetrical growth of discontinuous wavy laminae, similar to oncolites (Figure 11D).

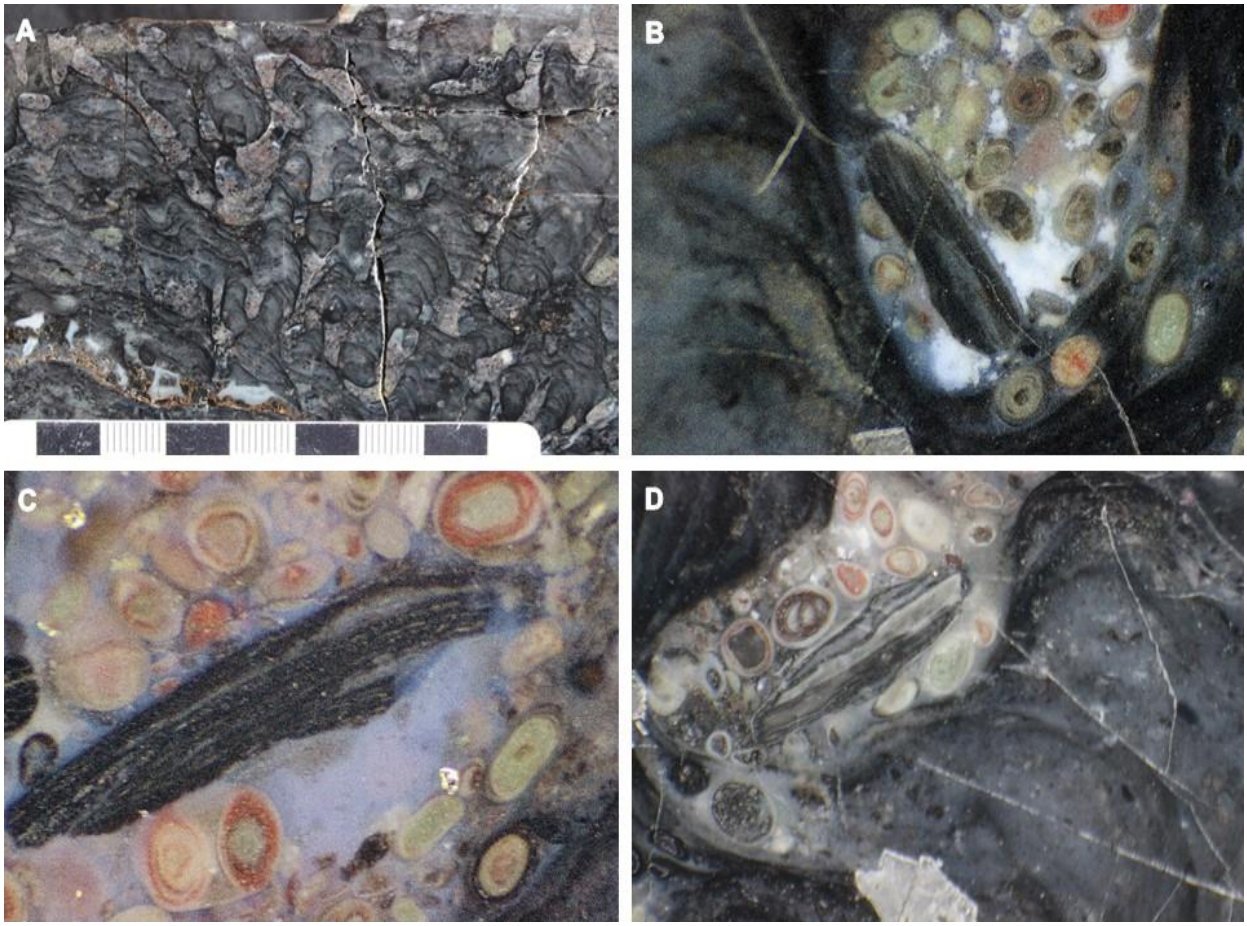

Figure 11. Photomicrographs of polished hand samples. (A) The stromatolite laminae are highly irregular, with individual columns rarely exceeding one centimeter before being overlain by newer laminae. These overgrowths regularly constrain the amount of interspace present, trapping ooids, granules and intraformational clasts. (B) Intraformational clasts show fine-scale laminations of alternating dark and light chert, comparable to that found in the stromatolite wall. These clasts range from rounded (B) to angular (c) suggesting varying degrees of erosion and transport. (D) Clast showing asymmetrical growth and wavy nature of the laminae.

The main component of the inter-columnar grainstone is loosely-packed ooids and granules, suggesting that cementation occurred before significant compaction (Figure 12A). The ooids are commonly composed of cortical lamination alternating between jasper and quartz, however greenalite is also common. The composition of ooid nuclei varies from quartz, iron oxides, and pyrite grains to multiple ooids cemented together (Figure 12C). Granules are most often composed of greenalite or pyrite. Two generations of intergranular cement are present. The

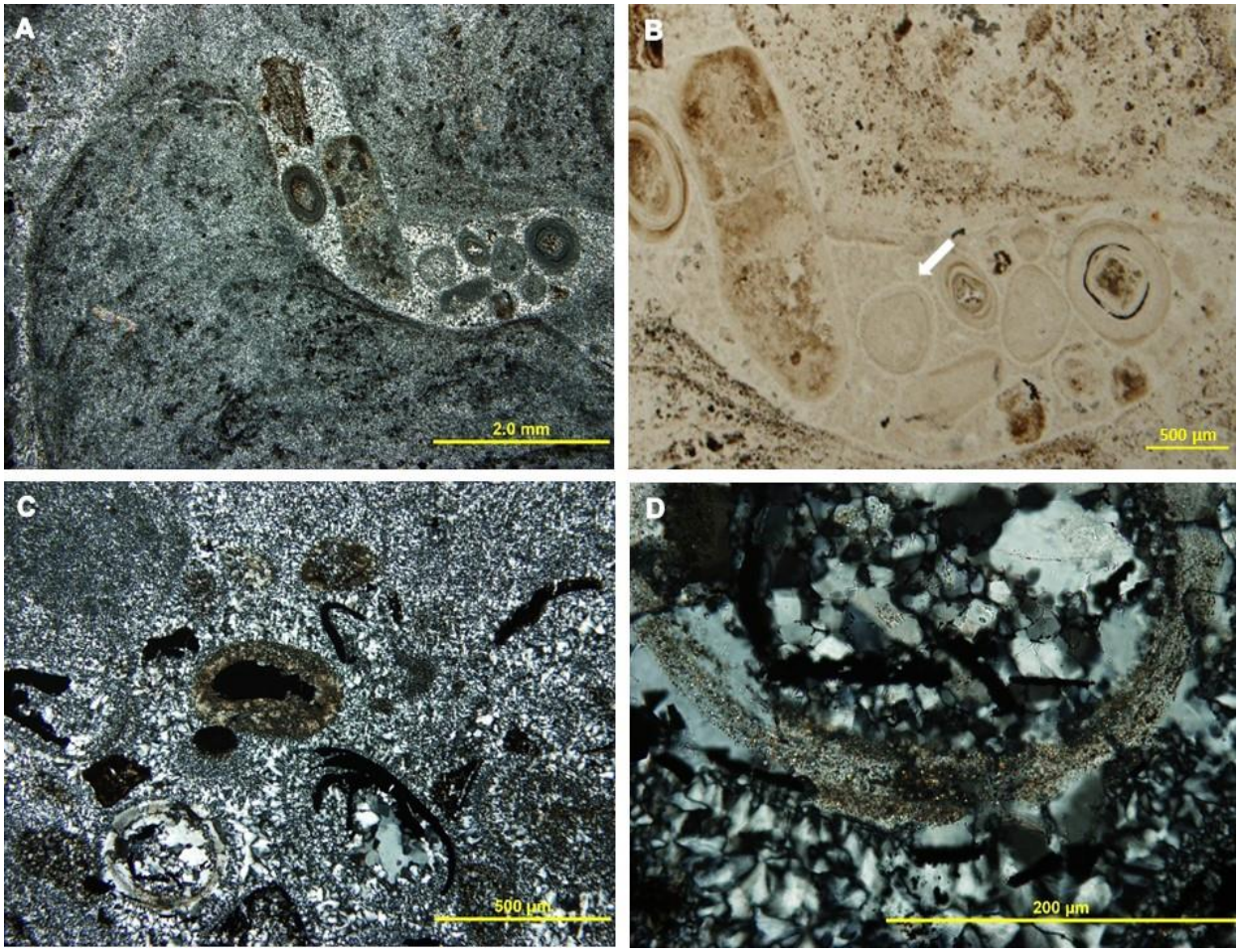

Figure 12. Grainstone features. (A) The intergranular cement present in the interspace is comprised of clean blocky quartz and rare chalcedony fans (XPL). (B) Close up of (A) showing two distinct generations of cement. The first is a ~100 µm rim of microquartz around the grains (white arrow) followed by blocky mosaic quartz or chalcedony fans (PPL). (C) Trace carbonate is present in the Schreiber Channel samples, generally occurring in ooids with a pyrite nucleus (XPL). (D) Ooid containing cryptocrystalline carbonate within blocky quartz (XPL).

first appears as a ~100 µm rim of microquartz surrounding most grains (white arrow, Figure 12B). The second is a pore fill, consisting mostly of megaquartz, with minor chalcedony fans. The quartz cement is clean and does not contain any inclusions. Rare cryptocrystalline inclusions of carbonate are present in some granules and ooids (Figure 12D).

When present, carbonate is a minor constituent, generally occurring as large (200 to 500 µm) euhedral rhomb-shaped crystals of ferroan dolomite which cross cut grainstone-stromatolite

boundaries. However, rare granules are present and are composed of fine-grained carbonate surrounding a pyrite core which appears as a secondary replacement mineral (Figure 12C). In one sample, cryptocrystalline carbonate inclusions were noted within quartz grains comprising the laminae of an ooid. The cryptocrystalline carbonate was concentrated in a 40 μm zone with diffuse boundaries both into and out of the ooid (Fig 11D).

As noted above, the lamination within the stromatolite is commonly poorly preserved and highly discontinuous. However, when present the darker laminae drape over one another at the outer edges of the column creating a thick, continuous wall structure. The dark laminae are composed of cryptocrystalline quartz with abundant iron-oxides and organic material. They are in stark contrast to the clean megaquartz present in the interspace (Figure 13A). Opaque zones within the dark bands are concentrated at the edges of the columns. At high magnification it can be seen that the opaque zones contain abundant microfossils (Figure 13B). Broken pieces of filaments are the most common microfossil form present, however intact filaments can exceed 150 μm in length. Similarly, spheres with diameters of 1 to 5 μm are often interspersed with the filaments.

One clast, similar to the oncolite in Figure 11D, revealed alternating laminae composed of dark, iron-rich, cryptocrystalline quartz and light, iron-poor microquartz (Figure 13C). Similar to the stromatolites, fossilized filamentous and coccoid microorganisms are closely associated with the dark iron-rich lamina (Figure 13D). Interestingly, the contact at the top of the dark laminae is often sharp and continuous whereas the contact at the base is often highly irregular and contains abundant microfossils. Investigation of the clean microquartz within the stromatolite and interspace turned up no microfossils.

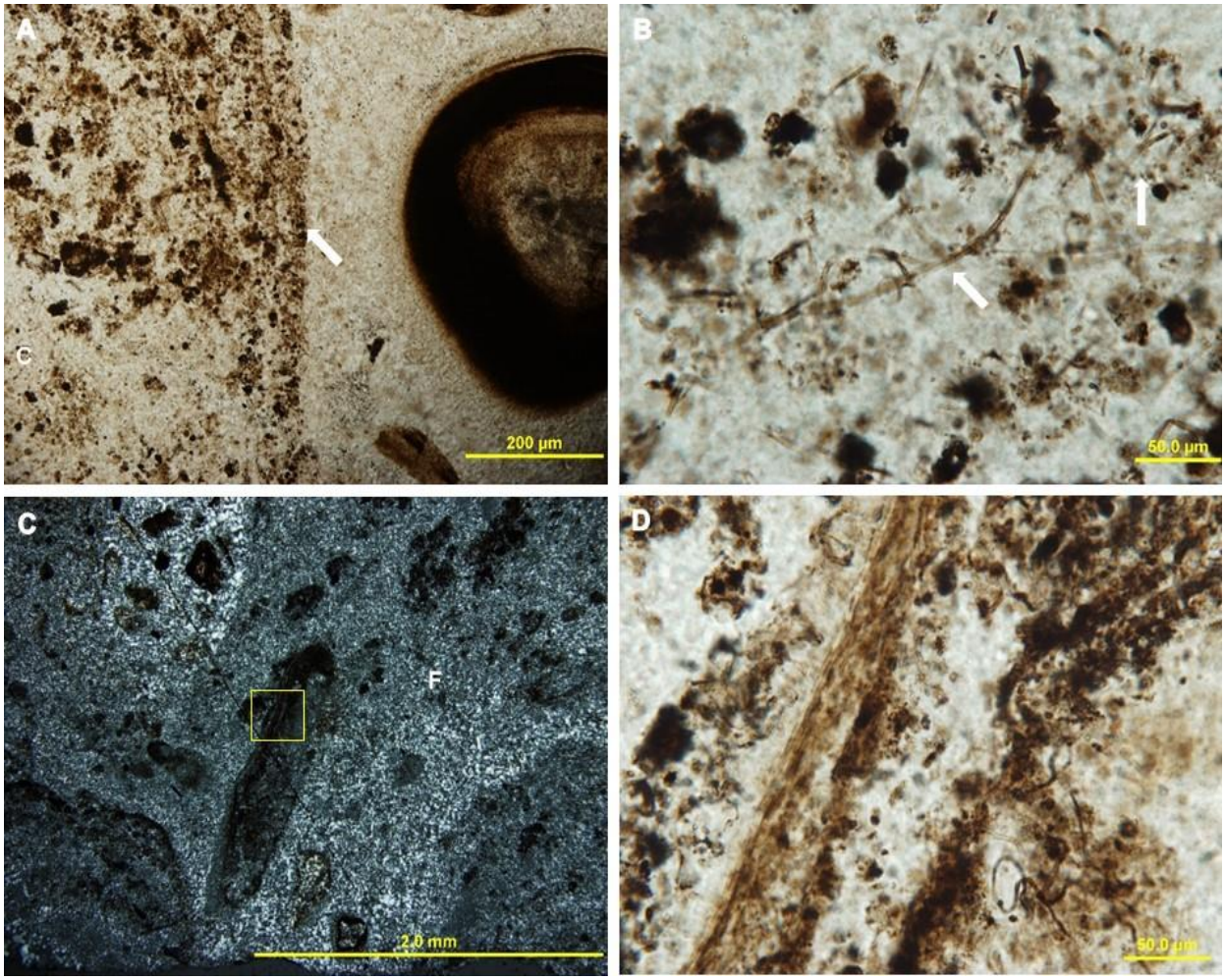

Figure 13. Photomicrographs of fossilized microorganisms within stromatolite laminae. (A) The sharp contact between the stromatolite wall and the grainstone filled interspace (XPL). The reddish-brown microquartz that make up the stromatolites is in stark contrast to the clean quartz cement filling in the intergranular space. The stromatolites are composed of reddish-brown microquartz, with 20 to 40 um opaque zones. (B) Within these zones clusters of spherical and filamentous forms are present similar to extant bacteria (PPL). (C) Laminated intraclast between stromatolite laminae. Note the multiple laminations (yellow box) present on one side but not the other (XPL). (D) 1000x magnification photomicrograph of the area within the yellow box in (C) highlighting the laminations and filamentous and spherical bacterial forms. The fossilized bacteria are concentrated in brown to opaque areas.

The ICP-MS measured rare earth element (REE) contents for samples collected from the Schreiber Channel location were normalized to PAAS values and plotted (Figure 14). The samples selected for analysis include three samples from unlaminated black chert domes (SC-3, SC-A and SC-B), and one from a digitate stromatolite (SC-X). The plot shows a consistent

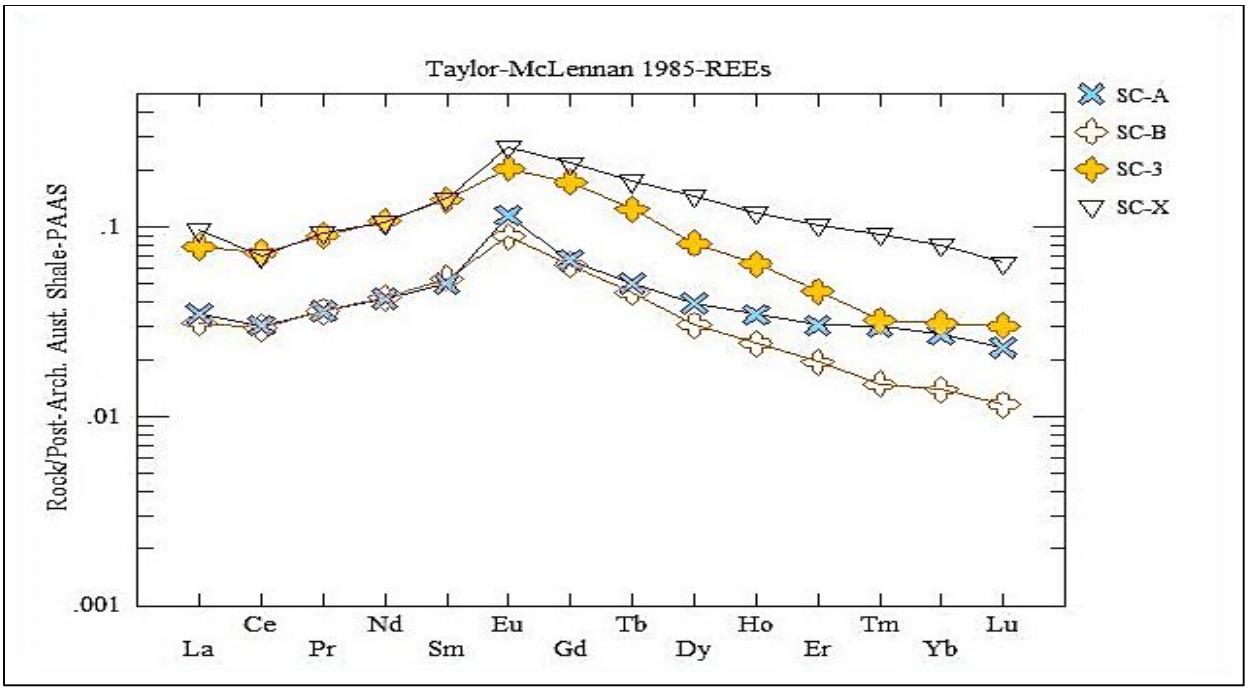

Figure 14. The PAAS normalized REE diagram for Schreiber Channel showing a very slightly negative Ce, distinctly positive Eu anomalies and a slight depletion in LREE and HREE in relation to the mid-REEs.

pattern among the four samples with a slight depletion in LREE and HREE, in relation to the middle-rare earth elements, a very slight negative Ce anomaly and a distinct positive Eu anomaly.

2.1.3 Whitefish Channel

UTM 289167E, 5351919N, 16N

The Whitefish Falls study site is located roughly 3.0 km west of Nolalu, Ontario. The stromatolites crop out continuously over 150 m on the river, on the south side of Hwy. 588 roughly 30 m downstream of the bridge. Two sites were delineated along the river: Site A dominated by several large subspherical bioherms and Site B where the removal of the upper

portions of the bioherms has revealed the internal decimeter scale domal, columnar, and pseudocolumnar forms.

The stromatolitic mounds present along the river at Site A range up to 2 m in diameter and 1 m height. Often, multiple bioherms in close proximity to one another are draped by a 5 to 10 cm thick layer of chert which imparts a hummocky appearance to the outcrop (Figure 15A). The bioherms form directly on the Archean basement diorite and rarely on cobbles from the basal conglomerate unit. An exposure of the basal contact between the diorite and the stromatolitic unit show undulatory, stratiform stromatolites 1 to 5 cm thick, which grade vertically to columnar, and pseudocolumnar forms within the bioherm (Figure 15B). The stromatolites are composed of chert in a range of colours from mostly black and grey to red, green and purple. Siliciclastic-carbonate grainstone with carbonate cement is present between the bioherms, and more rarely in the interspace between stromatolite columns.

Site B is located roughly 75 m downstream at the rapids. Due to the unusually high water levels at both site visits, much of the outcrop was underwater, with only a small section subaerially exposed for observation. This site is characterized by the conspicuous absence of the large hummocky bioherms present at Site A due to erosion. The erosion of the tops of the bioherms and natural polishing of the outcrop (absent at Site A) provides a detailed internal view of the bioherms. Large domes composed of alternating light and dark red jasper laminae make up the remains of a large meter-scale bioherm (Figures 15C, 15D). Erosion of the carbonate grainstone surrounding the siliceous stromatolites causes higher relief of the centimeter-scale columnar forms present with well-defined walls (Figures 15E, 1F). The interspace between stromatolites is composed of a medium- to fine-grained carbonate grainstone containing

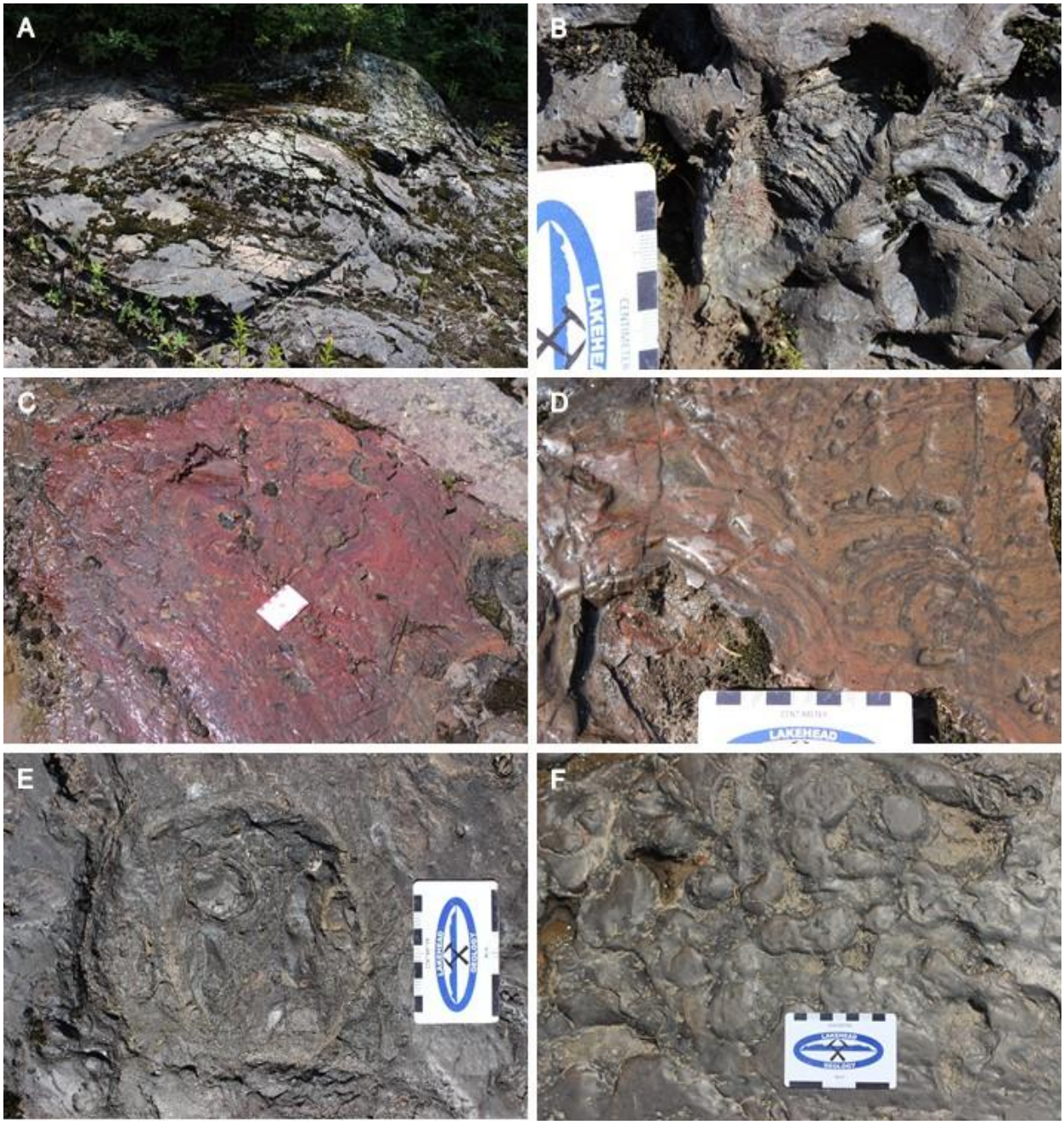

Figure 15. Outcrop photographs of the Whitefish Falls study site. (A) The outcrop consists of several large bioherms that range up to 2 meters in diameter, and 1.5 m height. (B) Internally they are composed of columnar and pseudocolumnar stromatolites. These are often present forming on a 1 to 5 cm thick layer of basal stratiform mat. (C) Erosion of the bioherms provides an internal view of the jasper-rich decimeter-scale domal, columnar, and pseudocolumnar forms. (D) Gently convex, red jasper decimeter-scale domes, 2 to 4 cm in relief are present on topographic highs near the rapids. (E) Domal stromatolites with well-defined wall structures composed of dark chert with carbonate grainstone surrounding them. (F) Internally the domes are made up of centimeter-scale columns.

abundant ooids and granules. In total, seven hand samples were collected; two from Site A and five from site B.

In common with previously described samples from Kakabeka and Schreiber, the preservation of the internal laminae varies depending on the sample. In some cases, the core of the stromatolitic domes is composed of massive black chert which grades into pale grey chert or iron silicate-rich outer zones (Figure 16A). The dark laminae are irregular and highly diffuse commonly grading into the lighter layers. Preservation of the laminae within the columnar and pseudocolumnar forms from Site B is better than that of found within the bioherms. The laminae alternate between millimeter-scale white chert and dark micrometer-scale black organic-rich laminae. Centimeter-scale digits with defined wall structures typify the stromatolites of Site B (Figures 16B, 16C). The digitate stromatolites made up of white chert (Figure 16B) are in contrast to the jasper-rich digitate forms (Figure 16C). Trapping of grainstone containing grains of white chert with green reduced-iron-rich laminae is prevalent in the interspace between columns and domes, similar to that of the other two basal sites (Figure 16D).

In thin section, the poor preservation of the lamination is evident with only faint alternation of dark and light layers present. Despite the poor preservation, examination of the dark laminae reveals a composition of chert with inclusions of cryptocrystalline iron oxides, carbonaceous material and minor euhedral pyrite grains. Microcrystalline quartz with little to no inclusions make up the light laminae.

Intraformational clasts up to a few millimeters in length are common in the interspace, and in some cases make up almost half of the grains (Figure 17A). A rim of cryptocrystalline quartz, 50 to 75 μm thick coats the nuclei grains (Figure 17B). SEM point analysis of the rims

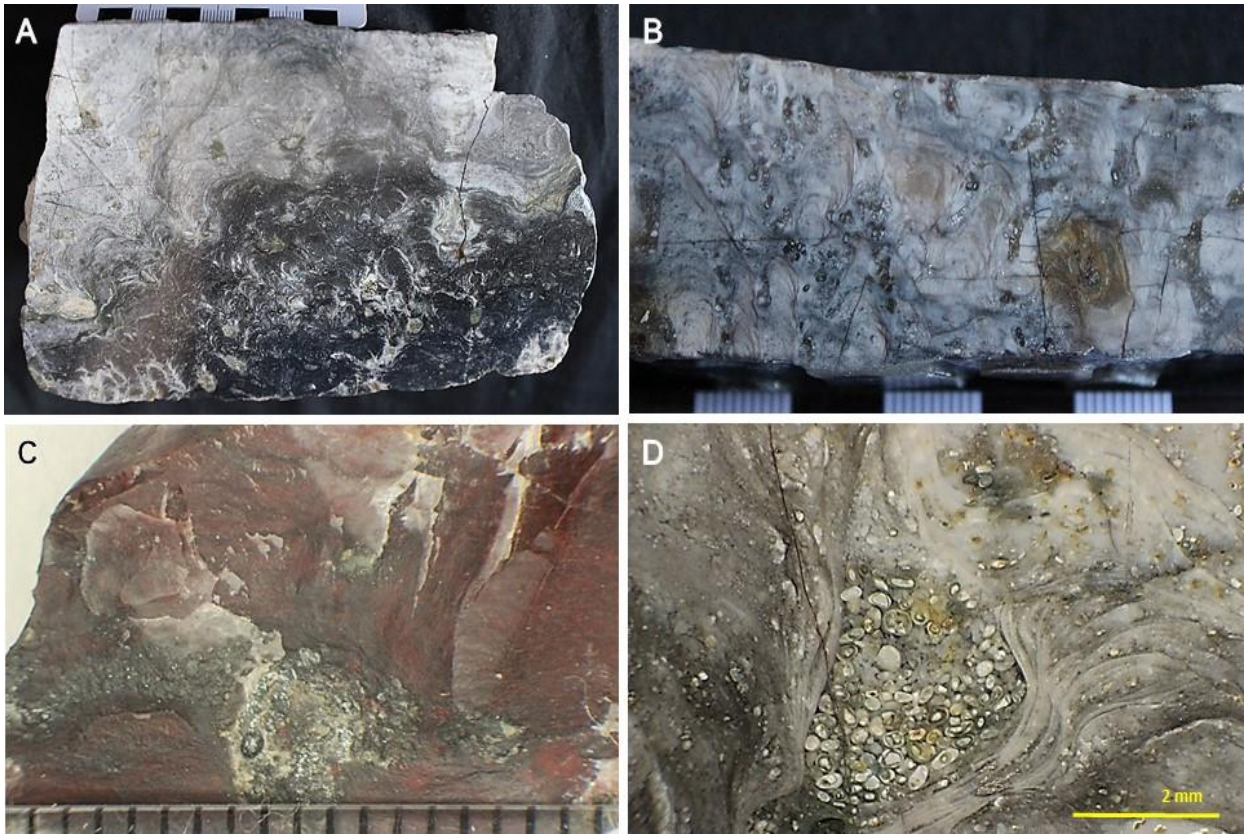

Figure 16. Whitefish Falls hand samples. (A) Photograph of siliceous domal stromatolite taken from large bioherm. Note the change from the massive black chert core to the light coloured laminated outer periphery. (B) Photograph highlighting the poor preservation of the laminae commonly found in the columnar and pseudocolumnar forms. (C) Photomicrograph of jasperlitic digitate stromatolite and interspace containing specularite granules (D) Pockets of grainstone made up of white chert with green (reduced iron) laminae, between columnar stromatolites.

shows iron concentrations up to 70% FeO, similar to the values found in the iron-rich stromatolite laminae. The rim is composed of micrometer-scale laminae with a distinct drape from one grain to the next, similar to a bacterial mat. Internally the clasts have a grumulose microtexture imparted by high organic content and diffuse cryptocrystalline iron oxides with minor euhedral pyrite grains (Figure 17C).

The jasperlitic material in Figure 16C is composed of centimeter-scale digitate stromatolites, surrounded by ooid- and peloid-rich grainstone (Figure 18A). The grains have varied compositions, ranging from chert, jasper, hematite, and greenalite. Interestingly, some of

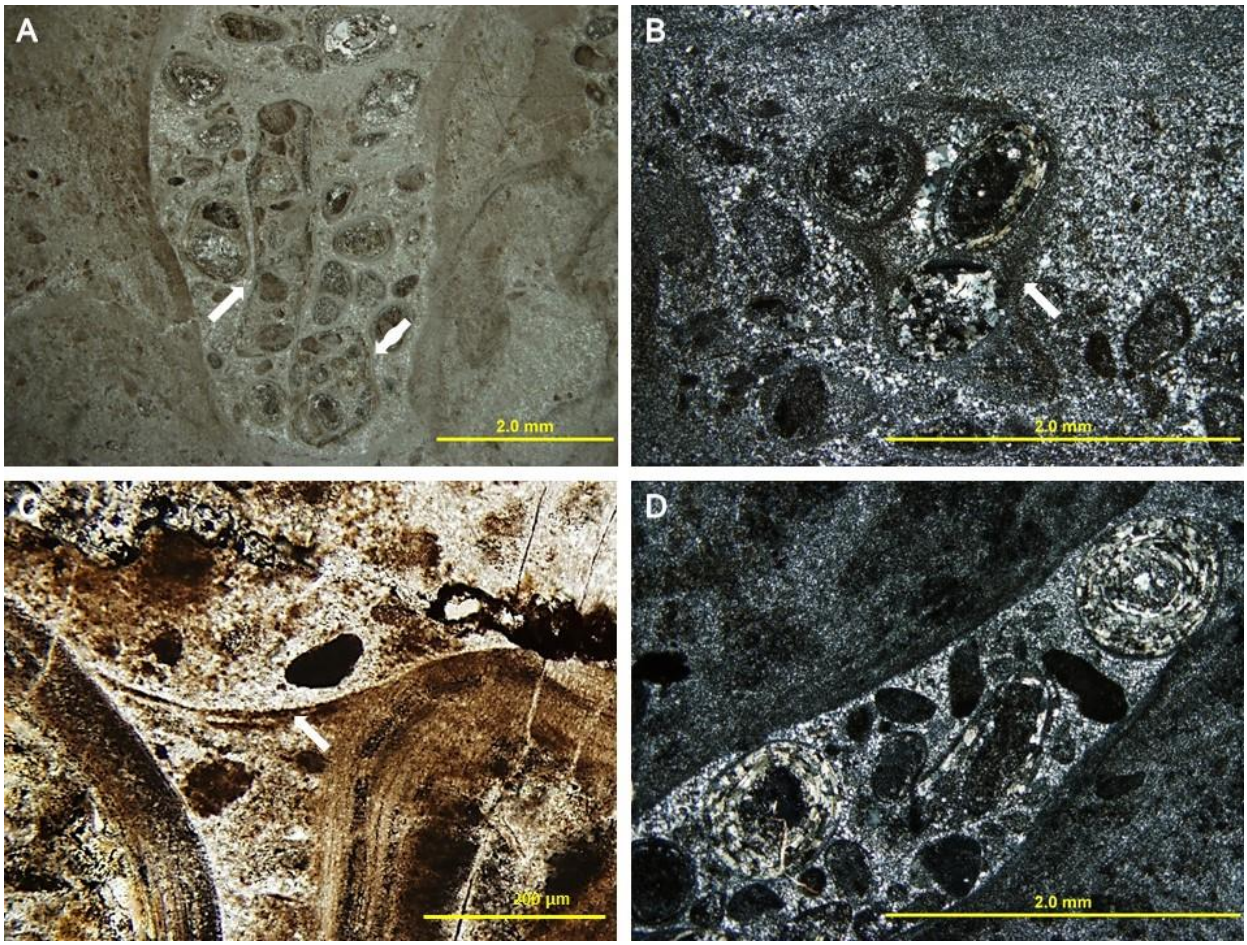

Figure 17. Photomicrographs of clasts in interspaces. (A) Photomicrograph of millimeter-scale clasts (white arrows) made up of multiple ooids and granules located in the interspace between columns (XPL). (B) Photomicrograph of clasts rimmed by a 50 to 75 um thick layer of fine grained quartz, similar to that of the stromatolite laminae (XPL). (C) Photomicrograph of the side of a 3 mm clast containing multiple ooids. A thin layer of fine-grained quartz exhibiting grumulose microtexture, drapes across the ooids (white arrow) (XPL). (D) Iron silicate ooids showing well defined cortical lamination.

the larger granules are composed of specularite. The digitate stromatolites are made up of alternating light and dark laminae. The light laminae are composed of microcrystalline quartz with rare cryptocrystalline hematite inclusions whereas the dark laminae are made up of dense concentrations of hematite-coated filaments, spheres and irregularly shaped star-like forms (Figures 18B, 18C).

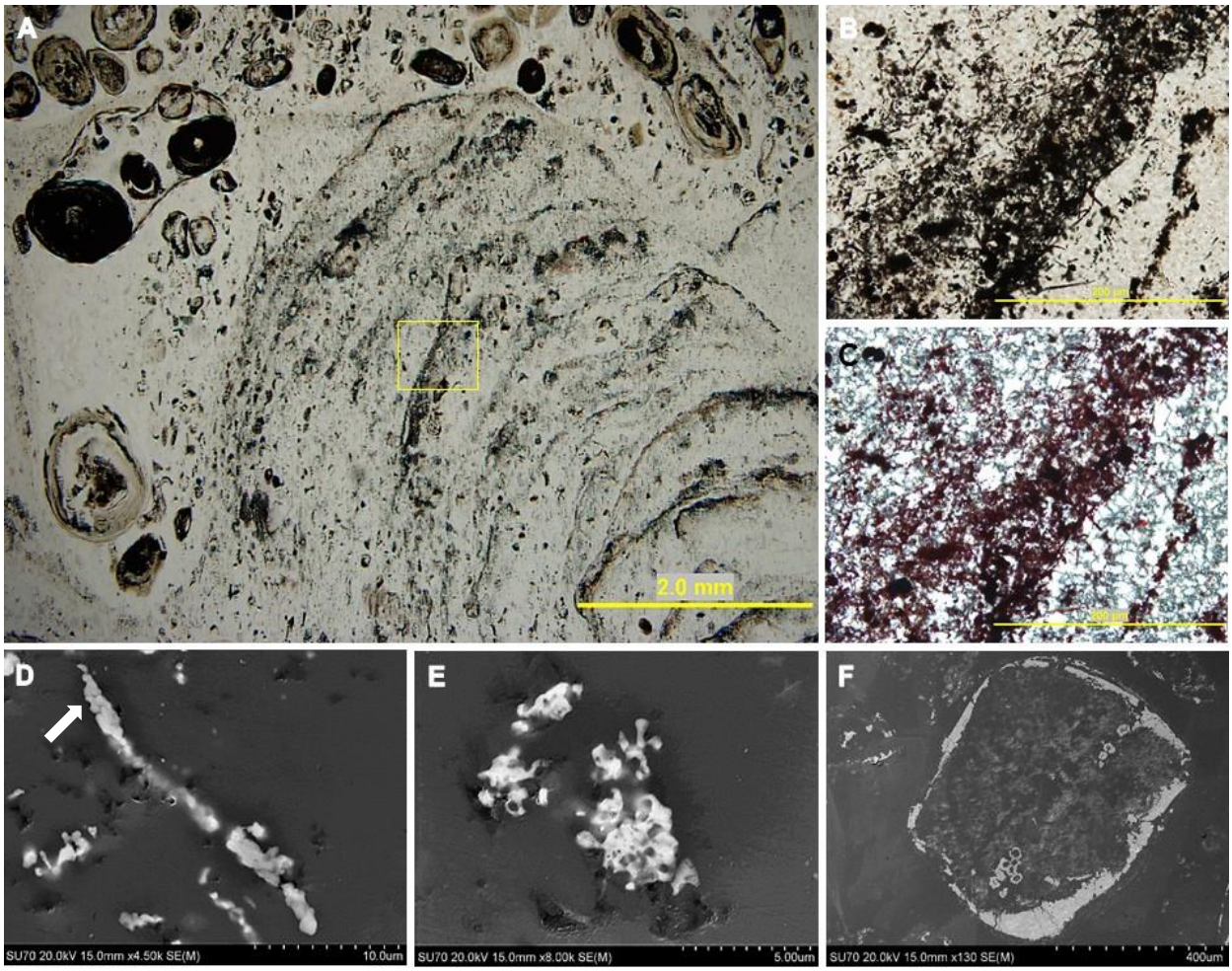

Figure 18. Microfossil-rich zones within the jasperlitic digitate stromatolites. (A) Digitate stromatolite composed of alternating light and dark laminae made up of chert and microfossil-rich jasper and hematite laminae respectively (PPL). (B) High magnification photomicrograph of yellow box in (a) illustrating dense concentration of filaments, spheres and irregularly shaped microfossils (PPL). (C) Same as (b) showing the cryptocrystalline hematite coating the microfossils (XPL). (D) Secondary electron (SE) image of a filament coated in blobs of hematite (white arrow). (E) SE image of star-shaped, micrometer-scale hematite coated structures intermixed with the filaments and spheres. (F) SE image of 20 to 30 µm hematite coated spheres within an iron-coated peloid.

SEM investigation of the dark laminae verified the petrographic observations that the microfossils were coated in hematite (Figure 18D). Intermixed with the filaments and spheres, star-shaped, micrometer-scale hematite-coated structures are present which have four to six appendages extending out from a central sphere (Figure 18E). Several granules were noted containing clusters of 20 to 30 µm hematite-coated spheres (Figure 18F). The preservation of the

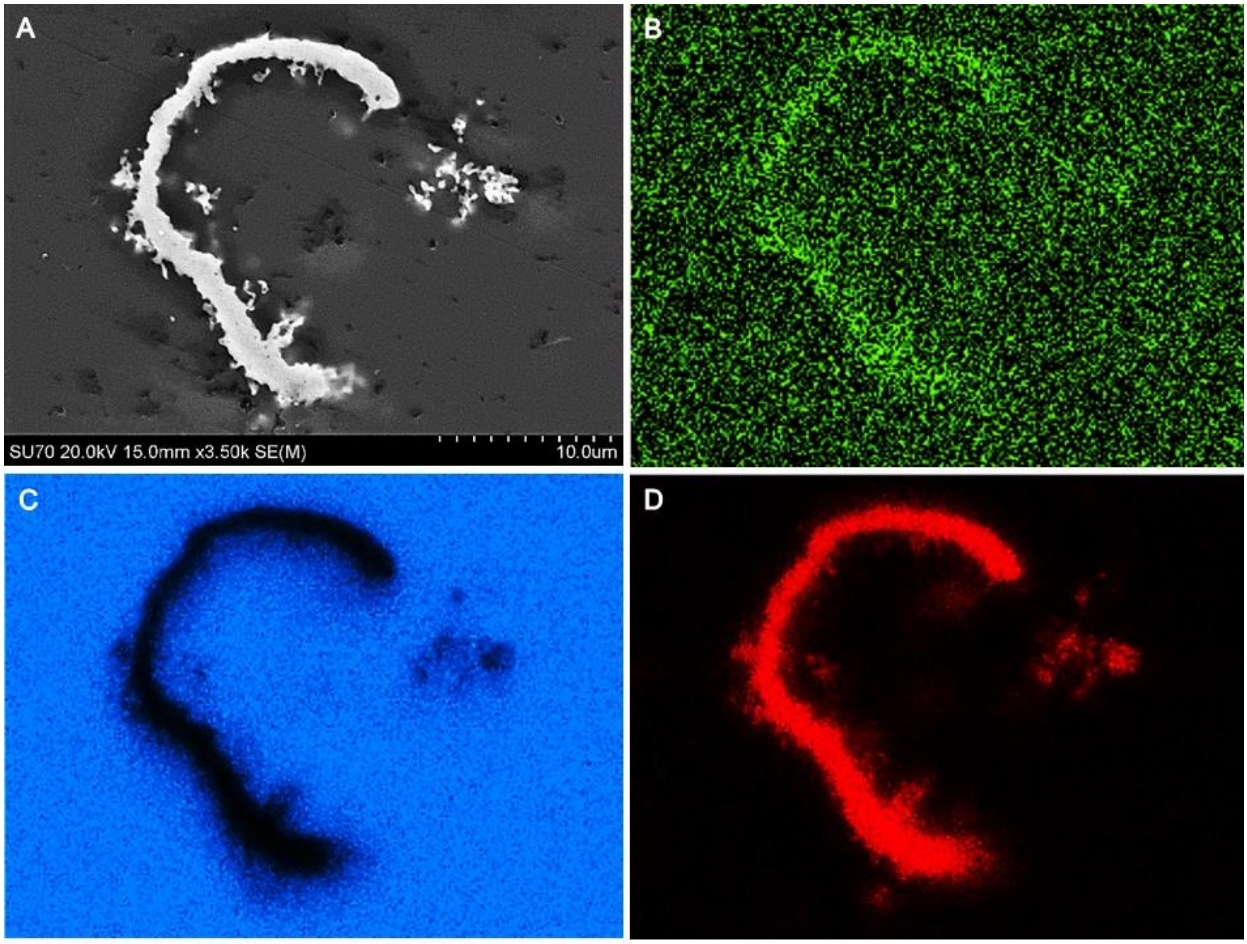

Figure 19. Elemental mapping of iron-coated microfossil. (A) Secondary electron image of an iron-coated filament surrounded by silica. False colour mapping of (a) showing the relative abundances of (B) Phosphorous, (C) Silicon, and (D) Iron.

microfossils is variable; however, some are exceptionally well preserved (Figure 19A). Elemental mapping a well preserved filament reveals the relative abundances of phosphorous (Figure 19B), silica (Figure 19C) and iron (Figure 19D).

Carbonate is present as a minor component in all samples examined. Most often it occurs as ankerite rhombs which cross-cut stromatolite laminae and grain boundaries within the grainstone. Figure 20 shows two quartz granules, in different stages of replacement. The peloid

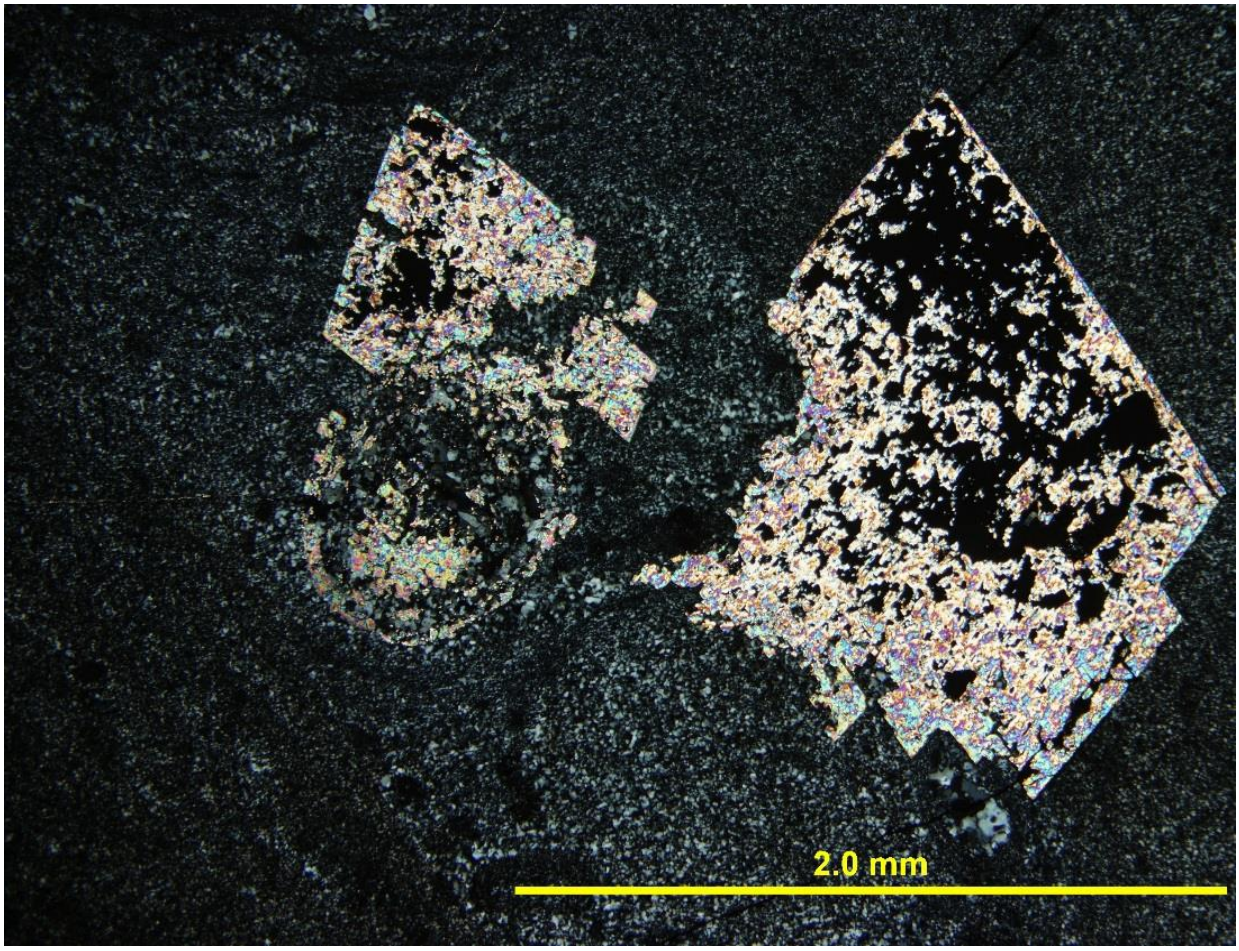

Figure 20. Ankerite rhomb replacing quartz granules (XPL). Note the almost complete replacement of the granule on the left. The grain on the right is partially replaced.

on the left has been almost completely replaced whereas the grain on the right is partially replaced as noted by the partial rim of carbonate making its way around the outer edge of the grain.

The ICP-MS measured rare earth element (REE) contents for samples collected from the Schreiber Channel location were normalized to PAAS values and plotted (Figure 21). The samples selected for analysis include two samples containing jasperlitic digitate stromatolites (WF-A, WF-B) and two samples containing digitate stromatolites composed of white and grey

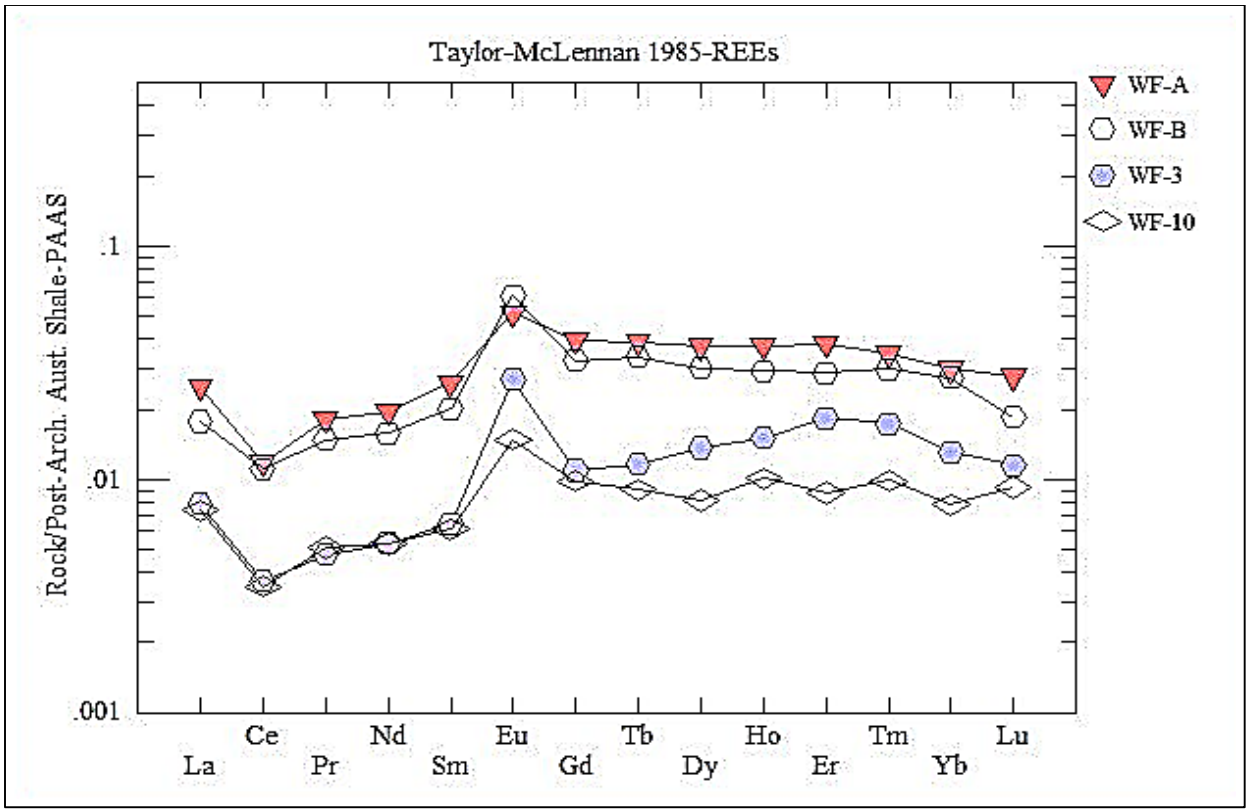

Figure 21. The PAAS normalized REE diagram for Whitefish Falls location showing distinctly negative Ce and distinctly positive Eu anomalies and a slight depletion in LREE in relation to the HREE.

chert (WF-3, WF-10). The plot shows a consistent pattern among the four samples with a slight depletion in LREE compared to the HREE, a distinct negative cerium Ce anomaly and a strongly positive europium Eu anomaly.

2.2 Middle Stromatolitic Member

2.2.1 Mink Mountain

UTM 710621E,5346233N 15N

The Mink Mountain study site is located roughly 30 km west of Nolalu, Ontario, just outside of the village of Soumi. Access is via an unmarked gravel road at the end of the paved portion of Highway 588. The Middle Stromatolitic Member crops out in two locations at this site. The first site is a 4 m cliff which provides a vertical profile of the grainstone and overlaying stromatolites (Figure 22A). At the base of the outcrop, a ~2.5 m layer of medium to coarse grainstone intermixed with fine grained jasperlitic muds is exposed. At the top of the grainstone a 30 to 40 cm breccia layer containing large (decimeter-scale) lithified blocks of grainstone is present. These blocks are overgrown by wavy stratiform stromatolites which grade into columnar and digitate forms (Figures 22B, 22C). The stromatolitic unit is 1.25 m thick and some places grades into a coarse to medium grainstone layer at the top of the outcrop. The second outcrop is a jasper quarry consisting of a 1.5 m vertical ledge and several square meters of horizontal exposure. At the base of the vertical exposure the breccia is exposed, with stratiform stromatolites growing on and filling in between the blocks. However, the bulk of the exposure is of the jasperlitic digitate and domal stromatolites (Figure 22D).

Representative hand samples of the stratiform, domal, and digitate forms were collected in situ, and polished for analysis. The decimeter-scale domes show the typical zonation found in the previously described samples from other locations (Figure 23A). The core of the domal stromatolite consists of centimeter-scale digitate stromatolites surrounded in a medium- to coarse- grained oolitic grainstone. The columns have well defined walls at the grainstone

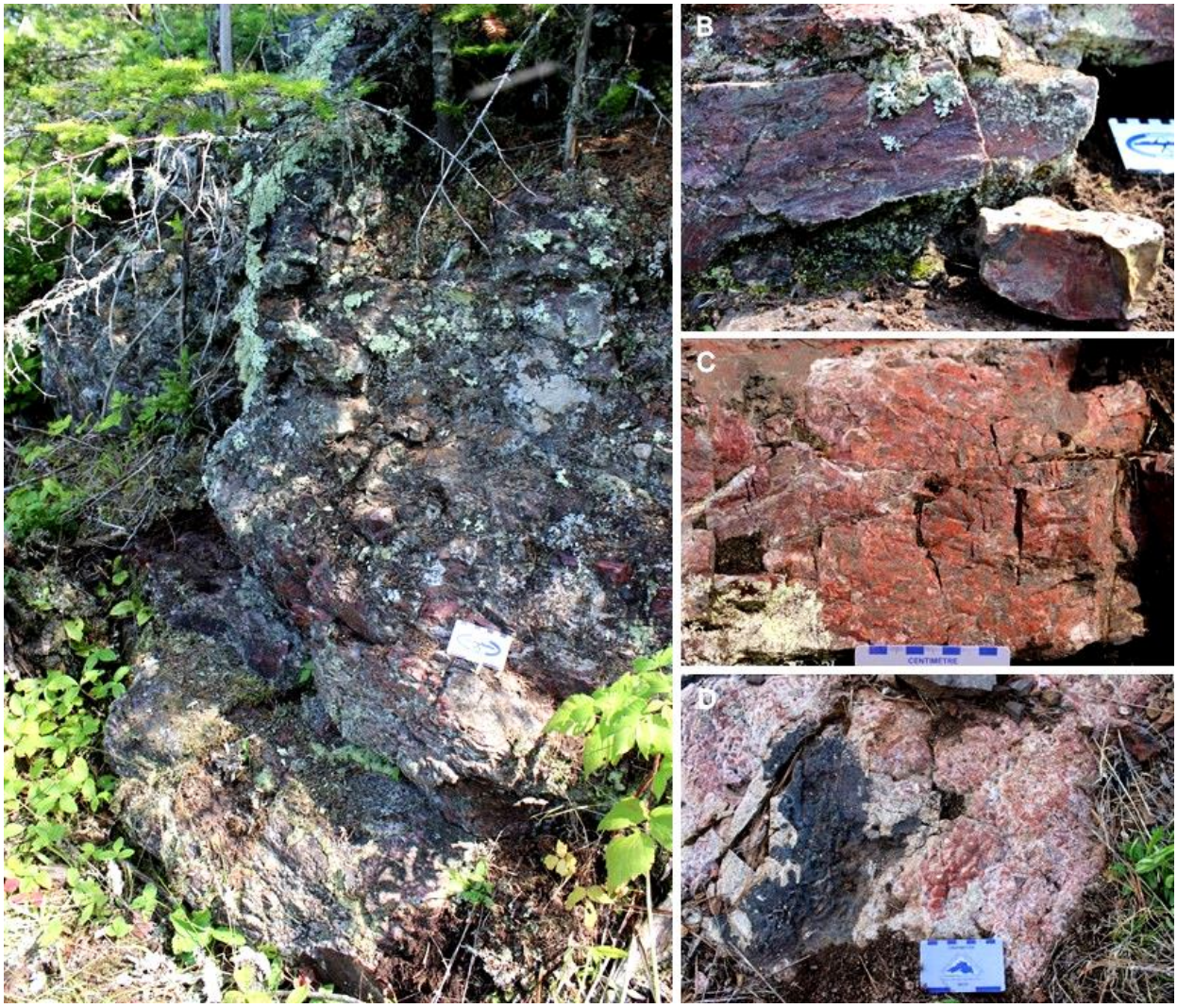

Figure 22. Outcrop photographs of the Mink Mountain study site. (A) Vertical exposure of the 2.5 m grainstone unit underlying the 1.25 m Middle Stromatolitic Member. (B) The base of the Stromatolitic unit is composed of 30 to 40 cm of stratiform and domal forms. They are composed of red to purple jasper. (C) Overlying the basal stratiform and domal forms, a 60 to 70 cm thick zone of digitate and pseudocolumnar forms are present. (D) Lateral view of closely spaced, centimeter-scale digitate stromatolites bordered by a zone of magnetite.

interface, with minimal trapping of grains within the laminae. The columns grade into pseudocolumnar forms, with a notable increase in the amount of grains trapped in the fossil microbial mat between laminae. The microbial mat in this zone is highly irregular, noted by the discontinuous laminae which fade into and out of the grainstone. At the outer periphery, the entire dome is covered by a thick (>5 mm) wavy stratiform mat. Interestingly, the stratiform mat

covering a dome has an almost complete lack of grains within the laminae. The stromatolites are composed of light-orange to red chert which alternate with hematite or rare specularite laminae.

Both γ-parallel and divergent branching is common, and rarely coalescing of multiple columns was noted. Branching occurs where the column diameter increases resulting in a marked decrease in the convexity of the laminae. Trapping of ambient grains within the laminae cause a minor buildup of the microbial mat, resulting in the development of the daughter columns (Figure 23B). The diameter of the daughter columns is roughly equal to that of the parent column prior to branching. A horizontal section through several columns shows the cylindrical to sub-polygonal shape of the columns (Figure 23C). The well-defined jasper stromatolites are in stark contrast to the dark silver specularite grains within the black chert interspace. Interestingly, the walls at the grainstone-stromatolite interface do not appear to contain specularite.

The layers within the columnar and domal stromatolites alternate between light and dark bands, with occasional discontinuous black zones within the dark laminae (Figure 24A). The light laminae are composed of clean, microcrystalline quartz, with thicknesses ranging up to 250 μm. In some samples the light laminae predominate over the dark. However, more commonly the majority of the laminae are dark and are composed of finely disseminated cryptocrystalline hematite inclusions in 10 to 25 μm microquartz crystals. Both the light and dark laminae range from highly continuous to highly discontinuous across the columns although the thicker (>200 μm) quartz laminae show excellent continuity over several millimeters (Figure 24B). The bridging of columns by the microbial mat is evidenced by the wispy microcrystalline jasper draping over the grains within the interspaces. Figure 24C shows a peloid at the base that was

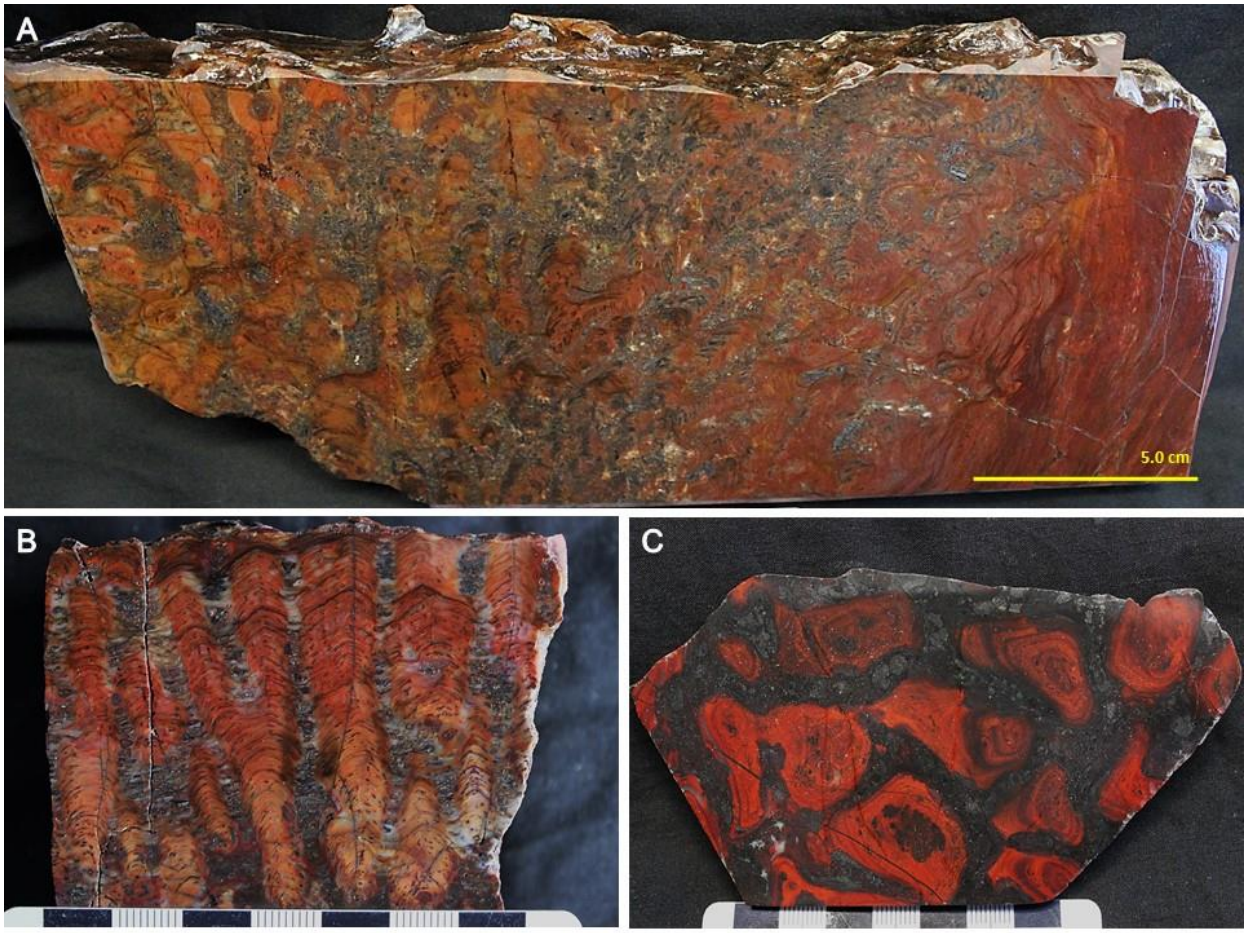

Figure 23. Photographs of polished hand samples. (A) Section through domal stromatolite. Digitate stromatolites surrounded by a specularite-rich grainstone comprise the core of the dome. In the middle of the sample the digits morph into pseudocolumnar forms, eventually resulting in a stratiform mat that covers the dome. (B) Branching occurs as γ-parallel and divergent forms with rare coalescing of columns. (C) The columns show a cylindrical to sub-polygonal form. The interspace is composed of a mix of black chert, hematite and millimeter-scale magnetite grains.

trapped by the microbial mat prior to the deposition of the larger fractured peloid that rests on top of it. The pore space created by the larger grain is filled by blocky megaquartz, which contrasts to the finer grained material making up the stromatolite laminae. Backscatter imaging and point analysis of the columnar lamination support the compositional alternation of quartz and iron oxides (Figure 24D). Concentrations up to 3.2% MnO are present within the columnar laminae, generally at the top of the iron oxide laminae.

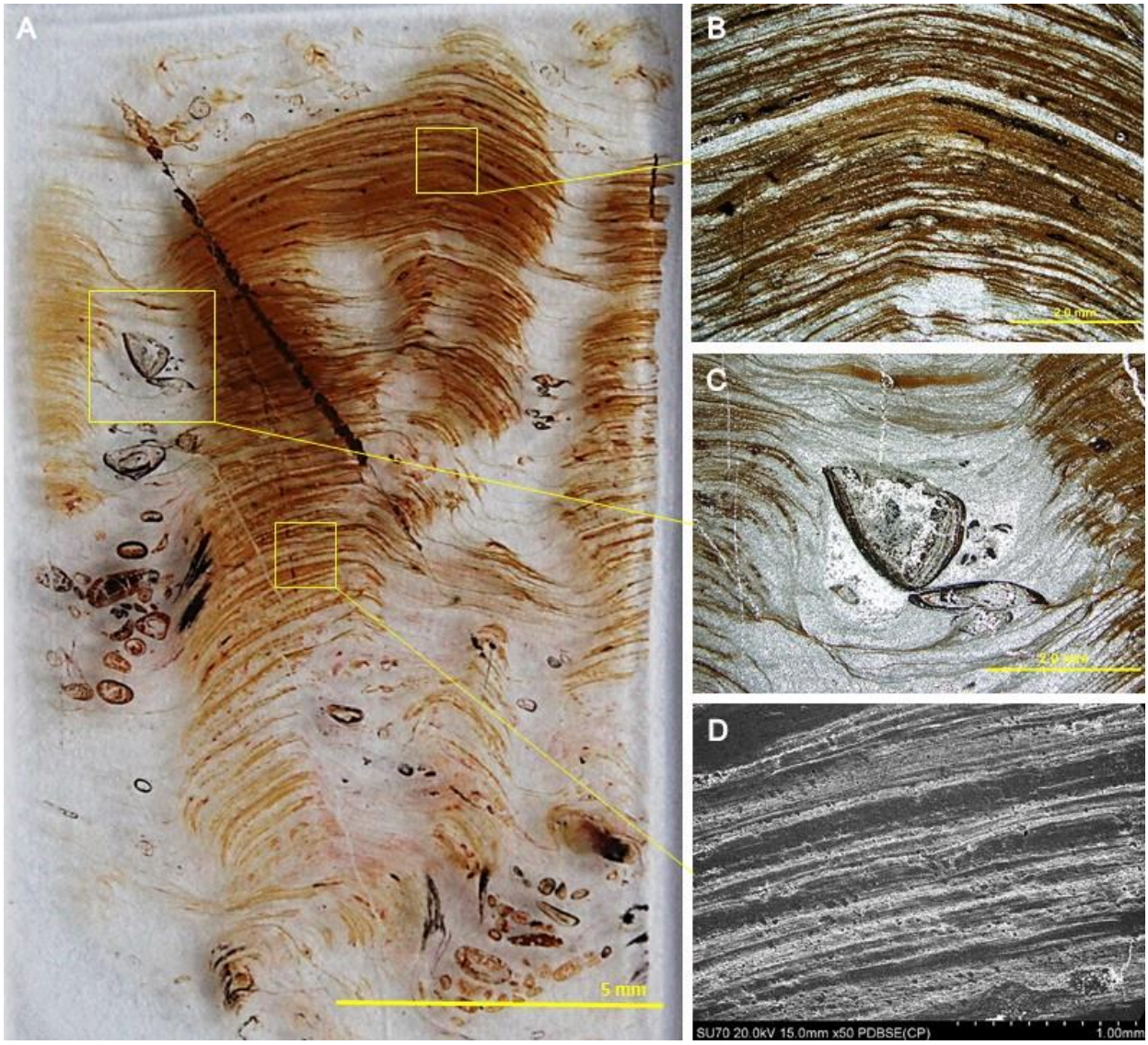

Figure 24. Lamination within Mink Mountain stromatolites. (A) Photograph of a polished thin section showing the typical lamination found in the Mink Mountain digitate stromatolites. (B) The columns are made up of alternating quartz and jasper laminae (XPL). (C) The interspace is made up of microcrystalline quartz, with jasperlitic wisps of microbial mat bridging adjacent columns. Individual grains resting against the stromatolite wall allow large pores to remain open and eventually fill with blocky quartz (XPL). (D) BSE image of laminae. Point analysis indicate areas of elevated manganese alternating with the hematite (pale grey) and quartz (dark grey).

The discontinuous black zones within granules and black zones contained within the hematite laminae are carbonaceous inclusions rich in microfossils (Figures 25A, 25B). Multiple granules containing carbonaceous reddish-black blobs revealed dense concentrations of coccoid microfossils similar to *Huroniospora*. The cells are ~25 µm spheres that are coated in a thin layer

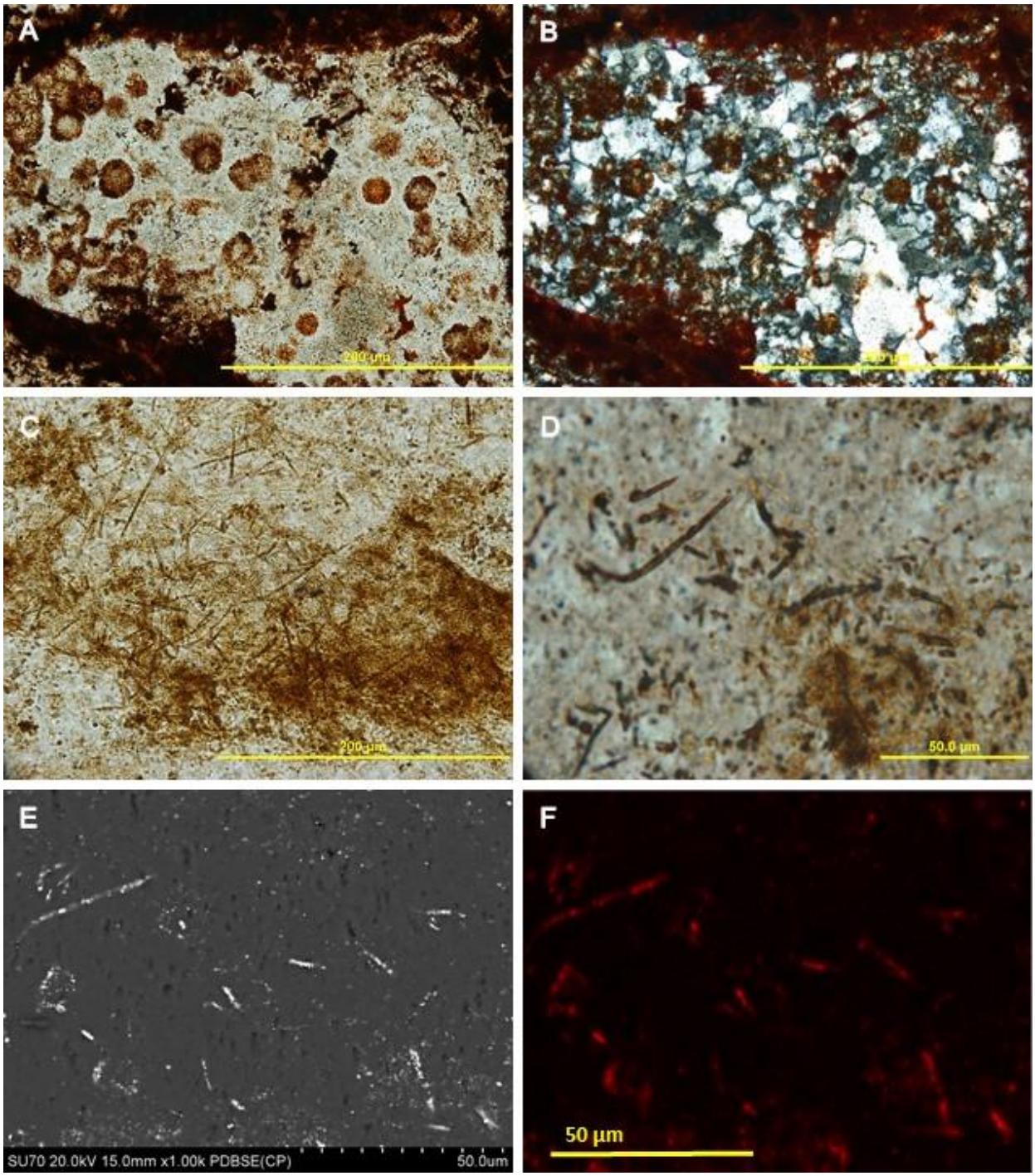

Figure 25. Iron-coated microfossils. (A) Granules containing abundant coccoid microfossils ~25 µm diameter coated in hematite (PPL). (B) The microfossils are embedded in a microquartz cement (XPL). (C) Dense mats of fossilized filaments coated in hematite make up the dark laminae (PPL). (D) The diameter of the filaments range up to 5 µm, with length up to 100 µm (PPL). (E) Backscatter image of filaments and spheres in a silica matrix. (F) False colour BSE image showing the increased iron concentration around the microfossils.

of iron oxides (most probably hematite). In some areas within the granules several spheres are attached to one another. In areas where the cells contact another cell, there is a notable thickening of the iron oxide (Figure 20A). The microfossils are encased in a microquartz cement, which contains cryptocrystalline hematite inclusions (Figure 20B).

The black zones within the dark laminae of the columns contain dense concentrations of fossilized filaments. They range up to 5 μm in diameter and over 100 μm length. However, an accurate estimate is difficult due to the broken nature of the filaments. Similar to the spheres, the filaments are coated in micro-globules of iron oxide and are often found clustered together (Figures 20C, 20D). SEM analysis and false colour mapping of the microfossil-rich areas illustrates the increase in iron concentration on and around the filaments and spheres (Figure 20E, 20F).

As noted above, the bridging of columns across the interspace occurs as thin layers of jasperlitic microbial mat (Figure 26A). The walls of the columns consist of 10 to 15 laminae that pinch together and extend out over the grainstone forming a bridge. A notable change in colour occurs at the grainstone-stromatolite contact from a pale orange in the column to bright red at the wall signifying an increase in hematite concentration within the microbial mat. Pieces of broken stromatolite are often resedimented in the interspace between columns. A thin rim of white chert cement surrounds the pieces and in some cases contains ooids and granules which were cemented together prior to erosion (Figure 26B). The fragments of stromatolite can then become the nucleation point for a column. In Figure 26C, the development of a microbial mat growing over a piece of lithified grainstone (white arrow) can be seen. The jasperlitic mat which started as a thin wisp bridging two columns grew over the fragment, and due to the increase in relief,

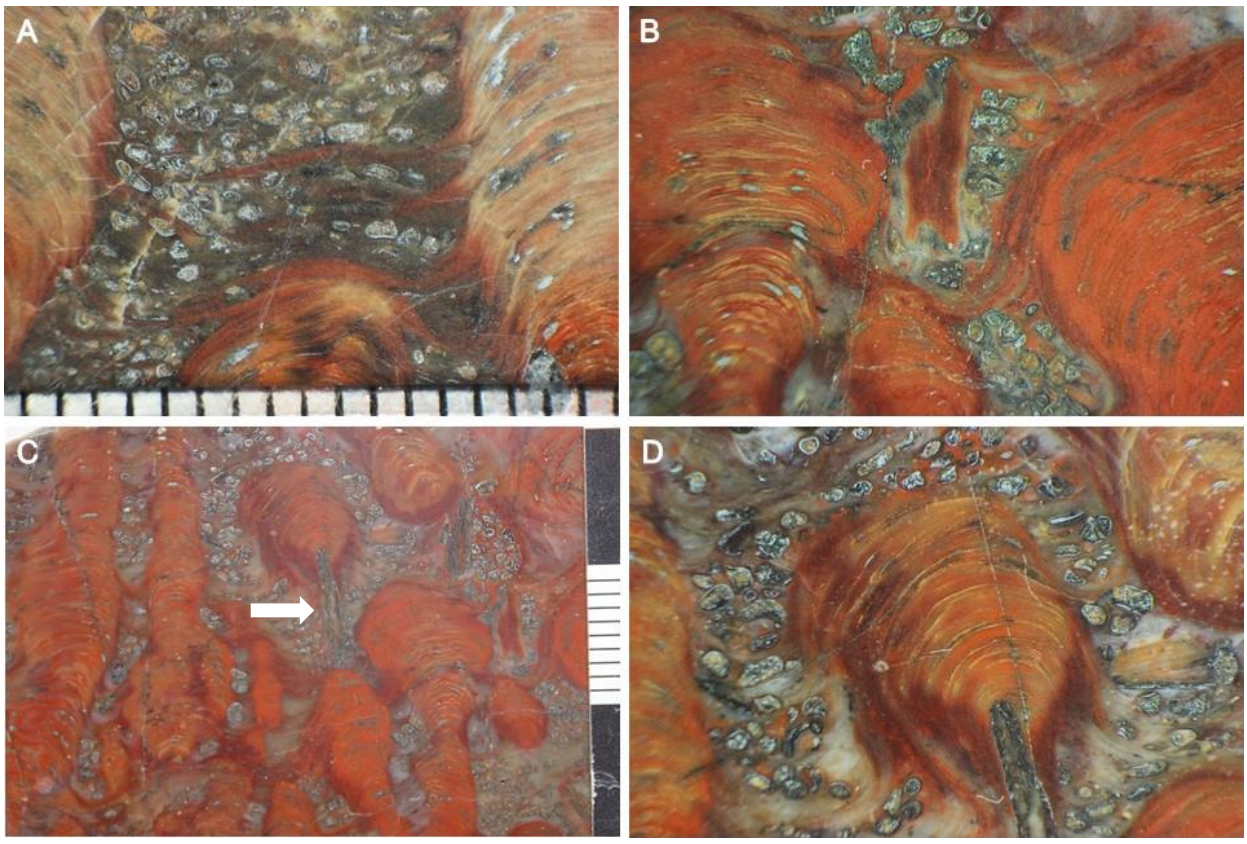

Figure 26. Photomicrographs of digitate stromatolites. (A) Bridging of columns by the development of the microbial mat across the interspace. Note the pinching out and colour intensity increase of the laminae at the grainstone interface. (B) Piece of broken jasperlitic stromatolite with a white quartz rim between columns. (C) Due to the convexity imparted from the stromatolitic mat growing over a clast (white arrow) similar to that found in (b) a new column is formed. (D) 5x magnification of (c). Note scale in millimeters.

developed the characteristic convex digitate form (Figure 26D). The development of the mat across the interspace also traps and binds the ambient granules and ooids in single-grain thick layers.

The grainstone within the interspace and overlying the stromatolites is composed primarily of ooids and granules. However, aggregate clasts similar to those described from the Whitefish Falls site are abundant in some samples. The aggregate clasts contain multiple ooids and granules in a dark microcrystalline cement (Figure 22). These millimeter-scale grains show

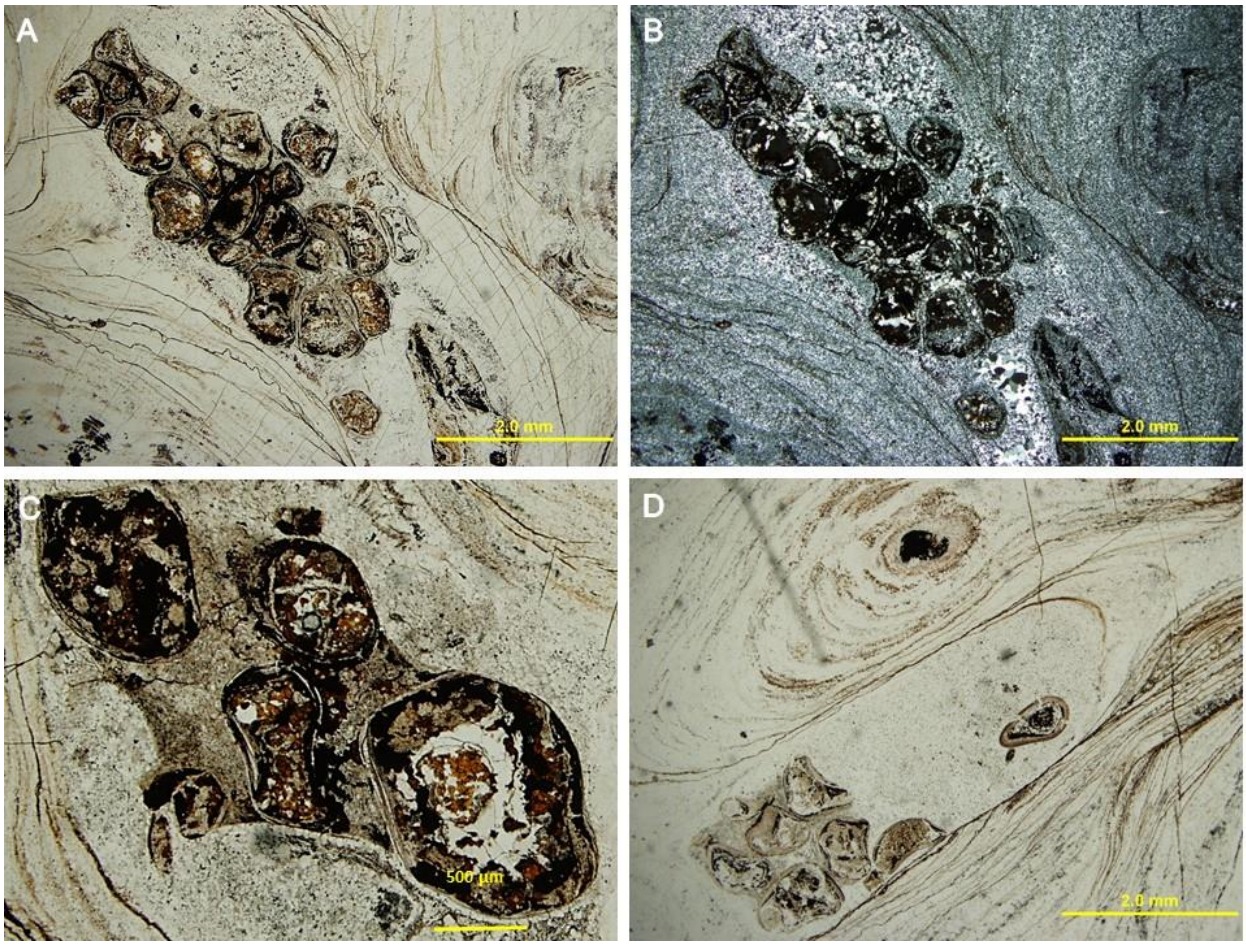

Figure 27. Intraformational aggragrate clasts embedded in the interspace between stromatolite columns. (A) The aggregate clasts contain a complex assortment of tightly packed granules and ooids in an iron oxide-stained cement (PPL). (B) The cement within the clasts is stained by iron oxides, and noticeably different than that of the intergranular cement surrounding the clasts (XPL). (C) The truncation of the granules at the outer edges can be seen at the top left and centre right (PPL). (D) The staining of the cement within the aggregate clasts by iron oxides is in sharp contrast to the clean blocky quartz cement surrounding the clast (PPL).

evidence of prior lithification and subsequent reworking. The granules within the aggregate grains are tightly packed with low intergranular porosity. The edges of the granules are truncated and the intergranular cement has been preferentially eroded. The cement within the aggregate grains is distinct from the surrounding intergranular cement. It is composed of microcrystalline quartz, stained with cryptocrystalline iron oxides imparting a dirty appearance (Figures. 27A, 27B). A micrometer-scale rim cement is rarely present around some of the aggregate grains (Figure 27C). The other two major components of the grainstone within the interspace are

randomly orientated ooids and less commonly granules (Figure 28A). In contrast to the aggregate grains, these grains show low packing density with only rare occurrences of grain to grain contact. The ooids and granules show little to no compaction. The low packing density allows for uninhibited cement development within the intergranular porosity. Multiple generations of cement are present on the grains (Figure 28B). The outermost laminae of the grain, most often iron oxide, has a ~30 μm thick layer of quartz cement orientated perpendicular the surface of the ooid. A second quartz rim cement made up of ~100 μm blades extends from the first. Finally chalcedony fans fill the remainder of the intergranular porosity. Within the ooids, the internal laminae are composed of concentrically laminated cortices of alternating quartz and specularite however magnetite and hematite are also common. The nuclei of the ooids are compositionally diverse. Some samples are composed of fragments of stromatolites and broken ooids (Figures. 28C, 23D), while others contain smaller ooids and granules (Figure 28A). Granules made up of massive greenalite are also common.

Dehydration cracks extending out from the nucleus are common in both the ooids and granules. They cross cut the original laminae and are filled by blocky quartz or more commonly chalcedony (Figures 28E, 28F). Interestingly, the fragmented ooid pieces within the nucleus also show dehydration cracks, which do not extend into the outer laminae.

The ICP-MS measured REE contents for samples collected from the Mink Mountain location were normalized to PAAS values and plotted (Figure 29). The samples selected for analysis include three samples from stratiform mats (CY-71, CY-73A, CY-73B) and a digitate stromatolite (CY-77).

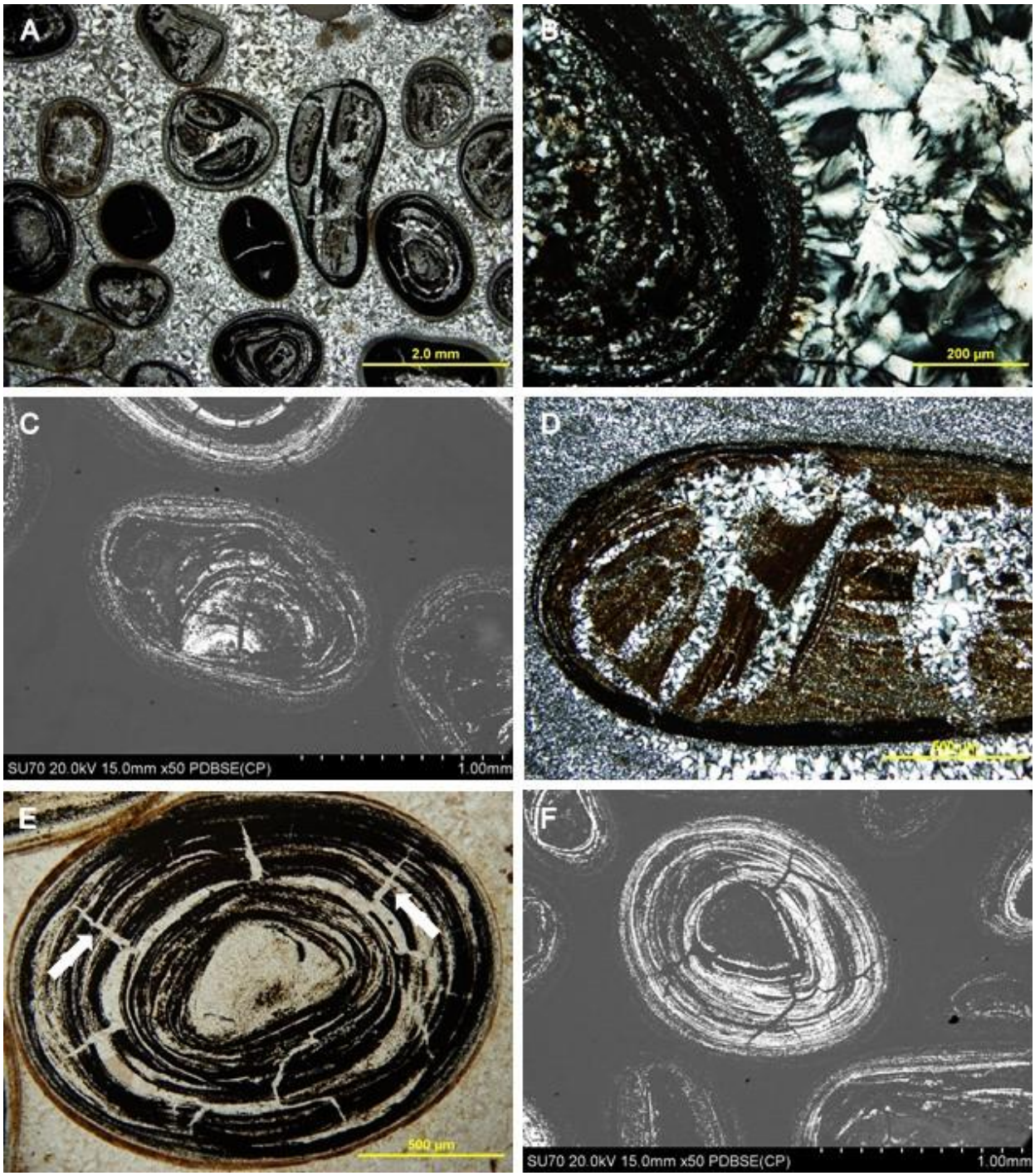

Figure 28. (A) The grainstone is composed predominantly of ooids with minor granules. (XPL). (B) Internally, the ooids are composed of concentrically laminated cortices, alternating between iron oxides (opaque) and quartz laminae. Three distinct phases of cementation can be seen; a thin micro to cryptocrystalline quartz outer rim, a second layer of cement consisting of bladed microquartz, and finally chalcedony filling the remainder of the porosity (XPL). (C) Fragments of ooids and stromatolites are common ooid nuclei (BSE). (D) Laminated fragments and greenalite within an ooid (XPL). (E) Radial septarian dehydration cracks are a common feature in most of the ooids and granules at Mink Mountain (PPL). (F) BSE image of dehydration cracks.

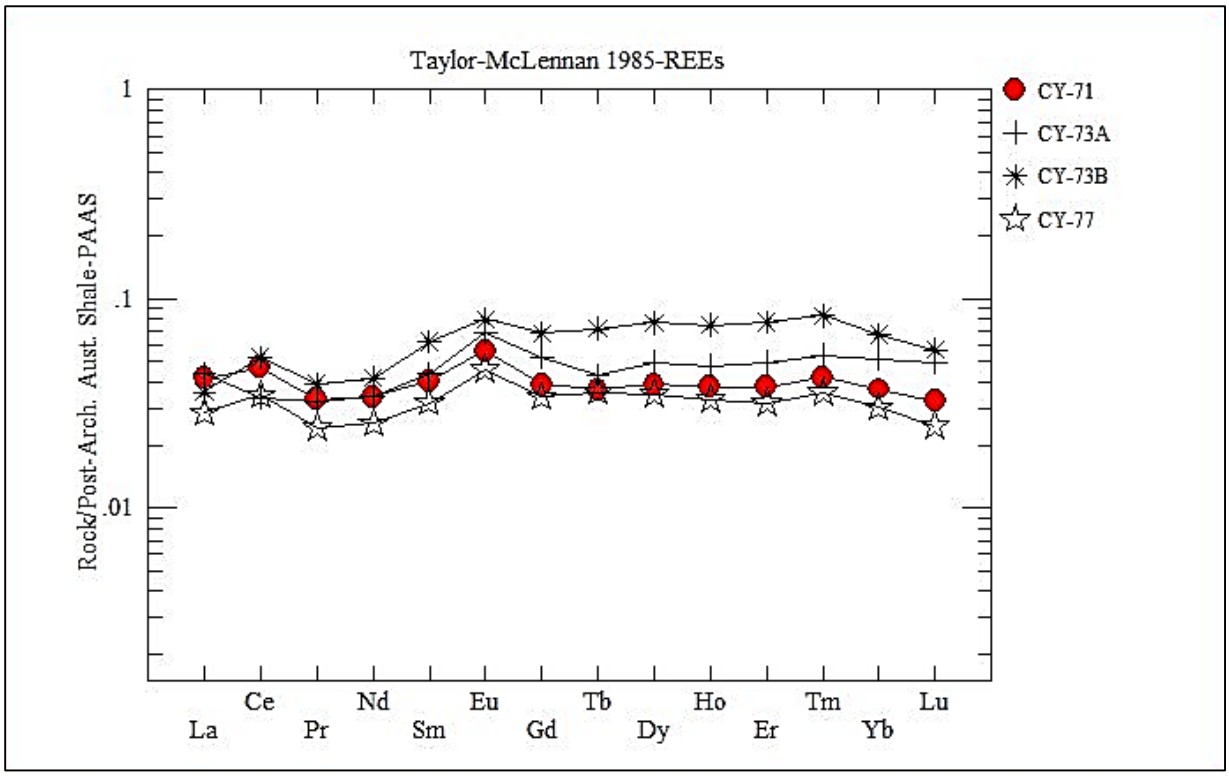

Figure 29. The PAAS normalized REE diagram for The Mink Mountain location showing distinctly positive Ce and Eu anomalies and a minor depletion in LREE in relation to the HREE.

The plot shows a consistent pattern among four samples, (CY-71, CY-73B, CY-77) with a slight depletion in LREE compared to the HREE, a positive Ce anomaly and a positive Eu anomaly. However, sample CY-73A shows a slightly positive La anomaly, resulting in the appearance of a negative Ce anomaly.

2.2.2 Old School Road

UTM 291713E, 5354771N, 16N

The Old School Road study site is located roughly 7 km north of Nolalu, Ontario on Old School Road off Highway 588. The Middle Stromatolitic Member intermittently crops out for 1.5 km on the left side of the road. Detailed site observations and acquisition of samples was difficult due to poor exposure, and much of it extending onto private property.

Morphologically the stromatolites bear a striking similarity to the Mink Mountain outcrop ~30 km to the east. Meter-scale bioherms directly overlying a grainstone breccia characterize the stromatolites at this location (Figures 30A, 30D). The domes are made up of irregular, wavy laminae composed of chert which varies from white to pale pink to red to deep purple. Multiple decimeter-scale domes in close proximity to one another coalesce into larger bioherms, commonly with a highly irregular, wavy layer draping over them (Figure 30C). At the base of the outcrop, brecciated blocks of lithified grainstone are overlain by contorted stratiform stromatolites.

One sample collected shows the decimeter-scale grainstone cobbles and the overlying stromatolites (Figure 31). The microbial mat grows directly off the cobbles as irregular stratiform layers which morph into centimeter- to decimeter-scale columns (Figure 31B). The stromatolites are composed of white, pink and red jasper, specularite, and hematite, surrounded by an ooid-peloid-rich grainstone. Columns develop from the stratiform layers as centimeter-scale convex digits that widen and show a decrease in convexity vertically.

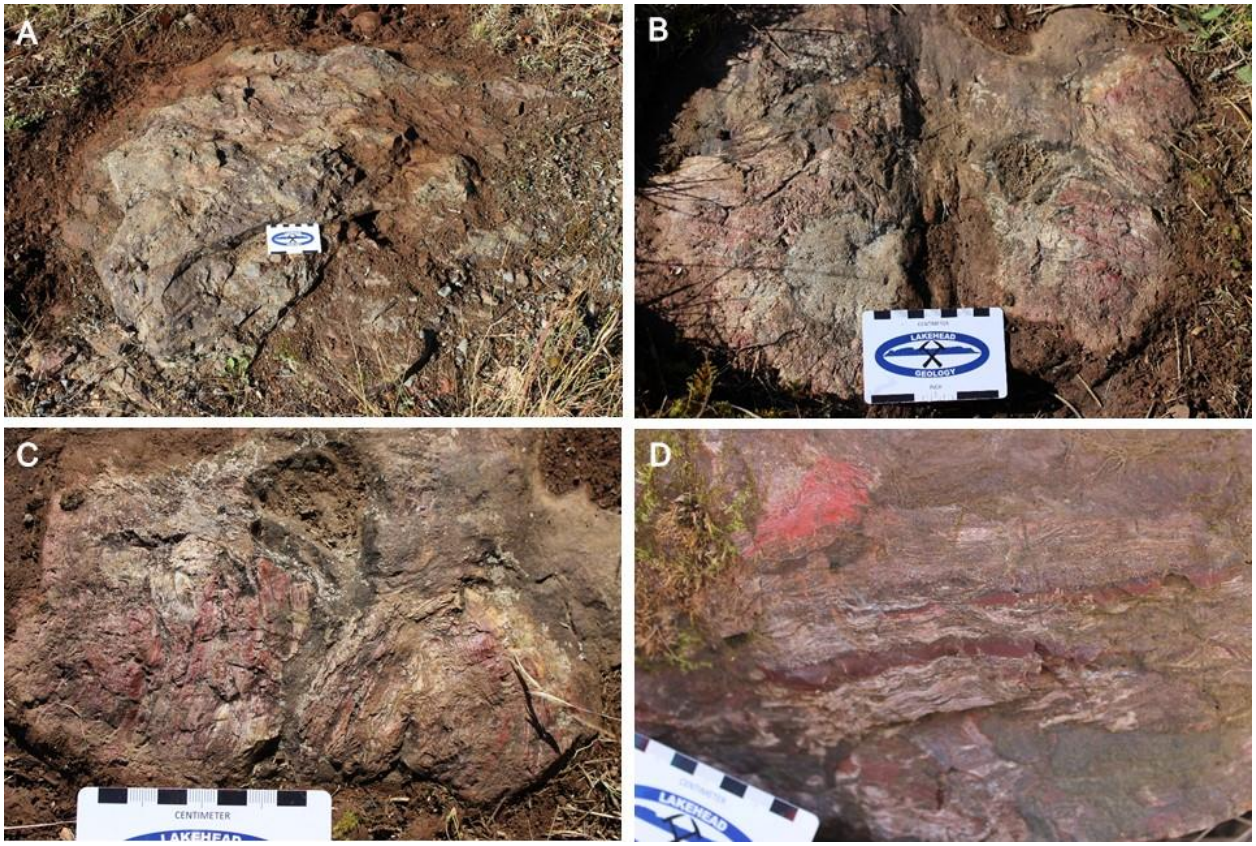

Figure 30. Outcrop photographs of the Old School Road study site. (A) Exposures of the meter-scale bioherms similar to Mink Mountain. (B-C) As the decimeter-scale domes laterally develop they merge creating the large bioherms. (D) Several boulders scattered along the road contain 10 to 20 cm thick layers of stratiform stromatolites. Within these mats are discontinuous centimeter-scale purple jasper zones.

Microscopically the Old School Road stromatolites are compositionally and morphologically similar to those at Mink Mountain. The columns are made up of alternating light and dark laminae (Figure 32A). The light laminae are composed of clean microcrystalline quartz which coarsen away from the dark laminae. The dark laminae, made up of 20 to 50 μm hematite crystals surrounded by greenalite range from 100 to 200 μm thick (Figure 32B). The boundary between the light and dark laminae is diffuse, often with hematite crystals present in the quartz. Samples taken from the stromatolites on the brecciated block have a more complex lamination structure. The clean microcrystalline quartz laminae present in the columns are generally absent.

Figure 31. Photographs of cobble sized breccia made up of lithified grainstone overlain by the Middle Stromatolitic member. (A) Side view of the decimeter-scale cobbles made up of lithified grainstone overlain by stratiform stromatolites. The microbial mat can be seen having grown in the space between the two cobbles. (B) Side view of centimeter-scale columns growing from the sides and tops of the blocks. (C) Top view highlighting the highly contorted, irregular nature of the stromatolite laminae.

Instead, jasper, and greenalite alternate with discontinuous hematite bands (Figures 32C, 26D). Patches of black carbonaceous material are present throughout the stromatolites.

The exceptional preservation and ubiquitous nature of the microfossils contained within the Old School Road stromatolites is remarkable. In every sample studied, structures with a diameter of 1 to 10 µm and lengths ranging from 20 to 100 µm are present (Figure 33A). The highest concentrations of the filaments are in the diffuse black zones between iron oxide-rich laminae (Figure 33B). These zones are often encased by microcrystalline quartz, with cryptocrystalline hematite disseminated throughout. The filaments are orientated roughly parallel

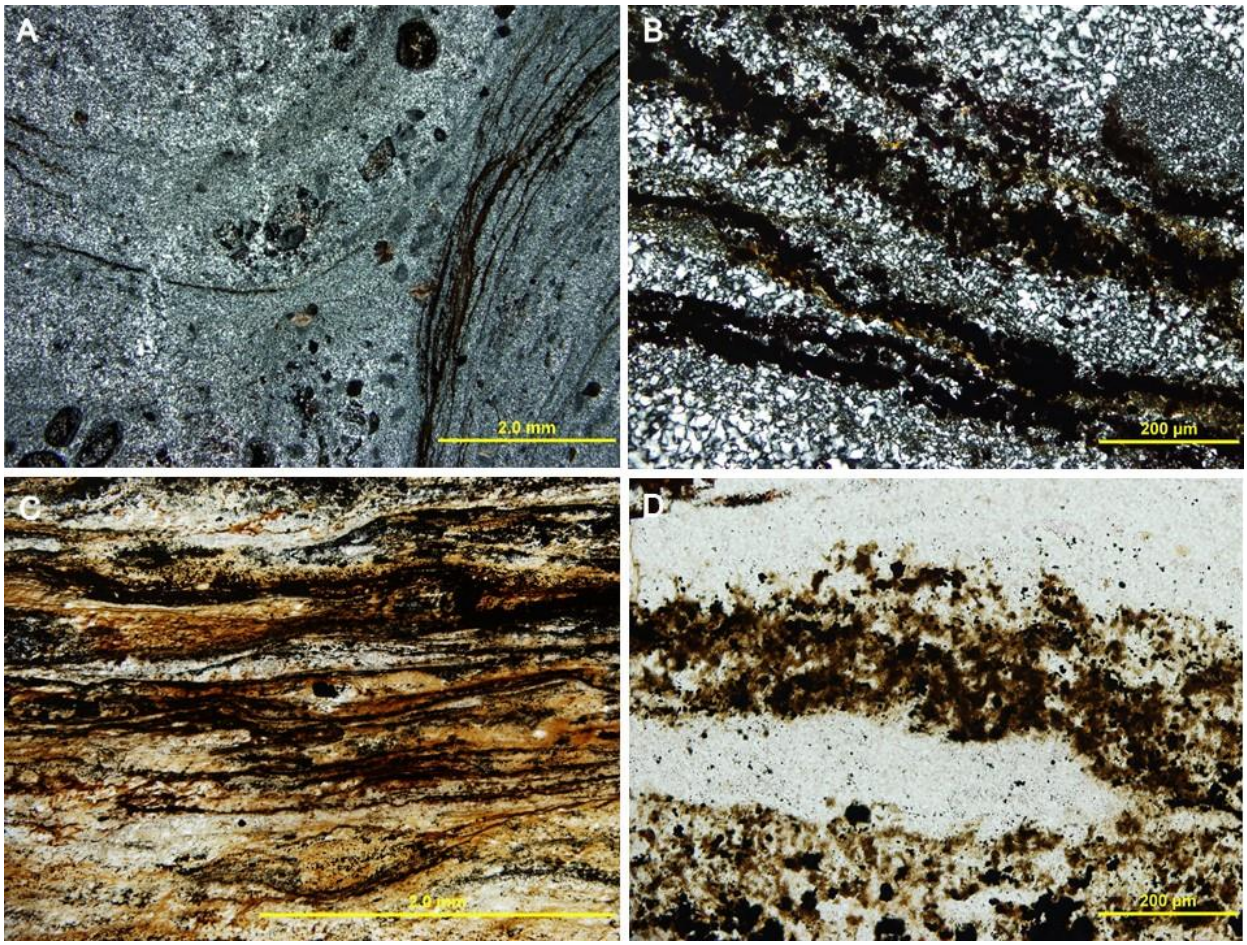

Figure 32. Composition of Old School Road stromatolite laminae. (A) Edge of columnar stromatolite showing the bridging of columns over grainstone. The opaque zones are hematite (XPL). (B) The dark laminae are made up of 20 to 50 µm hematite crystals surrounded by greenalite which alternate with the light microcrystalline quartz laminae (XPL). (C) The stratiform laminae are more complex, composed of dark hematite and greenalite laminae which grade into one another separated by thin, discontinuous layers of microcrystalline quartz (PPL). (D) 500x magnification of (c) (PPL).

to the laminae (Figure 33C). SEM analysis of the microfossil-rich zones supports the observations made with the petrographic microscope. Backscatter imaging of the microfossils shows the iron (white) is concentrated on the filaments and spheres and scarce elsewhere (Figures 33D, 33E). False-colour mapping of the fossilized microbial mat shows iron (red) is mostly concentrated along the cell wall boundaries (Figure 33F).

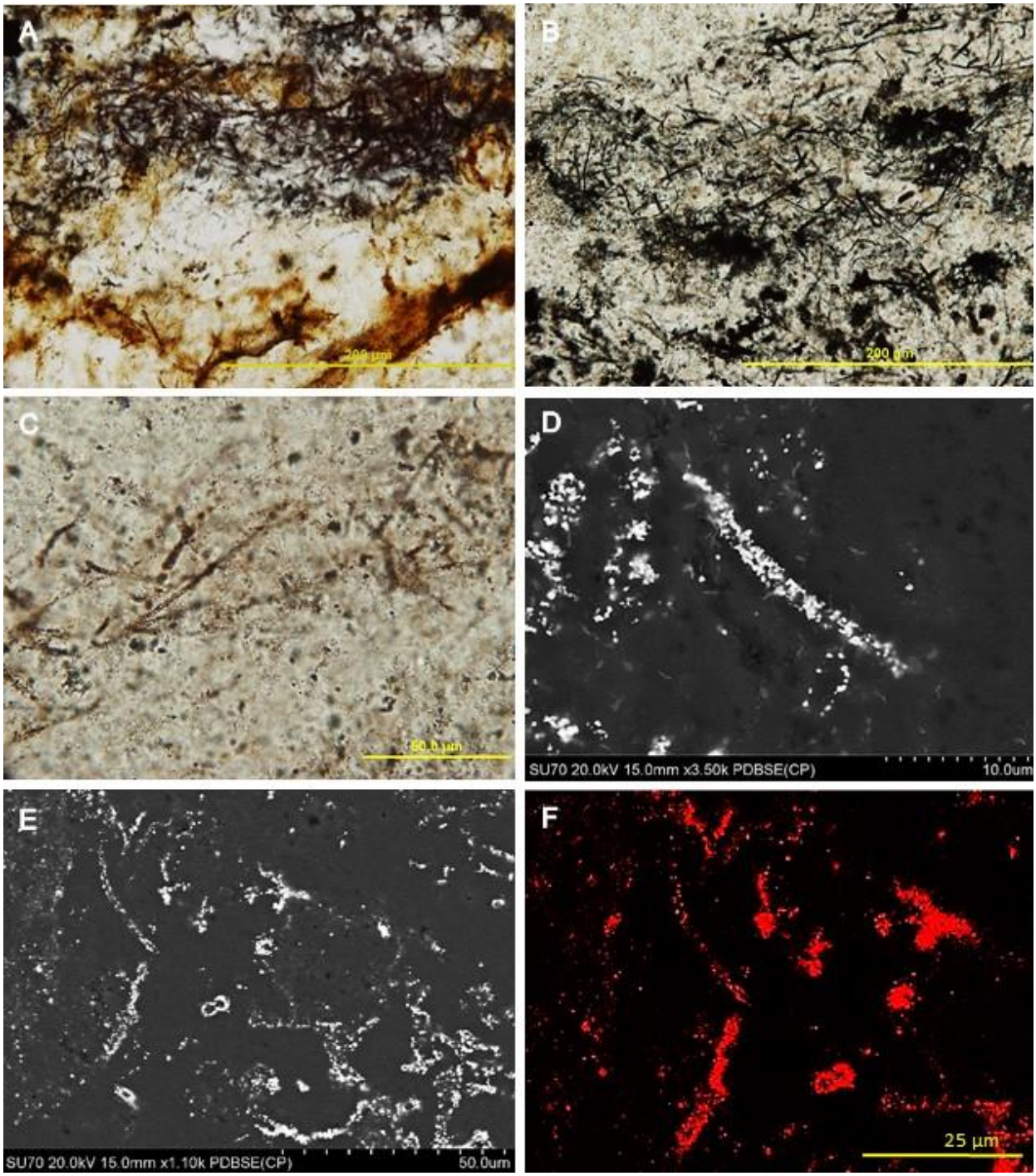

Figure 33. Filamentous iron-coated microfossils within the stromatolites. (A) Microfossils are present in 50 to 300 µm quartz layers, often surrounded by jasper (PPL). (B) The black laminae contain the highest concentration of the filaments (PPL). (C) The filaments range from 2 to 10 µm in diameter and are of variable length (up to 100 µm). Micrometer-sized crystals of iron oxide coat the structures (PPL). (D) Backscatter image of iron (white) coating a filament surrounded by silicon (black). (E) Backscatter image showing filaments and spheres coated in iron (white) and surrounded by silicon (black) (F) False colour elemental map showing the hematite (red) on the cell walls is in sharp contrast to the iron poor silicon (black) surrounding the microfossils.

2.2.3 Current River

UTM 337466E, 5370543N 16N

The Current River study site is located within the city of Thunder Bay, Ontario, along the Current River on the east side of the city. Access to the outcrop is via a 300 m walking path parallel to Lyon Blvd. The stromatolites crop out at two separate locations at this site. The first site, at the mouth of the Current River and Boulevard Lake, contains decimeter-scale domes surrounded by ferroan dolomite grainstone (Figure 34A). The black chert stromatolites are poorly preserved, showing little if any internal lamination (Figure 34B). When present the lamination is defined by the alternation of black and light grey chert laminae. A small vertical exposure shows the brecciated nature of some of the cherty stromatolites. The orange grainstone encases the pieces of the broken stromatolite which were later intruded by calcite. In Figures 34C and 34D, fragmented blocks of centimeter-scale, angular fragments of brecciated stromatolite (yellow arrow) are present within the grainstone near the decimeter-scale domes (white arrow). These pieces are visually similar to the black chert that make up the domes.

The second site is located 350 m upstream under the Arundel Street bridge. Here the stromatolites occur as meter-scale bioherms draped by black siltstone and shale (Figure 34E). Internally they are composed of carbonate, more closely resembling the clotted structure of thrombolites than the typical laminated structure characteristic of stromatolites (Figure 34F).

In thin section the stromatolites are composed of microcrystalline quartz, with cryptocrystalline inclusions of pyrite and carbonate. The preservation of the internal lamination is poor, and only faint traces of the convex laminae are present. Furthermore, extensive replacement of the quartz by carbonate is found throughout much of the stromatolitic

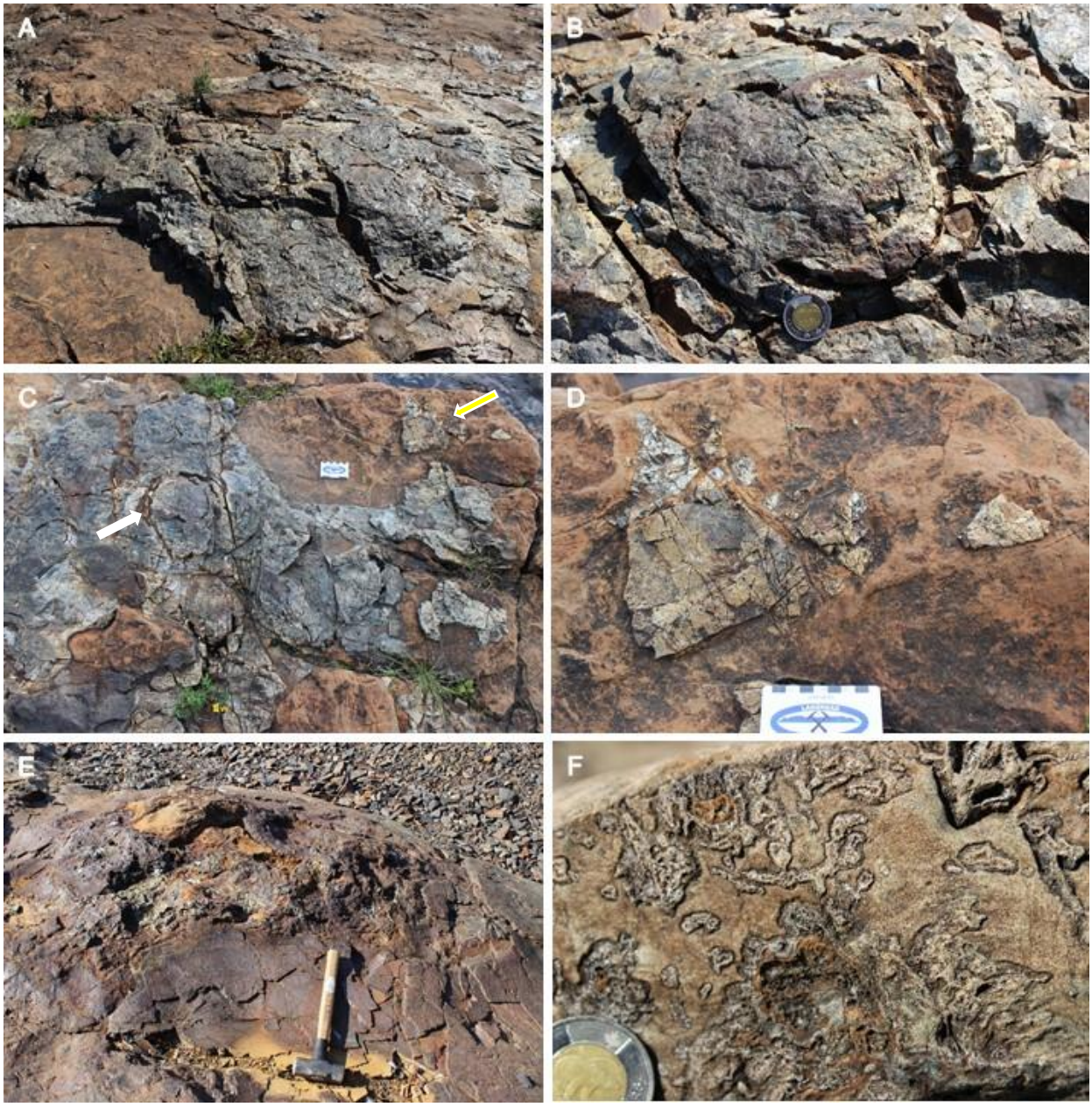

Figure 34. Outcrop photographs of the Current River study site. (A) Black chert stromatolitic domes in a ferroan dolomite grainstone. (B) Decimeter-scale, siliceous, domal stromatolite (C) Plan view of the siliceous stromatolites (white arrow) and a fragment of stromatolite in the carbonate grainstone (yellow arrow) (D) Close up of the angular chert fragments imbedded in the grainstone next to domal stromatolites in (c). (E) Meter-scale bioherms draped by a siltstone-shale layer. (F) Within the bioherms a distinct clotted texture is present.

material examined (Figure 35A). The stromatolite-grainstone contact is similar to that described previously at the Kakabeka study site. A zone of silicification extends out several millimeters

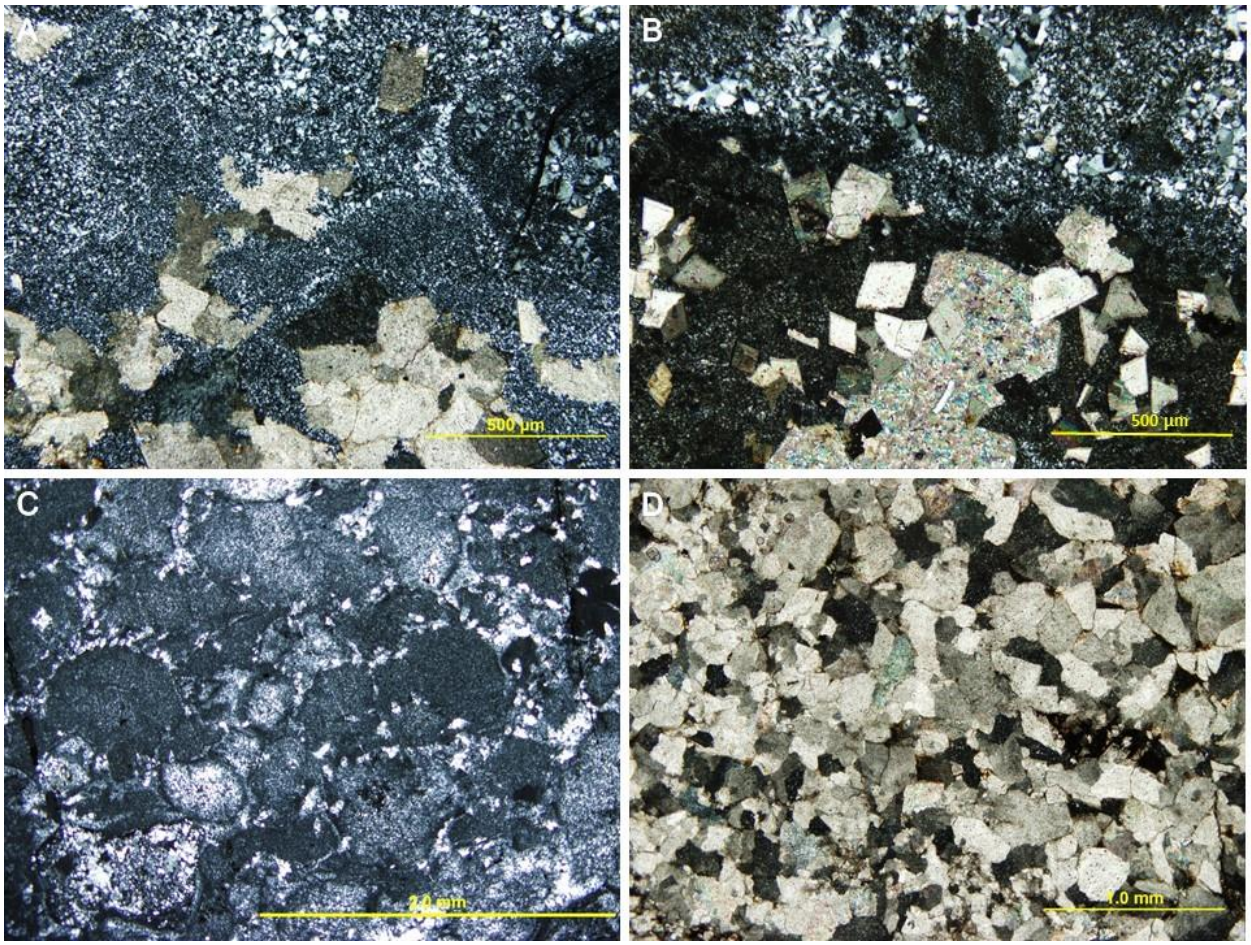

Figure 35. Petrographic photomicrographs of stromatolite and grainstone.(A) The stromatolites are composed of microcrystalline quartz with minimal preservation of the internal lamination. Carbonate rhombs can make up a large portion of the stromatolites locally. (B) Stromatolite-grainstone contact. Intense silicification of the grainstone (top of image) and development of carbonate rhombs within the stromatolite (bottom of image) highlights the complex replacement history. (C) Silicification of the carbonate grainstone extends several millimetres out from the cherty stromatolite. (D) The ferroan dolomite grainstone shows extensive neomorphism.

from the cherty stromatolite (Figure 35B) into the grainstone (Figure 35C). The silicified grainstone is composed of a peloidal, medium-grained quartz with occasional ghosted carbonate laminae. Further from the stromatolite, the grainstone is composed of ferroan dolomite with significant neomorphic spar replacement (Figure 35D).

The stromatolites and surrounding grainstone at Current River have a complex diagenetic alteration / replacement history. This includes the silicification and/or neomorphic spar

development within the carbonate grainstone as well as potential alteration of the stromatolite domes, based on the poor preservation of the internal laminae.

2.2.4 Magnetic Rock

UTM 662473E, 5329219N 15N

The Magnetic Rock study site is located roughly 75 km northwest of Grand Marais, Minnesota on the Gunflint Trail (Highway 12). This outcrop is situated within the metamorphic aureole of the Duluth Complex providing a good comparison between albite-epidote hornfels facies thermally metamorphosed iron formation and the unmetamorphosed sites previously described. The Middle Stromatolitic Member intermittently crops out for 2.5 km along the Magnetic Rock hiking trail. The main outcrop is found 500 m from the trailhead where a 2.5 m cliff allows for a detailed vertical view of the stromatolites (Figure 36A).

At the base of the cliff 40 cm of brecciated cobbles are overlain by a 50 cm zone of stromatolites. Wavy, stratiform stromatolites accrete directly on the breccia with decimeter-scale domal stromatolites growing from them (Figure 36B). Directly overlying the domes, a 30 cm zone of rip-up casts made up of chemical mudstone and fragments of stromatolite is present. Overlying this is 60 cm of medium-grained grainstone containing highly contorted layers capped off by a 3 cm thick strongly magnetic, black layer that is roughly continuous across the main outcrop. A further 60 cm of medium grainstone containing stratiform, domical, and digitate stromatolites extends to the top of the outcrop (Figures 36C, 30D).

The most noticeable difference between this outcrop and those previously described is the absence of the characteristic red jasper. Instead, shades of green and tan dominate the rocks of this site. The stromatolitic lamination is well preserved in the samples examined and consists of

Figure 36. Outcrop photographs of the Magnetic Rock study site. (A) The main site consists of a 2.5 m cliff exposing the entire Middle Stromatolitic Member. (B) Stratiform and decimeter-scale, flattened domes are present at the base of the outcrop accreting on breccia. (C) Four distinct layers of stratiform mat ~ 10 cm thick are present consisting of alternating tan and green laminae. (D) Millimeter-scale digitate stromatolites growing from stratiform mat.

light olive green to tan laminae alternating with discontinuous dark green laminae (Figure 37A). In thin section the light laminae are made up of megaquartz with abundant, randomly orientated acicular to bladed crystals many of which are <3 μm in diameter (Figure 37B). SEM point analysis of the crystals suggest a composition similar to actinolite or ferro-actinolite, however the lack of Ca in some would indicate grunerite is also present.

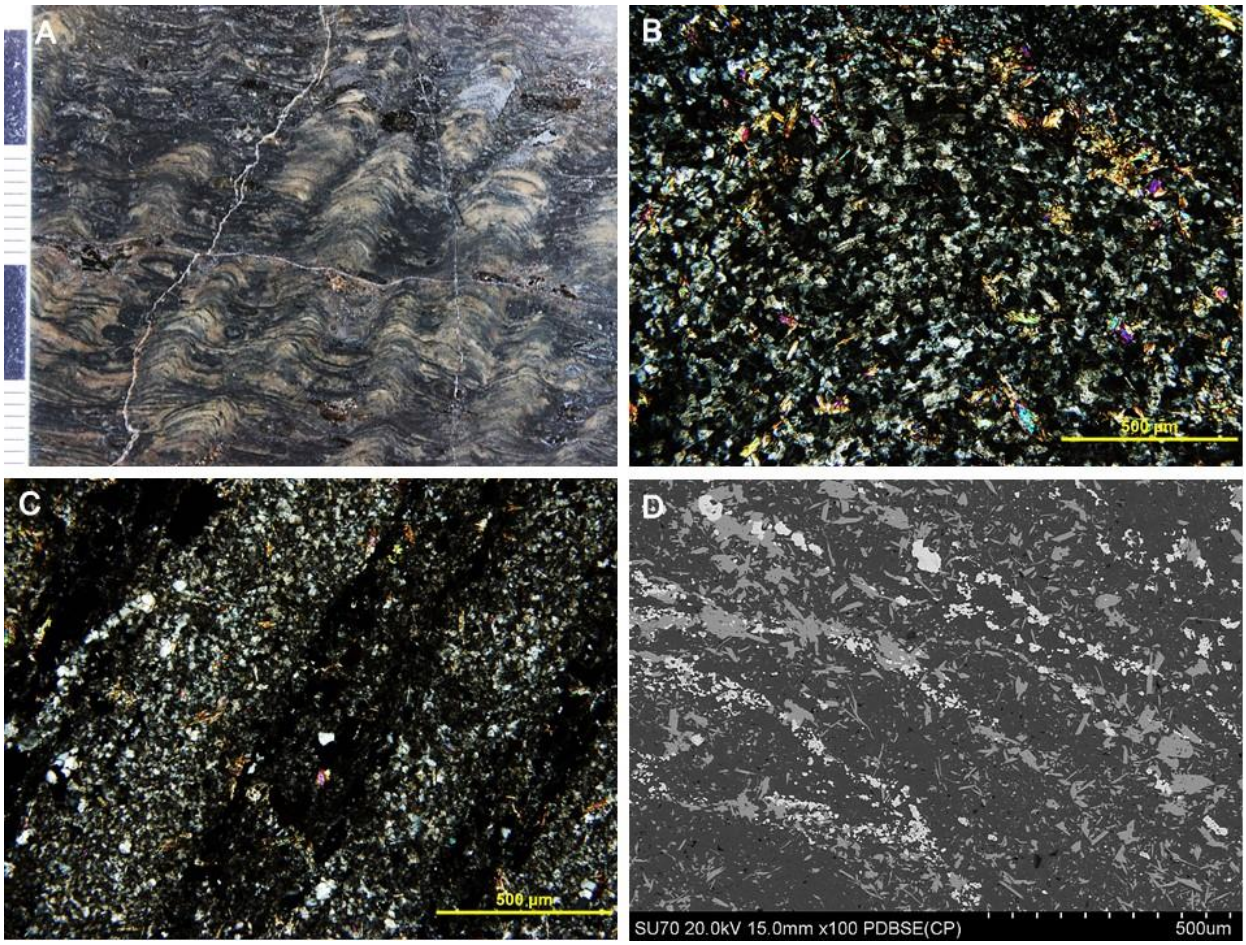

Figure 37. Stromatolitic lamination. (A) Photograph of digitate stromatolites with alternating green and tan laminae. (B) Randomly orientated, fibrous actinolite, acicular grunerite and megaquartz crystals make up the light laminae (XPL). (C) The well preserved dark laminae are mostly euhedral magnetite crystals with subordinate actinolite (XPL). (D) Backscatter imaging of magnetite laminae (white) alternating with quartz (dark grey) with amphiboles (light grey) orientated randomly throughout the sample.

The dark laminae are discontinuous, and consist of euhedral magnetite with abundant amphiboles disseminated throughout (Figure 37C). A backscatter image taken of a stromatolitic column gives emphasis to the lamination versus the randomly orientated amphiboles (Figure 37D). The iron-rich laminae (white) alternate with the thicker quartz layers (dark grey) in the typical convex-up stromatolitic form. The acicular to bladed crystals (medium grey) overprint the iron and quartz laminae.

2.2.5 Drill Core

Three drill cores, P-1, P-2 and DH-containing the Middle Stromatolitic Member were examined. All three were drilled between Whitefish Lake, Ontario and the Minnesota border. Due to the extremely poor preservation of the stromatolites in P-2, only P-1 and DH-3 were examined in detail.

2.2.5.1 P-1

The stromatolitic zone in P-1 is ~50 cm thick, which overlays 150 cm of jasperlitic, medium-grained peloid dominated grainstone. A 5 mm wide carbonate vein extends through the entire length of the stromatolitic layer (Figure 38A). Although difficult to differentiate between stratiform and domal stromatolites in drill core, the stromatolites at the base appear flat, with increasing convex curvature up column.

At the base of the stromatolitic section, zones containing trapped granules within the jasperlitic mat alternate with clear to smoky discontinuous quartz laminae (Figure 38B). Internally the millimeter-scale granules are composed of specularite or carbon-rich, fine-grained material. A thin, continuous outer coating of jasper is present on most of the grains. Interspersed with the peloid-rich laminae are zones containing abundant mud rip-up grains made up of black, carbon-rich subrounded grains (Figure 38C). At 35 cm the stromatolites transition from a stratiform mat to digitate forms (Figure 38D). The development of a digitate stromatolite is imaged in in Figure 38E. The stromatolite developed on an intraformational clast (white arrow) containing abundant cemented granules similar to those described earlier. The intraformational clast is resting on a non-jasper coated specularite-rich peloid beside a well-rounded, jasper-rimmed peloid. Subrounded rip-up clasts are commonly embedded into the stromatolitic laminae

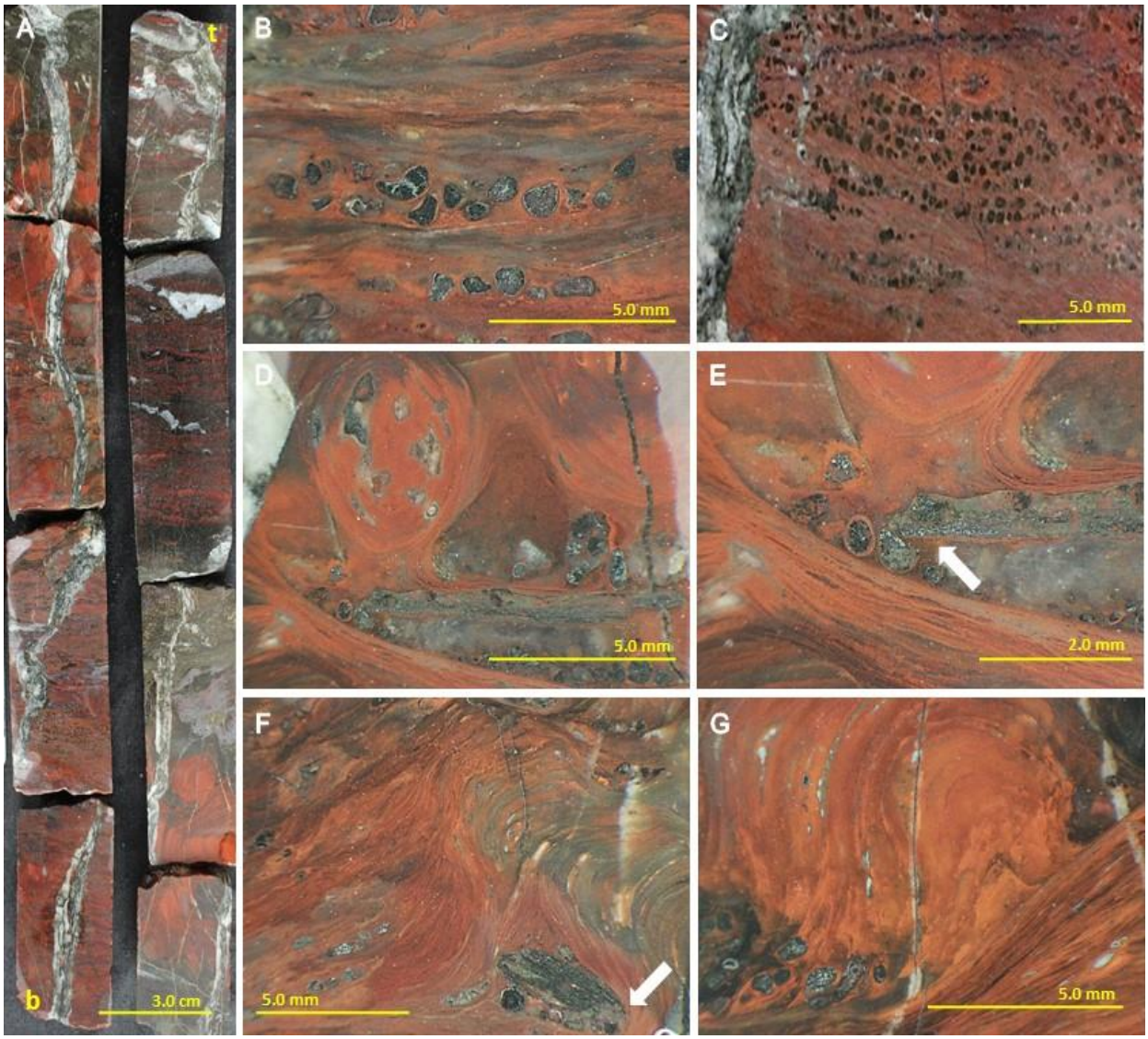

Figure 38. Photographs of drill core P-1. (A) Photograph of the 50 cm stromatolitic section (b-bottom, t- top of core). (B) Jasper-rich zones containing abundant granules alternate with clear to cloudy quartz laminae. The granules contain fine-grained specularite and greenalite internally, with a jasperlitic rim coating the grains. (C) Subrounded rip-up clasts, >1 mm in diameter are abundant throughout the sample. (D) 30 cm from the base, the stratiform stromatolites are replaced by microdigitate forms. (E) The microdigitate stromatolite developed on an intraformational clast (white arrow). The clast rests upon a specularite-rich peloid, next to a jasper coated peloid. (F) Millimeter scale mud-chip rip-up clasts (white arrow) are often embedded between stromatolitic laminae. (G) The laminae which make up the microdigitate stromatolites is more diffuse and lighter than that of developed columnar stromatolites (bottom right).

(white arrow) along with trace granules (Figure 38F). The development of microdigitate stromatolites from larger columnar forms highlights a distinct change in laminae. In Figure 38G the laminae within the column (bottom right) show a distinct alternation between red and black,

however, the jasper within the microdigitate stromatolite developing from it has a cloudy appearance and no black laminae.

The lamination within the stromatolites is well preserved in the form of alternating light silica-rich and dark-silica-poor laminae. The silica-rich laminae contain microcrystalline quartz with finely disseminated cryptocrystalline hematite. These laminae average 75 to 100 μm thick, and show good lateral continuity throughout the samples observed. The dark silica-poor laminae can be divided into three different types based on their composition (Figure 39A). The first, made up of euhedral hematite crystals, form laminae which are continuous over several millimeters, with sharp outer boundaries (bottom left of Figure 39A). They often exceed 100 μm in thickness and in thin section appear opaque. The second contain dense concentrations of cryptocrystalline hematite inclusions in microquartz. These laminae show poor lateral continuity and have highly diffuse boundaries and appear deep-red to purple in thin section (Figure 39B). Finally, highly diffuse black layers which grade into the silica-rich laminae contain abundant microfossils.

The bridging of columns across the interspace occurs as the stromatolitic laminae coalesce into compound laminae at the stromatolite wall, and drapes over individual grains (Figure 39C). There is a marked difference in crystal size between the stromatolitic laminae and that of the intergranular cement. Elongate granules are the most common grains, with ooids and intraformational clasts secondary. The granules are composed of iron silicates (greenalite with minor minnesotaite and possibly stilpnomelane) containing hematite and range up to 3 mm in diameter.

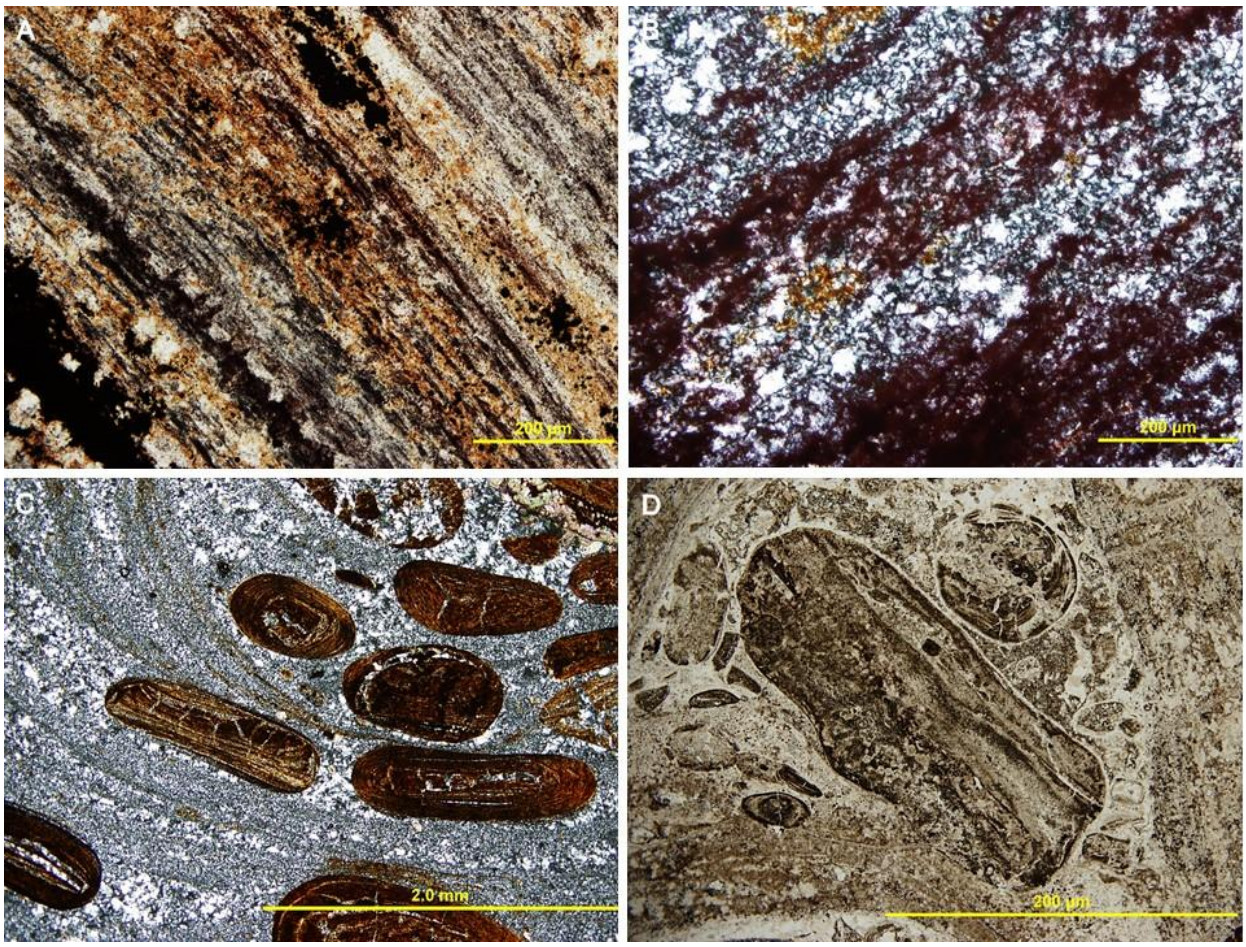

Figure 39. Photomicrographs of stromatolitic laminae and grainstone. (A) The laminae in the finely laminated stromatolites are composed of microcrystalline quartz containing abundant inclusions of cryptocrystalline hematite and carbon (PPL). (B) Laminae containing cryptocrystalline hematite in microquartz with diffuse laminae boundaries dominate the "poorly laminated" zones within the microdigitate stromatolites (XPL). (C) The stromatolitic laminae drape across the granules within the interspace, bridging adjacent columns. Note the finer grainsize of the stromatolite laminae in contrast to the coarser intergranular blocky quartz cement (XPL). (D) Intraformational rip-up clasts with a 10 to 15 µm clear quartz cement surrounding the grain (PPL).

Dehydration cracks are present in most of the grains examined (Figure 39C). Rip-up clasts containing zones of laminae and individual grains cemented together are a common constituent of the grainstone (Figure 39D). A 10 to 15 µm rim of clear quartz cement, with elongate crystals developing perpendicular to the grain surface occurs on many of the rip-ups.

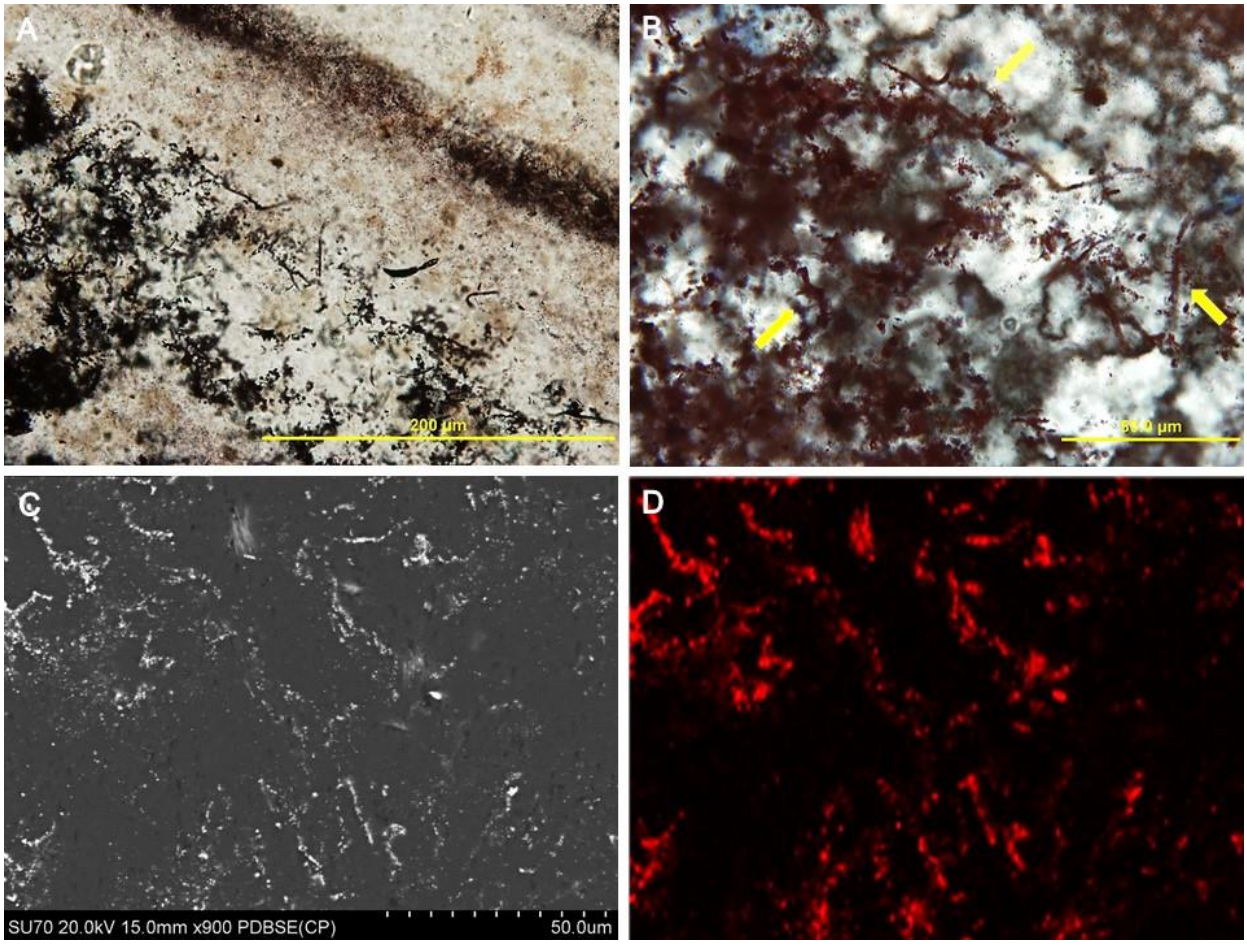

Figure 40. Iron-coated microfossils. (A) The filaments and spheres occur in diffuse, organic-rich black zones surrounded by quartz (PPL). (B) The concentration of cryptocrystalline hematite increases substantially near the filaments, especially on the walls of the 2 to 5 µm diameter filaments (yellow arrows) (XPL). (C) Backscatter image showing the increased concentration of iron (white) within the microbial mat, which is surrounded by quartz (dark grey). (D) False colour mapping shows the increase in iron on the filaments.

As noted previously, highly diffuse, carbon-rich laminae within the stromatolites contain abundant microfossils. These laminae contain cryptocrystalline hematite-coated filaments orientated roughly parallel to the bedding direction (Figure 40A). They are morphologically similar to those described previously at Mink Mountain, Old School Road, and Schreiber Channel, and most probably belong to the genus *Gunflintia* sp.. The microfossil-rich laminae are diffuse black zones overlying the jasperlitic laminae, and often grade into the light microquartz laminae. In cross-polarized light the fossils are deep red-purple due to the

cryptocrystalline hematite coating their outer surfaces (Figure 40B). Electron microprobe analysis corroborates the observations previously discussed of iron being preferentially deposited on or adjacent to the filaments. Figure 40C shows a backscatter image of the filaments (white) surrounded by quartz (dark grey). False colour mapping of the area reveals the iron (red) concentrating on and around the filaments surrounded by silica (black) (Figure 40D).

2.2.5.2 DH-3

The stromatolitic zone in DH-3 is ~45 cm thick, and overlays a medium-grained grainstone. The core is crosscut by multiple quartz and calcite filled fractures. At the base of the stromatolitic zone a 10 cm bulbous columnar stromatolite overlays a medium-grained grainstone. It consists of millimetre-scale, wavy laminae which range from white to pink, to red and green in colour (Figure 41A).

The lamination within the stromatolite is comparable to those previously described both in core and outcrop. Light iron-poor laminae alternate with thinner iron-oxide-rich laminae comparable to P-1 (Figure 41A). As was previously described three types of dark laminae are present: those containing euhedral hematite crystals, laminae made up of cryptocrystalline hematite inclusions in microquartz and diffuse laminae rich in black carbon-rich material (Figure 41C). The diffuse black laminae contain filamentous microfossils 2 to 5 μm in diameter with lengths exceeding 100 μm (Figure 41D). They are coated in iron oxides. The microfossil laminae overlay thick (~100 μm) jasperlitic laminae, and often grade into light laminae composed of microquartz.

The grainstone is composed of granules and ooids similar to those described in the P-1 core. However, ooids are present in greater amounts. The grains are composed of iron silicates

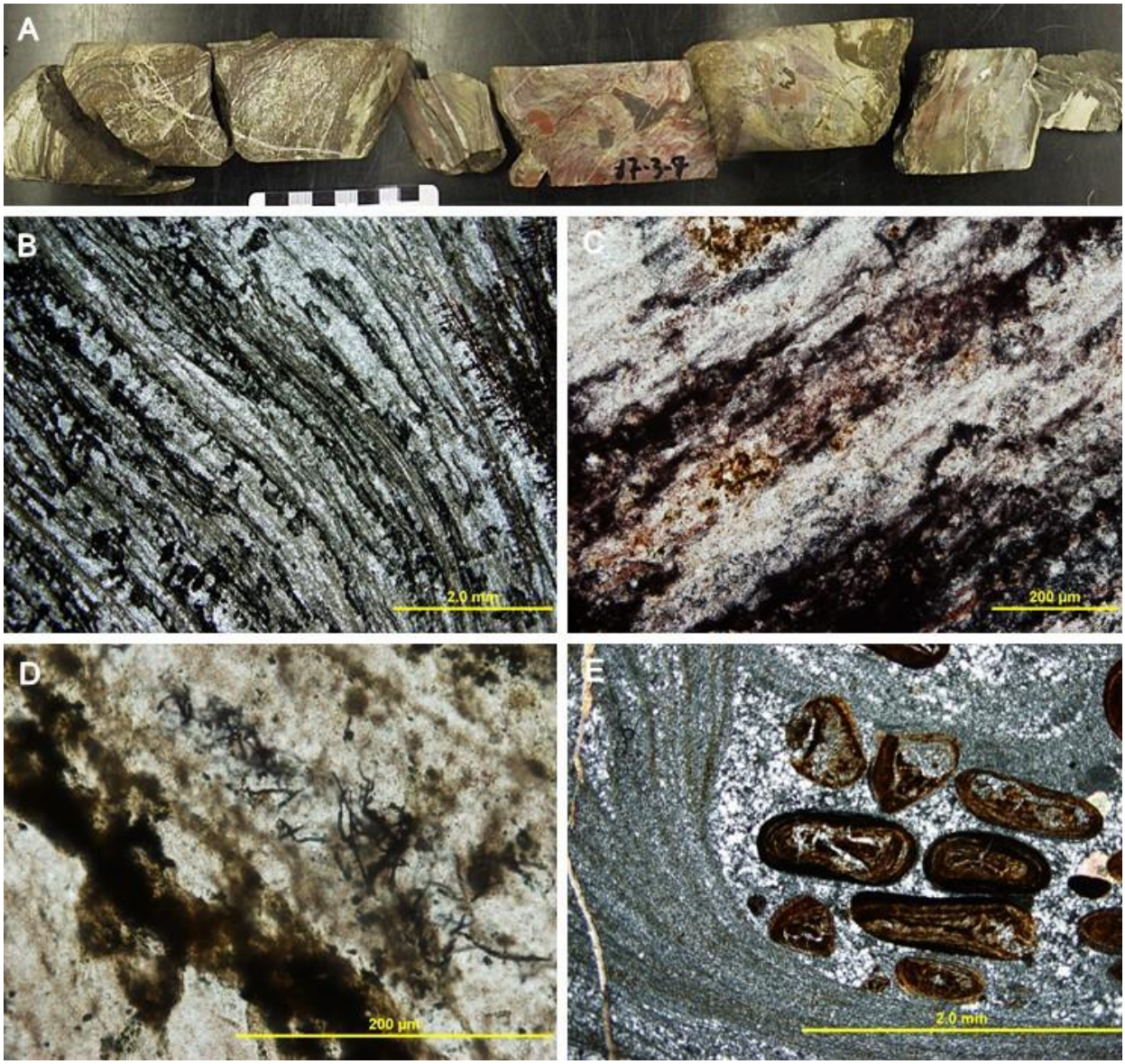

Figure 41. DH-3 photomicrographs. (A) Photograph of the 45 cm stromatolitic zone. The stromatolites are composed of wavy jasper, and chert laminae. (B) The laminae are composed of light iron-poor microquartz which alternate with iron-rich laminae (XPL). (C) Diffuse boundaries of some laminae contain cryptocrystalline hematite and high concentrations of carbon (PPL). (D) The carbon-rich laminae often contain filamentous microfossils, 2 to 5 µm in diameter and up to 100 µm long coated in iron oxides. (E) The grainstone is made up of ooids and granules composed of iron silicates and hematite. They are overlain by thin microbial mats bridging adjacent columns. Note the size difference between the stromatolite and the intergranular cement (XPL).

(greenalite, stilpnomelane, and minnesotaite) and when present, with internal laminae rich in euhedral hematite crystals. Bridging between stromatolite columns occurs as ~500 µm thick drapes of microcrystalline quartz with thin (>100 µm) layers of iron oxides.

The ICP-MS measured REE contents for samples collected from the DH-3 core were normalized to PAAS values and plotted (Figure 42). The samples selected for analysis include one sample form the grainstone directly below the stromatolites (DH-03-01), one sample from stromatolite (DH-3-02) and three samples of the overlying grainstone (DH-03-03, DH-03-04, DH-03-05). The plot shows a consistent pattern among five samples showing a slight depletion in LREE compared to the HREE, a slight positive to nil Ce anomaly and a distinct positive Eu anomaly.

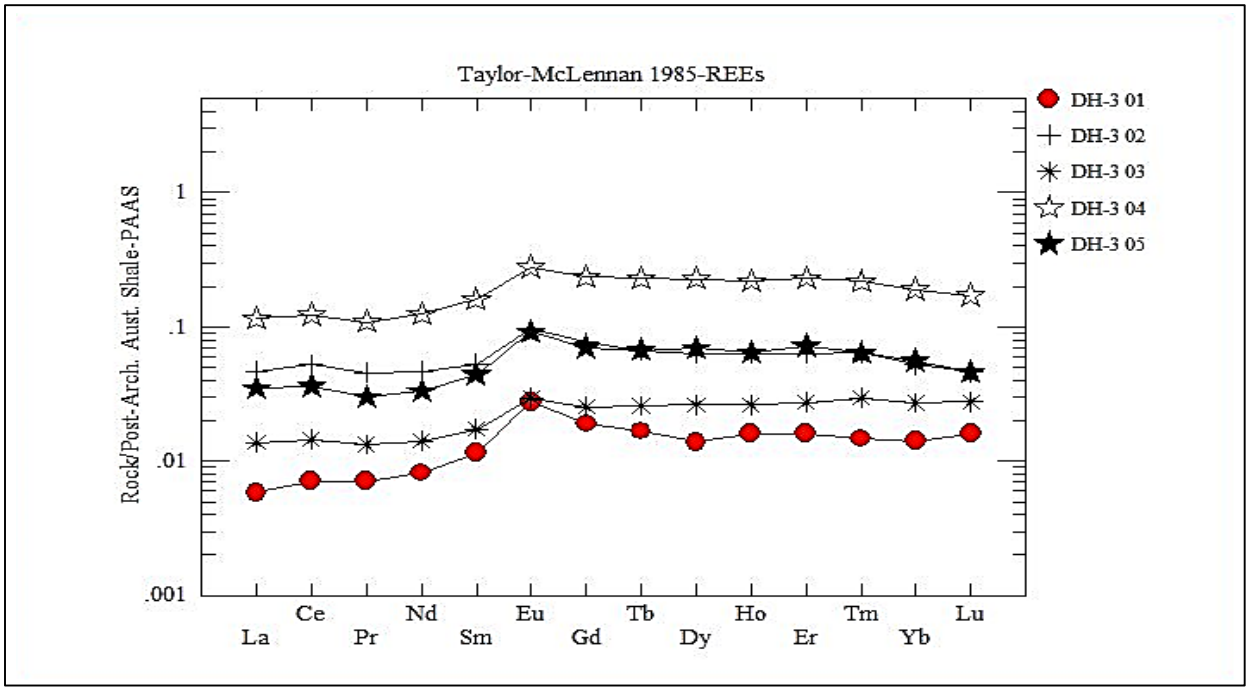

Figure 42. The PAAS normalized REE diagram for DH-3 drill core showing slightly positive Ce and distinctly positive Eu anomalies and a minor depletion in LREE in relation to the HREE.

2.3 Upper Stromatolitic Member

2.3.1 Mary Ellen Mine

UTM 578504E, 5279565N, 16N

This site is located on the western edge of Biwabik, Minnesota off Highway 135. It provides an excellent opportunity to observe the domal and columnar stromatolites in situ, through horizontal and vertical sections. Near the entrance to the pit the stromatolites crop out for several meters, allowing for a horizontal view of the top of the digitate stromatolites. Preferential weathering of the interspace material caused the siliceous stromatolite columns to have a higher relief in relation to the interspace.

Within the southeast corner of the pit, directly below the horizontal outcrop, a vertical exposure is visible 1 to 7 m in height varying with the size of the rubble pile abutting the wall. A zone of alteration is present, extending up from the base of the outcrop approximately 100 cm. In this zone, the stromatolite forms are rarely preserved, and if present, are highly altered by iron hydroxides. Above this zone, stratiform, domal, and columnar stromatolites are present and preserved in great detail (Figures 43A-C). The domal stromatolites have diameters ranging from 4 cm to over 15 cm and heights of up to 30 cm. The domes are closely spaced, often with less than 10 cm of interspace between them and are laterally linked by stratiform lamination (Figure 43A). The colour of the cherty stromatolites ranges from reds and purples to black.

At the base of the outcrop, several boulders containing oblong to polygonal domal stromatolites are present (Figure 44). The way in which the boulders broke provides a lateral

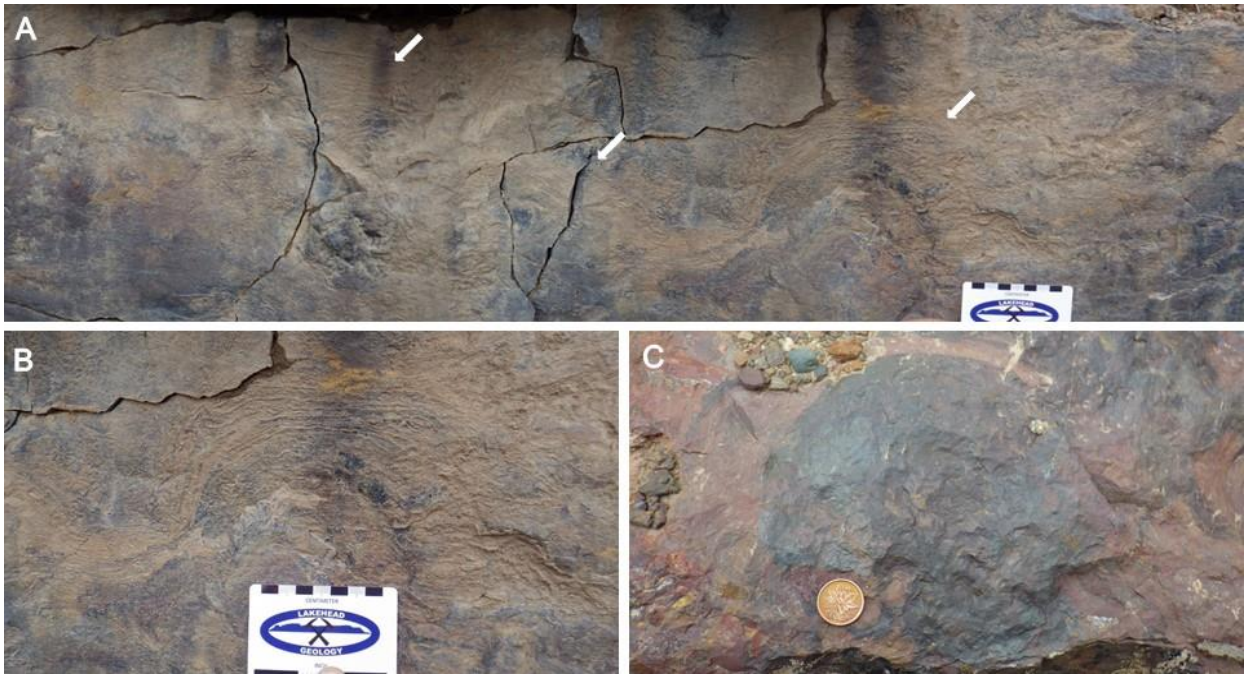

Figure 43. Photos of vertical exposure with siliceous domal stromatolites. (A) Panoramic view of three domal stromatolites (white arrows). (B) Close up of 10 cm dome from (A). (C) Lateral view of siliceous domal stromatolite at top of outcrop.

view of the internal structure of the stromatolites. The central nucleus is composed of white silica-rich grainstone or massive silica and rarely exceeds a diameter of 4 cm (Figure 44B). Concentric laminations growing out from the nucleus consist of dark red to purple jasper (Figure 37C). The jasperlitic layers are interrupted and cross cut by thin (1 to 2 mm), discontinuous and diffuse white quartz zones (Figure 44D). Similar to the columns described above, the domal stromatolites are closely spaced, often with less than 2 cm of interspace between them.

Columnar forms were difficult to study in situ, however 24 large stromatolitic rock samples were taken from the site for further study in the lab. The columnar stromatolites show a relatively consistent diameter throughout the columns, with a range from 0.5 to 1.5 cm with the majority of samples collected having a diameter of 0.75 cm (Figure 45A). In columns where the diameter increases upwards, the development of branching is common and takes the form of

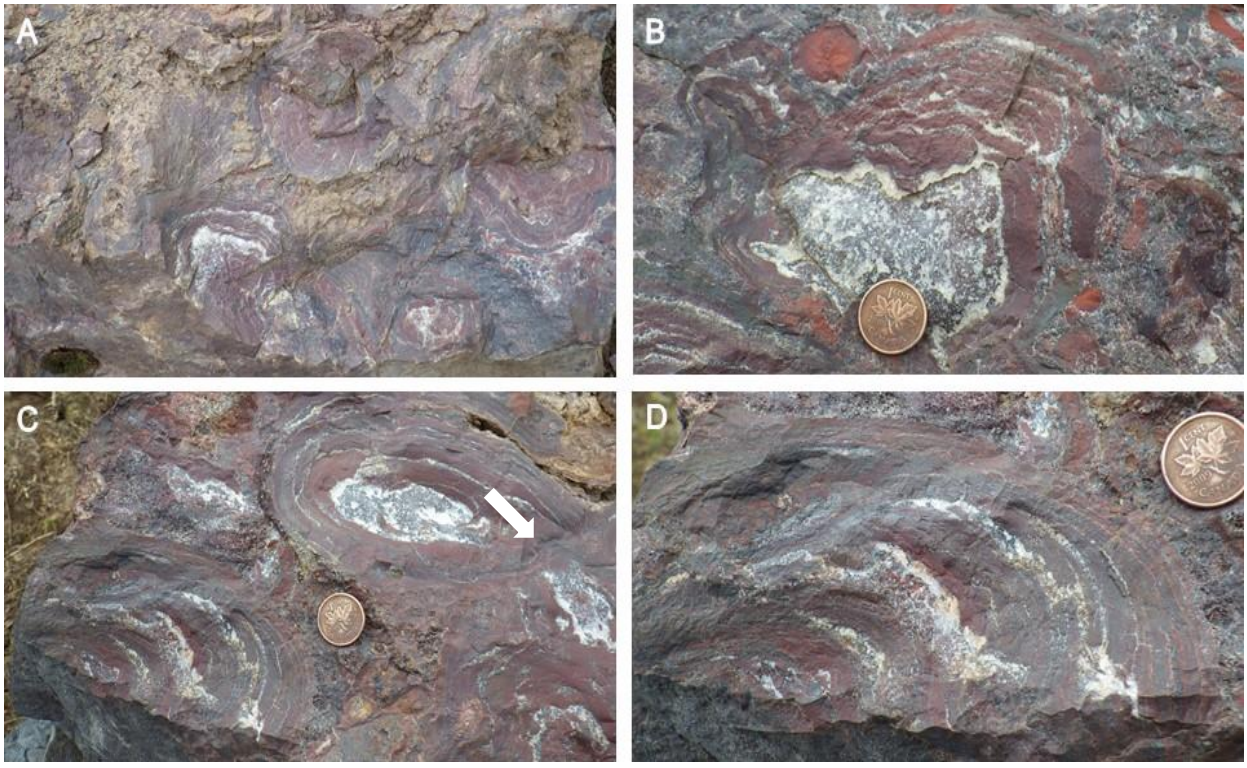

Figure 44. Lateral view of boulders containing cherty domal stromatolites. (A) The well-developed domal stromatolites are composed of deep-red to purple chert. (B) White quartz at the centre of the dome. (C) The domes are closely packed, often growing together (white arrow) (D) The jasperlitic layers are interrupted and cross cut by 1 to 2 mm discontinuous and diffuse white quartz zones.

either divergent or more rarely parallel branching. The bifurcation often starts as a winding of a single column, and due to the accumulation of several ooids in an area, creates an area of higher relief, resulting in the creation of a new column. In some cases it was noted that these columns would again bifurcate creating a dendritic or digitate pattern.

A lateral cut through a slab containing several digitate stromatolites illustrates the cylindrical growth pattern common in the Mary Ellen stromatolites (Figure 45B). Within this sample the microbial mat can be seen in the interspace as abundant jasper wisps, joining several of the columns which are encased in the magnetite-rich grainstone. In some columns, laminae composed of specularite alternate with jasper in the central portions of the stromatolite (Figure 45C). These bands are highly continuous, forming closed laminations within the column.

Figure 45. Photographs of typical digitate Mary Ellen stromatolites. (A) The brilliant red digitate stromatolites are composed of hematite-rich quartz (jasper) surrounded by a magnetite grainstone. Divergent and parallel branching of the columns is common. (B) Lateral cut through digitate stromatolites showing the cylindrical nature of the columns. The microbial mat, rich in jasper can be seen joining several columns and trapping the magnetite grainstone. (C) Internal laminations of alternating jasper and specularite are common within the columns (white arrow).

Some, such as the one on the right in Figure 45C (white arrow) are near the central portion of the column, whereas some columns near the top left of the image have specularite layers closer to the outer edges of the column. The magnetite layers closer to the edges are more diffuse and less continuous than those in the inner portions of the column. Within the interspace, a distinct zonation between jasper-rich and magnetite-rich cement is present. The central portion of the sample has a notably greater amount of jasper than the areas at the top left and bottom right, which are dominantly magnetite. The binding of the magnetite grainstone by the jasper-rich microbial mat is a prominent feature of the interspace. At the base of several columns the trapping of the grainstone and subsequent growth of the microbial mat is prominent (Figure 46A). The thin film of microbial mat grows out of the grainstone as wisps of dark red to light orange jasper, forming the base of the columns (Figure 46B). Subsequent growth of the biofilm in alternating dark and light laminae form a convex-up column (Figure 46C).

The laminae that make up the columns can be divided into two groups: light laminae, rich in silica and dark laminae, rich in iron oxides and jasper. The silica laminae are composed of micro- to cryptocrystalline quartz and are generally thicker than the iron oxide-rich lamina and many other places. The quartz laminae show a greater continuity within the stromatolites in relation to the iron oxide-rich bands which are often discontinuous with irregular boundaries. The iron oxides which make up the jasperlitic laminae (hematite and/or magnetite) generally occur as finely disseminated, cryptocrystalline inclusions in microcrystalline quartz. Less commonly, the dark laminae are made up of euhedral magnetite crystals. The images in Figure 47 demonstrate the various lamination styles found within the Mary Ellen stromatolites. In thin section the contact between the jasperlitic and quartz laminae range from sharp to gradational. The jasper often concentrates at the column walls and at the apex of the convexity.

Figure 46. Photographs highlighting the development of a digitate stromatolite. (A) Development of a columnar stromatolite from an iron-rich microbial mat. The stromatolite begins as an irregular accumulation of jasper-rich microbial mat (white arrow). (B-C) Thin jasper laminae (white arrow) growing out from the grainstone forming the basal portion of digitate stromatolites. Note scale in millimeters.

Elemental mapping through a segment of a digitate stromatolite revealed distinct iron, manganese and silica-rich zones (Figure 48). The silica is present throughout the column, representing the "background" or baseline precipitate within the column (Figure 48B). The zones with lower concentrations of silica have elevated iron, phosphorus and calcium (Figures 48C, 48E, 48F). Several laminae with elevated manganese are also present (Figure 48D). Interestingly, of the four distinct manganese-rich laminae, two are present without iron, and the remaining two show elevated Mn concentrations near the tops of iron-rich laminae (Figure 48C). Point analysis of the manganese bands provide MnO values up to 4.9%.

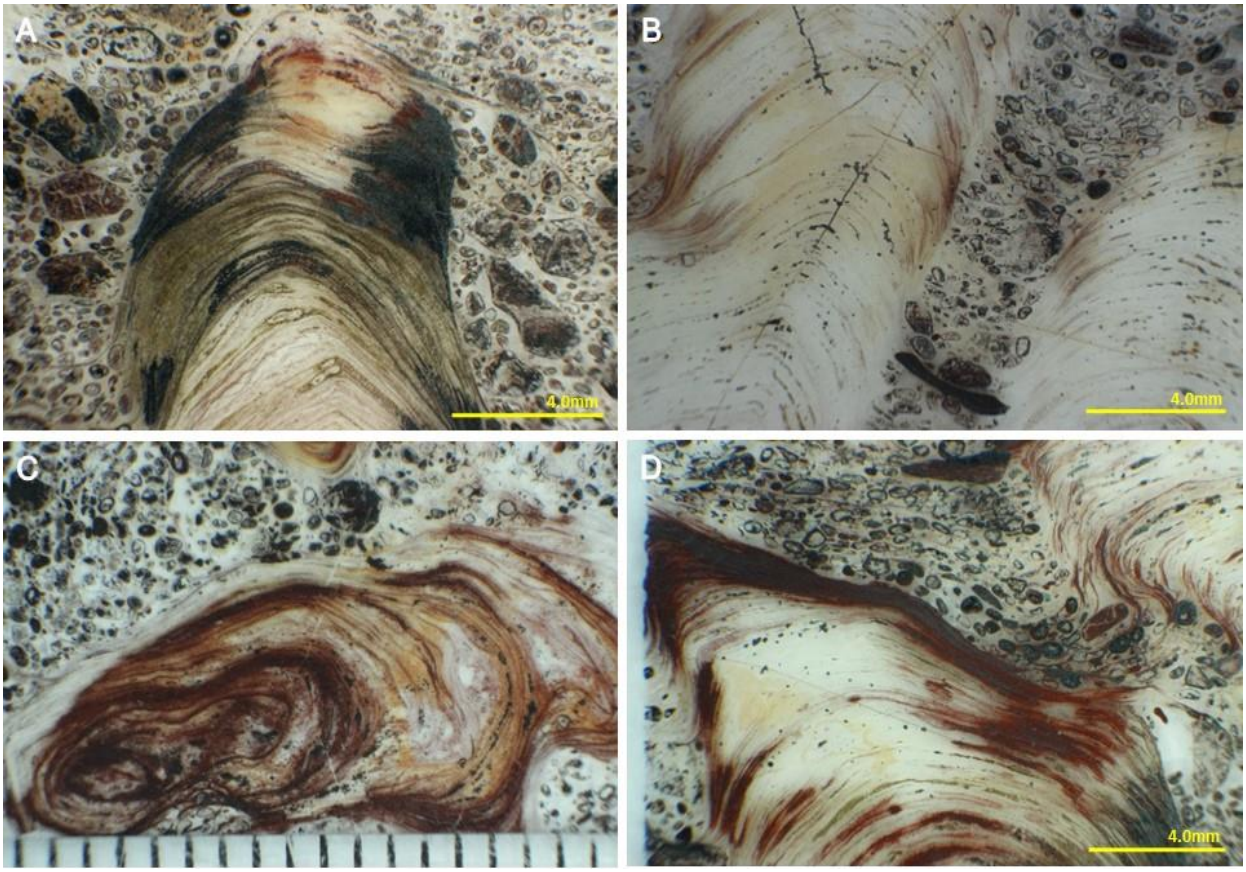

Figure 47. Photomicrographs illustrating typical lamination within the digitate columns from Mary Ellen Mine. (A, B, D) Vertical sections through columns. The layering is visible do to an alternation between light microquartz laminae and dark jasperlitic laminae. (C) Lateral cut through digitate stromatolite. Note scale in millimeters.

Micro-unconformities within the columns are common in the form of truncation of the stromatolite columns (Figure 49). Photomicrographs taken of the truncations show the millimeter-scale digitate stromatolites with the top of the stromatolite erosivly scoured off and the subsequent overgrowth of younger biofilm over the truncation (Figures 49A-F). The contact between the column and the new overlying microbial mat is sharp.

There is a notable difference in the size of crystals within the stromatolite laminae and that of the intergranular space. The quartz and jasper crystals within the stromatolitic laminae range from 5 to 25 μm. This is in contrast to the much larger blocky quartz crystals within the

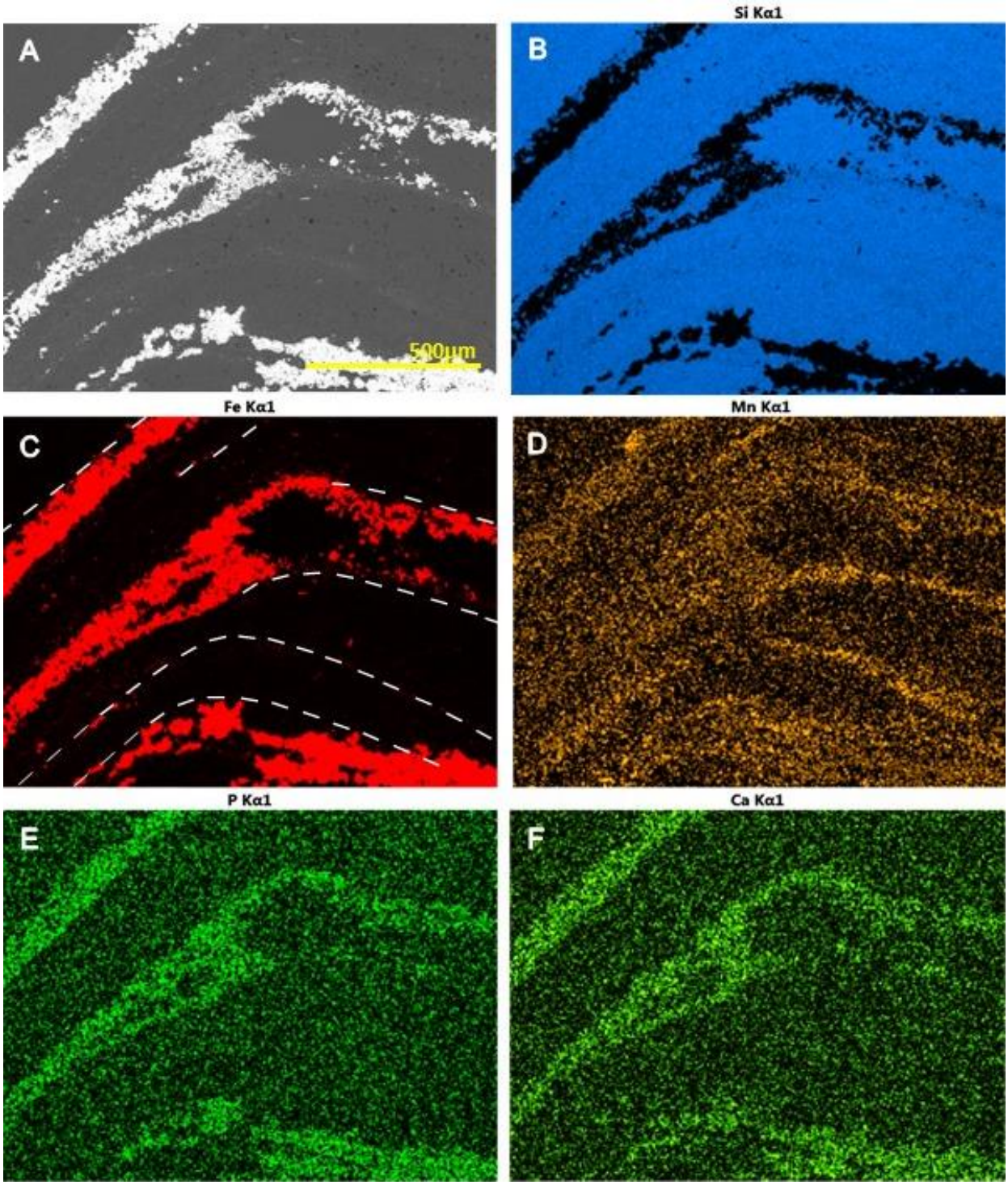

Figure 48. False colour BSE/elemental maps of stromatolite laminae. (A) Backscatter electron image, (B) Silica, (C) Iron, (D) Manganese, (E) Phosphorus, (F) Calcium. The dashed lines in (C) show the location of the manganese layers in relation to the iron.

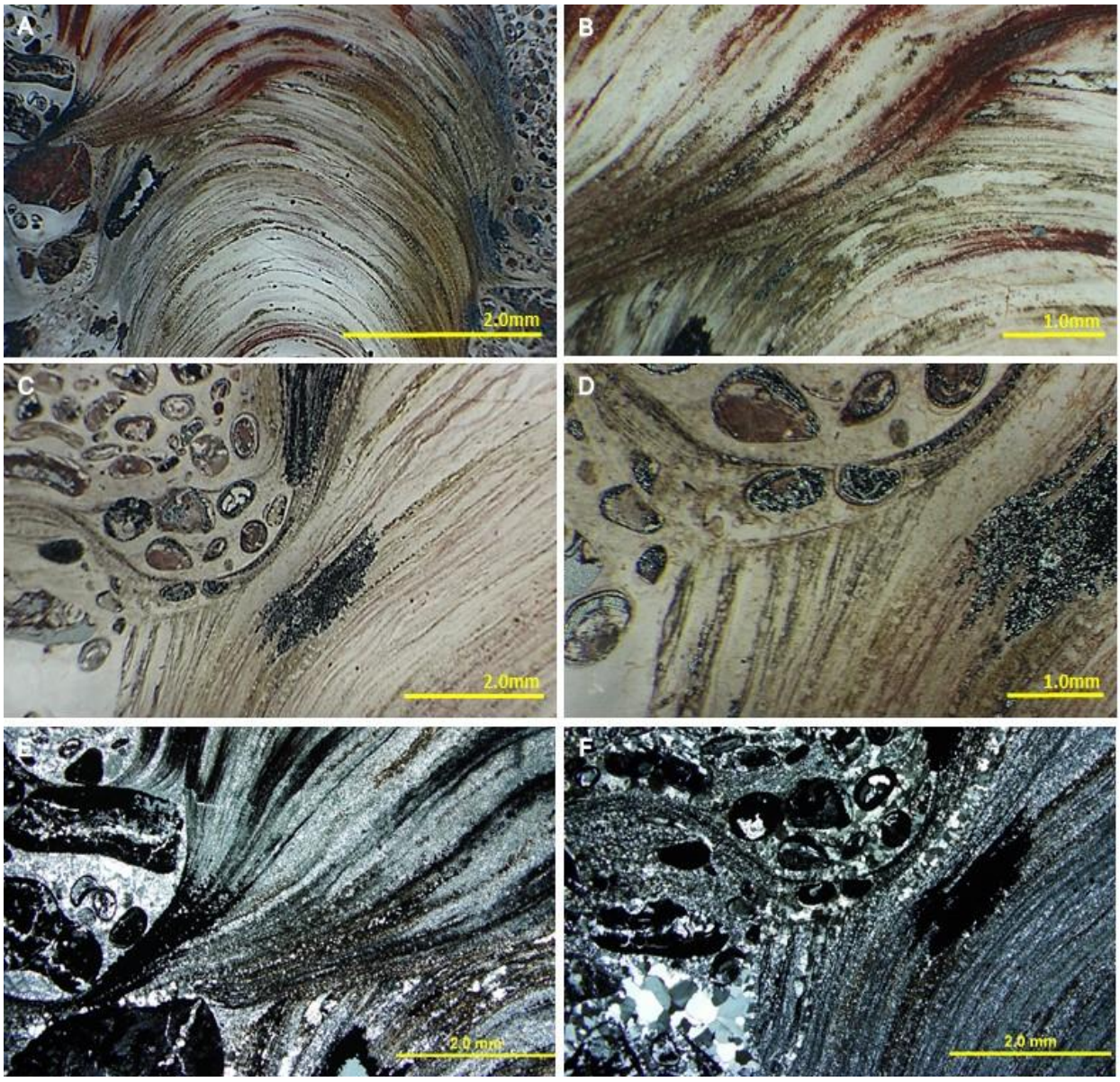

Figure 49. Photomicrographs of truncations of stromatolite columns and subsequent overgrowth. (A) Millimeter-scale digitate stromatolite showing an erosive hiatus. The top of the stromatolite was erosivly scoured off, with subsequent overgrowth of biofilm (PPL). (B) Higher magnification (100x) of sample in (A) showing the sharp contact caused by the erosive scouring of the original stromatolite laminae, and growth of later mat (PPL). (C-D) Centimeter-scale digitate stromatolite showing an erosive scour similar to previous example. Note the sharp contact of the stromatolite wall, and the bridging of the microbial mat over the granules (PPL). (E) XPL photomicrograph of area in (a). (F) XPL photomicrograph of area in (c).

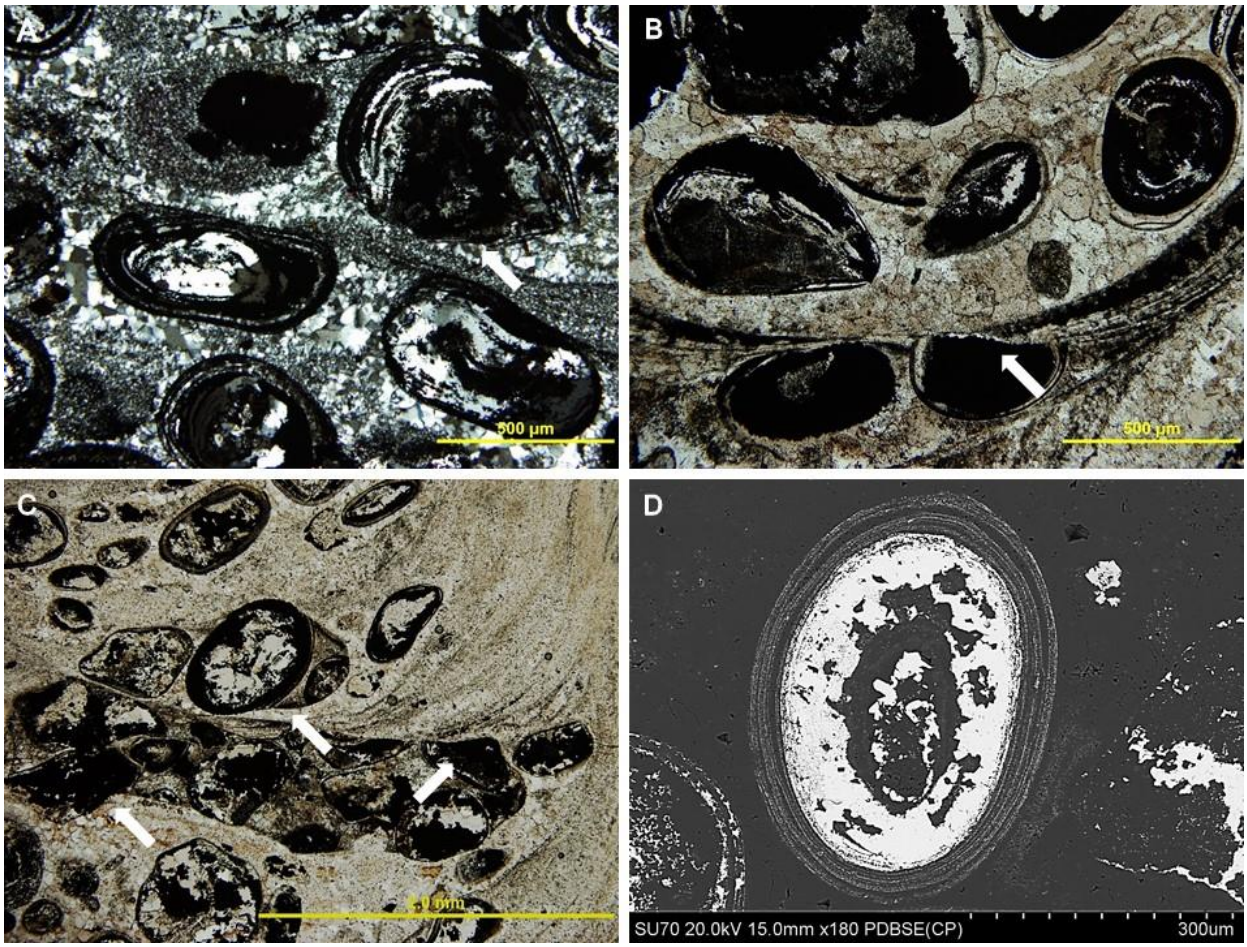

Figure 50. Photomicrographs of truncated ooids. (A) Dissolution surfaces of the truncated ooid (white arrow) XPL. (B) The truncated surface of a peloid being overgrown by a thin microbial mat containing magnetite. PPL. (C) Multiple intraformational aggregate grains containing multiple granules cemented together in the interspace between digitate stromatolites. PPL. (D) SEM backscatter electron image of the concentric cortices surrounding a magnetite nucleus. Point analysis of the individual laminae show concentrations of up to 3.1% MnO.

intergranular cement which often exceeds 50 µm (Figures 49E, 49F). There is also an increase in the crystal size immediately adjacent to the truncation surface (Figure 49F).

The grains within the interspace between columns are mostly granules, however ooids and aggregate grains are also present in all samples examined. Similar to the truncation of the stromatolite columns, the grains are often fractured and erosivley truncated prior to deposition (Figure 50A). These grains are randomly orientated, and are coated by a microcrystalline,

magnetite-rich microbial mat (Figure 50B). Aggregate grains made up of multiple ooids and granules cemented together are also a common feature (Figure 50C). These grains have distinct boundaries, where the scouring of the internal grains at the grain periphery is prominent (Figure 50C, white arrows). Cementation prior to deposition within the interspace is evident by the angular grain which can be seen sticking out in the bottom left of Figure 50C. The cement within the aggregate grains contains disseminated cryptocrystalline iron oxide imparting the stained, dirty appearance. The granules within the aggregate grain also show greater compaction in contrast to the non-aggregate granules and ooids found within the interspace. SEM analysis of several grains indicates a similar elemental alternation as that present in the stromatolite columns. Ooids with cortical laminae composed of up to 2.9% MnO alternate with iron oxide and silica-rich laminae (Figure 50D).

Scanning electron imagery of untreated rock chips provided a unique perspective of the lamination and mineralogical associations within a stromatolitic column. The alternation of the blocky iron oxide and fine-grained (<10 μm) silica laminae is distinct (Figure 51A). Backscatter imaging Figure 51A shows the iron oxide (light grey) alternating with the silica (dark grey) (Figure 51B). Fossilized EPS was noted in several samples as ropy structures with cryptocrystalline silica grains <1 μm embedded (white arrow, Figure 51C). Platy hematite was noted growing from a silica groundmass (Figure 51D). One sample showed two distinct forms of silica crystals, the first being a smooth mass with a sharp contact to elongated euhedral crystals up to 10 μm in length (Figure 51E). Similarly, large interlocking silica crystals up to 50 μm bordered by euhedral iron oxide crystals highlight the alternation of iron oxides and silica within the laminae (Figure 51F).

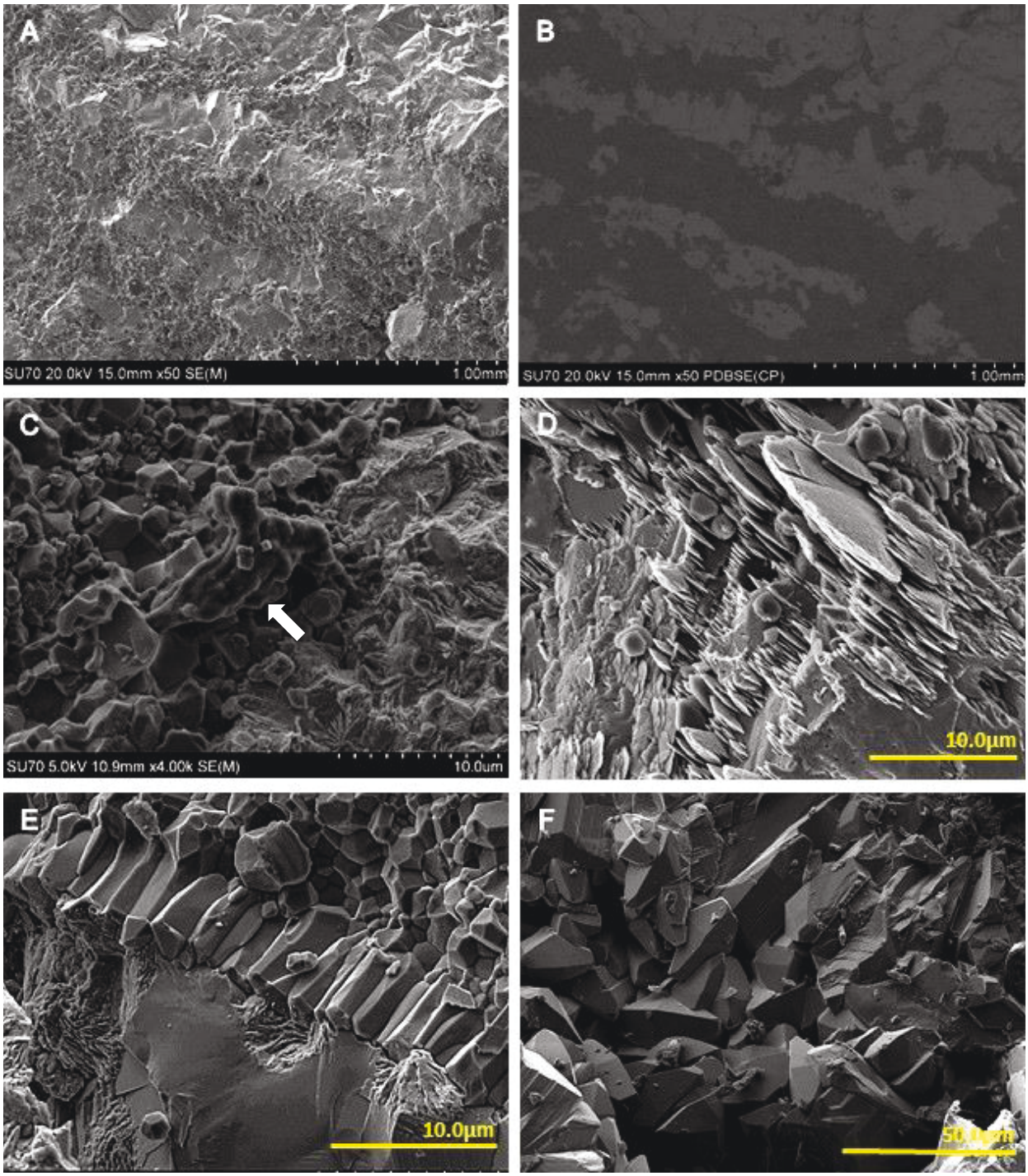

Figure 51. Scanning electron images of untreated stromatolite rock chips. (A) Secondary electron (SE) image showing the alternating blocky iron oxide and granular silica laminae. (B) Backscatter electron image (BSE) of (a) showing the alternating light (iron oxide) and dark (silica) laminae. (C) Fossilized EPS (white arrow) surrounded by cryptocrystalline silica. (D) Platy hematite growing from a silica groundmass. (E) Two generations of silica, the first is the smooth mass at base of image that is sharply overlain by the elongated blocky silica crystals at the top. (F) Interlocking blocky silica with euhedral magnetite crystals at bottom edges.

The ICP-MS measured REE contents for samples collected from the Mary Ellen Mine were normalized to PAAS values and plotted (Figure 52). The samples selected for analysis include one sample form the grainstone directly below the stromatolites (ME-01), two samples containing stromatolites (ME-06, ME-07) and two samples of the highly altered basal zone (ME-15, ME-16). The plot shows a consistent pattern showing a slight positive to nil Ce anomaly and a slightly positive to nil Eu anomaly. The ME-01 and ME-06 samples have a positive La anomaly imparting an apparent negative Ce anomaly, however, when factored in these samples show a slightly positive Ce anomaly.

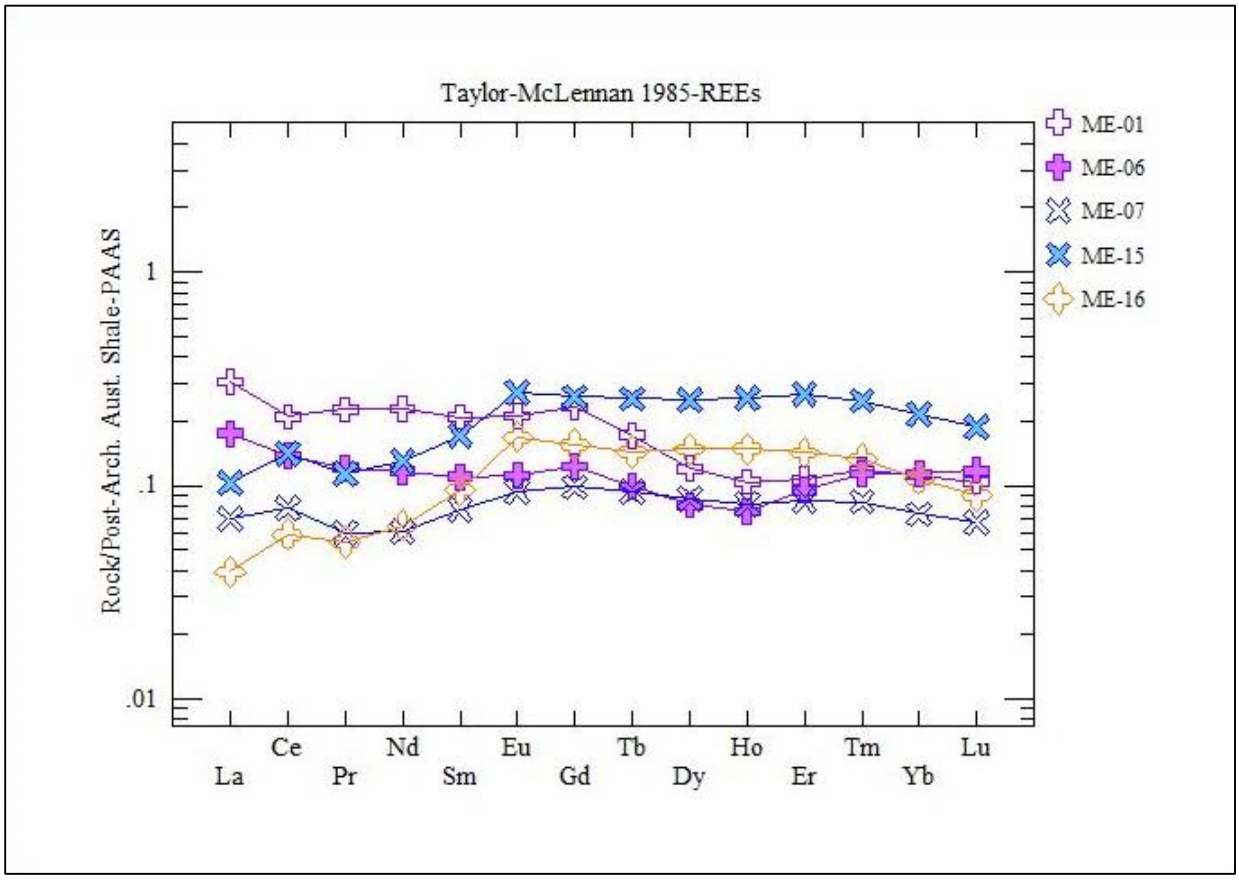

Figure 52. The PAAS normalized REE diagram for the Mary Ellen Mine site. Samples ME-01, Me-06, ME-.7 showing a slightly negative to nil, to positive Ce anomaly (respectively) and a minor depletion in HREE in relation to the LREE. Samples Me-16 and ME-17 were taken from the highly altered basal zone and show a distinct positive Ce anomaly and a minor depletion in LREE in relation to the HREE.

2.3.2 LTV (Old Cliffs-Erie) Mine

UTM 567859E, 5271899N 15N

The LTV mine is located 20 km northwest of Aurora, Minnesota. Access is via a private mining road (Dunka Road) with right of entry provided by Cliffs Natural Resources. Erosive scouring and subsequent glacial polishing exposed an area roughly 150 m long by 70 m wide containing multiple (over 30), meter-scale, cherty bioherms (Figure 53A). No samples were collected at the request of the mine geologist. At the base of the outcrop a ~30 cm breccia layer

Figure 53. Outcrop photographs of the LTV Mine study site. (A) Upper Stromatolitic Member crops out over a 150 m x 70 m glacially polished area containing multiple, meter-scale bioherms. (B) 75 cm vertical exposure of pebble to cobble sized brecciated grainstone which is overlain by the stromatolites. (C) Horizontal view of a domal stromatolite developing off the side of a cobble.

containing angular to subangular cobbles made up of grainstone is directly overlain by the stromatolitic unit (Figure 53B). In Figure 53C a domal stromatolite has developed off one side of a decimeter-scale subangular boulder. The laminae extend partially around the boulder before draping over the smaller cobbles adjacent to it.

The stromatolitic mounds range up to 2.5 m in diameter and consist of alternating zones of light and dark material (Figure 54A). The light zones range in thickness from a few centimeters up to a meter and are composed of centimetre-scale digitate stromatolites which grew perpendicular to the stratiform mat from which they developed.. The light digitate zones are subsequently overlain by dark, wavy stratiform laminae up to 4 cm thick (Figure 54B). The light-dark alternation occurs 2 to 4 times in the bioherms examined. The digitate stromatolites are closely packed, often with only a few millimetres between individual columns allowing for hundreds of digitate stromatolites within each bioherm. The individual digits range from 1 to 2 cm in diameter and have an irregular polygonal shape (Figure 54C). The internal lamination within the digits is reasonably well preserved and consists of alternating cream and light green laminae. Figure 54D provides a horizontal view through the centre of a large bioherm. Due to the development of the digits perpendicular to the mound the cross section offers an oblique view of the stromatolites.

The digitate stromatolites are made up of alternating cream and light-green chert laminae surrounded by a medium-grained chert grainstone. Abundant, randomly orientated, centimeter-scale rip-up clasts are present within the interspace (Figure 46E). These clasts are composed of green chert and often have stromatolites developing from them (Figure 46F).

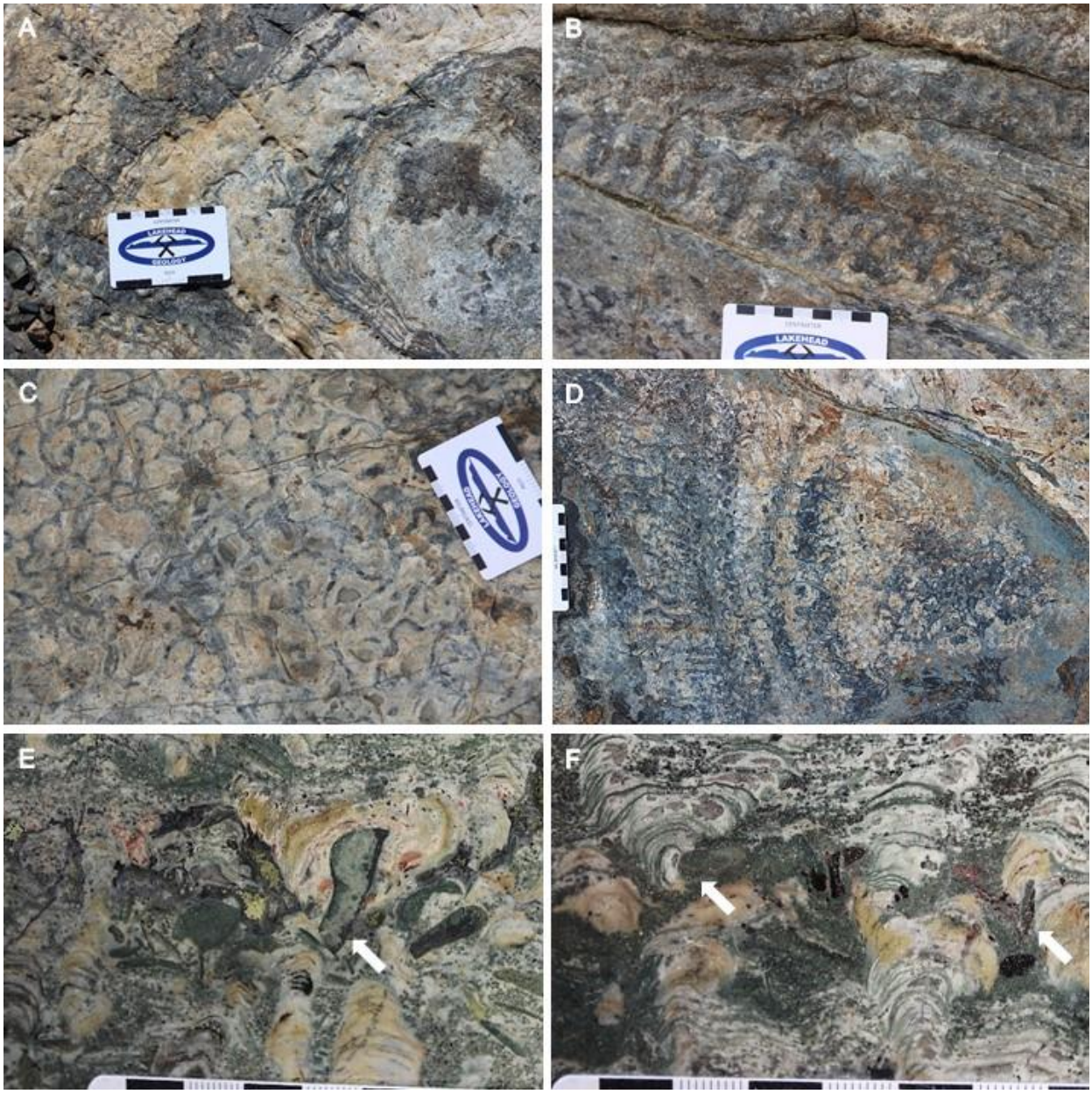

Figure 54. Photographs of stromatolite forms at LTV. (A) The bioherms develop as decimeter-scale domes made-up of wavy cream coloured laminae, alternating with dark green to black laminae. (B) A vertical outcrop showing digitate stromatolites overlain by a stratiform mat. (C) The centimeter-scale digitate stromatolites have a polygonal shape and are closely packed. Hundreds of digitate columns make up each bioherm. (D) Horizontal section through middle of bioherm. The digitate stromatolites developed perpendicular to the domal laminae allowing vertical, horizontal and oblique views through the digits. (E) The stromatolites are made up of alternating cream and light green chert laminae in a medium-grained grainstone containing abundant centimeter-scale rip-up clasts (white arrow). (F) The rip-up clasts often become nucleation points for the development of the stromatolites (white arrows).

2.3.3 Northshore Mine (Peter Mitchell Mine)

UTM 576421E, 5278854N, 15N

The Northshore mine is located 8 km southeast of Babbitt, Minnesota, off Forest Route 112. Entry to the property was provided by Cliffs Natural Resources. The outcrop consists of a 1.5 m vertical exposure which extends several meters laterally and contains an exceptionally well preserved section of the Upper Stromatolitic Member (Figure 55A).

At the base of the outcrop domes exceeding 15 cm in diameter develop from a conglomeratic layer. The domes are made up of highly contorted laminae containing deep red to pink chert (Figure 55B). They are surrounded by intraformational rip-up clasts within a medium grained cherty grainstone. Overlying the domes, ~60 cm of digitate stromatolites are present, which can be divided into three zones. The first extends up from the base ~50 cm and contains poorly developed jasperlitic digitate stromatolites. These forms show low to moderate inheritance, and have an average height of 1.5 cm. Above these, extending an additional 10 to 15 cm are exceptionally well preserved digitate forms (Figures 55C, 55A). These stromatolites show a consistent diameter of 1 cm throughout the columns. The digits have an inclined to curved habit of accretion, while maintaining a high degree of inheritance. Individual columns range up to 10 cm in relief, with minimal bridging structures. Alpha and beta branching is common, generally occurring from the left side of the columns. They range in colour from fire-red to cream laminae which irregularly alternate with black laminae. The top zone contains poorly developed digits, similar to the basal zone. However, the stromatolites within this zone are composed of white chert. The top of the outcrop contains abundant centimeter-scale rip-up clasts in a medium to coarse grainstone (Figure 55D).

Figure 55. Outcrop photographs of the Northshore Mine study site. (A) The outcrop consists of a 1.5 m vertical exposure of the Upper Stromatolitic Member. (B) At the base of the outcrop decimeter-scale cherty domal stromatolites overly intraformational conglomerate. (C) Exceptionally well preserved digitate stromatolites. The curved to inclined digits can reach a relative relief of up to 10 cm and show a high degree of inheritance. (D) A rip-up conglomerate layer containing centimeter-scale clasts embedded in a medium to coarse grainstone overlies the stromatolites.

At the outer edges of the column the laminae coalesce forming a well-defined wall structure (Figures 56A, and 56B). The width of the wall varies from 200 to 400 μm, and can be continuous over several centimeters. Interestingly, a notable increase in the intensity of colour occurs within the wall at the grainstone-stromatolite contact from a pale orange in the column to

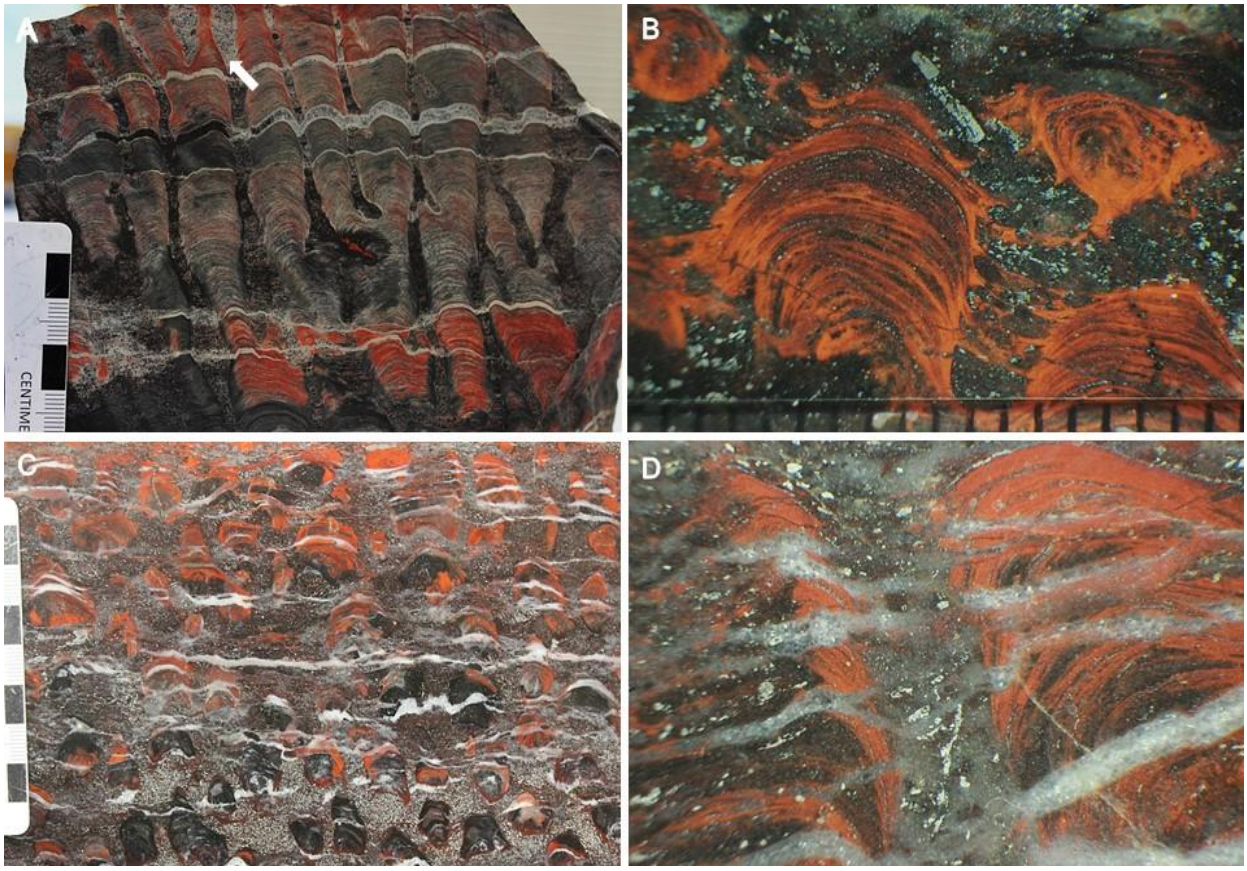

Figure 56. Photographs of stromatolite bearing hand samples. (A) Well defined digitate columns with alpha and beta branching. Bridging is rare in the large columns, however the wall structures are well developed often with higher relative amounts of iron oxides as noted by the brighter red colour. (B) Centimeter-scale columns directly underlying the larger columns. Bridging is common and can be seen as a continuation of the red wall at the stromatolite-grainstone interface. Note the difference in intensity of the wall and internal laminae (scale in mm). (C) Zones of magnetite-rich (bottom) versus jasperlitic rich (middle) grainstone are common. The microbial mat bridging the columns has grains of each trapped within the jasperlitic laminae. (D) Secondary white quartz zones, continuous across several centimeters, contain fragments of stromatolite and grainstone.

vibrant red signifying an increase in iron concentration within the microbial mat (white arrow Figure 56A). Bridging of the centimeter-scale columns is common, and occurs as thin wisps of microbial mat from the wall drapes over the grainstone, connecting adjacent columns (Figure 56B). Frequent trapping of individual grains in the microbial mat occurs, and records differences in grainstone composition. In Figure 56C a distinct change is evident from a magnetite dominated grainstone (silver) near the bottom to a more jasperlitic grainstone (dark red) in the middle. Individual grains trapped within the laminae show a similar compositional difference.

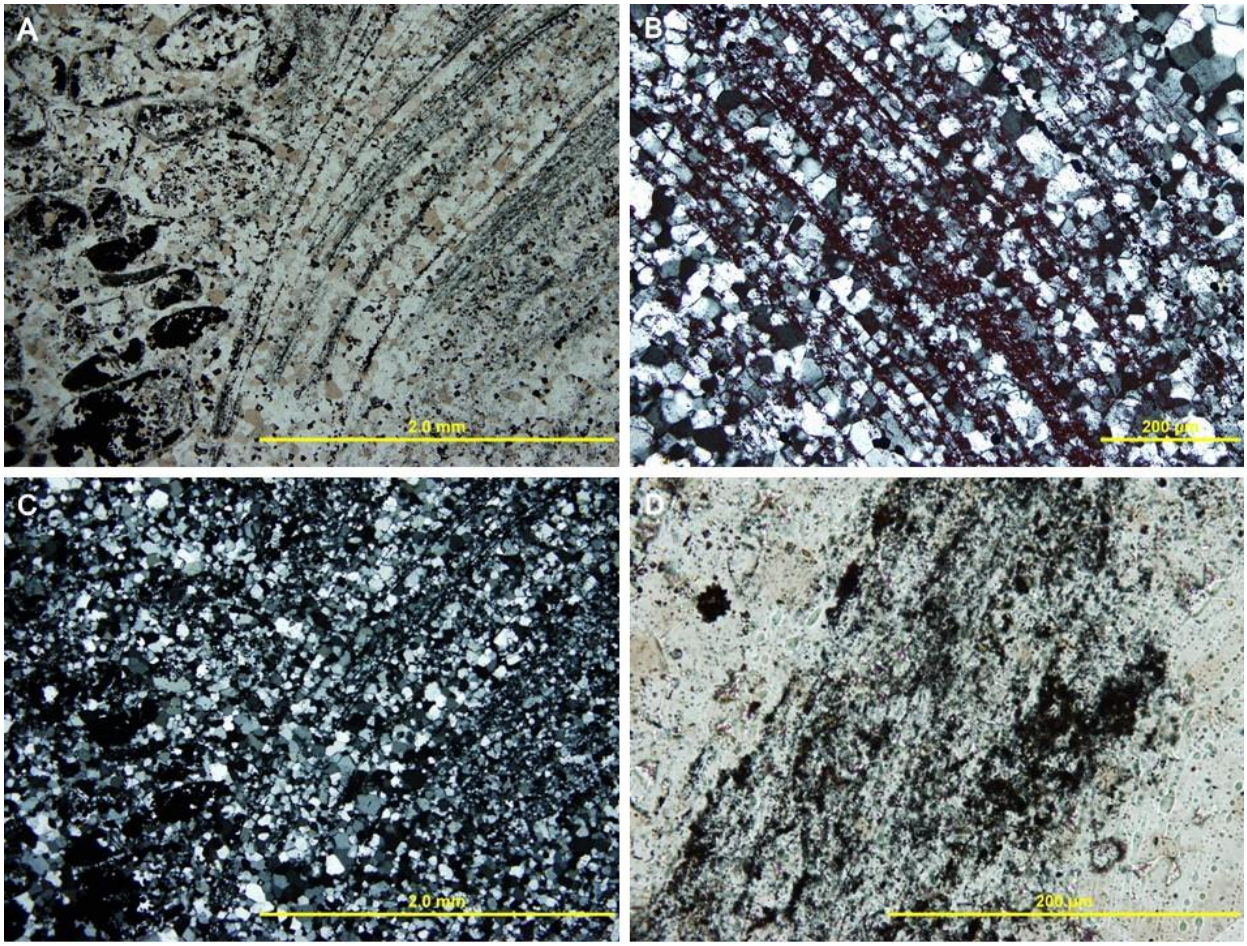

Figure 57. Photomicrographs of laminae. (A) The grainstone-stromatolite contact. Note the abundance of large quartz crystals (PPL). (B) The dark laminae are composed of concentrated inclusions of cryptocrystalline hematite with relatively sharp boundaries (XPL). (C) A predominance of blocky megaquartz crystals make up the light stromatolitic laminae as well as the intergranular cement (XPL image of (A)). (D) Diffuse black zones similar to those containing abundant microfossils at other sites contain no filamentous or spheroidal structures.

Secondary quartz is present in abundance in all samples examined. Translucent to white quartz zones can be continuous across several centimetres, and rarely in outcrop over one meter. In some cases they parallel the column laminae as can be seen in Figure 56A, while also crosscutting and destroying in the centimeter-scale columns (Figure 56D). In the smaller columns, angular fragments of stromatolite are present within the quartz, as well as millimeter-scale blocks of lithified grainstone.

In thin section, differences between the Northshore samples and those previously described are evident. The dark laminae are thinner (generally under 100 μm) and show a greater continuity along the convexity of the column (Figure 57A). They are composed of concentrated bands of cryptocrystalline hematite inclusions in blocky quartz with relatively sharp boundaries. The light laminae are composed of blocky megaquartz with crystal sizes ranging up to 90 μm in length (Figure 57B). This is in stark contrast to the microquartz crystals previously described within stromatolitic laminae, which had an average length of under 25 μm. The increase in the size of the quartz crystal is evident even at low magnification and the result of thermal metamorphism (Figure 57C). Interestingly, carbon-rich zones similar to the laminae containing microfossils in the Middle Stromatolitic Member are present in the Northshore samples, however no structures resembling spheres or filaments were found (Figure 57D).

2.3.4 Thunder Bird North Mine

UTM 535000E, 5257910N 15N

The United Taconite Thunderbird North Mine is located 8 km south of Virginia, Minnesota, off US Highway 53. Access was provided by Cliffs Natural Resources. Within the mine the Upper Stromatolitic Member is made up of resedimented stromatolites, termed oncolites. These structures make up a marker bed 70 to 100 cm thick that is continuous throughout the mine locally known as the UC-6 subunit (Figure 58A). It overlies a medium- to coarse-grained oolitic ankerite grainstone containing decimeter-scale zones of magnetite and is overlain by chert beds containing abundant coarse-gained jasper rip-up clasts. The UC-6 submember is exposed several meters above ground, thus in situ sampling was not possible. All

Figure 58. Photographs of the UTAC Thunder Bird North oncolites. (A) The UC-6 oncolite subunit ranges in thickness from 70-100 cm and is continuous throughout the mine. (B) In core the oncolites appear as wavy dark layers which alternate with white chert. (C) The oncolites are surrounded by a mottled, coarse-grained grainstone. (D) The oncolites occur as subrounded spheres, 4 to 8 cm in diameter and made up of millimeter-scale light granule-rich and dark iron-rich layers. (E-F) More commonly the oncolites occur as centimeter-scale elongated spheres composed of an angular chert grain surrounded by dark laminae.

samples were collected from blast piles below the exposure.

In core the oncolites occur as wavy, iron-rich layers, which alternate with pale red to purple grainstone layers (Figure 58B). Two distinct forms of oncolites were noted at the mine.

The first occurs as 4 to 8 cm, subrounded spheres embedded in a mottled, purple to red coarse-grained grainstone (Figure 58C). The mottled zones contain disseminated magnetite surrounded by purple to red chert. The oncolites are made up of dark, wavy, iron-rich laminae several millimeters thick, which alternate with creamy white chert containing rounded granules. The core of these oncolites is generally made up of cemented grainstone comparable to that surrounding the oncolites (Figure 58D). The second form are centimeter-scale elongated spheres composed of millimeter-scale dark laminae concentrically laminated around jasper rip-up clasts (Figures 58E, 58F).

The oncolites occur interspersed with multicentimeter-scale jasper and magnetite-rich rip-up clasts (Figure 59A). The rip-up clasts contain rare concentric laminae consisting of dark and light jasper and magnetite. Dehydration cracks within the rip-ups are common (Figure 59B). The rip-ups overlay a 2-mm-thick jasper layer which caps off a decimeter-scale zone containing 2 to 4 cm magnetite clasts in a chert matrix. Within this zone rare white chert clasts are present (Figure 59C). One sample collected contains a chaotic mix of angular black and white chert clasts, magnetite clasts, and oncolites composed of magnetite-jasper-carbonate (Figure 59D). The oncolites within this sample are highly fractured, containing abundant carbonate-filled cracks. This sample is however not typical of the oncolites.

Figure 60 illustrates typical Thunder Bird oncolite composition. The nucleus is an angular clast composed of cemented grainstone (magnetite and jasper grains) intermixed with millimeter-scale jasper- magnetite clasts and magnetite. Dehydration cracks extend through the magnetite, but do not extend into the cemented grainstone. The nucleus is surrounded by asymmetrical laminae of jasper, magnetite and grainstone. The laminae are noticeably thicker on the top of the oncolite

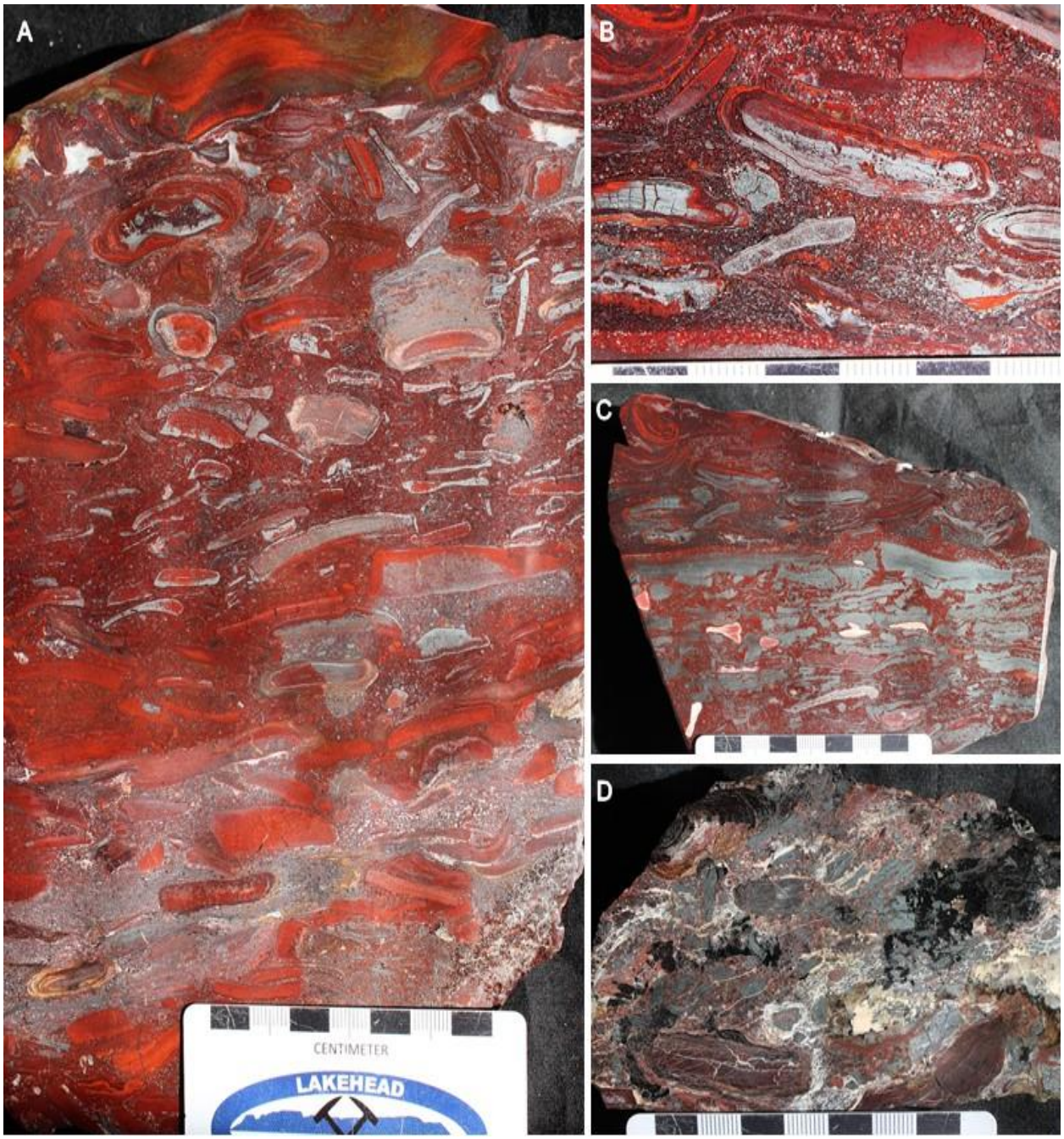

Figure 59. Photographs of oncolite bearing grab samples. (A-B) The oncolites are interspersed with abundant intraformational jasper and magnetite rip-up clasts in a coarse-grained grainstone. (C) The jasper rip-up clasts overlie a decimeter-scale zone of magnetite-rich clasts with rare white centimeter-scale chert grains. (D) Randomly oriented, angular clasts surrounding magnetite-jasper-carbonate oncolites.

Figure 60. Oncolite surrounded by medium- to coarse-grained grainstone composed of rounded jasper and magnetite grains. The nucleus is made up of cemented grainstone, magnetite containing dehydration cracks and millimeter-scale jasper rip-up clasts. This is surrounded by asymmetrical wavy laminae composed of jasper, grainstone, and hematite. The grainstone is a mix of submillimeter magnetite and jasper grains.

whereas the basal laminae are thin and mostly jasper.

A grainstone composed of submillimeter ooids, granules and coated grains as well as larger (<1 mm) clasts surrounds the oncolites. Interestingly granules composed of magnetite and those composed of jasper as well as magnetite grains with a jasper rim are intermixed with angular centimeter-scale clasts (Figure 60). The clasts are predominantly jasper containing dehydration cracks. However, some composed of laminated magnetite with rare jasper rims are also present.

In thin section the composition of the oncolites becomes more complicated. Some

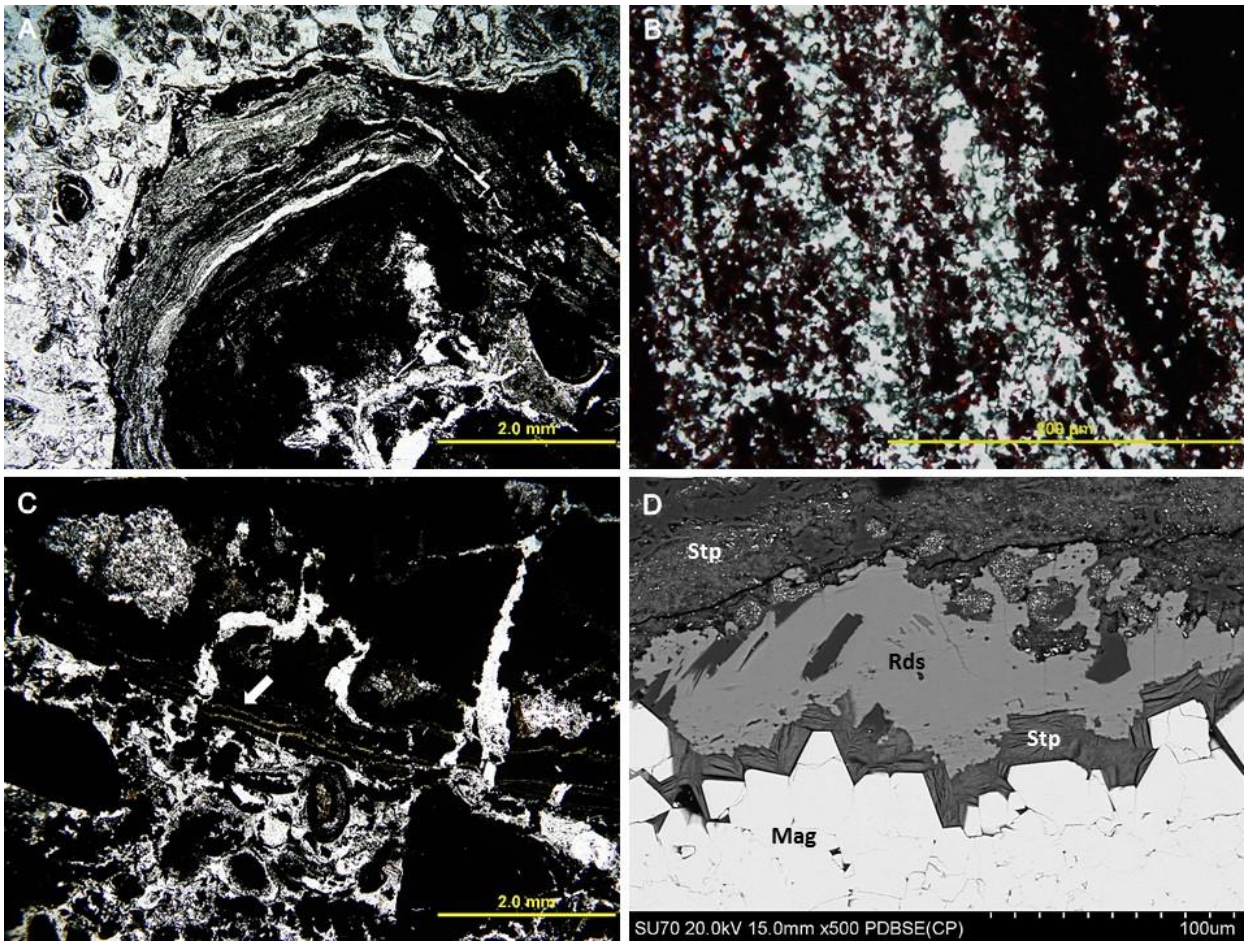

Figure 61. The laminae within the oncolite are compositionally diverse. (A) Discontinuous, wavy laminae composed of iron oxides irregularly alternate with quartz (XPL). (B) Diffuse layers, 25 to 50 µm thick containing micro- to cryptocrystalline hematite between opaque hematite laminae (XPL). (C) Thin (100 to 200 µm) layers of greenalite (white arrow) alternate with hematite at the outer edge of oncolite (XPL). (D) Backscatter image of ferroan-rhodochrosite (Rds) bound by stilpnomelane (Stl) overlying a magnetite (Mag) laminae.

samples examined have a simple composition of iron-oxide and quartz with minor cryptocrystalline inclusions of carbonate and/or hematite within the quartz (Figure 61A, 61B). However, others have varying compositions of iron oxides, iron silicates, quartz, and carbonates. In Figure 61C thin layers of greenalite (white arrow) alternate with hematite at the edges of the oncolite. Similarly, discontinuous zones of ferroan-rhodochrosite containing relict 30 to 50 µm chert crystals bound by well-defined layers of stilpnomelane are relatively common and often occur with magnetite laminae (Figure 61D).

As noted above, the oncolites are surrounded in a medium- to coarse-grained grainstone comprised of ooids, granules, coated grains and rip-up clasts. Within one of the cherty granules several spheres, each roughly 25 to 30 μm in diameter are present (Figure 62). These cores of these spheres are composed of chert with finely disseminated iron similar to the material between spheres and is coated in a 6 to 10 μm thick rim of iron oxide.

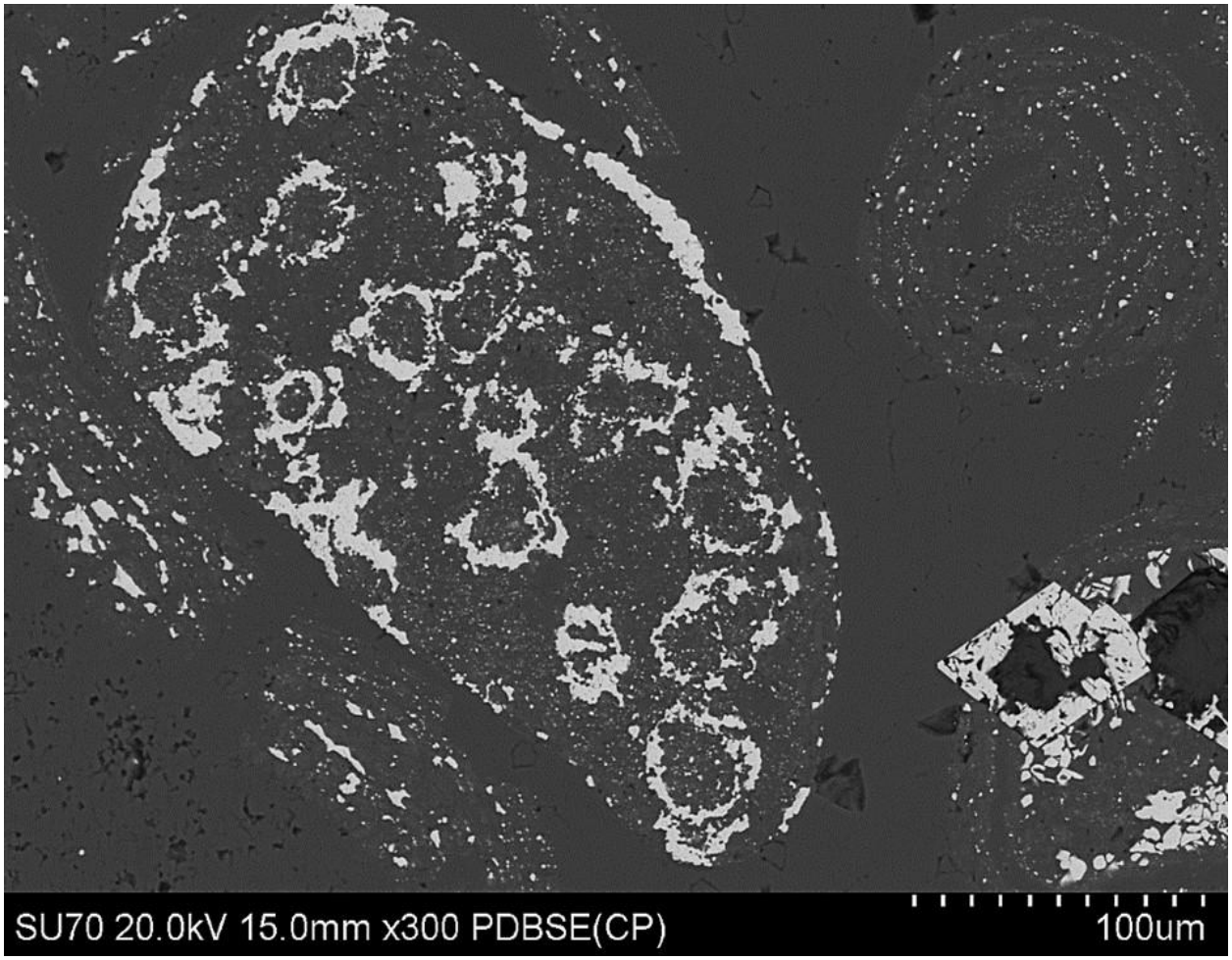

Figure 62. Backscatter image of a peloid containing multiple iron-oxide coated spheres measuring 25 to 30 μm in diameter.

2.3.5 Drill Core

2.3.5.1 VHD-001

UTM 530941E, 5257656N, 15N

The 482 m deep VHD hole was drilled by BHP Minerals near the town of Virginia, Minnesota, roughly 140 meters above the Pokegama-Biwabik contact. Within this core, 120 cm of the Upper Stromatolitic Member is present. At the bottom of the unit, 30 cm of stratiform and pseudocolumnar stromatolites overlie pebble conglomerate made up of cherty mud-chip rip-ups. These are overlain by 90 cm of oncolites in a mostly grainstone matrix. At the base of the section, the oncolites are surrounded in a medium- to coarse-grained grainstone (Figure 50A). Further up column, layers of magnetite mud interspersed with granules become common (Figure 50B), until the oncolites are completely surrounded by magnetite-chert rich mud at the top of the unit (Figure 50C).

In thin section the coarse grainstone surrounding the oncolites contains abundant granules ranging from sub-millimeter to several millimeters in length. They are composed primarily of jasper often with 100-to-200 μm thick outer rims of iron oxide. The wavy laminae within the oncolites are well preserved and are composed of black carbon-carbonate-iron oxide-rich laminae alternating with jasper (Figure 63A). The nucleus of the oncolites is composed of lithified grainstone (granules and ooids in a microcrystalline quartz cement), or jasper rip-up clasts. Often dehydration cracks extend through the nucleus and extend into the wavy oncolitic laminae. The carbonate within the oncolites ranges compositionally from siderite to ferroan-rhodochrosite and occurs as cryptocrystalline inclusions in microquartz and/or as large (≥100 μm) zoned rhombs which alternate with thin, discontinuous dark laminae (Figures 63B, 63C).

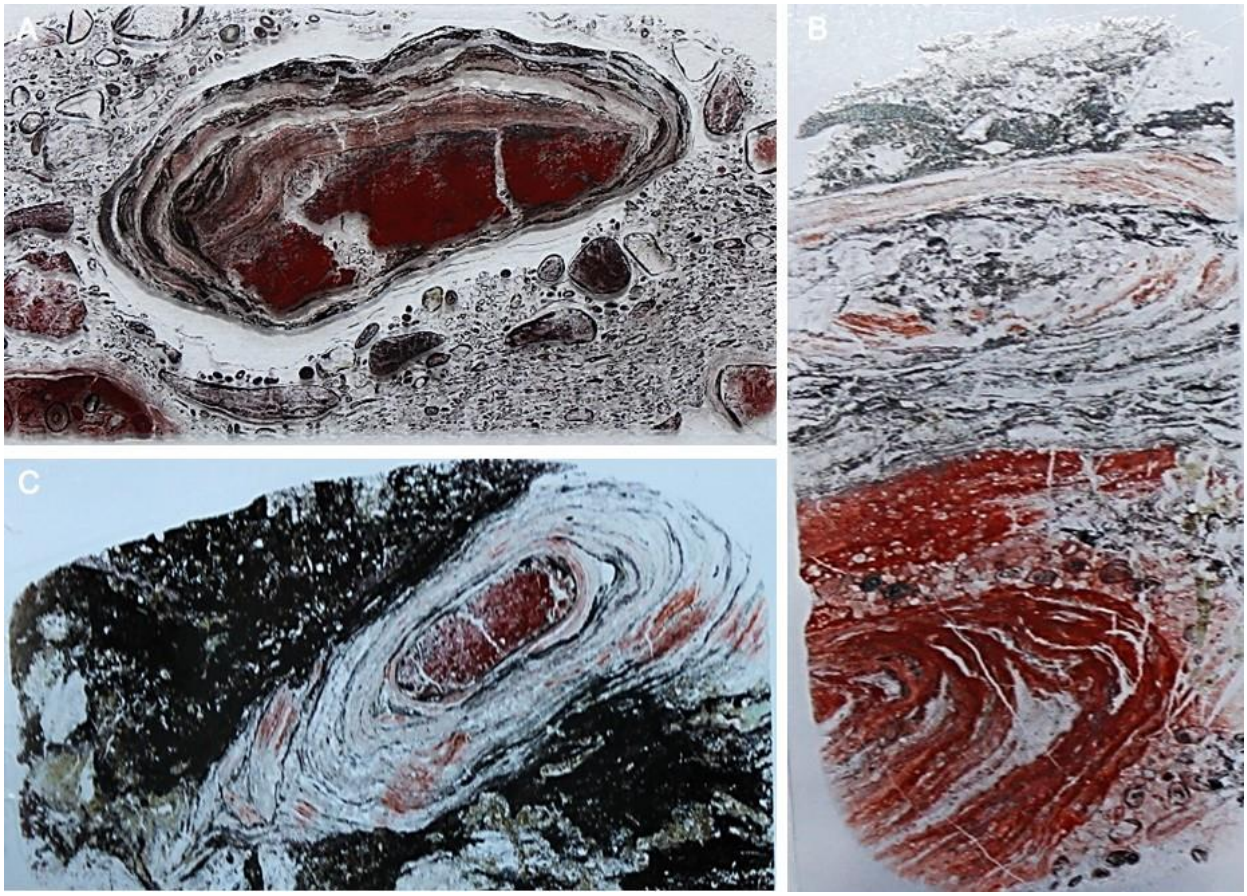

Figure 63. Photographs of oncolites in thin section. The oncolites are composed of a jasper core with alternating laminae of manganiferous carbonate and iron oxides. Note the dehydration cracks in each of the samples. (A) The basal oncolites have well preserved internal laminae, and are surrounded by a coarse grainstone, (B) The oncolites in the middle section are composed of jasper in a peloid grainstone. (C) The oncolites contained within the uppermost section are encased by magnetite with variable laminae preservation.

composed of microcrystalline quartz with cryptocrystalline hematite inclusions disseminated throughout (Figures 63C, 63D). Investigation conducted with the electron microscope confirm the optical observations showing the thin lamination within the oncolites are composed of alternating chert and manganiferous siderite laminae with thin zones of iron oxide (Figures 63E, 63F).

Elemental mapping of the oncolite in Figure 64F illustrate the compositional variation from the nucleus to the oncolite-grainstone interface (Figures 65A, 64F). The nucleus of the oncolite is composed of a manganiferous dolomite with an average of 10 point analyses yielding

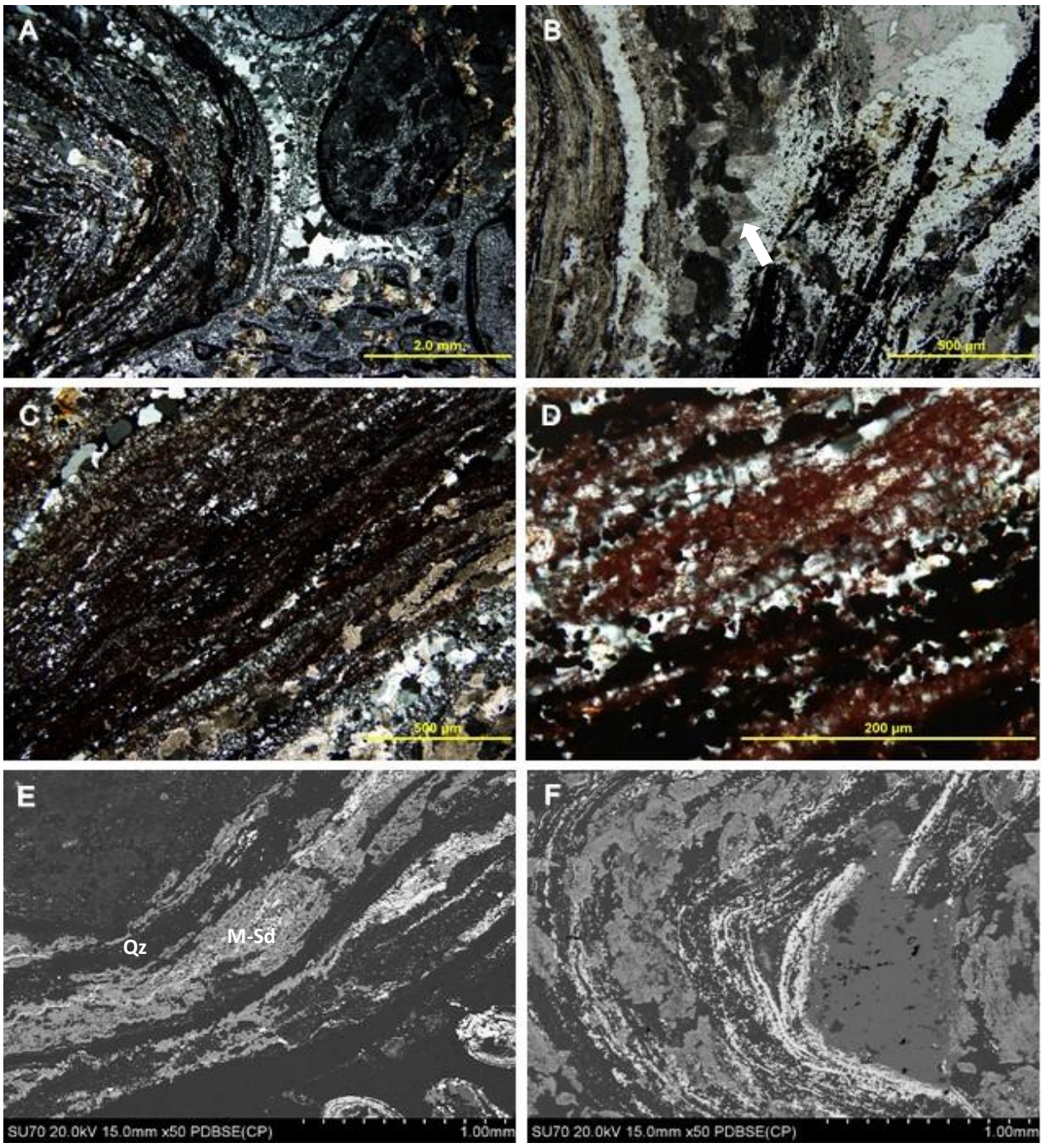

Figure 64. Photomicrographs of oncolite lamination. (A) The oncolites, surrounded by a coarse grainstone containing abundant granules, are composed primarily of microquartz alternating with irregular iron oxide or carbonate laminae. (B) The carbonate occurs as cryptocrystalline inclusions in microquartz and/or as large (100 µm) zoned rhombs (white arrow) (PPL). (C) Near the outer edge of the oncolite the laminae become thinner, and more iron-rich, alternating with layers of carbonate rhombohedra (XPL). The dark laminae are composed of microcrystalline quartz with cryptocrystalline hematite inclusions disseminated throughout (XPL). (E) Backscatter image of thinly laminated oncolite with alternating chert (Qz) and manganiferous siderite (M-Sd) laminae containing thin zones of iron oxide. (F) Backscatter image illustrating the compositional variation of the laminae (white - iron oxide, light grey - manganiferous siderite, dark grey - chert). Note the fracture of the innermost iron oxide laminae (See Figure 65 for more detail).

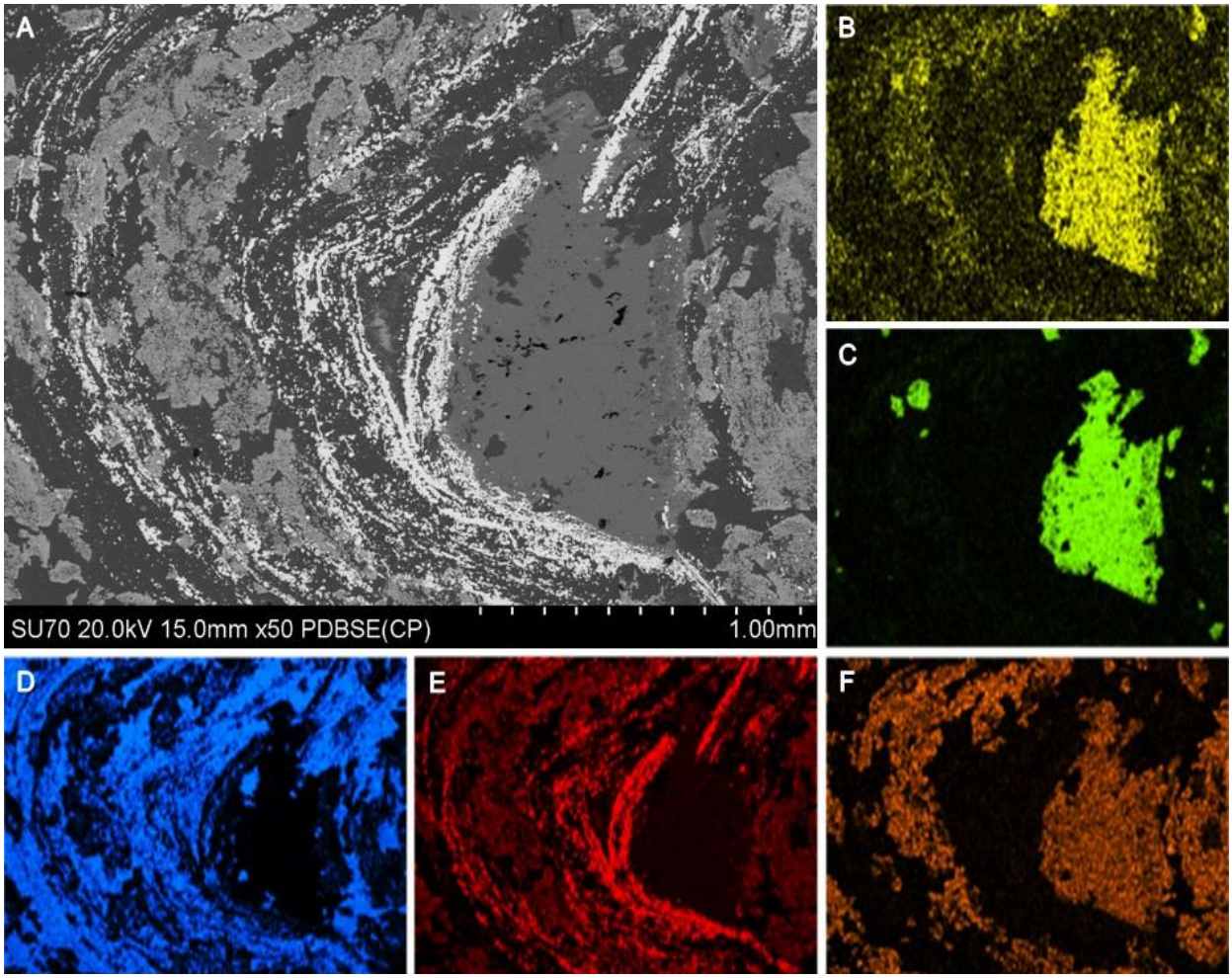

Figure 65. False colour EDS maps of oncolite lamination. (A) Backscatter image illustrating the variation in laminae composition and size. (B) magnesium, (C) calcium, (D) silicon, (E) iron, and (F) manganese.

a value of 10.2% manganese.

Outwards from the nucleus, the oncolite is composed of magnetite laminae ~100 µm thick which alternate with a manganiferous siderite with a Fe:Mn of 2:1 (Figures 65E, 65F). Point analysis revealed values up to 13.1% manganese in these layers. Present throughout the oncolite are discontinuous layers of silicon in the form of microquartz (Figure 65D). The magnetite lamina nearest the nucleus is fractured with the manganiferous dolomite extending into a quartz lamina (Figure 65E).

The ICP-MS measured REE contents for samples taken from the VHD-001 core were normalized to PAAS values and plotted (Figure 66). The samples selected for analysis all contained manganese-rich oncolites from the base (VHD-27A) middle (VHD-22) and top (VHD-X) of the oncolite section. The plot shows a consistent pattern for the VHD-22 and VHD-X samples showing a slight enrichment in HREE compared to the LREE, a negative Ce anomaly and a positive Eu anomaly. The VHD-27A sample shows no Ce anomaly, and a positive Eu anomaly.

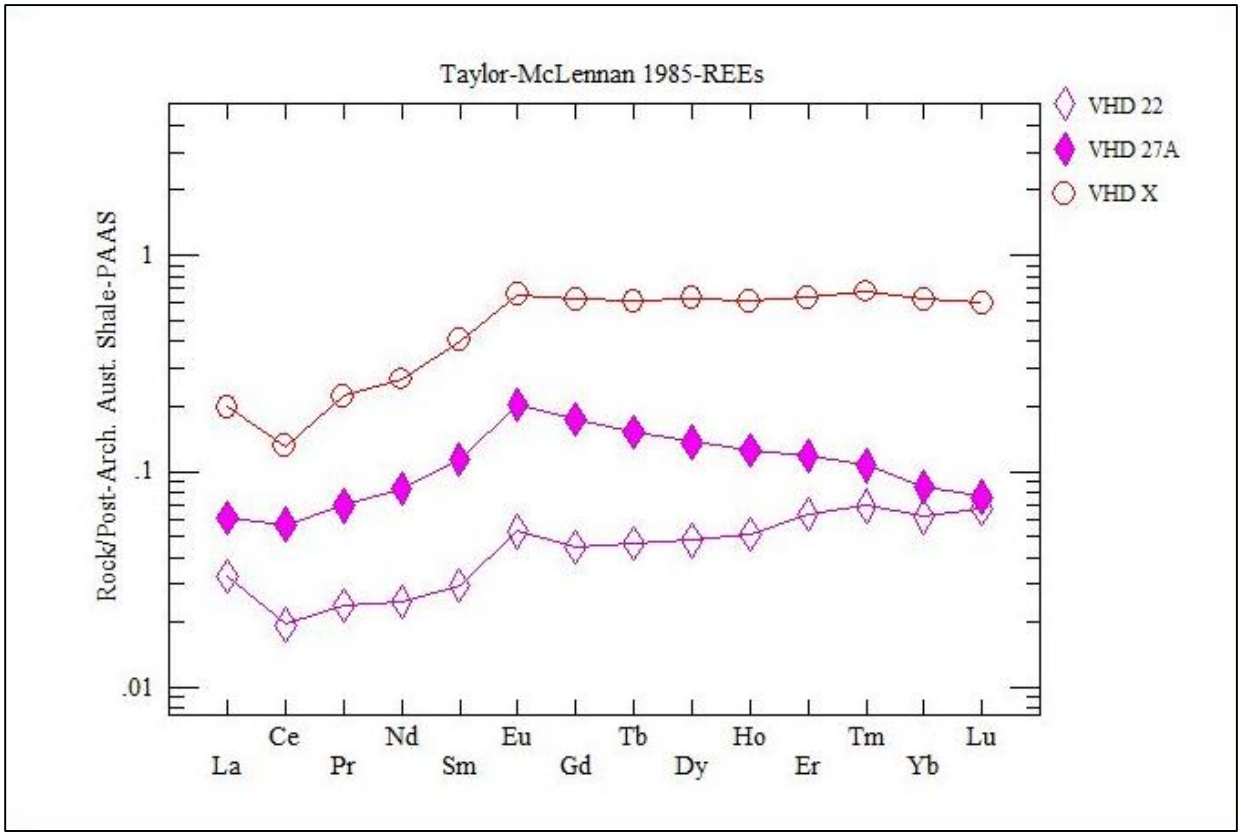

Figure 66. The PAAS normalized REE diagram for VHD-00-1 core showing a slightly negative to nil Ce anomaly, distinctly positive Eu anomalies and a slight depletion in LREE and HREE in relation to the mid-REEs.

2.3.5.2 LWD-99-1/ LWD-99-2

UTM 531571E, 5252837N 15N

The 423 m deep LWD-99-1 and 430 m deep LWD-99-2 holes were drilled by BHP Minerals 6 km southwest of the town of Eveleth, Minnesota. A distance of 2 km separates the drill holes. The Upper Stromatolitic Member in the LWD cores is located roughly 47 m below the Limestone Member at the top of the Gunflint. Regrettably a 1 to 1.5 m section of drill core was removed from each box leaving only a few centimeters of core containing the Upper Stromatolitic Member for study. Fortunately the LWD cores share a striking similarity in composition to the VHD core previously described. Despite the missing core, several samples were obtained for further investigation.

The stromatolitic unit overlays 100 cm of intraformational conglomerate made-up of elongated chert rip-up clasts, and centimeter-scale compound grains in a medium- to coarse-grained grainstone. Magnetite bands <5 mm are sporadically present throughout the conglomerate layer. The base of the stromatolitic unit is marked by the development of a stratiform mat, composed of wavy sub-millimeter jasper- and iron oxide-rich laminae. Directly above the missing core, 10-20 cm of centimeter-scale oncolites intercalated with jasper rip-up clasts are overlain by medium-grained, jasperlitic peloidal grainstone (Figure 67).

Compositionally the oncolites are similar to those described from the Thunderbird and VDH sites. Development of laminae often occurs on intraformational rip-up clasts composed of jasper. The oncolites in Figure 67 illustrate the typical asymmetrical laminar growth noted in the

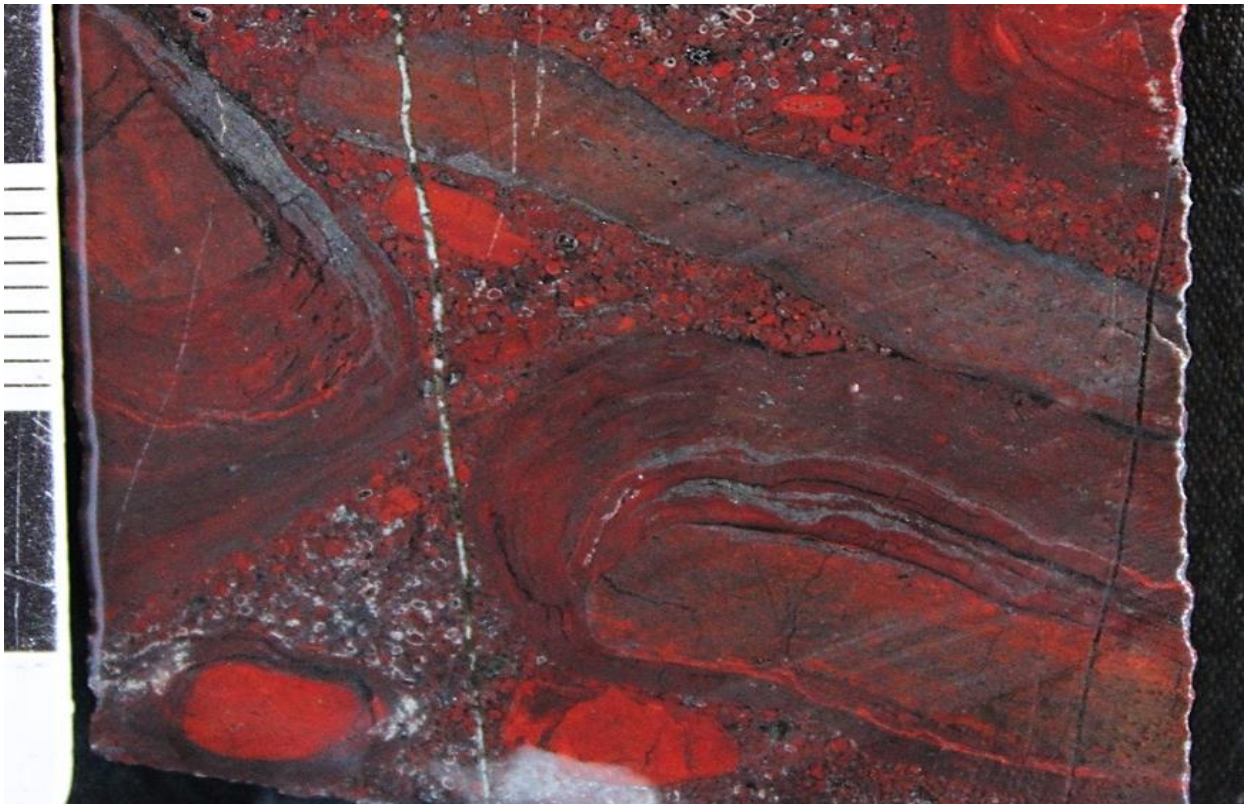

Figure 67. Photograph of oncolites in core. Intraformational rip-up clasts are common sites of oncolite development. Note the asymmetrical growth of laminae on the right.

majority of the samples examined. The laminae (if present) at the base of the oncolite are thin, with a total thickness of ~1 mm. This is in contrast to the well-defined multi-millimeter laminae that developed from the upper surface of the nucleus. Bands of euhedral magnetite are present crosscutting the jasperlitic laminae throughout the oncolites.

One unique feature of the LWD oncolites is the presence of microdigitate stromatolites within the laminae (Figures 68A, 68B). They range from 250 to 500 μm in width and are less than 1 mm in relief. Alternating iron oxide-rich and poor laminae define the internal microstructure. The iron oxide-poor laminae are composed of microcrystalline quartz with trace cryptocrystalline carbonate and/or hematite. The interspace between the microdigitate forms is

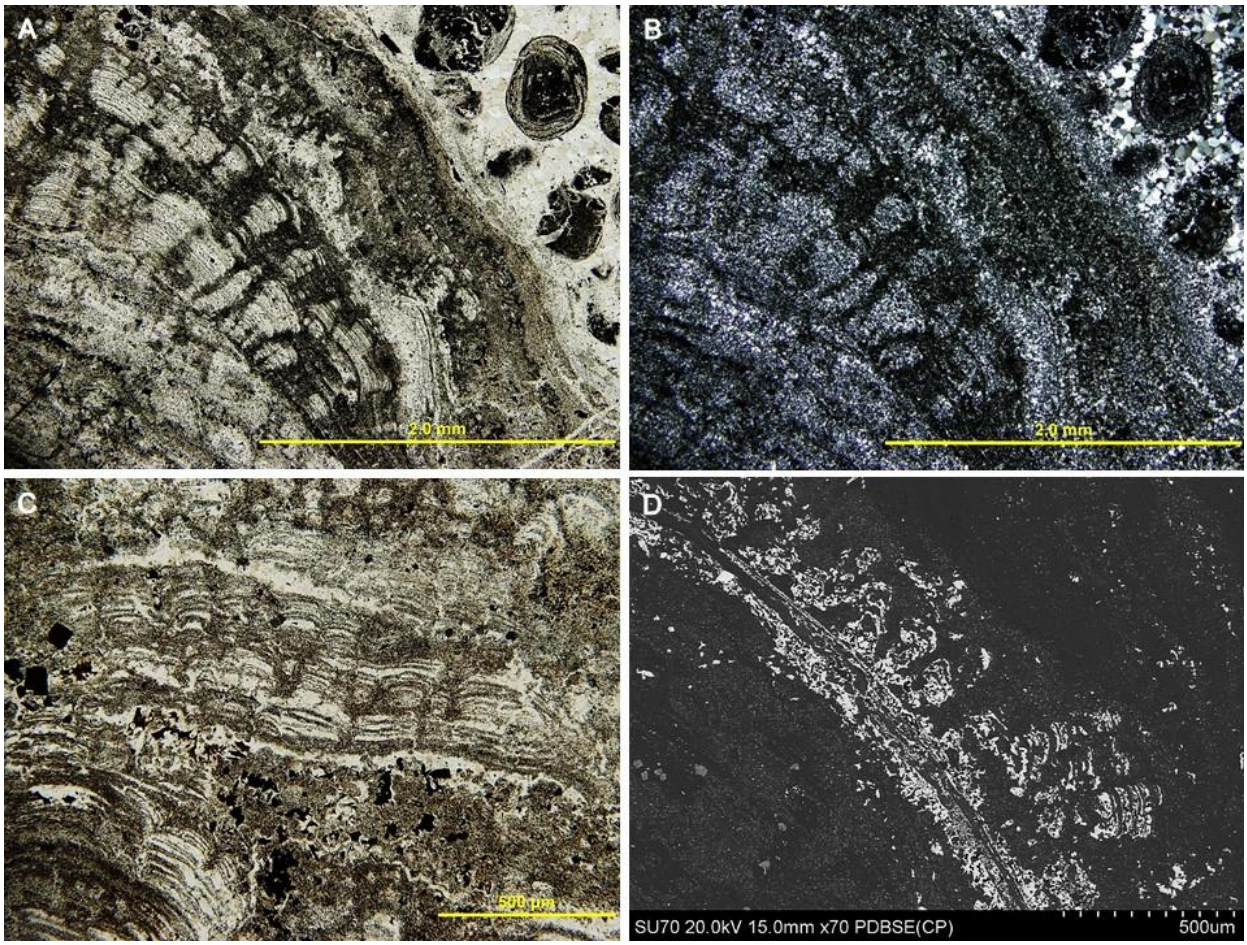

Figure 68. Microdigitate stromatolites within the oncolites. (A) Finely laminated, iron oxide-rich microdigitate stromatolites make up multiple layers within several of the oncolites (PPL). (B) Same as (a) in XPL showing iron-rich (dark) and iron-poor (light) zones surrounding the microdigitate stromatolites (XPL). (C) Three individual growth phases, each ~500 µm high developed successively on top of one another. A dark iron-rich wall surrounds the stromatolites (XPL). (D) Backscatter image showing the iron concentrating in/around the microdigitate stromatolites. Note the sharp contact at the base of the stromatolites.

made up of minor carbonaceous material and cryptocrystalline hematite in microquartz. When present, wall structures are well developed and appear as dark zones around the stromatolite (Figure 68C). The contact between the stromatolites and underlying laminae is sharp. Figure 68D illustrates the accumulation of iron (white) in and around the microdigitate stromatolites.

The oncolite-grainstone contact ranges from sharp to gradational. Where sharp, it is defined by a 100 to 200 µm thick jasper layer delineating the oncolite-grainstone boundary.

More commonly the contact is gradational, with an increase in the number of grains trapped within the outer oncolite laminae. The grains consist of granules, ooids, coated grains, intraformational clasts and aggregate clasts surrounded by microquartz with abundant carbonaceous material imparting a cloudy brown appearance.

The grainstone surrounding the oncolites is compositionally diverse with the grain types mentioned above present in varying abundances. Generally, the grains are <1 mm in diameter, rounded to subrounded and contain jasper, magnetite and carbonate (Figure 69A). Grains with irregular, wavy laminae similar to those found in the oncolites are common in the grainstone often exhibiting asymmetrical laminae development from one side (white arrow, Figure 69A). Aggregate clasts, similar to those previously described at Whitefish and Mink Mountain are common. They are composed of multiple grains in a microquartz cement containing diffuse cryptocrystalline hematite. Overlaying the grains are multiple, subparallel, iron-rich laminae interspersed with quartz (Figure 69B). Subrounded fragments of oncolite/ stromatolite were also noted in abundance. They are composed of alternating light and dark laminae composed of iron oxide and quartz respectively (Figure 69C). The ooids examined all contain well developed cortical laminae around a jasper nucleus. The laminae are made up of thin hematite laminae which alternate with microcrystalline quartz. The quartz crystals are well defined and do not crosscut the hematite laminae (Figure 69D). Many of the ooids contain dehydration cracks which extend through multiple cortical laminae (Figure 69E).

Carbonate is ubiquitous in all samples examined, both within the oncolites and surrounding grainstone. The oncolites show a composition similar to that described in the VHD and Thunderbird samples, with varying abundances of ankerite, manganiferous-ankerite and

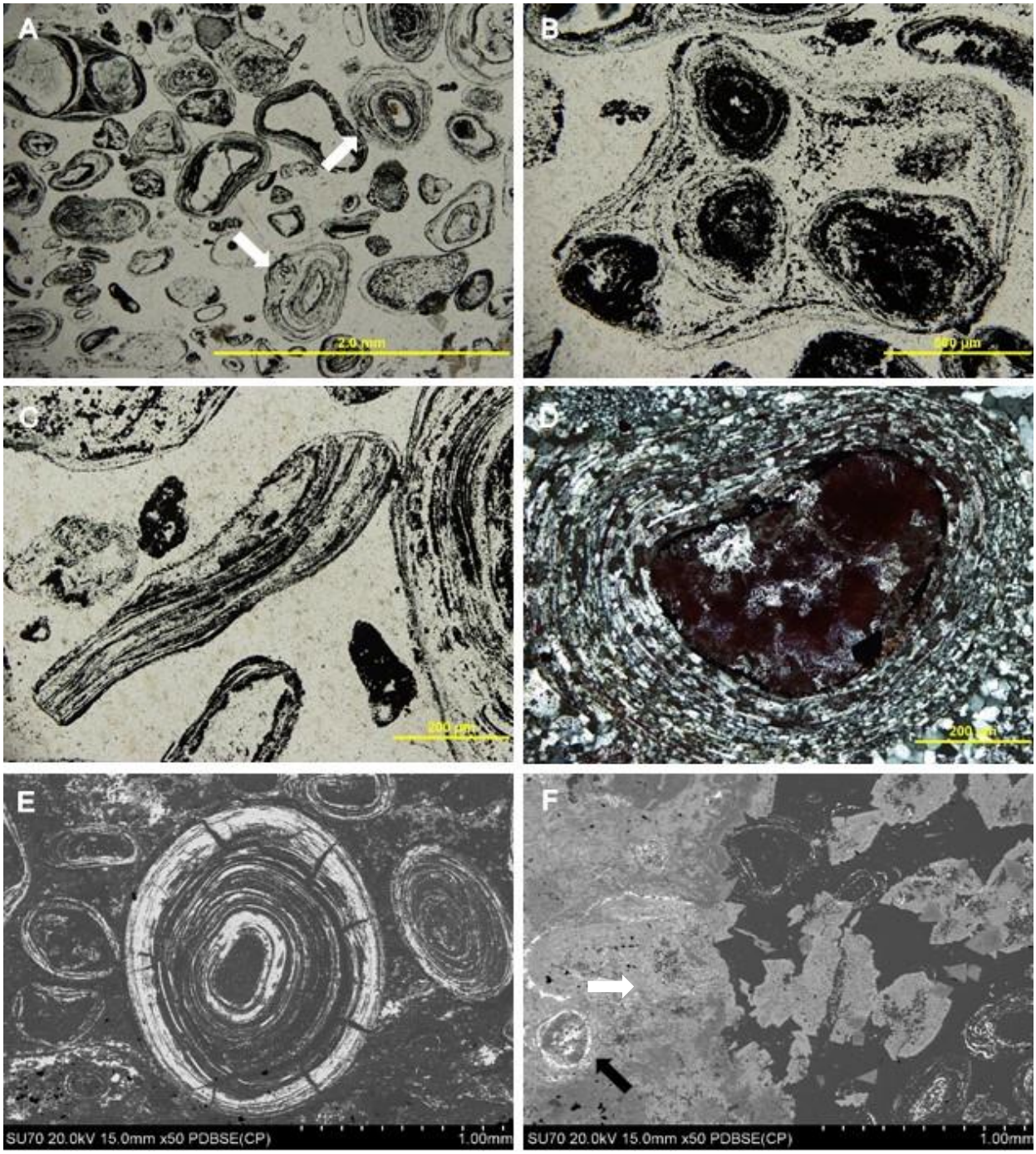

Figure 69. Grainstone features. (A) The grainstone surrounding the oncolites is compositionally diverse with varying abundances of ooids, granules, coated grains, intraformational clasts, aggregate clasts and micro-oncolites (white arrows), (PPL). (B) Aggregate clasts containing multiple grains cemented by microquartz containing cryptocrystalline hematite inclusions. Multiple subparallel iron-rich laminae coat the grain (PPL). (C) Fragments of laminated oncolite/stromatolite are common in the grainstone, exhibiting low angularity alluding to reworking prior to cementation (PPL). The ooids examined contain well developed cortical laminae surrounding a jasper nucleus. The quartz crystals are defined and do not crosscut the laminae boundaries (XPL). (E) Backscatter image illustrating dehydration cracks within hematite-quartz ooid. (F) Backscatter image of manganiferous ankerite (white arrow) replacing quartz. Note the residual hematite laminae (black arrow) within the micro-oncolite.

ferroan-rhodochrosite within the laminae. The grainstone contains zones of carbonate replacing the quartz cement. In Figure 69F manganiferous-ankerite (light grey) has replaced the quartz (dark grey), including a micro-oncolite. The iron-rich laminae (white) remain despite the pervasive replacement (black arrow).

Several spheres are present within a peloid (Figure 70). These spheres show a consistent diameter of 20 to 25 μm and occur in groups of three to five. They have a central core composed of quartz, surrounded by a thin iron-rich rim containing crystals ≤1 μm in diameter.

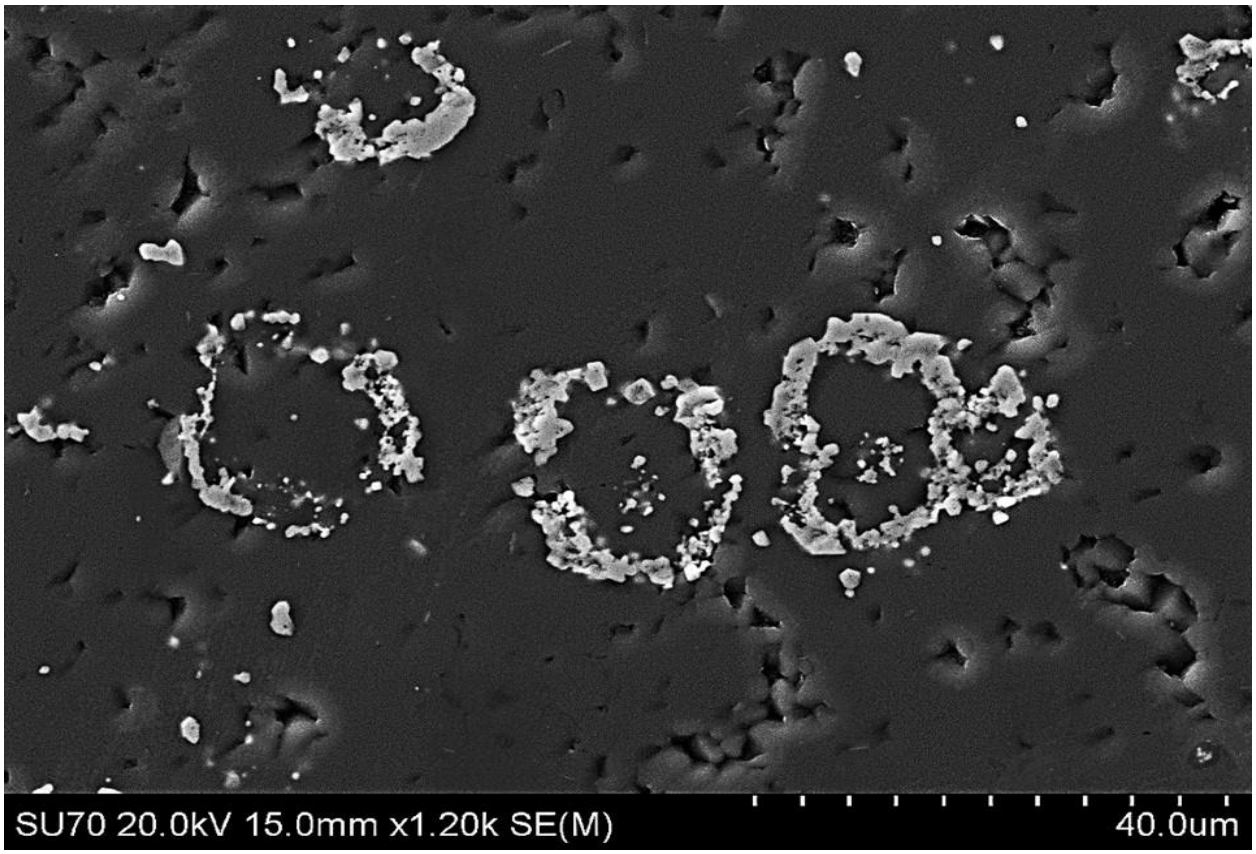

Figure 70. Iron-coated, 20 to 25 μm spheres within a peloid. They are composed of a central area composed of quartz, coated in an iron-rich rim of micron-scale crystals.

The ICP-MS measured REE contents for samples taken from the LWD-99-1 core were normalized to PAAS values and plotted (Figure 71). The samples selected for analysis consisted

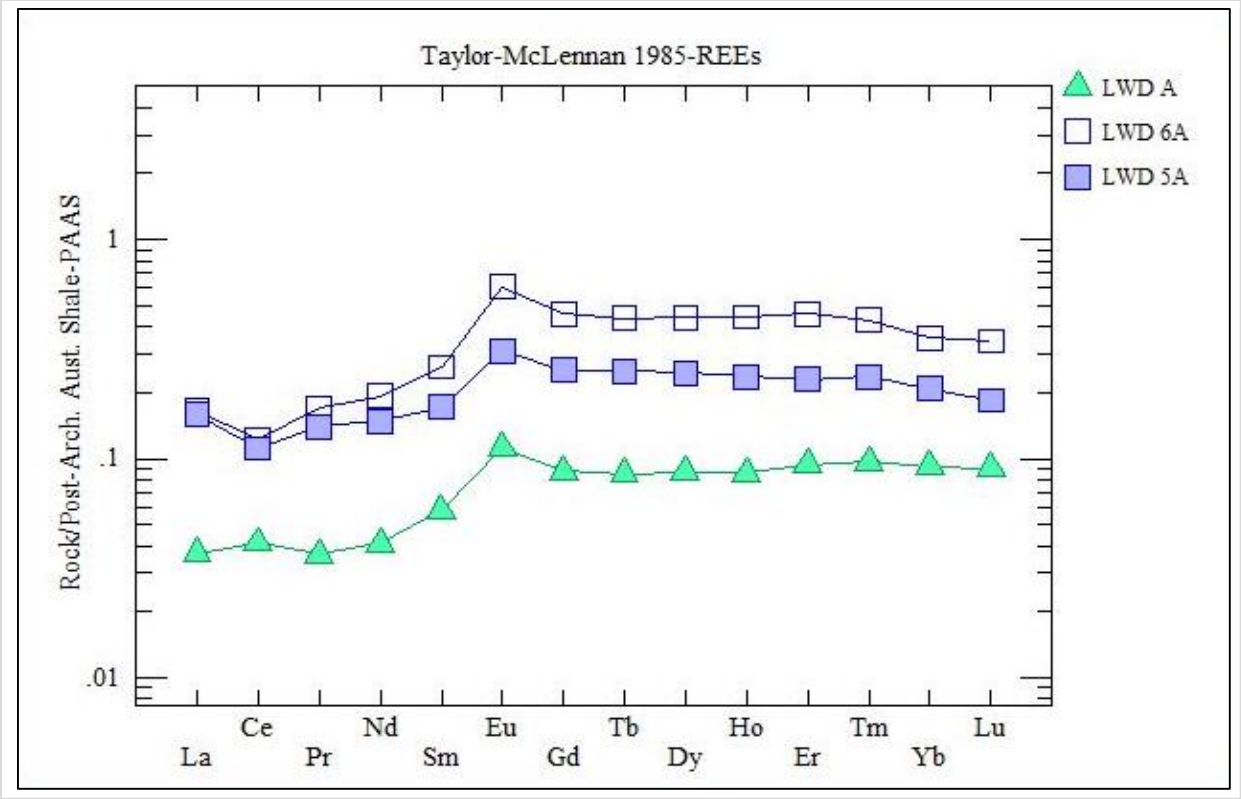

Figure 71. The PAAS normalized REE diagram for the LWD-99-1 core. Samples selected for analysis consisted of two manganiferous-ankerite oncolites (LWD-A, LWD-6A) and a jasper-rich wavy-laminated stromatolite (LWD-5A). LWD-5A and LWD-6A show a negative Ce anomaly, distinctly positive Eu anomalies and a slight depletion in LREE in relation to the HREE. LWD-A has a slightly positive Ce anomaly and distinctly positive Eu anomalies, with a depletion in LREE in relation to the HREE.

of two manganiferous-ankerite oncolites (LWD-A, LWD-6A) and a jasper-rich wavy-laminated stromatolite (LWD-5A). The LWD-5A and LWD-6A plots shows a consistent pattern with a negative Ce anomaly, a positive Eu anomaly and enrichment in the HREEs in relation to the LREEs . The LWD-A sample shows a slight positive Ce anomaly, a positive Eu anomaly and enrichment in the mid and HREEs in relation to the LREEs.

2.3.5.3 MGS-2

UTM 548449E, 5259726N 15N

Figure 72. Photograph of MGS-2 Core. The Upper Stromatolitic Unit is 110 cm thick, and consists of three distinct stromatolitic horizons separated by decimeter scale layers of chemical mud intercalated with medium-grainstone; white arrow indicates up direction, (a) is at the top of the section. (B) The basal stromatolites consist of columnar, stratiform and pseudocolumnar forms composed primarily of millimeter-scale jasper laminae alternating with cream to white chert. (C) The middle stromatolite contains well developed digitate forms overlain by stratiform mats containing abundant trapped grains within the laminae. (D) The top horizon contains chert rip-up clasts with rare centimeter-scale oncolites (white arrow).

The 691 m deep MGS-2 hole was drilled by the Minnesota Geological Survey 6 km southeast of Mckinley, Minnesota. No sampling was possible as a significant amount of the core had already been removed.

The Upper Stromatolitic Member is present in three sections totaling 110 cm (Figure 72A). The basal stromatolites directly overlie a fine-grained, iron-rich, magnetic, chemical mudstone intercalated with medium-grained peloidal grainstone. They consist of small (2 cm) columnar stromatolites overlain by 45 cm pseudocolumnar and centimeter-scale laterally linked digitate stromatolites (Figure 72B). Overlaying the basal stromatolitesis 10 cm of highly magnetic red chemical mudstone which is in turn overlain by 20 cm of stratiform and columnar stromatolites in a medium-grained grainstone (Figure 72C). Above this, 35 cm of rip-up clasts and rare centimeter-scale oncolites complete the stromatolitic section (Figure 72D). Jasper is the most common constituent of the stromatolites and oncolites, however, magnetite, hematite and carbonate are all present in varying abundances.

2.3.5.4 2627

UTM 578923E, 5275160N 15N

The 167 m deep 26-27 exploration hole was drilled by Northern Pacific Co. 15 km southwest of Babbitt, Minnesota, between the LTV and Northshore mines. Similar to the core previously described, only minimal sampling was possible due to the condition of the core and amount remaining in the box.

In the 2627 core, the Upper Stromatolitic Member occurs 44 m below the Limestone Member at the top of the Biwabik Formation. The 100 cm stromatolitic horizon contains stratiform and domal stromatolites at the base which overlie a coarse grainstone composed of jasper and chert rip-up clasts in a white chert cement (Figure 73A). The ~15 cm stratiform mat at the base consists of 2 to 4 mm thick undulatory laminae composed of hematite, quartz and minor carbonate. Centimeter-scale layers containing grainstone similar to that described below the mat

are present between the stromatolitic laminae. Above this, 85 cm of wavy, cream and dark green laminae alternate within laterally linked columnar stromatolites (Figure 73B). Overlying the stromatolites, 20 cm of oolitic grainstone caps off the section.

Figure 73. Photographs of stromatolites in the 2627 core. (A) At the base of the stromatolitic horizon, undulatory laminae 2-4 mm thick make up a 15 cm thick stratiform mat. The mat overlies coarse-grainstone containing abundant jasper rip-up clasts in a white chert cement (up direction to left). (B) Cream and dark green chert make up the stromatolites in the upper 100 cm stromatolitic horizon.

2.3.5.5 PR-98-1

UTM 578923E, 5275160N 16N

The PR-98-1 core was drilled ~4 km northeast of the Ontario-Minnesota border near Pine Bay. The core on contains a 74 cm section of the Upper Stromatolitic Member (Figure 74). This

is located roughly 40 meters below the Limestone Member at the top of the Gunflint. The base of the section consists of a medium-grained peloidal grainstone containing white and purple chert with thin (≤1 cm) magnetite layers. This is overlain by 24 cm of brecciated white chert grainstone containing centimeter-scale pink layers of ferroan-rhodochrosite bounded by

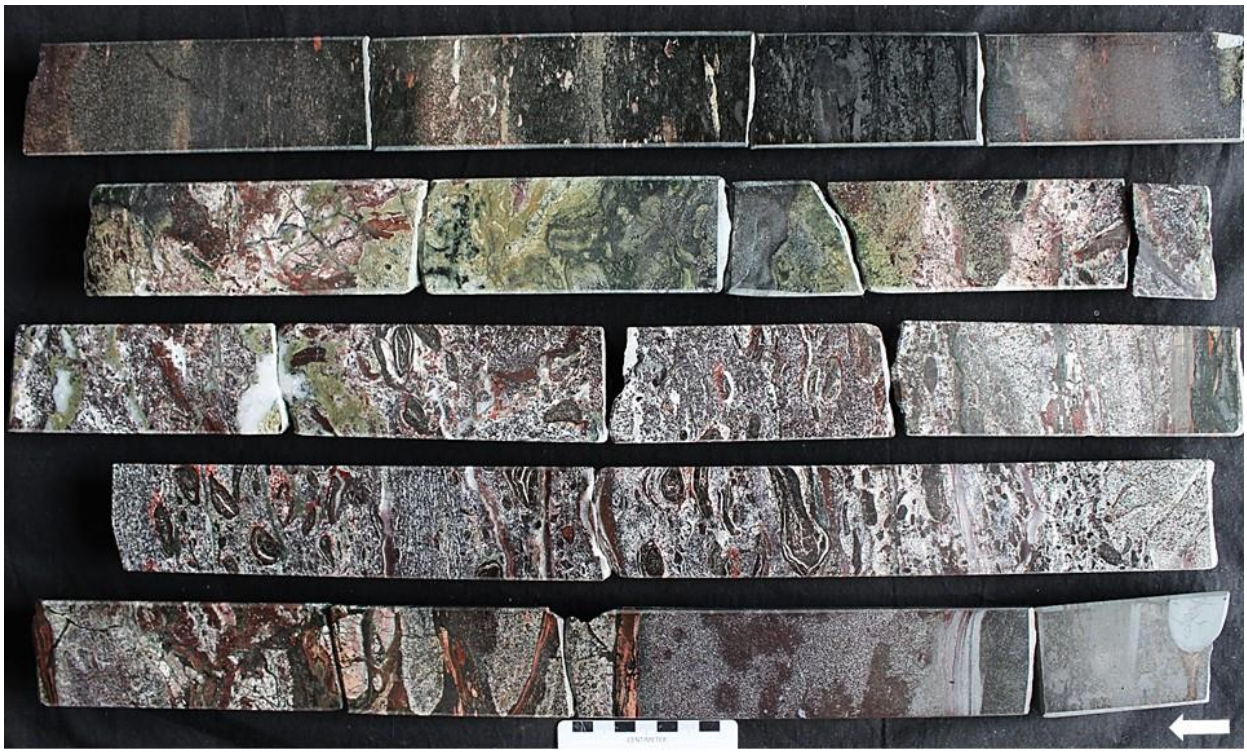

Figure 74. The PR-98-1 core contains a 74 cm section with iron-rich oncolites. The base of the section (white arrow facing in up direction) consists of typical Gunflint grainstone. It is overlain by a highly brecciated section, overlying the oncolites. The oncolites are overlain by thick green zone before being overlain by a medium-grained grainstone.

millimeter-scale magnetite laminae. Several centimeters of grainstone containing angular, shard-like grains in a white chert cement directly underlay the oncolites. The oncolites occur as either rounded or elongated iron-rich spheres in a magnetite-rich cherty grainstone. Overlying the oncolites is a 40 cm green zone containing highly irregularly bedding. A sharp contact separates the green zone and the overlying medium-grained, peloidal grainstone composed of chert and magnetite.

The oncolites occur as elongate or spherical structures composed of alternating white and dark laminae (Figure 75). The large (2 to 5 cm) elongate oncolites develop from magnetite or jasper rip-up clasts, and are subsequently surrounded by thin, discontinuous magnetite and quartz laminae (Figure 76A). Dehydration cracks extend through the oncolites. The magnetite and

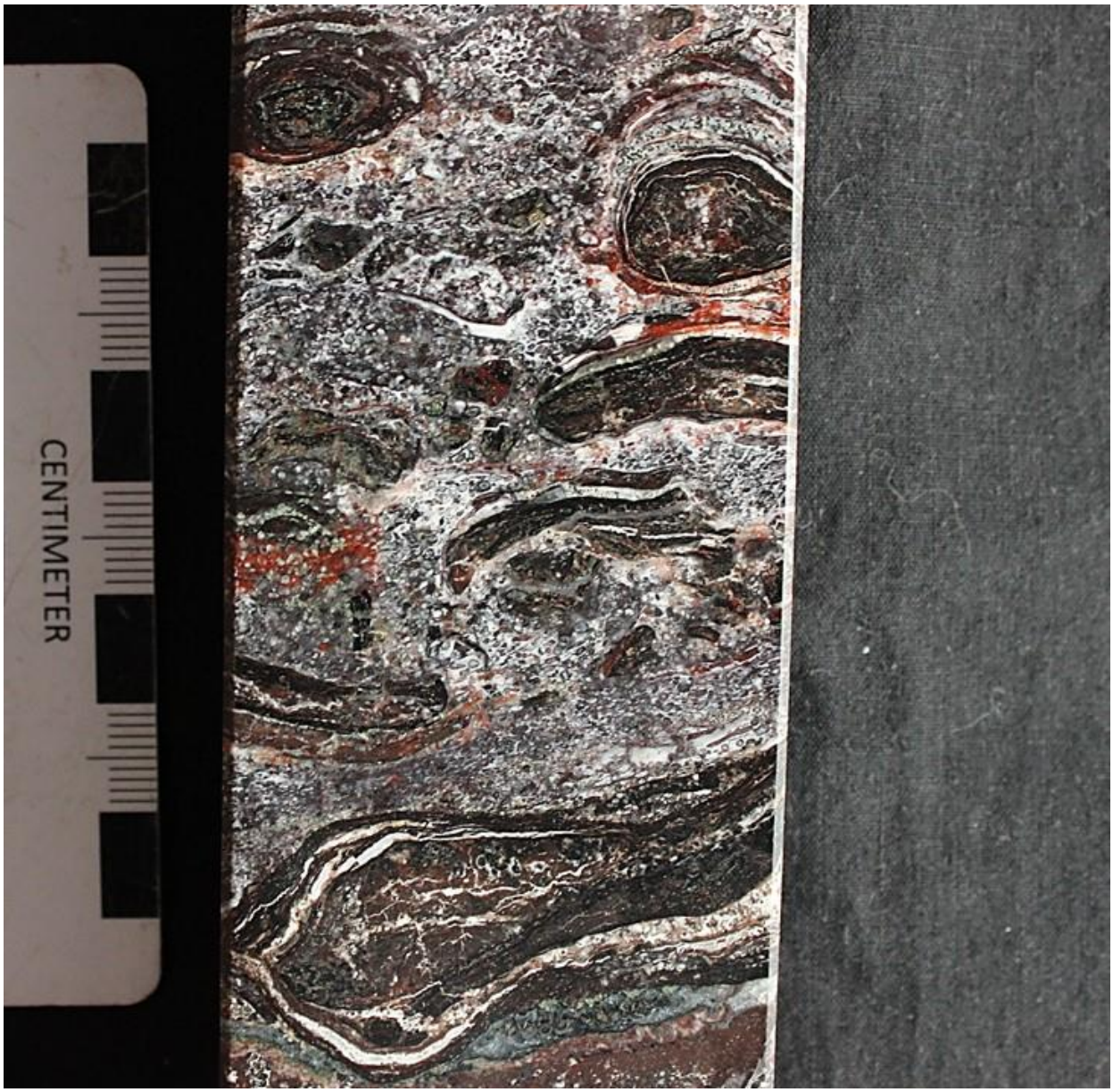

Figure 75. Two forms of oncolites are present in the PR-98-1 core. The elongate oncolites contain a nucleus of a jasper or magnetite rip-up clast containing dehydration cracks, surrounded by magnetite, chert, carbonate and iron silicate laminae. The spherical oncolites contain a nucleus composed of grainstone with asymmetrical laminae of magnetite and chert with minor carbonate and iron silicates.

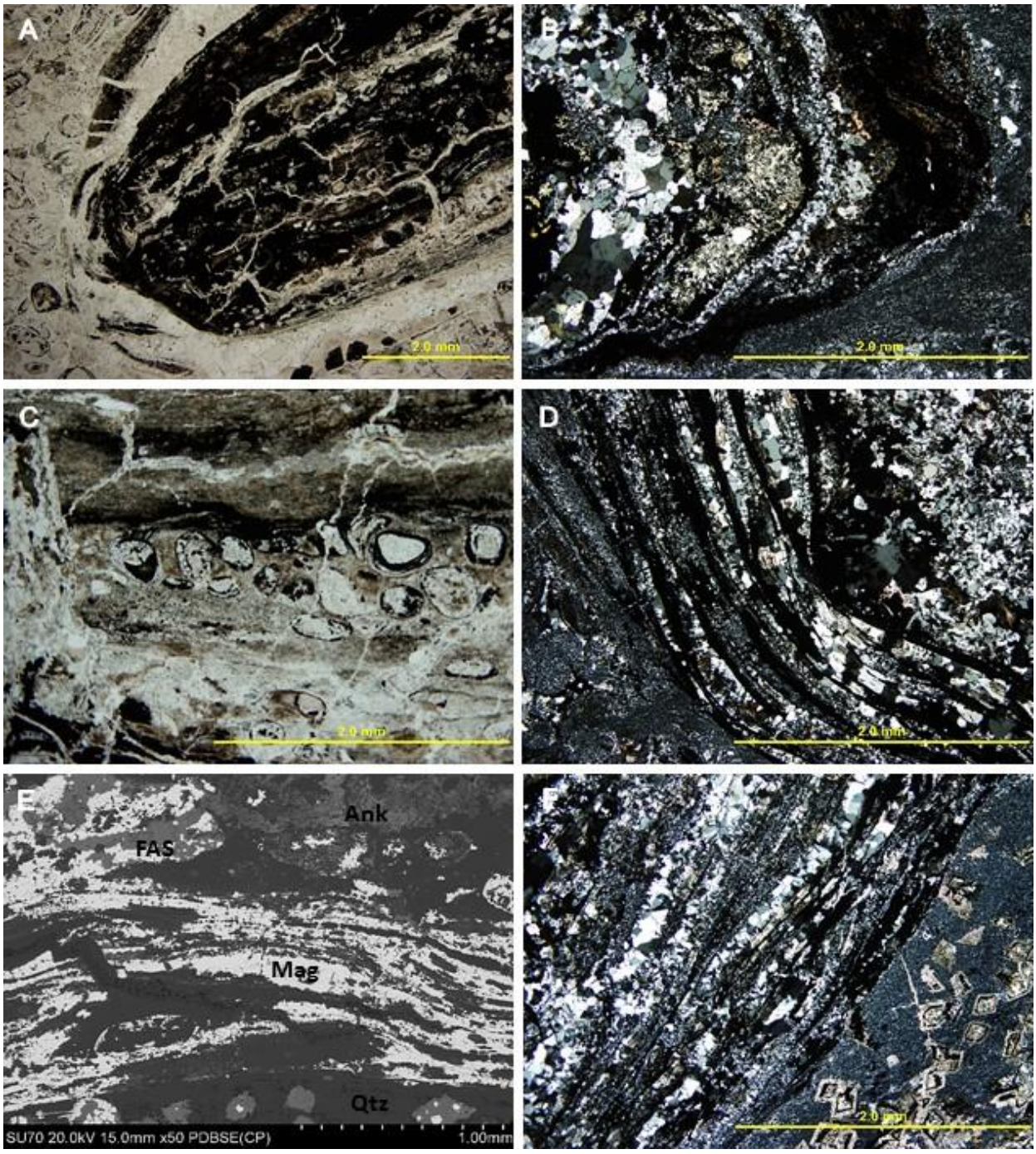

Figure 76. Photomicrographs of oncolite lamination. (A) Cross section through an elongated oncolite illustrating the magnetite-rich rip-up clast core surrounded by dark and light laminae composed of magnetite+ amphibole+ carbonate and quartz. Note the dehydration cracks throughout (PPL). (B) Iron-aluminum-silicates are regularly found within the elongate oncolites (XPL). (C) Coated grains trapped within the outer laminae of the elongate oncolites are common (PPL). (D) Subparallel lamination of magnetite (opaque) and quartz make up the spherical oncolites with only trace carbonate observed (XPL). (E) Backscatter image illustrating the compositional variation within the laminae. Magnetite (Mag) and quartz (Qtz) laminae are overprinted and replaced by an iron aluminum silicate (FAS) and ankerite (Ank). (F) Ankerite rhombs, rimmed by magnetite are present throughout the interspace (XPL).

quartz lamiae are often overprinted/replaced by zones of an iron aluminum silicate (Figure 76B). Abundant coated grains trapped within the outer laminae of the elongate oncolites are common. The coated grains contain a blocky quartz core with either jasper or magnetite defining their outer boundaries. The rounded oncolites contain a nucleus composed of peloidal grainstone containing grains of jasper, magnetite and iron silicate in a chert cement. Surrounding the nucleus, 100-to-200 μm thick magnetite laminae alternate with ~500 μm layers composed of megaquartz with minor carbonate (Figure 76D). The laminae are better defined and show a greater continuity than those of the elongate oncolites, however preferential asymmetrical laminae development on the top surface of the spheroidal oncolites was noted (Figure 75). Backscatter imaging illustrates the composition of the oncolite laminae (Figure 76E). Magnetite and quartz make up the majority of the oncolite, however, minor manganiferous ankerite and iron aluminum silicate are present throughout. The areas between oncolites is composed of a megaquartz cement between granules, ooids and rip-up clasts. Ankerite rhombs with a magnetite rim are commonly found near the edges of the oncolites (Figure 76F).

The ICP-MS measured REE contents for samples taken from the PR-98-1 core were normalized to PAAS values and plotted (Figure 77). The samples selected for analysis consisted of two elongate oncolites (PR98-6 LG, PR98-7 ONC), two spherical oncolites, (PR98-6 SM, PR98-11 ONC) and two samples of the cement (PR-7 CEM, PR98_11 CEM). The plot shows a consistent pattern among the six samples showing a distinct positive Ce anomaly and enrichment in the mid and HREEs compared to the LREEs.

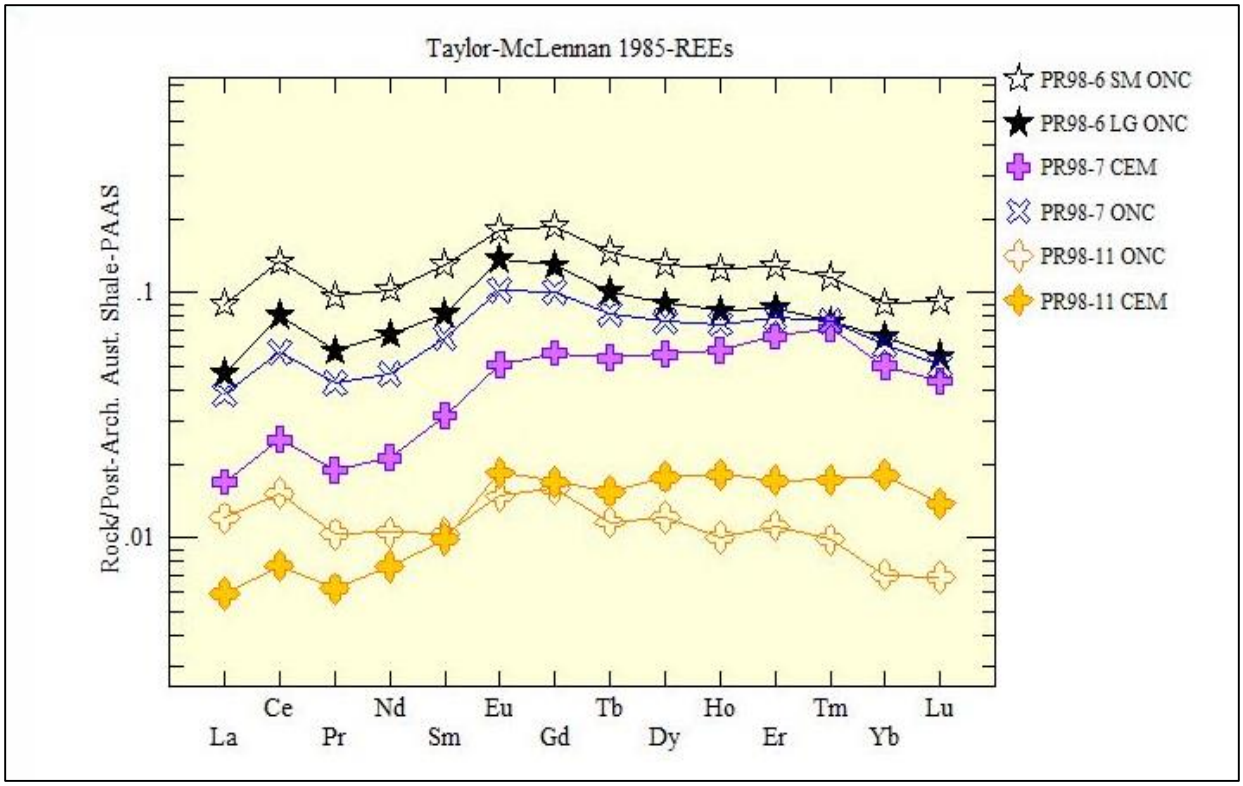

Figure 77. The PAAS normalized REE diagram for the PR-98-1 core. The samples selected for analysis consisted of two elongate oncolites (PR98-6 LG, PR98-7 ONC), two spherical oncolites, (PR98-6 SM, PR98-11 ONC) and two samples of the cement (PR-7 CEM, PR98-11 CEM). The plot shows a consistent pattern among the six samples with a distinct positive Ce anomaly and depletion in the LREEs in relation to the HREEs.

2.4 Limestone Member Stromatolites

Marking the top of the Gunflint and Biwabik Formations is the Limestone Member. The Limestone Member has a variable thickness ranging from tens of centimeters up to 6 meters. The primary carbonate stromatolites occurring within the Limestone Member are directly overlain by the Sudbury ejecta layer which in many cases overlie sheared off stromatolite domes (Figure 78).

Figure 78. Limestone Member domal stromatolite that has been sheared off by the Sudbury impact blast wave, with subsequent deposition of accretionary lapilli.

Three sites were selected for comparison with the iron oxide and silica-rich stromatolites of the Lower, Middle and Upper Stromatolitic units. The first location, is an outcrop on the side of Highway 588 where rock piles containing stromatolites and lapilli can be viewed in and ex situ. The second is an in situ outcrop on Hill Street illustrating the cabbage-shaped carbonate stromatolites. The final location is the "A" subunit at Northshore mine in Babbitt, Minnesota, which was thermally metamorphosed to marble, and does not contain any preserved stromatolitic structures.

2.4.1 Highway 588

UTM 306009E, 5357502N 16N

The stromatolites crop out over several meters along the side of the Highway 588, in Stanley, Ontario, 7 km southwest of the Stanley Inn. The stromatolites occur as decimeter-scale, cabbage shaped domes, made up of alternating dark and light laminae (Figure 79A). They are overlain by centimeter-scale accretionary lapilli. Figure 79B shows two domes which developed adjacent to one another and eventually merged into one larger dome. The dome on the right of the image is dominated by dark laminae consisting of very-fine grained chloritic ash which is intermittently interlayered with calcite cement. A close up image of the stromatolite on the left reveals a distinct difference in the development of the two domes. Unlike the relatively grain-free dome on the right, the stromatolite on the left contains zones of volcanic shards which appear to be agglutinated within the light carbonate laminae (Figure 79C). The agglutinated laminae alternate with millimeter-scale dark laminae composed of chlorite. In thin section the development of neomorphic spar can be seen fracturing the chlorite laminae (Figure 79D). A

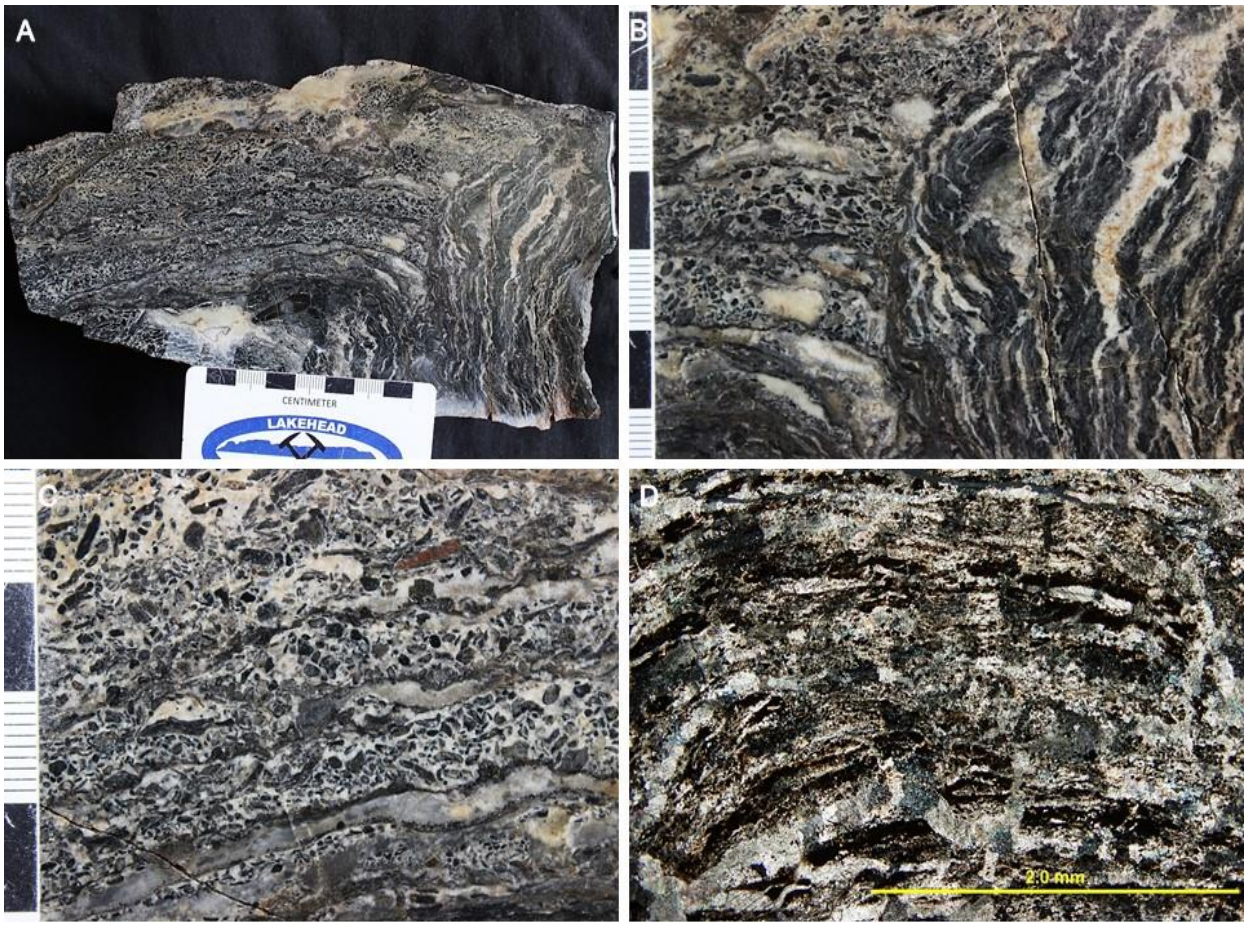

Figure 79. The primary carbonate stromatolites within the Limestone Member occur as decimeter-scale domes, made up of alternating light and dark laminae. (B) The merging of two adjacent domes with variation in laminar development. The dome on the right developed with a majority of chlorite-rich dark laminae with minor white carbonate laminae. However, the dome on the left contains abundant ash shards within the carbonate laminae. (C) Thin continuous chloritic ash layers alternate with thicker carbonate laminae containing agglutinated volcanic ash shards. (D) Layers of recrystallized primary carbonate alternating with thin, chlorite laminae (XPL).

complete absence of the iron oxides and quartz (jasper and chert), as well as the morphological differences highlight the difference between the stromatolites in the Lower, Middle and Upper Stromatolitic Members and these primary carbonate stromatolites at the Hwy 588 outcrop.

2.4.2 Hill Street

UTM 334405E, 5367076N, 16N

The Hill Street outcrop consists of an exposure roughly 5 m by 2 m located on a private driveway at the corner of Hill Street and Markland Street, Thunder Bay, Ontario. Multiple cabbage-shaped stromatolites tens of centimeters in diameter are present at this outcrop (Figure 80). As this site is on private property no sampling was permitted, and access is controlled by the owner.

Figure 80. The Hill St. outcrop contains multiple domal stromatolites. They occur as cabbage-shaped domes, tens of centimeters in diameter made up of calcite with thin ash layers. The development of multiple stromatolites in close proximity to one another caused them to coalesce.

The close proximity of the stromatolites during their development caused several of the individual domes to coalesce with adjacent domes creating large multi-dome stromatolites. Compositionally, the Hill St. stromatolites are the same as those described from Highway 588. They are composed of alternating light and dark laminae made up of calcite and chloritic ash respectively. As noted in the previous section there is a marked difference in the composition and morphology of the primary carbonate stromatolites at this site versus those found in the Lower, Middle and Upper Stromatolitic Member stromatolites, in particular the absence of iron oxides, jasper, chert, siderite and ankerite as well as the distinct crinkly laminae within the domes and the presence of blocky calcite cement.

2.4.3 Northshore Mine (Peter Mitchell)

UTM 576421E, 5278854N, 15N

The Northshore mine is located 8 km southeast of Babbitt, Minnesota off Forest Route 112. Entry to the property was provided by Cliffs Natural Resources. The Limestone Member is laterally continuous throughout the mine and comprises the "A" submember, however, contact thermal metamorphism has altered the limestone to marble. This member consists of a 0.5 to 1.5 m layer of marble containing 4 to 8 cm thick layers of wollastonite (Figure 81). It overlies the "B" submember compositionally dominated by magnetite, quartz, garnet, amphiboles and rare vesuvianite. Stromatolites are absent at this location, and in fact are not recorded in the Limestone Member south of the Canadian border. As noted in the two previous sections, there is a distinct absence of iron oxides, jasper, chert, iron silicates, siderite and ankerite in the Limestone Member.

Figure 81. The "A" submember at the Northshore Mine was thermally metamorphosed resulting in the development of marble with wollastonite. No stromatolites have been documented in this member south of the Canada border.

2.5 Modern Ferromanganese Nodules

Modern ferromanganese nodules were examined as these can provide one of the few modern examples of stromatolites built of precipitates rather than agglutination. They also represent iron and manganese precipitated in an environment with plentiful photosynthesizers and as such provide a possible analogue to Animikie stromatolites.

The growth and development of ferromanganese nodules occurs at redox boundaries where reduced iron-manganese-rich waters mix with oxygenated waters. This can occur when a diffuse flow of reduced groundwater, rich in ferrous iron and manganese, comes in contact with oxidized lake waters at or near the sediment-water interface (Kerkermeier, 2013). Conversely, upwelling of reduced basinal waters into oxygenated near shore surface waters can also facilitate their growth (Konhauser, 2007) .

2.5.1 Lake Superior, Ontario

Seven bays along the northshore of Lake Superior were surveyed for the presence of ferromanganese nodules (FMN). These included: Little Pigeon Bay, Little Trout Bay, Cloud Bay, Jarvis Bay, Squaw Bay, #5Bay, and Black Bay. Transects were run across each bay, using an underwater video camera for sample site selection. Sediment dredging and sampling was conducted along with multiple parameter probe readings of the water near the sediment water interface.

Despite several locations which had suitable physical characteristics for the development of FMN, none were found. The results of the dredging show that most of the bays contain a sandy to silty bottom (except Black Bay which was silt and mud), which transitions into a grey

clay basin-ward. Pebbles were common in most of the sediments. The multiprobe data showed the water near the sediment-water interface was oxygenated, with a pH range of 7.8 to 8.1.

2.5.2 Lake Charlotte, Nova Scotia

UTM 503545E, 4958545N, 20N

Lake Charlotte is located 70 km west of Halifax, Nova Scotia. Access to the lake is via Upper Lakeville Road with access to the bays and coves provided by private landowners. At the My Cove study site the lake bottom gradually slops out offshore. Nearest to shore the substrate was dominated by pebbles and boulder pavements. The substrate fines outwards towards the centre of the lake to medium and fine grained sand and further out silts and dense muds. The substrate on which the nodules were collected consisted of medium sand with a silt matrix at a depth of ~1.0 m. The nodules were covered on top by a 1 to 4 cm thick, green bacterial/algal mat. In many locations the growth of the nodules was so prolific that they formed a pavement-like layer underlain by sand.

The nodules occur as decimeter-scale concretions which can take multiple morphologies. However, most commonly they occur as concave disks forming concentrically around a central pebble or cobble nucleus (Figures 82A, 82B). A cross-sectional view through the nodules shows the development of millimeter-scale microcolumns (white arrow, Figure 82C) which grow from an iron hydroxide-rich layer below. The bottom surface of the nodules contains dense concentrations of millimeter-scale pustular growths (Figure 82D, 82E). These growths start as submillimeter spheres which accrete into the millimeter-scale pustular nobs. These growths develop on the bottom surface of the nodules slightly below the sediment-water interface.

Figure 82. Ferromanganese nodules form Lake Charlotte. (A) Top surface of a FMN showing the pustular growth habit of nodule. (B) Bottom surface of nodule in (a) showing the concentric growth pattern around a cobble nucleus. (C) Section through a FMN. Note the iron-rich basal zone (orange) underlying the dark upper layer. The upper layer is made up of millimetre-scale columns of alternating manganese and iron. (D) Pustular growth on bottom on FMN. Note these growths develop within the sediment, just below the sediment-water interface. (E) The pustular knobs start as submillimeter spheres which accrete forming larger spherical growths on the bottom of the nodule.

Microscopic analysis is difficult due to the abundance of opaque minerals (iron hydroxides and manganese oxides). However, some ultra-thin sections show the development of alternating light and dark zones composed of iron hydroxide-rich and manganese oxide-rich laminae respectively. The microcolumn (Figure 82C) growth occurs through the development of microcolumnar stromatolites (yellow arrows, Figure 83). The microcolumns develop outward in a radial pattern, consisting of <500 μm wide stromatolites. Accretion of multiple microcolumns causes the development of a microstratiform mat which again branches into microcolumns.

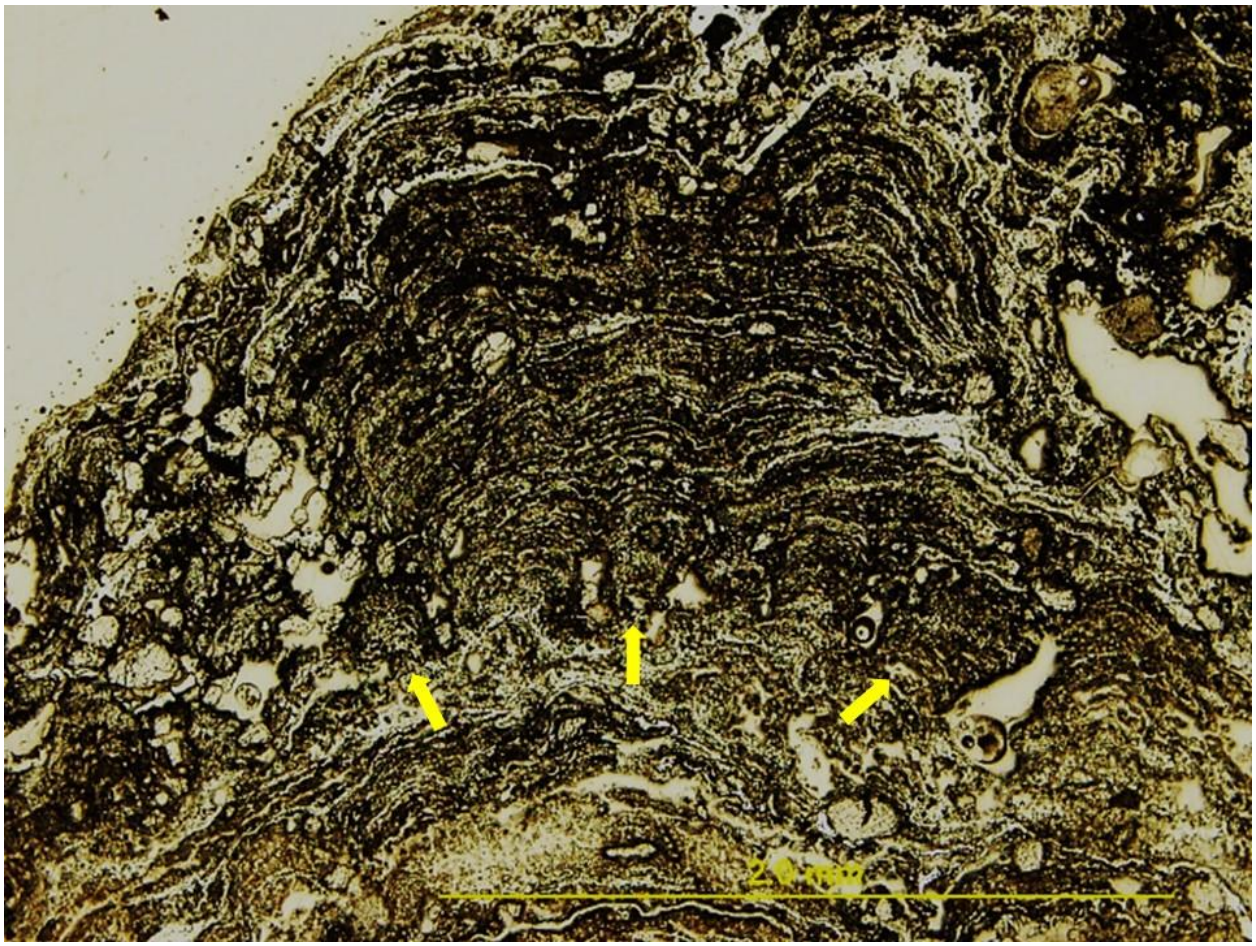

Figure 83. Microdigitate stromatolites. Photomicrograph illustrating the growth pattern within a cross section through a FMN. Note the microdigitate columns developing out in a spherical pattern. After several laminae have developed the microdigitate columns form larger stratiform laminae. The dark laminae are manganese oxides while the lighter laminae are composed of iron hydroxide.

Investigation with the SEM corroborates the petrographic observations that the FMNs grow through the alternate development of iron-rich and manganese-rich laminae. This is evident in backscatter analysis (Figure 84A) where the white laminae are composed of manganese oxides and the light grey are iron hydroxide. Elemental mapping further highlights this differentiation between laminae development. Areas containing abundant silicon indicate the presence of diatom frustules (Figure 84B), within the manganese-rich (Figure 84C) and iron-rich (84D) laminae.

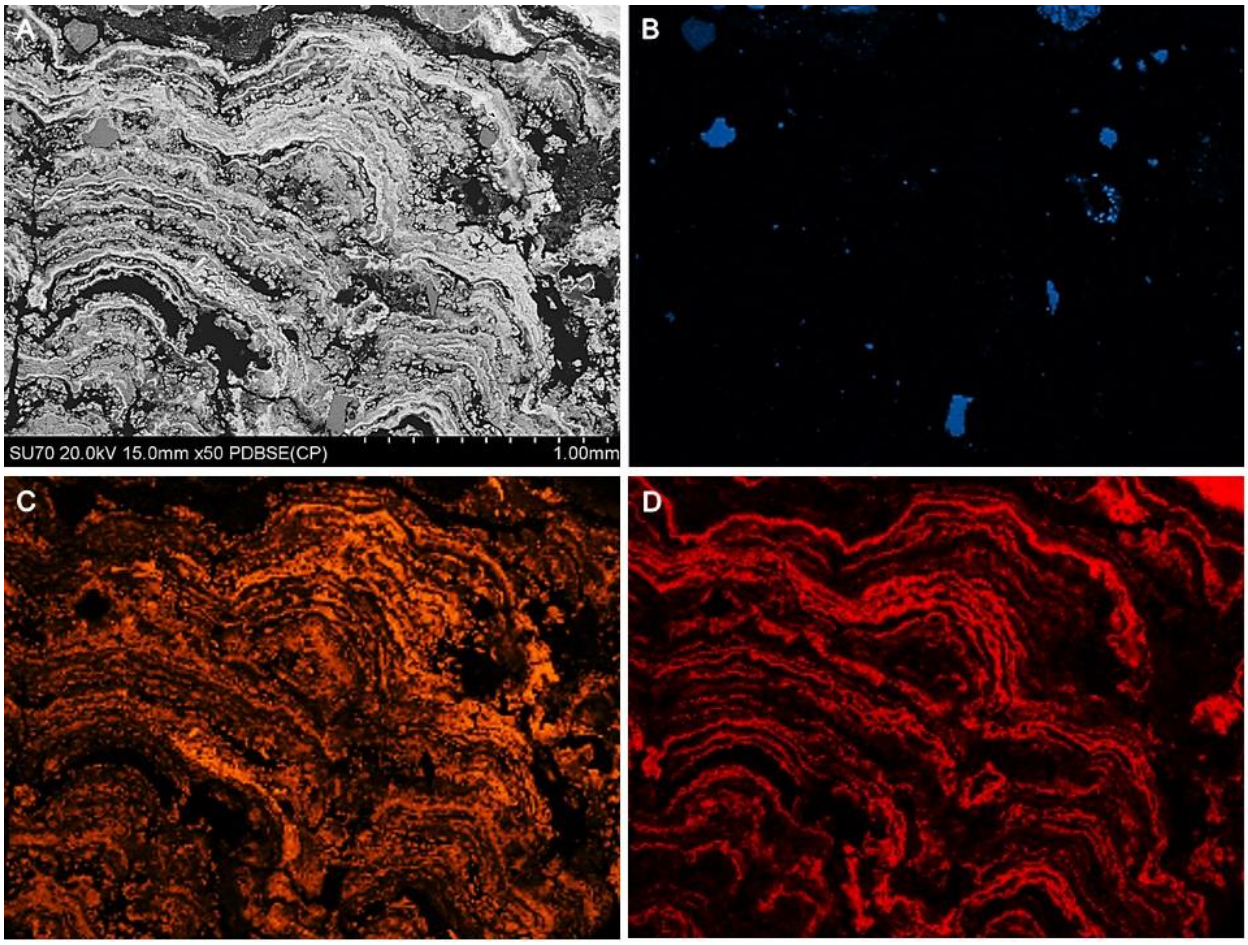

Figure 84. Elemental map of laminae within ferromanganese nodule. (A) Backscatter image illustrating the alternation between manganese (light)- and iron (dark)-rich laminae. (B) False colour image showing relative abundance of silicon. The high concentrations are caused by diatom frustules. (C) False colour image showing the relative abundance of manganese. (D) False colour image showing the relative abundance of iron.

Investigation of rock-chips broken from the upper and lower surfaces of several FMNs illustrates the intimate relationship that microbes play in their development. In the bottom surfaces of FMNs, rod-shaped forms, 1 μm in length and 500 nm in diameter are regularly embedded into iron hydroxide. Iron hydroxide can commonly be seen precipitating on the cell walls of the rods (white arrows, Figures 85A, 85B). The continued precipitation of iron hydroxides onto and around microorganisms leads to the complete encrustation of the cell as can be seen in Figure 85C. In this image two large (~5 μm) spheres are coated in iron hydroxide precipitate, and are joined by a smooth EPS later (white arrow). Furthermore, on the right side of the image, smaller (~500 μm) spheres are present embedded in the smooth EPS. Similarly, dense concentrations of rods 1 to 2 μm in length were observed in samples within the pustular growths from Figure 82D (Figure 85D). Rock chips taken from the top surfaces of FMNs revealed an abundance of microorganisms, dominated by diatoms. However, long chains of cyanobacteria, intertwined with the diatoms (Figure 85E) and fungal hypae with spores (Figure 85F) were also very common.

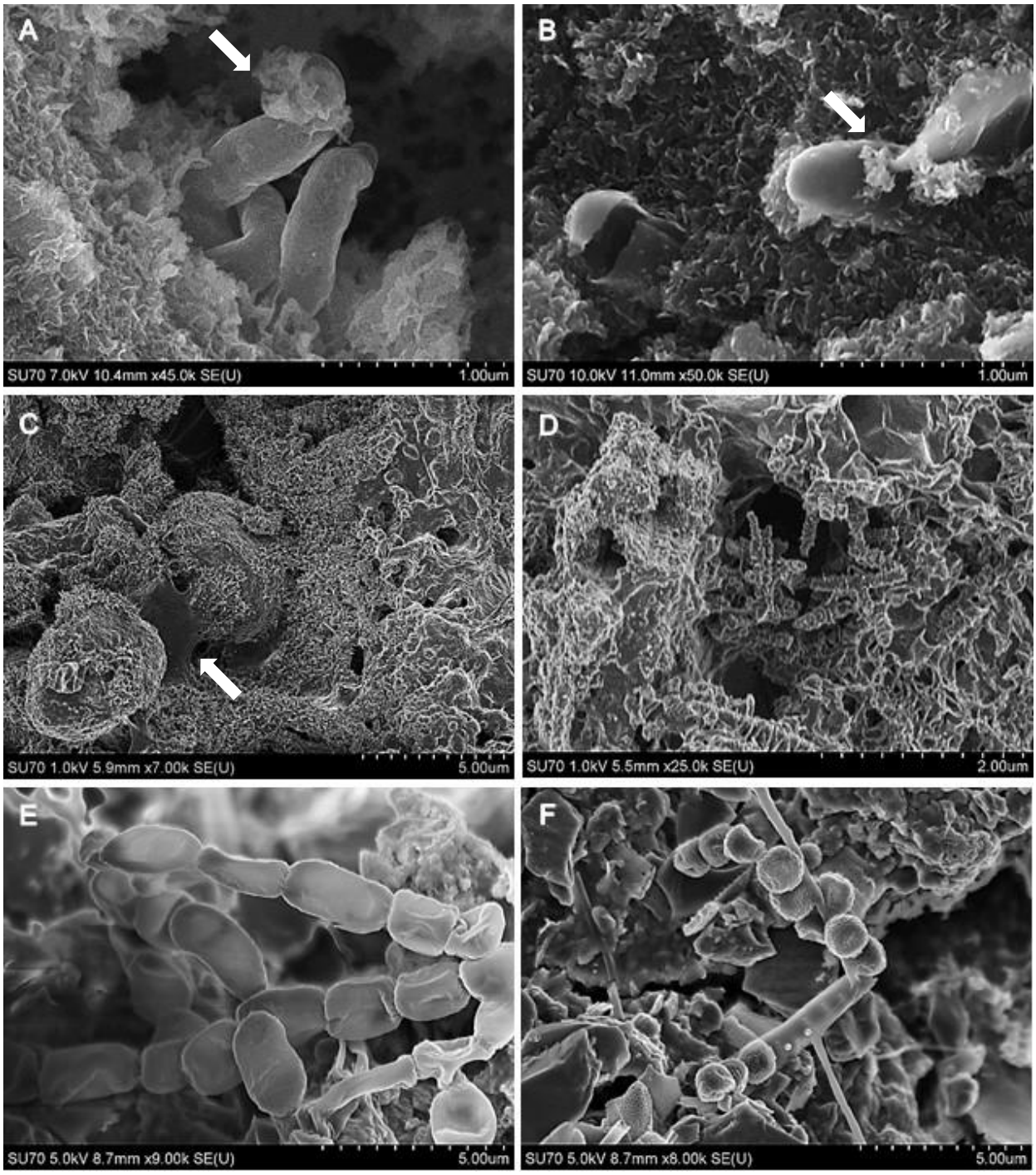

Figure 85. Secondary electron images of microorganisms within ferromanganese nodules. (A) Rod-shaped bacteria embedded into iron hydroxide matrix. Note the iron hydroxide precipitating on the cell wall. (B) Rod-shaped bacteria with iron hydroxide precipitate on cell wall. One cell has lysed exposing its interior. (C) Large coccus forms embedded in EPS coated in iron hydroxide and manganese oxide. Note the smooth EPS attaching the spheres (white arrow) (D) Rod-shaped structures completely coated in iron hydroxide. Note the smoother areas of EPS surrounding the rods. (E) Chain of cyanobacteria. (F) Fungi stock with spores attached to it surrounded by broken diatom frustules.

3 Discussion

3.1 Stromatolitic Members

The stratigraphic units containing stromatolites in the Gunflint and Biwabik Formations have traditionally been referred to as the "Algal Chert Facies" (Goodwin, 1956) or the Basal or Lower and Upper Algal Members. At the time of their discovery it was suggested that cyanobacteria played a significant role in their development (Cayeux, 1911; Tanton, 1926; 1931; Tyler and Barghoorn, 1954). At this time, cyanobacteria were incorrectly referred to as blue-green algae, resulting in the nomenclature of "Algal Members". As no conclusive algal affinities have yet to be discovered in the Gunflint and Biwabik formations, it is proposed here that the units containing stromatolites are referred to as the Lower, Middle and Upper Stromatolitic Members.

The commonly recognized division of a Lower, Upper and Limestone Member stromatolites is more complex than first believed. The examination of 12 drill core sections through the Gunflint and Biwabik shows that the stromatolitic members occur at appreciably different stratigraphic locations in the two ranges. Within the Gunflint, three distinct stromatolitic units are present; the Lower Stromatolitic Member located at the base of the Gunflint overlying Archean rock and the Kakabeka Conglomerate, a second Middle Stromatolitic Member 45 to 50 m up from the base, and a third newly described Upper Stromatolitic Member located ~40 below the Limestone Member at the top of the Gunflint. The newly defined Upper Stromatolitic Member consists of oncolites in the PR-98 core and is correlative to the stromatolitic horizon in the Upper Cherty of the Biwabik.

Within the Biwabik, the Stromatolitic Members are less defined. The Lower Stromatolitic Member occurs consistently throughout the Mesabi Range with only rare absences. Additional stromatolitic "horizons" have been described, rarely occurring at the top of the Lower Slaty, and in various locations within the Upper Cherty (Gunderson and Schwartz, 1962). Severson *et al.* (2009) provide a detailed correlation of the Biwabik Formation produced from logging multiple drill cores and mines along the Mesabi Range. Based on their work, the stratigraphic location of the Middle Stromatolitic Member in the Gunflint corresponds to an irregularly bedded and/or mottled pink unit which lies 45 to 50 m above the Pokegama-Biwabik contact. The Upper Stromatolitic Member is continuously present from Hibbing, Minnesota north to the Duluth Complex.

One possible explanation for the absence of the Middle Stromatolitic Member in the Biwabik is the lack of a suitable substrate for stromatolite development. In a recent review, Ginsberg and Planavsky (2008) postulate the large domal stromatolites found in modern carbonate systems require a stable, solid surface for accretion to occur. In areas lacking a cohesive substrate (i.e., unconsolidated sediment such as sand) large domal and columnar stromatolites tend not to develop. Similarly, Fralick (1989) noted that the stromatolites at the Current River location grew on a silicified, stabilized substrate and/or on large boulders of the basal contact in the Lower Stromatolitic Member which provided a stable substrate for stromatolite growth. Moreover, the limited spatial extent of the stromatolites in the Gunflint Formation was due to the occurrence of current activity causing the offshore granular substrate to be unstable (Fralick and Barrett, 1995). The necessity for a stable surface is corroborated in this work by the observations of stromatolitic growth directly on the peneplain Archean basement (Figure 4), large cobbles (Figures 9C, 53C), brecciated lithified grainstone (Figure 31), and

pebbles (Figures 26D, 38E, 54F). Furthermore, the stromatolites observed in this study are closely associated with zones of intraformational chert mud rip-ups. The rip-ups were most probably formed during low water conditions of a minor regression. The increased energy caused by lower-than-normal ocean levels would cause an increase of the normally subtidal zones creating the composite grains described in this work. Work conducted by Fischer and Knoll (2009) suggests that intraformational conglomerates often mark sequence-boundary exposure surfaces, further corroborating the theory of a regression.

Multiple samples containing a jasperlitic microbial mat were observed in this study, often containing a one- to two-grain-thick layer of sediment surrounded by microbial mat (Figures 26A, 32B, 38B, 39C, 41E, 46). In modern systems, established microbial communities containing cyanobacteria, sulphur bacteria and iron oxidizing bacteria are able to stabilize surrounding sediment through the development of a microbial mat (Burgos *et al.,* 2012). Laboratory experiments have shown that stabilization of the surrounding sediment by cyanophytes can occur in as little as 12 to 24 hours (Paterson *et al.,* 2008).

If the growth of stromatolites is dependent on a stabilized substrate as suggested, the lack of Middle Stromatolitic Member stromatolites in the Biwabik would indicate an area of deeper water within the Animikie Basin. This would preclude the development of a hardground due to subaerial exposure as has been shown to have occurred in the Middle Stromatolitic Member in the Gunflint Formation (Yip, 2015). Furthermore, the close association of the stromatolites and abundant intraformational chert mud rip-ups observed in this work bears a striking similarity to similar deposits described by Fischer and Knoll (2009). They suggest that intraformational conglomerates often mark sequence-boundary exposure surfaces.

3.2 Grainstone Features

The mineralogy and composition of the grainstone surrounding the stromatolites in all three units is morphologically and mineralogically diverse. Ooids, granules, aggregate grains, and rip-ups clasts are composed of several minerals including chert, jasper, greenalite, hematite, magnetite, siderite, ankerite with minor amounts of iron silicates, iron-aluminum silicates, and manganiferous carbonates.

At Kakabeka Falls, the conspicuous absence of grains trapped within the laminae of the large domal stromatolite, as well as the banking up of the ankerite grainstone against the dome imply that the dome was fully developed prior to the deposition of the grainstone. Had the stromatolite been actively growing at the time of grainstone deposition, grains would have been incorporated into the lamina as is seen in the Middle and Upper Stromatolitic Member (e.g., Figures 24C, 38B, 79C). Furthermore, the infilling of cracks with ankeritic grainstone, from which crosscut laminae within the basal stratiform mat (Figure 5C) indicates the mat was at least partially indurated prior to grainstone deposition.

At both Kakabeka and Current River, pebble- to cobble-sized angular fragments of eroded siliceous stromatolite are embedded in the surrounding grainstone (e.g. Figures 5D, 7A. 34D). Had the stromatolites at these locations been initially composed of carbonate, it would be reasonable to assume varying levels of replacement between the fragments and the domes which they were broken off. In fact, the fragments are composed of the same alternating light and dark chert laminae as the stratiform mat and domes. Furthermore the silicification of the grainstone immediately adjacent to the fragments and domes (Figures 5B, 6B, 35B) alludes to a primary origin for the chert. The possibility of the chert fragments being diagenetic chert nodules is

unlikely. In the Hamersley Basin, Australia, chert pods occur within iron formation as oblate spheroids or ovals elongated parallel to bedding, containing laminae with differential compaction (Trendall and Blockley, 1970; Fischer and Knoll, 2009, Figures 5G, 5H). Furthermore, diagenetic chert nodules often contain depositional textures similar to the initial carbonate, and occur as lenses, beds or rounded pods (Maliva *et al.,* 2005). The angular fragments described in this work do not show any of these characteristics.

At the Schreiber Channel and Whitefish Falls locations ooids composed of alternating cortical laminae of white chert and jasper are intermixed with ooids and granules containing reduced iron and carbonaceous material as well as carbonate granules and fragments of eroded stromatolite laminae (e.g., Figure 11B-11D, 16C-16D). It is doubtful that the complex mineralogy of these grains is the result of carbonate replacement. More likely, it is the result of sediment transport due to storm events (Pufahl and Grimm, 2003) or tidal reworking (Ojakangas *et al.,* 2001). Pufahl and Grimm (2003) suggest that the variation in mineralogy of the cortical laminae of coated grains can be explained by the agitation of grains on a platform floor containing opal-A and iron hydroxide gel muds. As the grains are moved across the floor, nucleation of the iron onto amorphous silica results in thin laminar development. Furthermore, they note that changes in the Eh and saturation of pore waters can play a pivotal role in grainstone mineral development just below the sediment-water interface. Dimroth and Chavel (1973) proposed a similar mechanism for the development of the complex internal structures and mineralogy of intraclasts and ooids in the Sokoman Formation. They evoke a system where silica- and iron-gels precipitate out onto the basin floor. Reworking and fragmentation of the sediment after induration results in the development of chert and jasper intraclasts which were further transported and deposited.

It is important to note, particularly in the Lower Stromatolitic Member of the Gunflint Formation, that the higher energy in this system could provide a means for the grains to have multiple origins, allowing for grains composed of primary carbonate, silica and/or iron to be transported and intermixed. Thus, the ooids and stromatolitic laminae described by Sommers *et al.* (2000) as evidence for replacement of carbonate by silica, may in fact be primary. The syndeposition of carbonate and amorphous silica nanoglobules can be a precursor to the formation of aragonite in some modern silica-rich systems (Kermer *et al.,* 2012). The recrystallization of the carbonate nanoglobules into aragonite needles is dependent on silica and carbonate saturation of the surrounding water. Therefore, early carbonate development can be impeded by the oversaturation of silica (Kermer *et al.,* 2012). This could lead to the development of trace carbonate rhomb ghosting as noted by Sommers *et al.* (2000).

Interestingly, the abundance and size of aggregate grains and mud-chip rip up clasts is notably larger in the Lower and Upper Stromatolitic Members than in the Middle Stromatolitic Member. The millimeter-scale aggregate grains are composed of closely spaced, multiple grains (granules, ooids and rare stromatolite fragments) bound by an iron-stained microquartz cement (e.g., Figures 17A, 17B, 27A-27D, 69B). There is a notable decrease in intergranular porosity between the aggregate grains and the grainstone in which they are contained. This indicates a greater compaction prior to cementation than what was occurring during their reworking (Simonson, 1986). The aggregate grains are often concentrically laminated by multiple iron-rich cortical laminae. The laminae show a distinct drape between nuclei (Figures 17C, 69B), with a grumulose texture internally. These clasts bear a striking similarity to grapestones forming in modern carbonate environments.

The primary nature of the iron-silica-rich stromatolites and surrounding grainstone is further supported by the presence of septarian cracks found within grains and stromatolitic material (Figures 28E, 28F, 39C, 69E) and oncolites (Figures 59D, 60, 63A-63C). The cracks crosscut the cortical lamination of ooids, develop as cracks in the centres of greenalite granules, and interestingly crosscut the chert and iron-rich laminae of oncolites. Similar structures in granules and ooids from the Sokoman Formation were described by Simonson (1986). The cracks were interpreted as shrinkage cracks caused by the dehydration of silica- and iron-rich gels inferred to be the precursor minerals of the jasper and chert that make up the granules and ooids.

Additionally, septarian cracks found in granules and ooids in the Frere Formation, Western Australia were also attributed to dehydration (Akin *et al.,* 2013). In their work they put forth a suboxic and anoxic paragenesis model to explain the deposition of opal-A, iron (oxyhydr)oxides as well as siderite and amorphous Fe-, Mg-, Al-silicates. They suggest these precursor phases occur syndepositionally with chert-chalcedony-quartz or hematite-magnetite. Furthermore, Frost *et al.* (2007) have suggested that the blocky quartz found within granules (Figure 28D) is due to diagenetic alteration of greenalite to quartz. Maliva *et al.* (2005) point out that septarian dehydration cracks are not found in known Phanerozoic carbonate-replacement cherts or in intraclastic and oolitic carbonates. This is due to the nonhydrous nature of carbonate precipitates.

The most abundant grains in the stromatolitic horizons are granules consisting of either greenalite (Figures 28D, 39C, 41E) or hematite (Figures 28A, 50) and ooids composed of alternating cortical laminae composed mostly of hematite and quartz Figures (28E, 50D, 69D,

69E). The primary nature of the iron and silica in these grains is further supported by the discovery of a modern unconsolidated iron ooid factory off the coast of Mahengetang, Indonesia (Heikoop *et al.,* 1996). In this system, diffuse upflow of cool (25-45°C) hydrothermal waters into the overlying ocean contain adequate concentrations of iron and silica to promote the development of iron ooid shoals. The 1 to 3 mm ooids are composed of finely laminated, alternating cortices composed of iron oxides or hydroxides which have nucleated around andesitic rock fragments. They bear a striking similarity to the ooids described in this research (see Figure 4; Heikoop *et al.,* 1996).

The rounded sand-sized granules of greenalite and hematite most probably represent reworked authigenic chemical muds precipitated as opal-A and iron hydroxides, with later diagenetic alteration to hematite/magnetite and quartz (Beukes and Klein, 1990; Pufahl *et al.,* 2014). Interestingly, Knoll and Simonson (1981) reported the presence of microfossils within reworked granules of the Sokoman Iron Formation (similar to Figures 18F, 25A, 62, 70). The microfossils were often found truncated at the granule boundary. They postulate that the granules represent intraclasts formed through the erosion of previously deposited chemical muds followed by abrasional rounding.

3.3 Microfossils

The method of preservation of the microfossils described in this research provides insight into the minerals initially precipitated within and onto the stromatolites, thus providing evidence of the primary nature of the iron-rich siliceous stromatolites. In addition, this information provides further understanding of the ecosystem structure of the Gunflint microbiota and the

environments which they inhabited. The preservation of the microfossils in the iron-poor chert in the Lower Stromatolitic Member (Figures 12B, 12D) is in stark contrast to the iron oxide coated microfossils in the Middle and Upper Stromatolitic Member (Figures 20, 27, 34, 35D, 54, 61). Interestingly, at the Whitefish location, microfossils were scarce to non-existent in the white and grey cherts but abundant in the red jasper (only found at this location). These observations are important as they suggest the ecological structure, environment of growth, or postdepositional alteration was different in the three Stromatolitic Members.

The determination of the ecosystem structure of Paleoproterozoic microfossil assemblages has been highly debated since their initial discovery (Barghoorn and Tyler, 1965). This has resulted largely from the difficulty of assigning metabolic activity based on morphology as both groups of microorganisms can have similar morphologies (e.g. filiments, spheres etc). However, a morphological distinction in the microfossil assemblage from the peritidal carbonates in the Belcher Islands Group, Nunavut (Golubik and Hofmann, 1976) and the intertidal zone of the Bitter Springs Formation, Australia (Schopf, 1968) versus the more diverse Gunflint microfossils has been recorded (Barghoorn and Tyler, 1965). The morphological dissimilarity lead Golubik and Hofmann (1976) to posit that environmentally and/or metabolically distinct communities were responsible for the development of the stromatolites. Moreover, their exceptional preservation was the direct result of encasement and permineralization by amorphous silica of living cyanobacteria (Schopf, 1968).

It is important to note that cyanobacteria and iron metabolizing bacteria are both capable of causing the precipitation of silica and iron on and around their cellular structure. However,

they do it through different mechanisms. Equation (1) represents the photosynthetic metabolic reaction of cyanobacteria:

$$6CO_2 + 6\ H_2O \xrightarrow{light} C_6H_2O_6\ + 6O_2 \qquad (1)$$

In this simplified reaction, the cyanobacteria remove carbon dioxide from the surrounding environment and produce oxygen gas. The increase in O_2 surrounding the cell drives oxidization of ferrous iron, causing the indiscriminate precipitation of ferrihydrite nanospeheres onto the slightly negative cellular material (e.g., sheaths, cell wall, EPS, etc,) (Konhauser, 2005). This reaction would support Cloud's (1973) hypothesis that nearshore 'oxygen oases' were responsible for the deposition of BIF. This hypothesis is corroborated by experimental results on extant cyanobacteria which show that for the quality of preservation found in the Gunflint microbiota to occur, silicification needs to take place in the first 10 to 12 days after cell death (Bartley, 1996). These results are supported by investigation of stromatolites developing in modern iron- and silica-rich systems.

The growth of stromatolites in Niuafo'ou Lake, Tonga, indicates that stromatolites containing cyanobacteria coated with opal nanospheres are remarkably well preserved, whereas recrystallization of carbonate nanoglobules into larger crystals of aragonite destroys the cell structure to the point where the cell morphology is no longer identifiable (Kermer *et al.,* 2012). Similarly, transmission electron microscopy (TEM) analysis of modern stromatolites from Frying Pan Lake, New Zealand, have shown that the nucleation of authigenic opal-A on cyanobacterial sheaths occurs as nanoglobules ~100 nm in diameter, which develops into a thick silica coating (Sanz-Montero *et al.,* 2008).The investigators suggest that the EPS preferentially binds silica (and carbonate) allowing for bacterial preservation.

Moreover, TEM analysis of microbial mats in three chemically distinct, silica-rich hot springs by Konhauser and Ferris (1996) revealed distinct bacterial communities encased in silica. In one microbial mat, filamentous bacterial cells were found covered by a several micron thick layer of amorphous silica nanospheres (Konhauser and Ferris, 1998; Figure 1). Similarly, rod-shaped bacteria with silica nanospheres embedded into an iron-rich capsule were noted in a mat with an unidentified filamentous bacteria coated in an amorphous iron-silica precipitate with fine-grained spheroids of ferric hydroxides. These results suggest that in silica-iron rich waters, vastly different communities of microorganisms can develop, and are preserved by different mechanisms. Furthermore, the probable lack of silica-secreting organisms during the Paleoproterozoic (Maliva *et al.,* 2005) would have resulted in oceans close to or at saturation with respect to amorphous silica (Siever, 1992).

The presence of dense concentrations of hematite coated microfossils is particularly important, especially at the Mink Mountain and Old School Road locations. It suggests the stromatolites in the Middle Stromatolitic Member developed in a different environment than the Lower Member previously described, or are composed of communities of iron-oxidizing bacteria that developed at a chemocline between upwelling deep, suboxic, ferruginous basinal waters and the upper oxidized surface ocean. The precipitation of iron onto microbial cell walls, sheaths, or EPS can occur through two unrelated processes (Konhauser and Riding, 2012). The first process was described in Equation (1), and is considered passive. However, the second process occurs through the active oxidation of ferrous iron due to direct metabolic activity.

$$2Fe^{2+} + 0.5O_2 + 2H^+ \rightarrow 2Fe^{3+} + H_2O \quad (2)$$

$$4Fe^{2+} + CO_2 + 11H_2O + hv \rightarrow 4Fe(OH)_3 + CH_2O + 8H^+ \quad (3)$$

In this way, communities of chemolithoautotrophic bacteria (Equation 2) such as *Gallionella, Leptothrix* and *Crenothrix* or photoautotrophic bacteria (Equation 3) such as green and purple sulphur and purple non-sulphur bacteria are able to cause the precipitation of ferric iron through the use of ferrous iron to fix carbon (Konhauser and Riding, 2012). However, it has been shown that equation (3) can also be used as a detoxification mechanism to remove toxic free oxygen from the environment surrounding the microbe (Henrich *et al*., 2011). This process has been proposed as one of the earliest metabolic pathways of life (Ehrenreich and Widdel, 1994) due to the abundance of ferrous iron and silica in the Precambrian oceans.

From this evidence, it is no surprise that Cloud (1965) hypothesised that iron based metabolisms were common in the Gunflint microbiota. This was reiterated by Cloud and Hagen (1965) who noted SEM images of vaguely spiraled filaments, non-spiraled filaments and spheres bore a striking resemblance to the modern iron oxidizers *Lepothrix, Crenothrix,* and *Gallionella*. In fact Knoll and Simonson (1981) noted the similarity between the microorganisms in the Gunflint and Sokoman Formations where the microfossils are preserved as cryptocrystalline hematite coatings around thin filaments, leading them to suggest the likelihood that iron oxidizers were a primary microbial community in these systems.

Correspondingly, stratigraphic analysis by Wilson *et al.* (2010) suggests that the deposition of cherts within the Duck Creek Formation occurred at a strong redoxcline. They advocate that the microfossils are of iron-metabolizing microbiota that occupied an environment near the sediment-water interface. This would allow for a source of readily available ferrous iron. Recognizing the morphological similarity between cyanobacteria and iron oxidizing bacteria stated earlier, Planavsky *et al.* (2009) applied the notion that variations in the rare earth elements

cerium (Ce) and europium (Eu) and iron isotope values could provide insight into the fossilized microbe's environment and thus their metabolic pathways. They postulated that the nil to positive Ce anomaly in the samples containing hematite-coated microfossils indicates that the Middle Stromatolitic Member stromatolites developed at or near a strong redoxcline in suboxic conditions. These findings provide support for the interpretation that the hematite-coated microfossils in the Middle Stromatolitic Member (Figures 20, 27, 34, 35D, 54, 61) represent a distinct iron-oxidizing microbial community from the cyanobacteria dominated Lower Stromatolitic Member.

Finally, recent studies of the Gunflint and Biwabik microbiota have suggested that the iron-oxide coating found on the microfossils is not primary, rather it is the result of taphanomic replacement (Shapiro and Konhauser, 2015). In this model, iron-rich, oxidized fluids related to metamorphism circulate through the Gunflint and Biwabik resulting in the precipitation of iron oxides onto the carbonaceous microfossils. Based on the findings in this thesis, it is highly unlikely this process was responsible for the precipitation of iron oxides. Most importantly, the authors evoke metamorphic fluids rich in ferrous iron as the source of the iron oxide precipitate. However, based on the presence of hematite-coated microfossils observed at the Whitefish Falls (Figures 18, 19), Mink Mountain (Figure 25), Old School Road (Figure 33) and the drill cores P-1 and DH-3 (Figures 40 and 41D) where there is no evidence of metamorphism, this seems highly unlikely.

Carbon-rich zones similar to the laminae containing microfossils in the unmetamorphosed Middle Stromatolitic Member are present in the Northshore samples (Figure 57D). However, no structures resembling spheres or filaments were found. Furthermore, the

conspicuous lack of stromatolites in the highly metamorphosed Limestone Member at Northshore Mine (Figure 81) is in stark contrast to the well-developed carbonate stromatolites at the top of the Gunflint (Figures 78, 79, 80). It is interesting that the recrystallization has obliterated the Limestone Member stromatolites at the Northshore Mine, but the stromatolites that were also high-grade metamorphosed in the Upper Stromatolitic Member (Magnetic Rock and Northshore) were preserved because the silica did not recrystallize like the calcite did.

Horodyski (1975) has shown that organics are readily mobilized during neomorphism, late stage diagenesis and low- to medium-grade metamorphism resulting in the destruction of the microfossil form. Thus, for Proterozoic microfossils to be preserved silicification must occur at the time of growth or very early during diagenesis. In fact, some of the earliest works suggested that the development of iron silicates during albite-epidote hornfels facies metamorphism (similar to that of the Biwabik study locations) results in the destruction of microorganism structures (LeBerg, 1967). This would explain the abundance and excellent preservation of microfossils within the generally unmetamorphosed Gunflint Formation presented in this work and the references within, and the relative absence of microfossils in the metamorphosed Biwabik Formation.

3.4 Geochemical Considerations

The three locations in the Lower Stromatolitic Member (Figures 8, 14, 21) all show similar trends, typified by strongly negative Ce anomalies and strongly positive Eu anomalies. Interestingly, Kakabeka Falls and Whitefish Falls show a similar trend of slight depletion in LREEs in relation to the HREEs. The Schreiber Channel REE data indicated a slight depletion in LREE and HREE in relation to the mid-REEs. Trace and REE data for two locations within

The Middle Stromatolitic Member include Mink Mountain and DH-3 core (Figures 29, 42). Both show similar trends with a slight positive to nil Ce anomaly, a distinct positive Eu anomaly and slight depletion in LREE compared to the HREE. The trace and REE data for the four locations within the Upper Stromatolitic Member include; Mary Ellen Mine, LWD-99-1, VHD-00-1, and PR-98-1 (Figures 52, 66, 71, 77). The LWD and VHD drill holes show similar trends, with a distinctly positive Eu anomaly, and depletion in LREE in relation to HRRE. The apparent negative Ce anomaly in the two cores is due to a positive La anomaly, and when corrected for shows a nil anomaly (see Bau and Dulski, 1996 for discussion of correction) results in a slight positive to nil Ce anomaly. The PR-98 REE curves have a similar pattern to the two other cores, however they show a strongly positive Ce anomaly.

The presumed pH of the Archean-Paleoproterozoic ocean lies in the 7.5 to 8.5 range (Grotzinger and Kasting. 1993). This is well above the theoretical pH limit (>5) of oxidative scavenging of Ce by iron oxyhydroxides (Bau, 1999). Therefore, iron-oxide-rich authigenic precipitates can act as a proxy for paleobasin redox conditions, based on relative Ce anomalies. Thus, oxygenated marine waters will show a strong negative Ce anomaly, while suboxic and anoxic waters will tend to have a slightly negative, nil, or positive Ce anomaly (German and Elderfield, 1990; Winter and Knauth, 1992; Bau, 1999; Kato, 2006). Furthermore, in oxidized marine water, the preferential removal of LREEs versus HREEs onto iron hydroxide and manganese oxide particles, organic matter, and clay particles results in the relative depletion of LREEs in relation to HREEs (German *et al,* 1991).

Coupled with sequence stratigraphy (Ojakangas, 1983), Planavsky *et al*. (2009), suggest the presence of a strong redoxcline in the Animikie Basin separating the oxygenated nearshore facies (indicated by strongly negative Ce anomalies) and a suboxic to anoxic deep-water facies

(indicated by slightly positive or nil Ce anomalies). Based on these results, it can be inferred that the strongly negative Ce anomalies recorded in the stromatolitic cherts of the Lower Stromatolitic Member, along with the greater abundance of aggregate and rip-up clasts is indicative of an oxygenated, shallow environment. Furthermore, the slightly positive Ce anomaly recorded in the stromatolites from the Middle Stromatolitic Member is in agreement with the findings of Planavsky *et al*. (2009) and indicates they developed at or below a redoxcline in suboxic waters. It is likely the increased manganese concentration recorded in the oncolites in the Upper Stromatolitic Member has influenced the REEs as variable Ce anomalies (both positive and negative) are present. The variation in Ce anomaly can occur through significant Ce scavenging by manganese oxides or it could indicate that the oncolites and stromatolites were developing under changing redox conditions (Planavsky et al, 2009).

The consistently strong positive Eu anomaly in all samples analysed suggests a significant contribution of hydrothermal fluids to the seawater (Kamber and Webb, 2001). This is the result of preferential solution of Eu^{2+} during high-temperature alteration of basalt by reducing hydrothermal waters during the cyclic pumping of marine waters through submarine volcanic piles (Danielson *et al*., 1992). This is consistent with the interpretation by Holland (1984) suggesting the primary source of dissolved iron in the early oceans was hydrothermal and not terrigenous. In fact, recent findings of Rasmussen *et al.* (2012) have shown that major mantle activity in the Paleoproterozoic would have provided a significant source of hydrothermally sourced iron and silica in deep basinal waters. Transport of these waters via upwelling would have provided a constant source of Eu-enriched ferrous iron on shallow shelves (Derry and Jacobsen, 1990).

Comparable geochemical studies of the Sokoman Formation showed similar results to those reported here in that strongly positive Eu anomalies and minor negative Ce anomalies and relative depletion in LREEs in relation to HREEs were present (Fryer, 1977). This led the author to suggest that the siderite, iron silicates and iron hydroxides examined represented a primary mineralogy and not a replacement after limestone as suggested by previous authors (Dimroth and Kimberly, 1976).

3.5 Manganese Zonation

Elevated manganese concentrations were recorded in the Upper Stromatolitic Member at the Mary Ellen and Thunderbird North Mines and in the VHD-001, LWD-01, and PR-98-1 cores. An alternation of manganese-rich and iron-rich laminae was observed in several stromatolitic columns in the Mary Ellen digitate stromatolites (Figure 48C, 48D), as well as observations of manganese within the ooid cortical laminae. Furthermore, manganiferous siderite (Figures 65F, 69F) and rhodochrosite (Figure 61D) are common minerals in the laminae making up the oncolites.

The development of distinct manganese laminae within the stromatolites is a good indicator of the primary precipitation of the iron, silica and manganese within these stromatolites. The deposition of alternating manganese- and iron-rich laminae can be explained based on fluctuating oxygen levels or a change in the Eh-pH of the water. In their model for depositional controls on iron formation in the Gogebic Range, Wisconsin, Pufahl and Fralick (2004) evoke episodic, basin-directed, storm currents disrupting the redoxcline through the transport of photosynthetically oxygenated nearshore waters out into suboxic basinal waters.

Since iron compounds oxidize more readily than manganese compounds (Krauskopf, 1979), the precipitation of iron oxides would occur, resulting in a lower Fe:Mn ratio in the water column. Thin, millimetre-scale laminae of manganese oxides would develop in the upper portions of some chemically graded iron oxide laminae similar to that observed in the Mary Ellen Stromatolites. Similarly, Krauskopf (1979) has shown that variations in pH can drive the preferential separation of iron and manganese precipitates. In this model, a slow rise in the pH of the water column would result in iron reaching saturation prior to manganese. This would cause the precipitation of iron compounds out of solution before manganese. This model can occur in a cyclic pattern, causing the alternating deposition of iron and manganese compounds.

The manganese-rich oncolites of the Upper Stromatolitic Member of the Biwabik Formation (Figures 58, 60, 63, 67) are important for the premise of the primary nature of the iron-silica stromatolites in the Gunflint and Biwabik in that they have been interpreted to be direct carbonate precipitates (Zielinski *et al.,* 1994). This provides a comparison between the microstructure of primary, precipitated iron-silica-rich stromatolites and primary, precipitated carbonate stromatolites (oncolites). In their report, Zielinski *et al*. (1994) propose the oncolites formed in an oxygenated, high energy environment (tidal channel). They suggest that the grey-green chert rip-up clasts surrounded by red jasper are the result of a minor marine regression, when sediments deposited in an anoxic to suboxic environment were overlain by sediments deposited in a photosynthetically oxygenated environment. This would explain the presence of reduced and oxidized iron and manganese minerals intermixed with one another. This theory is supported by the findings of Planavsky *et al*. (2009) who noted variations in the Ce anomalies in the oncolites which they attributed to varying redox conditions and scavenging of Ce by the manganese oxides.

The rhodochrosite, siderite, magnetite mineral assemblage of the oncolites has been interpreted to represent primary chemical precipitation, facilitated by manganese-iron metabolizing bacteria. The development of manganese oxides and carbonates can occur abiotically as described above, however, a significant portion of Mn^{2+} oxidation and Mn^{4+} reduction occurs via microbial catalysis (Ehrlich, 2002). Furthermore, the presence of probitumen reported in association with the oncolites further supports the importance of microbial activity in the formation of the oncolites (Mancuso et al., 1989). Moreover, Walter *et al.* (1976) described novel microfossils in the Frere Formation bearing a striking similarity to the modern *Metallogenium*, and *Gallionella* which can facilitate the deposition of manganiferous carbonates and oxides (Walsh and Mitchell, 1973). The likelihood that the oncolites represent an original, precipitated mineral assemblage is further supported by the discovery of manganese stromatolites within a cave in Spain (Rossi *et al.*, 2010). At this location, the development of large domal stromatolites has been attributed to extracellular precipitation of manganese by chemolithotrophic bacteria. Furthermore, the authors suggest that the presence of amorphous manganese nanoparticles which encase the bacterial cells are the reason for the exceptional preservation of the microfossils.

3.6 Ferromanganese Nodules

Ferromanganese nodules are found at the sediment-water interface in neutral to slightly acidic, freshwater lakes (Harriss and Troup, 1970). An investigation into the formational mechanisms of nodule development was conducted by Kerkermeier (2013). It was found that FMN develop on a porous substrate (sand) which allows the diffuse upflow of reduced

groundwater. When this reduced water reaches the oxidized sediment-water interface, bacterially mediated deposition of manganese and iron hydroxides occurs (Sommers *et al.,* 2002). The presence of millimeter-scale pustular growths on the bottom surface (Figure 82D, 82E) indicates the importance of iron and manganese metabolizing bacteria as these growths occur in darkness, below centimetre-thick opaque precipitates.

The remarkable similarity between the microcolumns observed in oncolites in the Upper Stromatolite Member (Figure 68) and modern ferromanganese nodules (Figure 83) and the alternation of manganese and iron hydroxide laminae within FMNs (Figure 84) is consistent with a similar developmental processes and that of ancient iron-silica rich stromatolites. Most importantly, they provide a modern analogue for the growth of authigenic, precipitated stromatolites.

The importance of microorganisms in the growth of FMNs has been proposed by several authors (Tazaki, 1997; Sommers *et al*., 2000; Konhauser, 2007). Results of this investigation have shown rod-shaped bacteria coated in an iron hydroxide precipitate (Figure 85A, 85B, 85D) and coccus forms embedded in a iron-mineralized layer of EPS (Figure 85C). Furthermore, microscopic analysis of the sediments directly below several FMNs at Lake Charlotte revealed diatoms and cyanobacteria embedded in mucilage, coated in thick iron hydroxide precipitates (Wepruk, 2014, Figure 86). Similar results were reported by Tazaki (1997) in laboratory and field experiments. They found a brown iron hydroxide precipitate on stocks of iron-oxidizing bacteria forming FMNs. Furthermore, their results show that the precipitation of iron- aluminum silicates can be mediated by microbial activity, in that thin, layer silicates were noted forming by interactions of hydrated iron-manganese precipitates and bacterial activity.

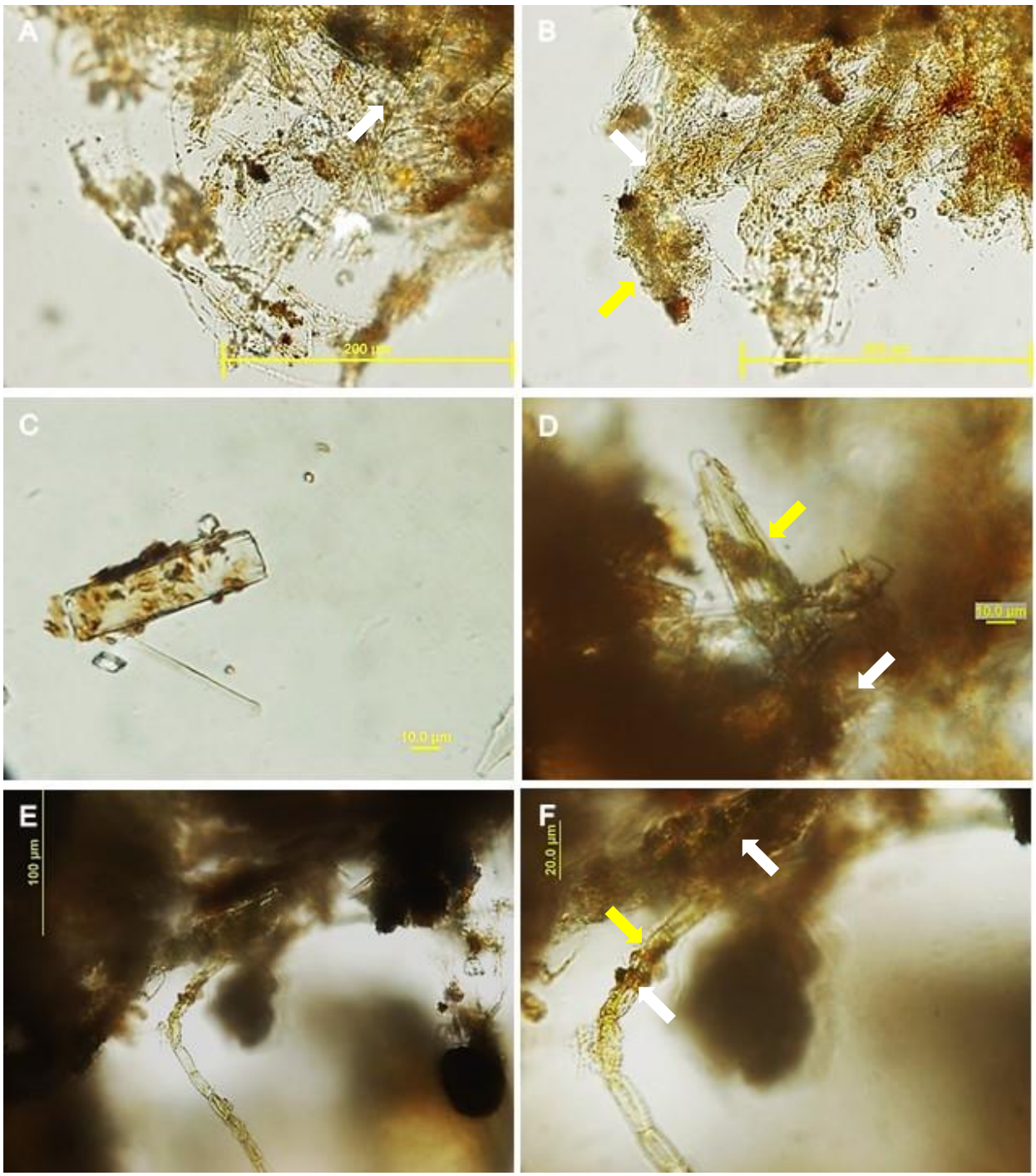

Figure 86. Encrustation of diatom and cyanobacteria by iron-hydroxides in ferromanganese-rich sediment associated with nodules. (A-B) Mucilage development White arrow) surrounding diatom frustule (yellow arrow) promoting the precipitation of iron hydroxides. (C) Nearly complete encrustation of a diatom frustule by iron hydroxides. (D) Advanced iron hydroxide precipitation in mucilage (white arrow) surrounding diatom frustule (yellow arrow). (E-F) Precipitation of iron hydroxide (white arrow) on cyanobacteria (yellow arrow) and mucilage (white arrow). All images were reproduced from Wepruk (2014).

The brown iron hydroxide noted in Figure 86 bears a striking similarity to the iron-stained zones associated with the Gunflint microfossils (Figures 18B, 25C, 33A, 40A, 41D) providing further evidence that the stromatolites were deposited as chemically precipitated amorphous iron and silica.

4 Conclusions

Many of the stromatolites described from the rock record as well as modern examples are composed of agglutinated carbonate formed by diverse communities dominated by cyanobacteria. However, stromatolites from the 1.87 Ga Gunflint and Biwabik Formations are composed of fine-grained, alternating bands of iron and silica, with minor carbonate. Since their initial discovery, speculation as to whether they represent silicification and/or replacement of carbonate, or represent primary chemical precipitates has been raised.

The unmetamorphosed Middle Stromatolitic Member in the Gunflint provides the best example of the ecological structure and environments occupied by the Animikie stromatolites. Based on REE data it is probable that iron and silica in the Animikie Basin was maintained at or near saturation through hydrothermal inputs. The stromatolites were formed by iron metabolizing bacteria, near a redoxcline in suboxic ferruginous waters. Deposition of silica and iron was initiated through the adsorption of nanoparticles of amorphous silica and iron hydroxides onto cellular material (e.g. EPS, sheaths, filiments, etc.). Due to the impregnation of nanoparticulate iron and silica into the microbial material, remarkable preservation of the cell structure occurred. The stromatolites are surrounded by granules and ooids composed of hematite, silica and greenalite containing dehydration cracks. Dissolved silica and iron at saturation in the water column would react to form amorphous iron-silicate gels. Dehydration of these gels would readily react to form early diagenetic minerals, including chert, greenalite, siderite, and hematite that make up the current mineral assemblage.

In contrast to the Middle Stromatolitic Member, the complex mineralogy of the Lower Stromatolitic Member of the Gunflint and Biwabik Formations is suggestive of a complicated

depositional, and diagenetic history. The presence of red jasperlitic stromatolites overlying ones composed of black, green and grey chert indicates a variable redox boundary possibly tied to minor transgressive-regressive stages. REE data and petrographic observations indicate the stromatolites formed in a high energy, oxygenated environment. The pervasive replacement of primary carbonate, silica and iron minerals further indicates a complex environment.

The Upper Stromatolitic Member is indicative of two distinct environments. The well-developed digitate stromatolites likely represent an environment and ecological structure similar to or the same as the stromatolites in the Middle Stromatolitic Member. They formed through the direct chemical precipitation of amorphous silica and iron hydroxides at or near a redoxcline in suboxic waters. In higher energy environments such as tidal channels, where no stable substrate was available, oncolites developed. REE data indicates the oncolites developed in oxygenated, iron-rich waters. As with modern reef systems, niche communities develop based on the nutrients and resources available. It is possible that the elevated quantities of manganese present in the oncolites are the result of manganese metabolising microorganisms. These organisms would have caused the direct precipitation of manganese-rich carbonates (rhodochrosite and manganiferous siderite) onto the EPS. This would also allow for the deposition of primary magnetite within the oncolites.

Comparison of the Lower, Middle and Upper Stromatolitic Members to the primary calcite stromatolites at the top of the Gunflint in the Limestone Member provides further evidence for their primary mineralogy. The coarse microstructure of the cabbage-shaped, recrystallized calcite stromatolites is in stark contrast to the finely laminated centimeter-scale stromatolites. Furthermore, the lack of iron oxides in the metamorphosed Limestone Member in

the Biwabik Formation indicates that the presence of iron within the Lower, Middle and Upper Member stromatolites is not due to iron-rich metamorphic fluids circulating through the Gunflint and Biwabik Formations.

This research provides fresh insight on the redox structure of the shallow areas of the Paleoproterozoic Animikie Basin. The contrast between the strongly negative Ce contents of the stromatolites in the Lower Stromatolitic Member and nil to positive contents of the Middle Stromatolitic Member indicate a fluctuating redoxcline. An increase in oxygenated waters caused by photosynthetic microbes in the near shore environments would drive the redoxcline basin ward. An increase in the amount of ferrous iron into the system via increased hydrothermal activity would push the redoxcline shoreward into the microbial mat itself, causing the nil to positive Ce contents described here. As the nearshore photosynthetic oxygen concentrations gradually increase, the redoxcline is once again pushed basinward and a negative Ce anomaly is recorded in the nearshore rocks. These findings are significant as it challenges the long held belief of a "2 box" system where the oceans were stratified into an oxygenated upper and an anoxic, ferruginous lower zone. These findings suggest the redoxcline was not horizontal, but in fact, diagonal or vertical with changes affected by te rate of photosynthetic oxygen production in the nearshore environment and hydrothermal input of reductants in the deep basin, saturating the Paleoproterozoic oceans with ferrous iron.

Finally, a modern analogue for direct chemical precipitation of iron and manganese is provided. Ferromanganese nodules forming at the sediment-water redox boundary of modern lakes provides further understanding into ancient systems responsible for the deposition of chemically precipitated iron-rich siliceous stromatolites. Furthermore, the intimate relationship

between microorganisms and the deposition of amorphous silica and iron and manganese oxyhydroxides is highlighted.

The stromatolites that formed in the Animikie basin 1.87 billion years ago developed in a fundamentally different ocean from what is present today. Thus, analogues for their formation are hard to elucidate based on the scarcity of similar modern systems. However, based on petrographic and geochemical observations, and a careful literature review, it is put forth that the stromatolites and surrounding sediments described in this work represent a primary mineral assemblage of chert, jasper, greenalite, hematite, magnetite, siderite, and rare rhodochrosite and do not represent the product of silicification of a carbonate precursor.

5 References

Addison, W.D., Brumpton, G.R., Vallini, D.A., McNaughton, N.J., Davis, D.W., Kissin, S.A., Fralick, P.W., Hammond, A.L. 2005. Discovery of distal ejecta from the 1850 Ma Sudbury impact event. Geology, 33, 193–196.

Akin, S.J., Pufahl, P.K., Hiatt, E.E., Pirajno, F. 2013. Oxygenation of shallow marine environments and chemical sedimentation in Paleoproterozoic peritidal settings: Frere Formation, Western Australia. Sedimentology, 60, 1559-1582

Amard, B. Bertrand-Sarfati, J. 1997. Microfossils in the 2000 Ma old cherty stromatolites of the Franceville Group, Gabon. Precambrian Research, 81, 197-221.

Asikainen, C.A., Werle, S.F. 2007. Accretion of ferromanganese nodules that form pavement in Second Connecticut Lake, New Hampshire. Proceedings of the National Academy of Science, 104, 17579-17581.

Awramik, S.M. 1976. Gunflint Stromatolites: Microfossil distribution in relation to stromatolite morphology, in Walter, M.R. ed., Stromatolites: Elsevier, Amsterdam, 311-320.

Awramik, S.M., Barghoorn, E.S. 1977. The Gunflint microbiota. Precambrian Research, 5, 121-142.

Ayres, D.E. 1972. Genesis of iron-bearing minerals of in banded iron formation mesobands in the Dales Gorge Member, Hamersley Group, Western Australia. Economic Geology, 67, 1214-1233.

Barghoorn, E.S., Tyler, S.A. 1965. Microorganisms from the Gunflint chert. Science, 147, 563-577.

Bartley, J.K. 1996. Actualistic taphonomy of cyanobacteria: Implications for the Precambrian fossil record. Palaios, 11, 571-586.

Bau, M., Dulski, P. 1996. Distribution of yttrium and rare-earth elements in the Penge and Kuruman Iron-Formations, Transvaal Supergroup, South Africa. Precambrian Research, 79, 37–55.

Bau, M., 1999. Scavenging of dissolved yttrium and rare earths by precipitating iron oxyhydroxide: Experimental evidence for Ce oxidation, Y–Ho fractionation, and lanthanide tetrad effect. Geochima Cosmochima Acta, 63, 67–77.

Bazylinski, D.A., Frankel, R.B., Heywood, B.R., Mann, S., King, J.W., Donaghay, P.L., Hanson, A.K. 1995. Controlled Biomineralization of magnetite (Fe_3O_4) and greigite (Fe_3S_4) in a magnetotactic bacterium. Applied and Environmental Microbiology, 61, 3232-3239.

Bazylinski, D.A., Frankel, R.B. 2003. Biologically induced mineralization by bacteria. Reviews in Mineralogy and Geochemistry, 54, 95-114.

Behl, R. J., & Garrison, R. E. (1994). The origin of chert in the Monterey Formation of California (USA). In Siliceous, phosphatic and glauconitic sediments of the Tertiary and Mesozoic: Proceedings of the 29th International Geological Congress, Part C (pp. 101-132).

Beukes, N. J., Klein, C. 1990. Geochemistry and Sedimentology of a Facies Transition - from Microbanded to Granular Iron-Formation - in the Early Proterozoic Transvaal Supergroup, South-Africa: Precambrian Research, 47, 99-139.

Bontognali, T.R., Vasconcelos, C. Warthmann, R.J.,McKenzie, J.A. 2007. Dolomite nucleation on extracellular polymeric substances. IN: 17th annual V M Goldschmidt Conference, Cologne, A108-A108 p.

Bontognali, T.R., Vasconcelos, C. Warthmann, R.J., Dupraz, C., Bernasconi, S.M., McKenzie, J.A. 2008. Microbes produce nanobacteria-like structures, avoiding cell entombment. Geology, 36, 663-666.

Bowen, B.B., Benison, K.C., Oboh-Ikuenobe, F.E., Story, S., Mormile, M.R. 2008. Active hematite concretion formation in modern acid saline lake sediments, Lake Brown, Western Australia. Earth and Planetary Science Letters, 268, 52-63.

Broderick, T.M. 1920. Economic Geology and stratigraphy of the Gunflint Iron District, Minnesota. Economic Geology, 15, 422-452.

Bunting, A.J. 1986. Geology of the eastern part of the Nabberu Basin, Western Australia. Geologic Survey of Western Australia Bulletin, 131, 130p.

Burgos, A., Seder-Colomina, M., Maldonado, J., Solé, A., Esteve, I. 2012. Scanning electron microscopy coupled to an energy dispersive X-ray detector to study copper removal on different phototrophic microorganisms. Current Microscopy Contributions to Advances in Science and Technology Book Series, 1Formatex, 222-229.

Cannon, W.F., and Addison, W.A., 2007. Distal ejecta from the 1850 Ma Sudbury impact in the Lake Superior iron ranges. Geological Society of America Abstracts with Programs, 39, p. 220.

Cayeux, L. 1911, Comparaison entre les minerais de fer huroniens des Etats-Unis et les minerais de fer oolithiques de France: Acad. Sei. Comptes Rendus, 153, 1188-1190.

Cloud, P, 1965. Significance of the Gunflint (Precambrian) microflora. Science, 148, 27-35.

Cloud, P. 1973. Paleoecological significance of the banded iron-formation. Economic Geology, 68, 1135-1143.

Cloud, P.E., and Hagen, H, 1965. Electron microscopy of the Gunflint Microflora: Preliminary results. Proceedings of the National Academy of Science, 54, 1-8

Cloud, P.E., Licari, G.R. 1968. Microbiotas of banded iron formations. Proceedings of the National Academy of Sciences, 61, 779-786.

Dai, Y., Song, H., Shen, J. 2004. Fossil bacteria in Xuanlong iron ore deposits of Hebei Province. Science in China, 47, 347-356.

Danielson, A., Möller, P., Dulski, P. 1992. The europium anomalies in banded iron formations and the thermal history of the oceanic crust. Chemical Geology, 97, 89-100.

Decho, A.W. 1990. Microbial exopolymer secretions in ocean environments: their role(s) in food webs and marine processes. Oceanographic Marine Biology Annual Review, 28, 73 – 153.

Derry, L.A., Jacobsen, S.B. 1990. The chemical evolution of Precambrian seawater: Evidence from REEs in banded iron formations. Geochimica Cosmochimica Acta, 54, 2965-2977.

Dill, R.F., Shinn, F.A., Jones, A.T., Kelly, K, Steinen, R.P. 1986. Giant stromatolites forming in normal salinity waters. Nature, 345, 55-58.

Dimroth, E., Chauvel, J.J., 1973. Petrography of the Sokoman iron formation in part of the Central Labrador Trough, Quebec, Canada. Geological Society of America Bulletin, 84, 111-134.

Dimroth, E, Kimberley, M.M. 1976. Precambrian atmospheric oxygen: Evidence in the sedimentary distributions of carbon, sulfur, uranium, and iron. Canadian Journal of Earth Sciences, 13, 1161-1185.

Ehrlich, H.L. 2002. Geomicrobiology, 4th edition. Marcel Dekker, New York, 768p.

Ehrenreich A.,Widdel F. 1994. Anaerobic oxidation of ferrous iron by purple bacteria, a new type of phototrophic metabolism. Applied Environmental Microbiology, 60, 4517–4526.

Fischer, W.W., Knoll, A.H. 2009. Origin of late Archean and early Paleoproterozoic iron formation. Geologic Society of America Bulletin, 121, 222-235.

Floran, R.L., and Papike, J.J. 1975, Petrology of the low-grade rocks of the Gunflint iron Formation, Ontario-Minnesota. Geological Society of America Bulletin, 86, 1169-1190.

Floran, R.J., and Papike, J.J. 1978. Mineralogy and petrology of the Gunflint Iron Formation, Minnesota-Ontario, Correlation of compositional and assemblage variations at low to moderate grade. Journal of Petrology, 19, 215-288.

Folk, R.L. 1974 Petrology of sedimentary rocks. Austin Texas, Hemphill Publication Co. 182p.

Fralick, P.W. 1988, Microbial bioherms, Lower Proterozoic Gunflint Formation, Thunder Bay, Ontario, in Geldsetzer, H.H.J, James, N.P., Tebbutt, G.E., eds., Reefs: Canada and adjacent areas: Memoirs of the Canadian Society of Petroleum Geologists, Calgary, 13, 24-29.

Fralick, P.W., and Barrett, T.J. 1995. Depositional controls on iron formation associations in Canada: Special Publications of the International Association of Sedimentology, 22, 137-156.

Fralick, P.W., Davis, D.W., and Kissin, S.A. 2002. The age of the Gunflint Formation, Ontario, Canada: Single zircon U-Pb age determinations from reworked volcanic ash. Canadian Journal of Earth Sciences, 39, 1089-1091.

Frankel, R.B., Bazylinski, D.A. 2003. Biologically induced mineralization by bacteria. IN: Dove, P.M., Weiner, S., De Yoreo, J.J. Eds. Biomineralization. Mineralogical Society of America, Reviews in Mineralogy and Geochemistry, 54, 95–114.

French, B.M., 1968. Progressive contact metamorphism of the Biwabik Iron Formation, Mesabi Iron Range, Minnesota. Minnesota Geological Survey Bulletin, 45, 103p.

French, B.M., 1973. Mineral assemblages in Diagenetic and Low-Grade Metamorphic iron formations. Economic Geology, 68, 1063-1074.

Frost, C. D. von Blanckenburg, F., Schoenberg, R., Frost, B.R., Swapp, S.M. 2007. Preservation of Fe isotope heterogeneities during diagenesis and metamorphism of banded iron formations, Contributions to Mineral Petrology, 153, 211-235.

Fryer, B.J. 1977. Trace element geochemistry of the Sokoman Iron Formation, Canadian Journal of Earth Science, 14, 1598-1610.

German, C.R., Elderfield, H. 1990. Application of the Ce-anomaly as a paleoredox indicator: The ground rules. Paleoceanography, 5, 823–833.

German, C.R., Holliday, B.P., Elderfield, H. 1991. Redox cycling of rare earth elements in the suboxic zone of the Black Sea. Geochimica Cosmochimica Acta, 55, 3553–3558.

Geul, J.C. 1970. Geology of the Devon and Pardee Townships and the Stuart location. Ontario Department of Mines, Geologic Report 87, 52p.

Ghiorse, W.C. 1984. Biology of iron and manganese depositing bacteria. Annual Review of Microbiology, 38, 515-550.

Gill, J.E., 1926. Gunflint iron-bearing formation, Ontario, in Summary Report: Geological Survey of Canada, 1924 Part C, 28-88.

Gill, J.E., 1927. Origin of the Gunflint iron-bearing formation. Economic Geology, 22, 687-728.

Ginsberg, R.N. 1967. Algal stromatolites: Deepwater forms in the Devonian of Australia. Science, 165, 1008-1010.

Ginsberg, R.N., Planavsky, N.J. 2008. Diversity of Bahamian microbialite substrates, IN Links between geological processes, microbial activities and evolution of life: Microbes and Geology. Dilek, Furnes, Muehlenbachs Eds., Springer Netherlands, 348 p.

Golubic, S., Hofmann, H.J. 1976. Comparison of Holocene and Mid-Precambrian Entophysalidaceae (Cyanophyta) in stromatolitic mats: Cell division and degradation. Journal of Paleontology, 50, 1074-1082.

Goodwin, A.M. 1956. Facies relations in the Gunflint Iron Formation. Economic Geology, 51, 565-595.

Goodwin, A.M., 1960. Gunflint Iron Formation of the Whitefish Lake area. Ontario Department of Mines, 69, 41-63.

Grotzinger, J.P., Kasting, J.F. 1993. New constraints on Precambrian ocean composition. Journal of Geology, 101, 235-243.

Grey, K. 1982, Aspects of Proterozoic stromatolite biostratigraphy in Western Australia. Precambrian Research, 18, 347-365.

Grey, K. 1993. Stromatolites from the Paleoproterozoic Earaheedy Group, Earaheedy Basin, Western Australia. Acheringa, 18, 187-218.

Grout, F.F. and Broderick, T.M. 1919. Organic structures in the Biwabik iron bearing formation of the Huronian in Minnesota. American Journal of Science, 48, 199-205.

Gruner, J.W. 1922. The origin of the sedimentary iron formations: the Biwabik formation of the Mesabi Range. Economic Geology, 17, 407-460.

Gruner, J.W. 1936. The structure and chemical composition of Greenalite. American Mineralogist, 21, 449-455.

Gruner, J.W. 1937. Composition and structure of Stilpnomelane. American Mineralogist, 22, 912-924.

Gruner, J.W. 1944. The composition and structure of Minnesotaite. American Mineralogist, 29, 363-372.

Gruner, J.W. 1946. The mineralogy and geology of the taconites and iron ores of the Mesabi Range, Minnesota. Office of the Commissioner Iron Range Resources and Rehabilitation, St. Paul, Minnesota Geological Survey, 127p.

Guel, J.J.C. 1970. Geology of Devon and Pardee Townships, and the Stuart Location. Ontario Department of Mines and Northern Affairs, Geological Report, 87, 52p.

Harriss, R.C, and Troup, A.G. 1970. Chemistry and Origin of freshwater ferromanganese concretions. Limnology and Ocenaography, 15, 702-712.

Heaman, L.M., Easton, R.M., Hart, T.R., Hollings, P., MacDonald, C.A., Smyk, M. 2007. Further refinement of the timing of Mesoproterozoic magmatism, Lake Nipigon region, Ontario, Canadian Journal of Earth Sciences, 44, 1055–1086.

Heikoop, J.M., Tsujita, C.J., Risk, M.J., Tomascik, T., Mah, A.J. 1996. Modern iron ooids from a shallow-marine volcanic setting: Mahengetang, Indonesia. Geology, 24, 759-762.

Hemming, S.R., McLennan, S.M., Hanson, G.N. 1995. Geochemical and Nd/Pb isotopic evidence for the provenance of the Early Proterozoic Virginia Formation, Minnesota: Implications for tectonic setting of the Animikie Basin. Journal of Geology, 103, 147-168.

Henrich, S., Schloman, M., Johnson, D.B. 2011. The iron-oxidizing proterobacteria, Microbiology, 157, 1551-1564.

Hoffmann, P. 1987. Early Proterozoic foredeeps, foredeep magmatism and Superior-type iron-formations of the Canadian Shield. IN: A. Kroner Ed., Proterozoic Lithosphere Evolution. Geodynamics Series, vol. 17 American Geophysical Union, 85–98.

Hofmann, H.J. 1969. Stromatolites from the Proterozoic Animikie and Sibley Groups, Ontario, Geologic Survey of Canada, paper 68-69, 77p.

Hofmann, H.J. 1973. Stromatolites: Characteristics and utility. Earth-Science reviews, 9, 339-373.

Holland, H.D.1984. The chemical evolution of the atmosphere and oceans. NJ, Princeton University Press, 598 p.

Horodyski, R.J, 1975. Stromatolites of the lower Missoula Group (Middle Proterozoic) Belt Supergroup, Glacier National Park, Montana. Precambrian Research, 2, 215-254.

Ingall, E.D. 1888. Mines and mining on Lake Superior. Part I, in Annual Report: Geological and Natural history survey of Canada, Report, 3, 1-131.

James, H.L. 1954. Sedimentary facies of iron-formation. Economic Geology, 49, 235-293.

James, H.L. 1983. Distribution of banded iron-formation in space and time. IN: Iron Formation: Facts and Problems. Eds A.F. Trendall and R.C. Morris, Elsevier, Amsterdam, 471–490.

Kalkowsky, E., 1908. Oolith und stromatolithin norddeutschen Buntsandstein. Zeitschrift Deutschen geol. Gesellschaft, 60, 68-125.

Kamber, B.S.,Webb, G.E., 2001. The geochemistry of late Archaean microbial carbonate: Implications for ocean chemistry and continental erosion history. Geochimica Cosmochimica Acta, 65, 2509–2525.

Kappler, A., Pasquero, C., Konhauser, K.O., Newman, D.K. 2005. Deposition of banded iron formations by anoxygenic phototrophic Fe(II)-oxidizing bacteria. Geology, 33, 865-868.

Kato, Y. 2006. Rare earth elements in the Precambrian banded iron formations; secular chances of Ce and Eu anomalies and evolution of atmospheric oxygen. Geological Society of America, 198, 269-289.

Kerkermeier, L., 2013. Formational processes of recent arsenic rich ferromanganese lacustrine precipitates in Nova Scotia and Northern Ontario. MSc Thesis, Lakehead University. 281 p.

Klein, C. 1974. Greenalite, stilpnomelane, minnesotaite, crocidolite, and carbonates in very low-grade metamorphic Precambrian iron-formation. Canadian Mineralogist, 12, 475-498.

Knoll, A, Barghoorn, E.S. 1976. A gunflint-type microbiota from the Duck Creek Dolomite, Western Australia. Origins of Life, 7, 417-426.3

Knoll, A.H., Barghoorn, E.S., and Awramik, S.M. 1978. New microorganisms of the Aphebian Gunflint Iron Formation, Ontario. Journal of Paleontology, 5, 976-992.

Knoll, A.H., Simonson, B. 1981. Early Proterozoic microfossils and penecontemporaneous quartz cementation in the Sokoman Iron Formation, Canada. Science, New Series 211, 478-480.

Konhauser, K.O., Ferris, F.G. 1996. Diversity of iron and silica precipitation by microbial mats in hydrothermal waters, Iceland: Implications for Precambrian iron formations. Geology, 24, 323-326.

Konhauser, K.O., Newman, D.K., Kappler, A. 2005. The potential significance of microbial Fe(III) reduction during deposition of Precambrian banded iron formations. Geobiology, 3, 167-177.

Konhauser, K.O. 2007. Introduction to Geomicrobiology. Wiley-Blackwell, 440p.

Konhauser, K.O., Riding, R. 2012. Bacterial Mineralization. IN Fundamentals of Geobiology, Eds Andrew Knoll, Donald E Canfield and Kurt Konhauser, Wiley-Balckwell, Oxford, 443p.

Krauskopf, K.B. 1957. Separation of manganese from iron in sedimentary processes. Geochimica Cosmochimica Acta, 12, 61-84.

Kremer, B., Kazmierczak, J., Lukomska-Kowalczyk, m., Kempe, S. 2012. Calcification and Silicification: Fossilization potential of cyanobacteria from stromatolites of Niuafo'ou's Caldera lakes (Tonga) and implications for the early fossil record. Astrobiology, 12, 535-548.

LaBerge, G.L. 1964. Development of magnetite in iron-formations of the Lake Superior region. Economic Geology, 59, 1313-1342.

LaBerge, G.L. 1967. Microfossils and Precambrian iron-formations. Geological Society of America Bulletin, 78: 331-342.

Logan, B.W. 1961. Cryptozona and associated stromatolites from the recent Shark Bay, Western Australia. Journal of Geology, 69, 517-533.

Logan, B.W., Rezak, R., Ginsburg, R.N. 1964. Classification and environmental significance of algal stromatolites. The Journal of Geology, 72, 68-83.

Lougheed, M.S. 1983. Origin of Precambrian iron-formations in the Lake Superior region. Geological Society of America Bulletin, 94, 325-340.

Lowenstam, H.A. 1981. Minerals formed by organisms. Science, 211,1126-1131.

Lowenstam, H.A., Weiner, S. 1983. Mineralization by organisms and the evolution of Biomineralization. Biomineralization and Biological Metal Accumulation, 191-203. In Biomineralization and Biological Metal Accumulation, eds P. Westbrook and E.W. de Jong.

Maliva, R.G., Knoll, A.H., Simonson, B.M. 2005. Secular change in the Precambrian silica cycle: Insights from chert petrology. Geological Society of America Bulletin, 117, 835-845.

Maric, M. 2006. Sedimentology and sequence stratigraphy of the Paleoproterozoic Rove and Virginia Formations, southwest Superior Province. MSc Thesis, Lakehead University. 111p.

Markun, R.G., and Randazzo. 1980. Sedimentary structures in the Gunflint Iron Formation, Schreiber Beach, Ontario. Precambrian Research, 12, 287-310.

Moore, E.S. 1918. The iron formation on Belcher Islands, Hudson Bay, with special reference to its origin and its associated limestones. Journal of Geology, 412-438.

Moorhouse, W.W, 1960. Gunflint iron range in the vicinity of Port Arthur, Ontario Department of Mines, 69, 1-40.

Moorhouse, W.W., Beales, F.W. 1962. Fossils from the Animikie, Port Arthur, Ontario. Royal Society of Canada transactions, 56, 97-110.

Morey, 1967. Stratigraphy and Sedimentology of the Middle Precambrian Rove Formation in northeastern Minnesota. Journal of sedimentary petrology, 37, 1154-1162.

Morey G.B. 1983. Animikie Basin, Lake Superior Region, U.S.A. in Trendall, A.F. and Morriss, R.C., eds, Iron-Formation facts and problems, Elsevier, Amsterdam, 13-67.

Ojakangas, R.W. 1983. Tidal deposits in the early Proterozoic basin of Lake Superior region. The Palms and the Pokegama Formations; Evidence for sub tidal-shelf deposition of Superior-type banded iron formation: in L.G. Medaris, Jr. ed., Early Proterozoic Geology of the Lake Superior Region. Geological Society of America Memoir 160, 49-66.

Ojakangas, R.W., Morey, G.B., Southwick, D.L. 2001. Paleoproterozoic basin development and sedimentation in the Lake Superior region, North America. Sedimentary Geology, 141, 319-341.

Paterson, D.M., Aspden, R.J., Visscher, P.T., Consalvey, M., Andres, M.S., Decho, A.W., Stolz, J., Ried, P. 2008. Light-dependent biostabilisation of sediments by stromatolite assemblages. PLOS ONE, 3, e3176.

Planavsky, N., Rouxel, O., Bekker, A., Shapiro, R., Fralick, P., Knudsen, A. 2009. Iron-oxidizing microbial ecosystems thrived in late Paleoproterozoic redox-stratified oceans. Earth and Planetary Science Letters, 286, 230-242.

Pierson, B.K., Parenteau, M.N., Griffin, B.M. 1999. Phototrophs in high-iron concentration microbial mats: Physiological ecology of phototrophs in an iron-depositing hot sping. Applied and Environmental Microbiology, 65, 5474-5483.

Poulton, S.W., Fralick, P.W., Canfield, D.E. 2004. The transition to a sulphidic ocean ~1.84 billion years ago. Nature, 43, 173-177.

Pufhal, P.K. 1996. Stratigraphic architecture of a Paleoproterozoic iron formation depositional system: The Gunflint, Mesabi, and Cuyuna Iron Ranges. MSc Thesis, Lakehead University, 152 p.

Pufhal, P.K., Grimm, K.A. 2003. Coated phosphorite grains: Proxy for physical, chemical and ecological changes in seawater. Geology, 31, 801-804.

Pufahl, P.K., Fralick, P.W. 2004. Depositional controls on Paleoproterozoic iron formation accumulation, Gogebic Range, Lake Superior region, USA. Sedimentology, 51, 791-808.

Pufahl, P.K., Anderson, S.L., Hiatt, E.E., Piraino, F. 2014. Dynamic sedimentation of Paleoproterozoic continental margin iron formation, Labrador Trough, Canada: Paleoenvironments and sequence stratigraphy. Sedimentary Geology, 309, 48-65

Randazzo, A.F., and Markun, C.D. 1980. Sedimentary structures in the Gunflint Iron Formation, Schreiber Beach, Ontario. Precambrian Research, 12, 287-310.

Rasmussen, B., Fletcher, I.R., Bekker, A., Muhling, J.R., Gregory, C.J., Thorne, A.M. 2012. Deposition of 1.88-billion-year-old iron formations as a consequence of rapid crustal growth. Nature, 484,498-501.

Reid, R.P., Visscher, P.T., Decho, A.W., Stolz, J.F., Bebout, B.M., Dupraz, C., MacIntyre, I.G., Paerl, H.W., Pinckney, J.L., Prufert-Bebout, L., Steppe, T.F., DesMarais, D.J. 2000. THe role of microbes in accretion, lamination and early lithification of modern marine stromatolites. Nature, 400, 989-992.

Reid, P., Dupraz, C.D., Visscher, P.T. Sumner, D.Y. 2003. Microbial processes forming marine stromatolites. In Fossil and Recent Biofilms: A Natural History of Life on Earth. Springer Netherlands, 103-118.

Renaut, R.W., Jones, B., Tiercelin, J.J. 1998. Rapid in situ silicification of microbes at Loburu hot springs, Lake Bogoria, Kenya Rift Valley. Sedimentology, 45, 1083-1103.

Riding, R., 1991. Classification of microbial carbonates. In: Riding, R. (Ed.), Calcareous Algae and Stromatolites. Springer, Berlin, 21–51.

Riding, R., 2000. Microbial carbonates: the geological record of calcified bacterial-algal mats and biofilms. Sedimentology 47 (Suppl. 1), 179–214.

Rossi, C., Loranzo, R.P., Isanta, N., Hellstrom, J. 2010. Manganese stromatolites in caves: El Soplao (Cantabria, Spain). Geology, 38, 1119-1122.

Sánchez-Román, M., Fernández-Remolar, D., Amils, R., Sánchez-Navas, A., Schmid, T., Martin-Uriz, P.S., Rodriguez, N., McKenzie, J.A., Vasconcelos, C. 2014. Microbial mediated formation of Fe-carbonate minerals under extreme acidic conditions. Nature, 4767, 1-7.

Sanz-Montero, M.E., Rodríguez-Aranda, J.P., García del Cura, M.A. 2008. Dolomite-silica stromatolites in Miocene lacustrine deposits from the Duero Basin, Spain: the role of orgaotemplates in the precipitation of dolomite. Sedimentology, 55, 729-750.

Schelble, R.T., Westall, F., and Allen, C.C. 2004. ~1.8 Ga iron-mineralized microbiota from the Gunflint Iron Formation, Ontario: implications for Mars. Advances in Space Research, 33, 1268-1273.

Schneider, D.A., Bickford, M.E., Cannon, W.F., Schulz, K.J., Hamilton, M.A., 2002. Age of volcanic rocks and syndepositional iron formations, Marquette Range Supergroup: implications for the tectonic setting of Paleoproterozoic, iron formations of the Lake Superior region. Canadian Journal of Earth Science 39, 999–1012.

Schopf, J.W. 1968. Microflora of the Bitter Springs Formation, Later Precambrian, central Australia. Journal of Paleontology, 42, 652-688.

Severson, M.J., Heine, J.J. Patelke, M.M. 2009. Geologic and stratigraphic controls of the Biwabik Iron Formation and the aggregate potential of the Mesabi Iron Range, Minnesota. Technical Report, National Resources Research Institute, University of Minnesota, Duluth.

Severson, M.J., Ojakangas, R.W., Bird, J., Campbell, T.J. 2010 Field Trip 3A: Geology and Metamorphism of the Eastern Mesabi Iron Range, in Field Guide to the geology of Precambrian iron formations in the western Lake Superior region, Minnesota and Michigan. Precambrian Research Center Guidebook, 53-66.

Shapiro, R.S., Konhauser, K.O. 2015. Hematite-coated microfossils: Primary ecological fingerprint of taphonomic oddity of the Paleoproterozoic? Geobiology, 13, 209-224.

Siever, R. 1992. The silica cycle in the Precambrian. Geochimica Cosmochimica Acta, 56, 3265-3272.

Silver, L.P. 1906. The Animikie iron range, in Annual Report, Ontario Bureau of Mines, part 1, 15(5), 156-172.

Simonson, B.M. 1985. Sedimentological constraints on the origins of Precambrian iron-formations. Geological Society of America Bulletin, 96, 244-252.

Simonson, B.M. 1987. Early silica cementation and subsequent diagenesis in arenites from four Early Proterozoic iron formations of North America. Journal of Sedimentary Petrology, 57, 494-511.

Simonson, B.M., Hassler, S.W. 1996. Was the deposition of large Precambrian iron formations linked to major marine transgressions? The Journal of Geology,104, 665-676.

Smith, W.N. 1905. Loon Lake iron bearing district. Annual Report, Ontario Bureau of Mines, 14, 254-260.

Sommers, M.G., Awramik, S.M., Woo, K.S. 2000. Evidence for initial calcite-aragonite composition of Lower Algal Chert member ooids and stromatolites, Paleoproterozoic Gunflint Formation, Ontario, Canada. Canadian Journal of Earth Sciences, 37, 1229-1243.

Sommers, M.G., Dollhopf, M.E., Douglas, S. 2002. Freshwater ferromanganese stromatolites from lake Vermilion, Minnesota: Microbial culturing and environmental scanning electron microscopy investigations. Geomicrobiology Journal, 19, 407-427.

Southwick, D.L. and Morey, G.B. 1991. Tectonic imbrication and foredeep development in the Penokean orogeny, east-central Minnesota. An interpretation based on regional geophysical and the result of test drilling. U.S. Geological Survey Bulletin 1904-C. 17p.

Sun, S., Konhauser, K.O., Kappler, A., Li, Y.L. 2015. Primary hematite in Neoarchean to Paleoproterozoic oceans. Geologic Society of America Bulletin, 5, 850-861.

Tanton, T.L. 1923. Iron formations at Gravel Lakes, Thunder Bay District, Ontario. Summary report: Geological Survey of Canada, Part C, 1-75.

Tanton, T.L. 1926. Eastern part of the Matawin Iron Range, Thunder Bay District, Ontario. Geologic Survey of Canada, Memoir, 167, 222p.

Tanton, T.L. 1931. Fort William and Port Arthur and Thunder Cap map areas, Thunder Bay District, Ontario. Geologic Survey of Canada, Memoir 167.

Taylor, S.R., McLennan, S.M. 1985. The continental crust; its composition and evolution; an examination of the geochemical record preserved in sedimentary rocks. Blackwell, Oxford, 312 p.

Tazaki, K. 1997. Biomineralization of layer silicates and hydrated Fe/Mn oxides in microbial mats: An electron microscopical study. Clays and Clay Minerals, 45, 203-212.

Trendall, A.F., Blockley, J.G. 1970. The iron formations of the Precambrian Hamersley Group, Western Australia. Geologic Survey of Western Australia Bulletin, 119, 366p.

Tyler, S.A., and Barghoorn, E.S. 1954. Occurrence of structurally preserved plants in Precambrian rocks of the Canadian Shield. Science, 199, 606-608.

Van Hise, C.R., and Leith, C.K. 1911. The geology of the Lake Superior Region. United States Geological Survey Monograph 57, 641p.

Walsh, F., Mitchell, R. 1973. Differentiation between *Gallionella* and *Metallogenium.* Archives of Microbiology, 90, 19-25.

Walter, M.R., Goode, A.D.T., Half, W.M.D. 1976. Microfossils from a newly discovered Precambrian stromatolitic iron-formation in Western Australia. Nature, 261, 221-223.

Walter, M.R., 1976. Developments in sedimentology: Stromatolites. Ed. M.R. Walter Elsevier Scientific Publishing Amsterdam 790p.

Wepruk, E.C. 2014. Eukaryotes and their role in the formation of ferromanganese nodules, Lake Charlotte, Nova Scotia. HBSc Thesis. Lakehead University, Thunder Bay.47p.

White, D.A., 1954. The stratigraphy and structure of the Mesabi Range, Minnesota. Minnesota Geological Survey Bulletin, 38, 92p.

Wilson, J.P.. Woodward, W.F., Johnston, D.T., Knoll, A.H., Grotzinger, J.P., Walter, M.R., McNaughton, N.J., Simon, M., Abelson, J., Schrag, D.P., Summons, R., Allwood, A., Andrew, M., Gammon, C., Garvin, J., Rashby, S., Schwizer, M., Watters, W .A. (2010), Geobiology of the late Paleoproterozoic Duck Creek Formation, Western Australia. Precambrian Research, 179, 135-149.

Winchell, N.H. 1983. Twentieth annual report for the year 1891: Minnesota Geological Natural Histroy Survey, 344p.

Winter, B.L., Knauth, P,L. 1992. Stable isotope geochemistry of cherts and carbonates from the 2.0 Ga Gunflint Iron Formation: Implications for the depositional setting, and the effects of diagenesis and metamorphism. Precambrian Research, 59, 283-313.

Wolff, J.F. 1917. Recent geologic developments on the Mesabi Iron Range, Minnesota. America Institute of Mining and Metallurgical Engineers, Transactions, 56, 229-257.

Yip, C. 2015. Sedimentology and geochemistry of regressive and transgressive surfaces in the Gunflint Formation, Northwestern Ontario. MSc Thesis, Lakehead University.

Zielinski, A.M., Manusco, J.J., Frizado, J.P., and Waidler, R.J. 1994. Manganese-rich oncolites in the Biwabik iron formation, Eveleth mine, Mesabi North Range, Minnesota,: *in* Southwick,

D.L., ed., Short communications to the geology of Minnesota: St. Paul, Minnesota Geological Survey, 48–59

6 Appendices

6.1 Bulk Geochemical Data

Table 2. Major element bulk geochemical values for Lower Stromatolitic Member

	Al_2O_3	CaO	Fe_2O_3	K_2O	MgO	Na_2O	MnO	P_2O_5	TiO_2
KF-A	0.0231	1.3328	0.6520	0.0115	0.2739	0.0104	0.1378	0.0000	0.0005
KF-B	0.0315	2.6055	1.4057	0.0107	0.8649	0.0273	0.2129	0.0000	0.0023
KF-C	0.0368	3.5659	0.3565	0.0098	0.1409	0.0158	0.0821	0.0000	0.0008
KF-S	0.0492	2.2412	0.6039	0.0124	0.2546	0.0140	0.1189	0.0000	0.0006
SC-A	0.1551	0.2058	0.1536	0.0160	0.0081	0.0408	0.0049	0.0000	0.0044
SC-B	0.1322	0.1269	0.1834	0.0135	0.0078	0.0299	0.0032	0.0000	0.0043
SC-3	0.1471	0.1555	0.2148	0.0171	0.0104	0.0462	0.0031	0.0000	0.0066
SC-X	0.1114	4.3562	0.5076	0.0178	0.0433	0.0380	0.0372	0.0000	0.0096
WF-A	0.0109	0.0372	4.2308	0.0082	0.0085	0.0212	0.0364	0.0000	0.0014
WF-B	0.0135	0.0449	4.5437	0.0065	0.0127	0.0078	0.0177	0.0000	0.0014
WF-3	0.0709	0.0529	0.2535	0.0146	0.0139	0.0134	0.0151	0.0000	0.0040
WF-10	0.0675	0.0215	0.2996	0.0106	0.0159	0.0116	0.0147	0.0000	0.0020

Table 3. Major element bulk geochemical values for Middle Stromatolitic Member

	Al_2O_3	CaO	Fe_2O_3	K_2O	MgO	Na_2O	MnO	P_2O_5	TiO_2
DH3-01	ND	ND	15.4483	0.0247	1.0838	ND	0.0203	0.0008	0.0034
DH3-02	0.2645	3.5228	17.1697	0.0390	0.5860	ND	0.0260	0.0104	0.0093
DH3-03	ND	0.2193	7.3132	0.0047	0.1731	ND	ND	0.0008	0.0022
DH3-04	0.4199	5.6860	20.2264	0.2605	0.7572	0.0823	0.0940	0.0172	0.0160
DH3-05	ND	2.7924	19.1741	ND	0.7973	ND	0.0783	0.0000	ND

Table 4. Major element bulk geochemical values for Upper Stromatolitic Member

	Al_2O_3	CaO	Fe_2O_3	K_2O	MgO	Na_2O	MnO	P_2O_5	TiO_2
LWD A	0.11258	0.18401	12.96988	0.01947	0.13292	0.01405	0.06899	0.00980	0.02492
LWD 5A	0.13926	0.90689	20.17568	0.01517	0.47145	0.01750	0.77163	0.00145	0.01409
LWD 6A	0.11129	7.99637	24.49916	0.01452	3.49873	0.02889	1.26281	0.00000	0.01058
ME-01	ND	ND	15.92011	ND	0.03170	ND	ND	0.01514	0.01056
ME-06	0.07305	ND	8.98311	ND	0.01084	ND	0.01528	0.00762	0.03174
ME-07	ND	ND	23.99802	ND	0.01254	ND	0.02210	0.00503	0.00179
PR98-6 LG ONC	0.12263	0.74678	22.35648	ND	0.25176	0.04276	0.22402	0.05032	0.00415
PR98-6 SM ONC	0.24016	1.79423	19.96313	ND	0.46560	0.27574	0.33907	0.04666	0.00339
PR98-7 ONC	0.18128	1.08903	22.42511	ND	0.27999	0.10361	0.19373	0.02442	0.00381
PR98-7 CEM	0.07037	1.05377	10.16667	ND	0.25836	0.02307	0.07666	0.00473	0.00176
PR98-11 ONC	0.52012	1.53957	4.74230	ND	0.07490	0.04597	0.05631	0.01315	0.00600
PR98-11C	0.03356	1.27428	3.55563	ND	0.61848	0.04103	0.14306	0.00143	ND
VHD 22	0.08960	0.25626	11.84325	0.02619	0.23141	0.02025	0.49954	0.00000	0.00511
VHD 27A	0.07237	1.10166	17.57358	0.01112	0.42774	0.01495	1.66825	0.04162	0.01137
VHD X	0.27138	4.68865	38.84213	0.08069	1.74837	0.03300	2.22038	0.01105	0.00880

6.2 REE Geochemical Data

Table 5. PAAS normalized REE values for Lower Stromatolitic Member

	La	Ce	Pr	Nd	Sm	Eu	Gd	Tb	Dy	Ho	Er	Tm	Yb	Lu
KF-A	0.0239	0.0112	0.0163	0.0183	0.0209	0.0481	0.0352	0.0310	0.0267	0.0323	0.0302	0.0296	0.0266	0.0231
KF-B	0.0317	0.0157	0.0245	0.0276	0.0323	0.0676	0.0513	0.0413	0.0395	0.0404	0.0435	0.0395	0.0362	0.0323
KF-C	0.0463	0.0265	0.0319	0.0354	0.0427	0.0759	0.0659	0.0556	0.0457	0.0464	0.0460	0.0469	0.0426	0.0462
KF-S	0.0332	0.0186	0.0239	0.0272	0.0335	0.0685	0.0494	0.0439	0.0359	0.0373	0.0361	0.0346	0.0298	0.0254
SC-A	0.0347	0.0301	0.0358	0.0417	0.0503	0.1148	0.0667	0.0504	0.0395	0.0343	0.0302	0.0296	0.0270	0.0231
SC-B	0.0312	0.0293	0.0359	0.0422	0.0533	0.0889	0.0633	0.0452	0.0303	0.0242	0.0193	0.0148	0.0138	0.0115
SC-3	0.0785	0.0727	0.0900	0.1072	0.1384	0.2037	0.1725	0.1240	0.0818	0.0636	0.0456	0.0321	0.0312	0.0300
SC-X	0.0960	0.0699	0.0930	0.1053	0.1416	0.2639	0.2167	0.1744	0.1455	0.1191	0.1021	0.0914	0.0801	0.0647
WF-A	0.0249	0.0119	0.0181	0.0196	0.0259	0.0519	0.0397	0.0388	0.0372	0.0373	0.0382	0.0346	0.0298	0.0277
WF-B	0.0177	0.0111	0.0148	0.0159	0.0202	0.0611	0.0322	0.0336	0.0299	0.0293	0.0288	0.0296	0.0273	0.0185
WF-3	0.0079	0.0037	0.0048	0.0053	0.0065	0.0269	0.0109	0.0116	0.0137	0.0151	0.0182	0.0173	0.0131	0.0115
WF-10	0.0074	0.0035	0.0051	0.0053	0.0061	0.0148	0.0099	0.0090	0.0081	0.0101	0.0088	0.0099	0.0078	0.0092

Table 6. PAAS normalized REE values for Middle Stromatolitic Member

	La	Ce	Pr	Nd	Sm	Eu	Gd	Tb	Dy	Ho	Er	Tm	Yb	Lu
DH-3 01	0.0059	0.0071	0.0071	0.0082	0.0115	0.0278	0.0191	0.0168	0.0139	0.0161	0.0161	0.0148	0.0142	0.0162
DH-3 02	0.0468	0.0528	0.0455	0.0470	0.0533	0.0972	0.0768	0.0672	0.0639	0.0636	0.0632	0.0642	0.0525	0.0462
DH-3 03	0.0138	0.0145	0.0134	0.0142	0.0173	0.0296	0.0255	0.0258	0.0265	0.0262	0.0274	0.0296	0.0273	0.0277
DH-3 04	0.1154	0.1231	0.1089	0.1244	0.1607	0.2796	0.2348	0.2300	0.2282	0.2190	0.2305	0.2173	0.1887	0.1709
DH-3 05	0.0350	0.0363	0.0300	0.0333	0.0441	0.0917	0.0702	0.0672	0.0690	0.0646	0.0719	0.0642	0.0560	0.0462
CY-71	0.0419	0.0467	0.0330	0.0442	0.0405	0.0562	0.0388	0.0366	0.0389	0.0378	0.0379	0.0420	0.0369	0.0323
CY-73A	0.0437	0.0337	0.0319	0.0446	0.0436	0.0689	0.0526	0.0432	0.0498	0.0477	0.0498	0.0536	0.0518	0.0499
CY-73B	0.0359	0.0525	0.0392	0.0546	0.0625	0.0796	0.0687	0.0718	0.0771	0.0748	0.0772	0.0832	0.0674	0.0570
CY-77	0.0285	0.0345	0.0241	0.0331	0.0319	0.0458	0.0339	0.0358	0.0350	0.0331	0.0316	0.0356	0.0301	0.0247

Table 7. PAAS normalized REE values for Upper Stromatolitic Member

	La	Ce	Pr	Nd	Sm	Eu	Gd	Tb	Dy	Ho	Er	Tm	Yb	Lu
LWD 5A	0.1587	0.1111	0.1401	0.1481	0.1714	0.3111	0.2541	0.2506	0.2455	0.2371	0.2305	0.2370	0.2082	0.1848
LWD A	0.0367	0.0411	0.0366	0.0409	0.0582	0.1111	0.0873	0.0853	0.0863	0.0858	0.0933	0.0963	0.0915	0.0901
LWD 6A	0.1653	0.1220	0.1704	0.1924	0.2625	0.6093	0.4571	0.4354	0.4410	0.4420	0.4582	0.4296	0.3564	0.3441
ME-01	0.3060	0.2096	0.2264	0.2279	0.2092	0.2120	0.2330	0.1718	0.1197	0.1039	0.1063	0.1185	0.1124	0.1039
ME-06	0.1750	0.1380	0.1208	0.1162	0.1099	0.1111	0.1232	0.0995	0.0810	0.0757	0.0947	0.1136	0.1135	0.1178
ME-07	0.0696	0.0782	0.0599	0.0607	0.0769	0.0935	0.0981	0.0930	0.0870	0.0817	0.0849	0.0840	0.0734	0.0670
PR98-6 SM ONC	0.0901	0.1338	0.0967	0.1033	0.1301	0.1806	0.1863	0.1473	0.1308	0.1251	0.1288	0.1160	0.0904	0.0924
PR98-6 LG ONC	0.0471	0.0809	0.0580	0.0676	0.0825	0.1370	0.1296	0.1008	0.0908	0.0848	0.0870	0.0765	0.0660	0.0554
PR98-7 CEM	0.0169	0.0252	0.0189	0.0213	0.0317	0.0509	0.0569	0.0543	0.0562	0.0585	0.0663	0.0716	0.0504	0.0439
PR98-7 ONC	0.0385	0.0574	0.0428	0.0467	0.0658	0.1028	0.1013	0.0827	0.0765	0.0747	0.0793	0.0765	0.0610	0.0508
PR98-11 ONC	0.0121	0.0152	0.0104	0.0106	0.0105	0.0148	0.0159	0.0116	0.0122	0.0101	0.0112	0.0099	0.0071	0.0069
PR98-11 CEM	0.0059	0.0077	0.0062	0.0077	0.0099	0.0185	0.0170	0.0155	0.0177	0.0182	0.0172	0.0173	0.0181	0.0139
VHD X	0.1986	0.1309	0.2225	0.2666	0.4052	0.6593	0.6240	0.6124	0.6303	0.6135	0.6389	0.6790	0.6255	0.6005
VHD 27A	0.0610	0.0568	0.0692	0.0833	0.1132	0.2037	0.1751	0.1525	0.1365	0.1251	0.1175	0.1062	0.0844	0.0762
VHD 22	0.0329	0.0195	0.0240	0.0250	0.0295	0.0528	0.0448	0.0465	0.0479	0.0515	0.0635	0.0691	0.0617	0.0670